TRANSITION-METAL IMIDAZOLATE POLYMERS: A NEW FAMILY OF MOLECULE-BASED MAGNETS

by

VICTOR SANCHEZ

B.Sc., Universidad Autónoma del Estado de México, 1986
M.Sc., Universidad Autónoma del Estado de Morelos, 1992

A THESIS SUBMITTED IN PARTIAL FULFILMENT OF THE REQUIREMENTS FOR THE DEGREE OF

DOCTOR OF PHILOSOPHY

in

THE FACULTY OF GRADUATE STUDIES
(Department of Chemistry)

We accept this thesis as conforming
to the required standard

THE UNIVERSITY OF BRITISH COLUMBIA

July 2001

In presenting this thesis in partial fulfilment of the requirements for an advanced degree at the University of British Columbia, I agree that the Library shall make it freely available for reference and study. I further agree that permission for extensive copying of this thesis for scholarly purposes may be granted by the head of my department or by his or her representatives. It is understood that copying or publication of this thesis for financial gain shall not be allowed without my written permission.

Department of Chemistry

The University of British Columbia
Vancouver, Canada

Date July 19, 2001

DE-6 (2/88)

ABSTRACT

One-, two- and three-dimensional transition-metal coordination polymers involving imidazolate-based ligands have been prepared and characterized structurally and magnetically.

A 1-D material, $[Fe(pz)_2]_x$ (pz = pyrazolate), which exhibits weak antiferromagnetic exchange (short-range), was found to possess a chain type structure in which metal ions are doubly bridged by pyrazolate ligands. In contrast, when imidazolate-type ligands were utilized in the synthesis of binary metal-azolate complexes, 3-D extended systems were produced as a consequence of the single-bridging of metal ions characteristic of imidazolate ligands. Hence, $[Fe(4\text{-abimid})_2]_x$ (4-abimid = 4-azabenzimidazolate), and its cobalt analogue, both of which have a novel 3-D single diamondoid structure, were prepared. Both of these materials exhibit long-range ferromagnetic ordering at low temperatures. $[Co(imid)_2]_x$, (imid = imidazolate); $[Cu(2\text{-meimid})_2]_x$ (2-meimid = 2-methylimidazolate); $[Co(benzimid)_2]_x$, $[Ni(benzimid)_2]_x$ and $[Cu(benzimid)_2]_x$ (benzimid = benzimidazolate); $[Cu(4,5\text{-dichloroimid})_2]_x$ (4,5-dichloroimid = 4,5-dichloroimidazolate); and $[Co_3(imid)_6(imidH)_2]_x$ (imidH = imidazole), all exhibit magnetic behaviour that classifies them as molecule-based magnets. Indirect evidence suggests that these materials also have extended 3-D lattices.

$[Fe_2(imid)_4(bipy)]_x$ (bipy = 2,2'-bipyridine), $[Co_2(imid)_4(bipy)]_x$ and $[Fe_4(imid)_8(terpy)]_x$ (terpy = 2,2':6',2"-terpyridine), have 2-D structures, a structural motif never before seen in polymetallic imidazolates. The 'pyridine' molecules act as chelating,

capping, ligands which separate the extended sheets of imidazolate-bridged metal ions in these materials. $[Fe_2(imid)_4(bipy)]_x$ is unique in exhibiting two structural phase transitions. Both $[Fe_2(imid)_4(bipy)]_x$ and $[Co_2(imid)_4(bipy)]_x$ exhibit long-range ferromagnetic ordering at low temperatures while $[Fe_4(imid)_8(terpy)]_x$ shows more complex magnetization behaviour. All three of these materials can be considered molecule-based magnets.

$[Fe(1\text{-Me-2-S-imid})_2 \cdot 0.5Cp_2Fe]_x$ (1-Me-2-S-imid = 1-methyl-2-thioimidazolate; Cp_2Fe = ferrocene), was obtained as a rare example of a 1-D chain polymer that exhibits long-range magnetic ordering. Alternating FeN_4 and FeS_4 chromophores along the chains is a unique structural feature of this material.

The single-bridging imidazolate ligands involved in most of the compounds studied here are efficient mediators of magnetic exchange interaction between metal centres. The observation of antiferromagnetic behaviour above a critical temperature, T_c, and long-range ferromagnetic ordering below T_c suggests canted spin structures for many of these compounds. Importantly, long-range three-dimensional ordering of the residual spins, arising from the canting, leads to net magnetization at zero applied field. These magnetic properties classify these novel materials as molecule-based magnets.

TABLE OF CONTENTS

LIST OF TABLES

LIST OF FIGURES

LIST OF ABBREVIATIONS AND SYMBOLS

~	approximately
%	percent
χ	magnetic susceptibility
χ'	in-phase magnetic susceptibility
χ''	out-of-phase magnetic susceptibility
° or deg	degree(s)
η	hapticity
δ	isomer shift
° C	degree(s) Celsius
μ_B	Bohr magneton
μ_{eff}	effective magnetic moment
θ	X-ray diffraction angle or Curie-Weiss law correction term
ΔE	quadrupole splitting
H	applied magnetic field
H_o	applied magnetic field static component
H_1	applied magnetic field oscillating component
1-D	one-dimensional
2-D	two-dimensional

3-D	three-dimensional
F	goodness-of-fit parameter
f	frequency
cm^{-1}	wavenumber(s)
S	length of the coil
v	strength of the induced voltage
μ	permeability of a material
ω	period of oscillation
φ	phase angle
Cp_2Fe or $FeCp_2$	ferrocene
Å	Angstrom(s)
bipy	2,2'-bipyridine
C	Curie constant
cm	centimeter(s)
cos	cosine
coth	hyperbolic cotangent
FCM	field-cooled magnetization
fw	formula weight
g	Landé splitting factor
G	Gauss
g	gram(s)
Hz	hertz

imidH	imidazole
imid	imidazolate
IR	infrared
J	magnetic exchange coupling constant
k	Boltzmann constant
K	Kelvin
Me or me	methyl
ml	mililiter(s)
mmol	milimole(s)
mol	mole(s)
M	magnetization
M_s	saturation magnetization
N	Avogadro's number
NIR	near infrared
nm	nanometer(s)
NMR	nuclear magnetic resonance
ORTEP	Oakridge thermal ellipsoid plot
P	relative proportion of paramagnetism impurity
pz	pyrazolate
Ref.	reference
REM or M_{rem}	remnant magnetization
S	total spin

sin	sine
SQUID	superconducting quantum interference device
t	time
T or *T*	temperature
tan	tangent
T_C	Curie temperature
T_c	critical temperature
terpy	2,2':6',2"-terpyiridine
T_N	Néel temperature
TGA	thermal gravimetric analysis
UV	ultraviolet
Vis or VIS	visible
VSM	vibrating sample magnetometer
ZFCM	zero-field-cooled magnetization

ACKNOWLEDGMENTS

I would like to express my sincere gratitude to my research supervisors, Drs. Robert C. Thompson and Alan Storr, for their remarkable support, guidance and great professional commitment during the development of this thesis.

I am grateful to Dr. William M. Reiff at Northeastern University for his valuable contribution to this work and for fruitful discussions on Mössbauer spectroscopy.

I would like also to thank the members of my guidance committee, Drs. C. Orvig, M. Wolf and D. Douglas for their knowledgeable suggestions during the final preparation of this dissertation.

My gratitude is also extended to Drs. S. J. Rettig and B. O. Patrick of this Department for their expert crystal structure determinations, to Mr. P. Borda of this Department for microanalytical services, and to Mr. Pinder Dosanjh of the Advanced Materials and Process Engineering Laboratory at U.B.C. for assistance on the SQUID magnetometer. Many thanks are also extended to the experts in the glassblowing, electronics and mechanical shops for their aid.

I also thank my colleagues Dr. D. A. Summers, Dr. Z. Xu, Ms. I. Sham and Ms. C. L. Stevens for their assistance and for making my time in this Department more enjoyable.

I want to give special thanks to my parents, and dedicate this work in commemoration of their fiftieth wedding anniversary.

Finally, I wish to offer my deepest gratitude to my wife Emma Verónica, for her love and endless encouragement throughout this endeavour.

Chapter 1 *INTRODUCTION*

The search for and study of new molecule-based magnets, molecular materials that show spontaneous magnetization below some critical temperature, has become an area of considerable interest and activity in recent years [1]. Coordination polymers of the transition metals exhibiting such properties constitute a sub-classification of molecule-based magnets. The structural diversity of these materials and the fact that many contain ligands that are amenable to systematic derivatization, raises the possibility of tailoring their properties to specific desired applications [2].

Molecular magnetism is a multidisciplinary area of investigation that requires the combined efforts of chemists, physicists and materials scientists to establish the necessary fundamentals. In magnetochemistry, a chemist must be able to explain the magneto-structural correlations in a material. This work requires the use of a variety of techniques for both structural and magnetic characterization. Also important is the ability to synthesize multidimensional extended molecular systems, such as coordination polymers, with potentially interesting magnetic properties.

One of the aims in the current work was to synthesize coordination polymers of transition metals, with different dimensionality, capable of exhibiting long-range magnetic ordering. The ligands chosen to connect the transition metals in this study

were diazolates, mainly 1,3-diazolates. It was anticipated that, due to the positioning of the nitrogen coordinating atoms in 1,3-diazolates, the formation of 2-D or 3-D structures (involving single azolate bridges) could be achieved.

Fundamental concepts in (i) magnetism and molecule-based magnets, (ii) dimensionality and connectivity in extended systems (coordination polymers) and (iii) the azolates as bridging ligands of transition metals are outlined in this Chapter. The techniques employed in this work in the physical characterization of materials are also briefly described. The general objectives of the research and a description of the organization of this dissertation are also included at the end of this Chapter.

1.1 MAGNETISM

1.1.1 INTRODUCTION

Magnetism can be measured using two different techniques, by the response (attraction or repulsion) of a material to a magnetic field, which is the basis for the outdated force methods [3], or by state-of-the-art induction methods that determine directly the change in magnetic flux density resulting from placement of the material in a magnetic field [4]. Magnetism is a collective effect based on the coupling of the spin or internal angular momentum of unpaired electrons throughout an entire material [5]. To simplify the following discussion, the orbital angular momentum contribution to the bulk magnetization of materials will be ignored. In other words, a spin-only model will

be employed. Paramagnetism is typically a consequence of the spin associated with an unpaired electron (m_s = ½ ↑ or m_s = -½ ↓) [5]. If a molecule or ion has only paired electrons, it is diamagnetic and will be repelled slightly in an applied magnetic field. If a molecule has an odd number of electrons, there will be at least one unpaired electron, and the molecule would have a net spin. Such molecules or ions are usually sufficiently isolated so that their spin-spin coupling energy, J (as deduced from the Hamiltonian $H = -2JS_A \cdot S_B$) is small compared to (coupling-breaking) thermal energy. Their spins do not couple in the absence of an applied field; these are called simple paramagnets (Figure 1.1).

When two paramagnetic metal ions interact directly such that their magnetic orbitals (those that contain the unpaired electrons) overlap, direct spin coupling operates [6]. In contrast, when paramagnetic metal ions are bridged by ligands, as in many molecule-based magnets (*vide infra*), superexchange coupling [7] takes place as the main mechanism responsible for spin interactions. Hence, spin-spin interactions may be large enough to enable an effective parallel –called ferromagnetic (↑↑)– or antiparallel –called antiferromagnetic (↓↑)– coupling (Figure 1.1).

It is important to describe at this point a distinction between short-range and long range magnetic ordering. Short-range order may be described as the tendency of the paramagnetic spins to orient themselves locally relative to one another when a

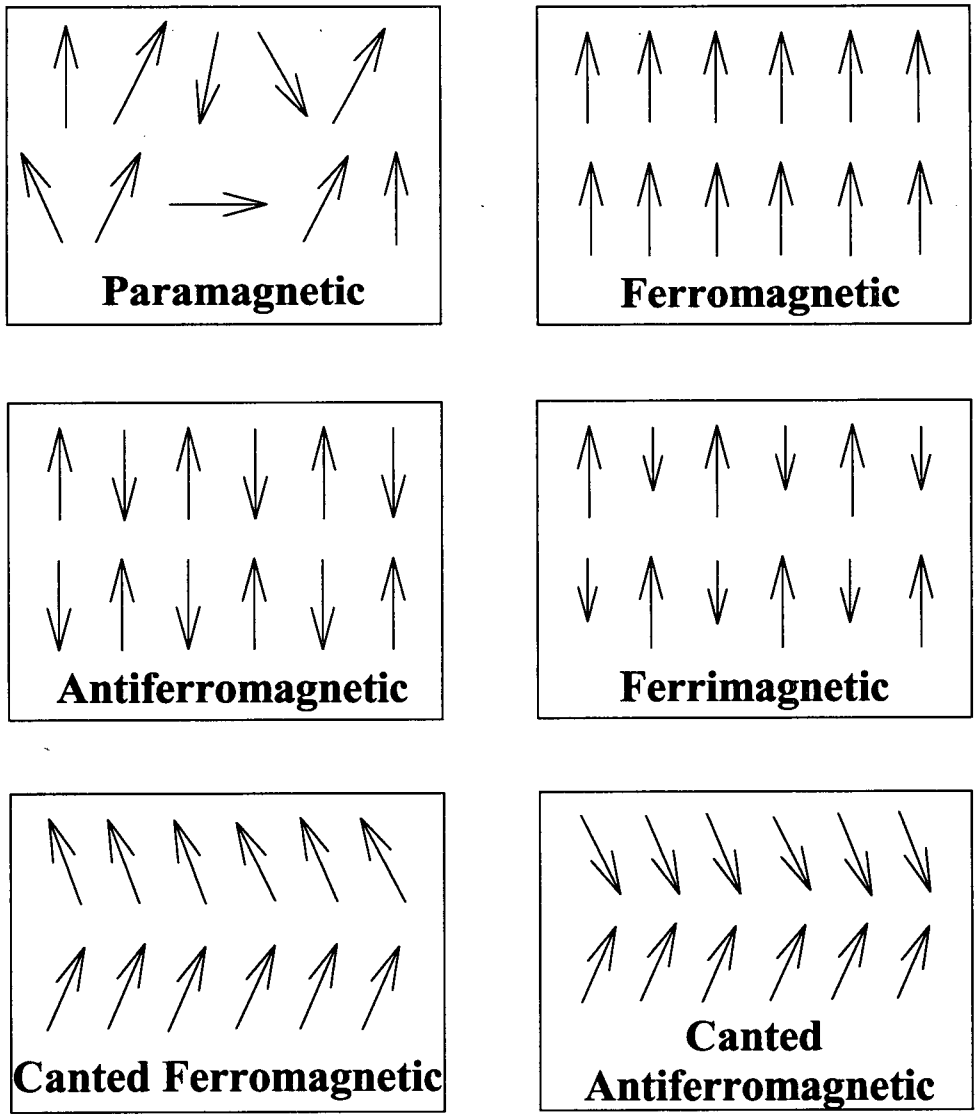

Figure 1.1 Schematic illustration of magnetic behaviors.

material is cooled [8]. Magnetic interactions in clusters are an example of short-range order [9]. Long-range magnetic ordering, on the other hand, is the result of an extended and cooperative ordering of the spins throughout the lattice. Long-range order

accompanies a change in the spin phase of a material [10]. Therefore, bulk ferromagnetic behaviour occurs when the spins in a material undergo long-range alignment in the same direction, resulting in a net magnetic moment. Hence, ferromagnetism requires that the individual unpaired spins interact collectively with each other aligning themselves parallel and in the same direction. Ferrimagnetism occurs when, due to the presence of magnetic dipoles of different size, antiferromagnetic coupling does not lead to complete cancellation of moments and a net moment remains (Figure 1.1). It is important to note that potentially commercially useful ferro– or ferrimagnetic behavior is not a property of a single molecule or ion; it, like superconductivity, is a cooperative solid-state bulk property [11].

As mentioned previously, paramagnets are characterized by their response to an applied magnetic field, H. For ideal, non-interacting spins a net magnetic moment or magnetization, M, is induced in the material when exposed to an applied field, H; where M is proportional to H,

$$M = \chi H$$

The proportionality constant is termed the molar magnetic susceptibility, χ. A material is magnetically isotropic when both the magnitude and the direction of M do not depend on orientation. In this case the direction of M is coincident with that of H, regardless of

the specimen orientation. If, on the contrary, a material is magnetically anisotropic, the direction and magnitude of M depend on orientation [12].

The magnetic susceptibility of a simple paramagnet has a temperature dependence that is characterized by the Curie expression [13],

$$\chi = \frac{C}{T}$$

The Curie constant C in cm^3 K mol^{-1}, is defined according to the following equation,

$$C = \frac{Ng^2\mu_B^2 S(S+1)}{3k}$$

in which S is the spin quantum number, N is Avogadro's number, g is the Landé factor, μ_B is the Bohr magneton, and k is the Boltzmann constant. If the spins experience an effective parallel (or antiparallel) exchange field due to cooperative interactions with neighboring spins this will increase (or decrease) the measured susceptibility from that predicted for independent spins by the Curie law. In these instances, the high-temperature susceptibility data often can be fit to the Curie- Weiss law [14],

$$\chi = \frac{C}{T-\theta}$$

where for parallel (ferromagnetic) or antiparallel (antiferromagnetic) interactions, θ is greater or less than zero, respectively. The value of θ can be determined from the intercept obtained in the linear extrapolation of the plot of χ^{-1} versus T at high temperature. The temperature dependencies of χ^{-1} are illustrated for independent spins (Curie law) and spins with ferro–, and antiferromagnetic interactions in Figure 1.2.

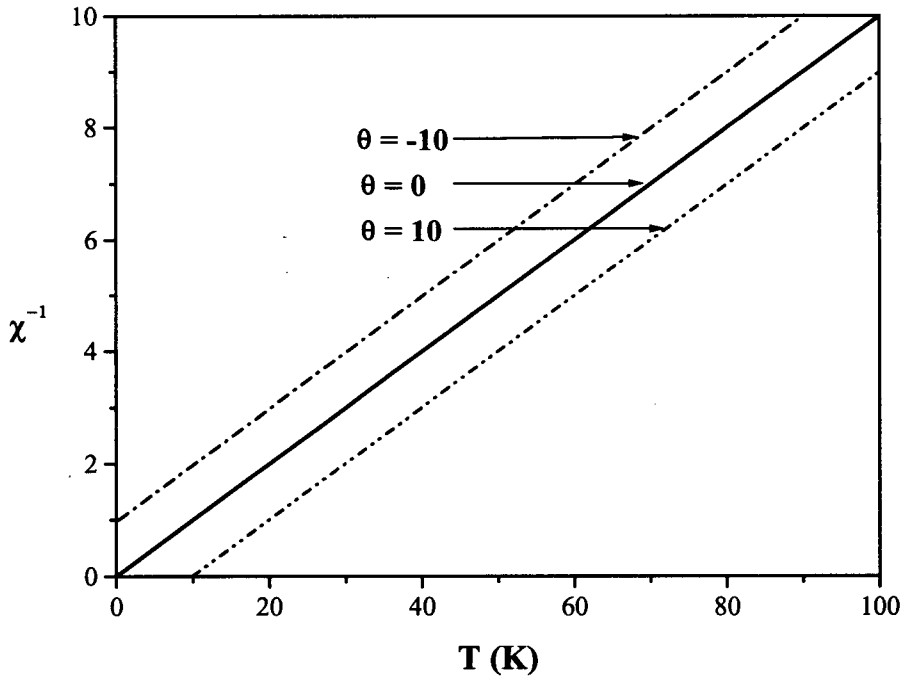

Figure 1.2 The reciprocal susceptibility χ^{-1} extrapolated from the high-temperature region as a function of temperature for independent $g = 2$, $S = ½$ spins as well as ferromagnetically coupled (θ = 10 K) and antiferromagnetically coupled (θ = -10 K) spins.

Very frequently in magnetic studies of materials the effective moment, μ_{eff}, or simply χT, is reported [15]. The effective moment, in units of the Bohr magneton (μ_B), is defined by the following equation,

$$\mu_{eff} = \sqrt{\frac{3\chi kT}{N}} = 2.828\sqrt{\chi T}$$

For a simple system comprising one mole of non-interacting spins (i.e., $\theta = 0$), and where S is a valid spin quantum number, μ_{eff} is temperature-independent [15],

$$\mu_{eff} = \sqrt{g^2 S(S+1)}$$

At low temperatures and high magnetic fields, conditions under which the magnetic energy ($gS\mu_{eff}H$) is comparable in magnitude to the thermal energy (kT), the magnetization no longer obeys the equation $M = \chi H$, but approaches the limiting value or saturation magnetization, M_s,

$$M_S = \mu_B NSg$$

For a system with non-interacting spins (i.e., $\theta = 0$) the temperature dependence of M can be calculated from the Brillouin function [16],

$$M = \mu_B NSgB$$

where

$$B = \frac{2S+1}{2S}\coth\left(\frac{2S+1}{2S}\right) - \frac{1}{2S}\coth\left(\frac{x}{2S}\right)$$

and

$$x = \frac{gS\mu_B B}{kT}$$

Because the response to an applied magnetic field varies depending on the type of magnetic coupling within the material, a plot of magnetization as a function of applied field produces a curve with a shape characteristic of the type of magnetic coupling occurring in the material [5] (Figure 1.3). In Figure 1.3 the line labelled paramagnetic represents a simple paramagnetic system where there is no spin coupling. In this case the initial slope of the observed M versus H data is as expected for the equation $M = \mu_B NSgB$. Antiferromagnetic coupling is evident if the initial slope is less than this and ferromagnetic coupling is evident if the initial slope exceeds the value expected by this equation. The M versus H plot of a diamagnetic sample will contrast with that of a paramagnetic one by having a negative slope (Figure 1.3). Metamagnetism is a transformation from an antiferromagnetic state to a high-moment ferromagnetic state; that is, the spin alignment changes from antiparallel to parallel by the occurrence of an applied magnetic field [17]. This generates an M versus H curve of the type shown in Figure 1.3.

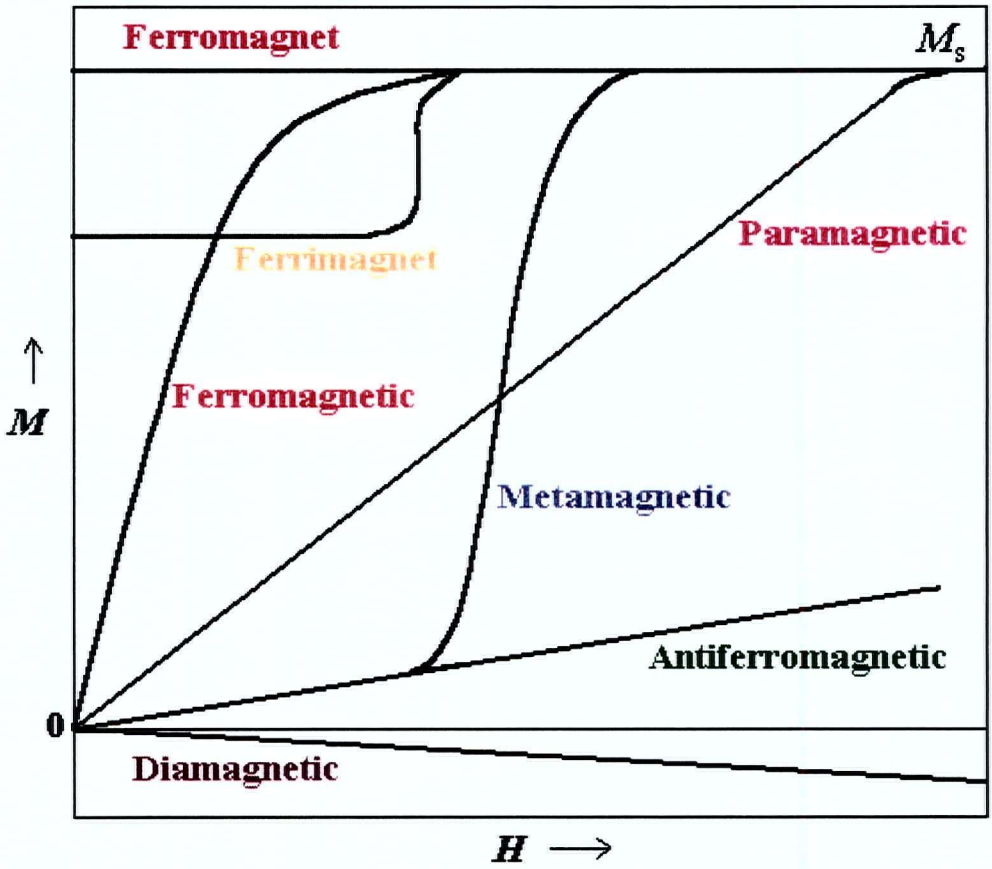

Figure 1.3 Schematic illustration of the magnetization, M, as a function of applied magnetic field, H, for several types of commonly observed magnetic behavior.

When long-range magnetic ordering is present in a material, the temperature at which the spins order is termed the critical temperature, T_c. If the spins align ferromagnetically, a spontaneous magnetization in zero applied field is present and below T_c the material is a ferromagnet and the M versus H plot (Figure 1.3) does not extrapolate to zero magnetization at zero applied field. The critical temperature in this case is sometimes referred to as the Curie temperature, T_C. If a long-range antiparallel

alignment of spins occurs, there is no net moment below T_c and the susceptibility is zero. In this situation the critical temperature is sometimes referred to as the Néel temperature, T_N. When ferrimagnetism is present in the system, the critical temperature is also referred to as the Néel temperature, T_N, and below T_N the material is a ferrimagnet and under these conditions the M versus H plot (Figure 1.3), like that of a ferromagnet, does not extrapolate to zero magnetization at zero applied field.

Below T_c the magnetic moments for ferro– and ferrimagnets align in small regions (domains). The direction of the magnetic moment of adjacent domains differs, but can be aligned by application of a minimal magnetic field. This leads to history dependent magnetic behavior (hysteresis) characteristic of ferri– and ferromagnets. Thus, applying an external magnetic field will cause the domains to coalesce and form a single domain aligned with the external field. At low temperatures and high applied magnetic field, the magnet can rapidly reach a maximum magnetization, which is limited by its saturation magnetization, M_s. When the applied field is decreased, the spin alignment of the domains relaxes, but more slowly than the original alignment occurred, so that when the external field reaches zero, some remnant magnetization, M_{rem}, remains. Reversing the direction of the external magnetic field will cause the spins within the magnet to reverse. At a large enough applied magnetic field, the magnetization reaches saturation again, but in the opposite direction. Increasing, then, the applied magnetic field to positive values results in an approximately symmetric closed loop termed a hysteresis loop. A typical hysteresis loop is shown in Figure 1.4.

The coercive field, H_c, is the reverse magnetic field required to reduce the magnetization of a sample to zero starting from a saturation condition magnetization. "Hard" magnets have values of $H_c > 100$ G, whereas "soft" magnets have values of < 10 G. Medium to large values (hundreds of G) of H_c are necessary for permanent magnetic storage of data, while low values (mG) are required for ac motors, magnetic shielding, and in the recording heads necessary to write, read and erase the recording information [18]. Hence, the T_c, M_s, and H_c are key parameters in ascertaining the commercial utility of a magnet.

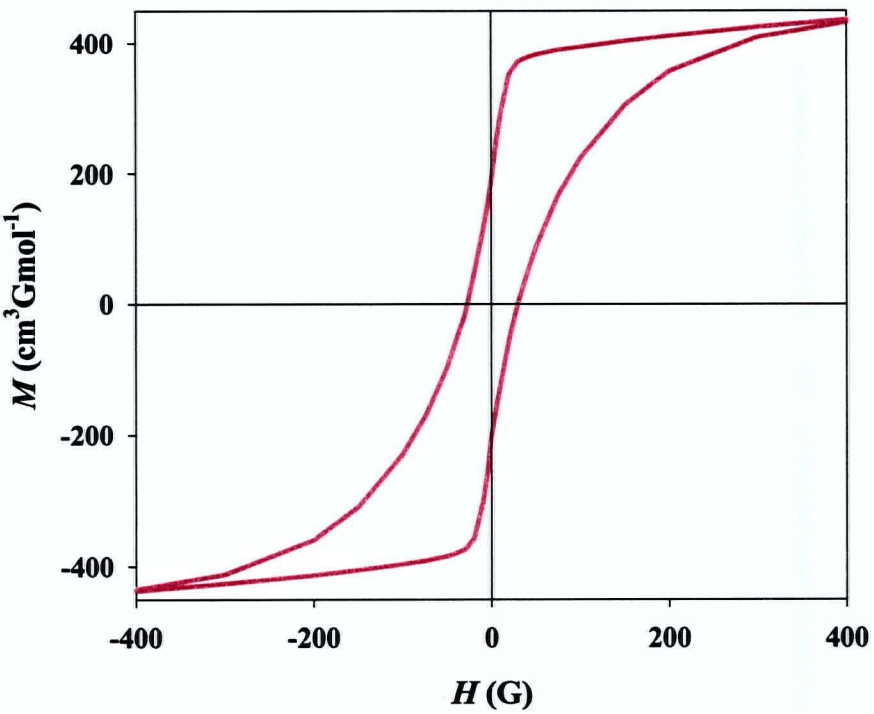

Figure 1.4 A typical magnetic hysteresis loop.

Canted antiferromagnetism, canted ferromagnetism, metamagnetism, and spin-glass behaviors are examples of other possible magnetic phenomena. The canted antiferromagnetic behavior (Figure 1.1, page 4) results from the action of antisymmetric exchange in anisotropic materials in which the coupled magnetic dipoles are not related by an inversion center [19]. The weak ferromagnetism, produced in this type of spin coupling, is due to the fact the antiparallel alignment of spins on the two sublattices have orientations slightly canted to each other. This canting leads to a non-zero magnetization at zero-applied field [20]. A material exhibiting canted antiferromagnetic behavior is referred to as a weak ferromagnet [20]. It should be noted that canted antiferromagnetism is considered to be the primary mechanism accounting for the residual magnetization observed in the molecule-based magnets studied in this dissertation. A canted ferromagnet, on the other hand, results from the relative tilting of ferromagnetically coupled spins (Figure 1.1, page 4) such that, though the material is ferromagnetic, there is a reduction of the residual moment. Finally, a spin glass occurs when there are local spatial correlations in the directions of neighboring spins, but no long-range order. For a spin glass the spin alignment is as described for a paramagnet (Figure 1.1, page 4). However, unlike a paramagnet where the directions of the spins vary with time, the spins remain fixed in their orientations for a spin glass. Hence, a spin glass has spins pointing in similar directions for short distances, but no long-range order [17].

1.1.2 MAGNETIC EXCHANGE

The type of spin coupling, whether ferromagnetic or antiferromagnetic, and the magnitude, can be described by the coupling interaction energy, *J*. When *J* is positive, the coupling is ferromagnetic; when it is negative, the coupling is antiferromagnetic. The value of *J* cannot be measured directly, but can be deduced from a mathematical model fitted to the magnetic data. Different models can give different values of *J* even in systems with a well defined T_c. Three distinct mechanisms for spin coupling have been proposed to lead to ferro– or antiferromagnetism. (Table 1.1). It is difficult to predict in advance which mechanism may dominate in a particular system, and more than one mechanism may be operational.

The most straightforward type of spin coupling occurs between unpaired electrons in orthogonal orbitals in the same spatial region. These spins couple ferromagnetically, and the closer the orbitals are in space (less than 3 Å), the stronger the coupling [21]. This mechanism can lead only to ferromagnetic coupling.

Ferromagnetic coupling can also occur between unpaired electrons that are nominally not in the same spatial region. The most important and powerful exchange mechanism of this type is the termed superexchange. In superexchange [7], non-magnetic moieties (atoms or molecules) can function as mediators for spin coupling between spin carriers. Anderson's theory [22] established that superexchange occurs

Table 1.1 Mechanisms for achieving ferro– or antiferromagnetic spin coupling.

Mechanism	Spin interaction	Spin coupling
1. Spins in Orthogonal Orbitals	Intramolecular	Ferromagnetic
2. Spin coupling via Superexchange	Intramolecular	Ferro– or antiferromagnetic
3. Dipole-dipole (through-space interactions)	Intra– or intermolecular	Ferro– or antiferromagnetic

because the metal d-orbitals, where the unpaired spins originate, overlap with filled s or p orbitals of the mediator atom or atoms. Consequently, delocalized magnetic antibonding orbitals, which include the metal ion and the intermediary atom or atoms, are formed. The spins in two such delocalized magnetic orbitals can interact in two ways: kinetic and potential exchange. Kinetic exchange arises when there is a non-orthogonal orbital interaction pathway between the bridging ligand and two magnetic centres. This process, which is illustrated in Figure 1.5, yields antiferrromagnetic coupling. On the contrary, potential exchange (Figure 1.5) happens when there is orthogonality in the orbital interaction pathway, and ferromagnetic coupling results.

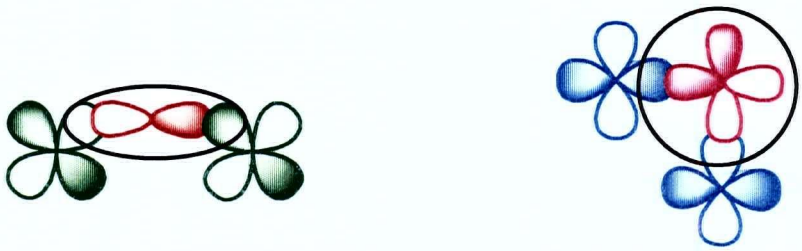

(a) (b)

Figure 1.5 Illustration of the two types of superexchange. (a) kinetic exchange, and (b) potential exchange.

The majority of the compounds studied in this work are paramagnetic transition metal ions separated by imidazolate or pyrazolate ligands, which yields distances between metal ions larger than 3 Å. Hence, superexchange is the main mechanism involved in the magnetic coupling exhibited by the compounds described in this work.

A third type of spin coupling can occur through space between spins in orbitals that do not overlap. These interactions, which occur via the magnetic fields generated with each spin, are very weak and only produce magnetic ordering at temperatures below a few degrees Kelvin [21].

1.1.3 MOLECULE-BASED MAGNETS

Traditional magnetic materials are atom-based, which means that they have d- or f- orbital spin sites, and posses extended network magnetic "bonding" in at least two dimensions. Furthermore, they are prepared by high temperature methodologies. In contrast, molecule-based magnets [23] are materials prepared utilizing the low-temperature synthetic procedures of organic, organometallic, or coordination metal chemistry. As a result, the organic fragment may (i) be an active component with spin sites (free radicals) contributing to both the high magnetic moment and the spin coupling, or (ii) can mediate the spin coupling interaction by delocalization of the spins on the metal ions throughout the ligand molecules (superexchange) [24].

The first molecular ferromagnetic compound was reported by Wickman *et al.* in 1967 [25]. This five-coordinate, square-pyramidal complex, chlorobis(diethyldithiocarbamato)iron(III), orders ferromagnetically at 2.46 K and is rather unusual because it represents a true molecular solid. By definition, a true molecular solid consists of neutral species bonded intermolecularly only by van der Waals interactions and/or hydrogen bonds [26]. Other examples of true molecular ferromagnets that have been described include the purely organic ferromagnets such as β-(p-nitrophenyl)nitronylnitroxide, which has a Curie temperature of 0.6 K [27], and Rassat's dinitroxide [28], which has the highest reported ordering temperature for a purely organic compound with T_c = 1.48 K. In contrast, most of the recently reported

ferromagnetic molecular solids are more accurately described as "molecule-based". Examples include the metallocene charge-transfer salts which consist of organic and organometallic anions and cations bound by Coulomb interactions [29] and the Prussian Blue analog magnets which are three-dimensional coordination polymers involving bridging of metal ions by cyanide anions [30]. The field of molecule-based magnets is a relatively new branch of chemistry [31]. The first compounds of this kind were reported in 1986 [32], and in the last few years an increasing number of research groups have started some activity along this line. The typical synthetic approach to design molecule-based magnets consists of starting from precursors bearing a spin, then assembling them in such a way that there is no compensation of the spins at the scale of the crystal lattice.

Several chemical features can stabilize long-range ferromagnetic coupling. These include having as many spins as possible in orbitals oriented so that the spins can couple strongly to form a magnet. As described, the interactions between spin carriers may occur through space or through bonds. In the former case, a genuine molecular lattice with molecules or molecular ions at the lattice points is involved. In the latter case, a polymeric or extended structure is involved and in this case the magnets are termed "molecule-based". Most often the interactions are much stronger when they occur through bonds (superexchange). This is particularly true when the bridging linkages (ligands) are conjugated [7]. Therefore, an efficient strategy to obtain a molecule-based magnet is to assemble the spin bearing precursors using conjugated

bridging ligands with the structural capability of forming extended structures. This fundamental strategy was followed in the preparation of the molecule-based magnets investigated in the present thesis

Many other important aspects of magnetism may have been left out of the brief account presented here. The interested reader is encouraged to explore further some of the many interesting books and reviews published about this fascinating subject [1, 2, 33 – 42].

1.2 DIMENSIONALITY AND CONNECTIVITY

Dimensionality plays a critical role in determining the properties of materials due to, for example, the different ways that electrons interact in three-dimensional (3-D), two-dimensional (2-D), and one-dimensional (1-D) structures [43]. The study of dimensionality has a long history in chemistry and physics, although this has been primarily with the prefix "quasi" added to the description of materials. That is, quasi-1D solids, such as square-planar platinum chain compounds [44], and quasi-2D layered solids, such as copper oxide superconductors [45].

The control of dimensionality is a major challenge within the metal coordination polymer field [46]. Even when polyfunctional ligands are used to obtain high dimensional polymers, ancillary ligation by water or other solvent ligands may result in

low dimensionality [47]. Hence, the relatively new field of metallo-organic polymers [48], although offering great potential for chemical and structural diversity, suffers from general difficulties in the control of polymer dimensionality or framework stability. Sometimes low-dimensional coordination polymers can lack framework integrity [49], in other cases the resulting coordination polymers are frequently plagued by lattice interpenetration [50] or a framework breakdown upon removal of absorbates [51].

Synthesis at relatively higher temperatures can promote the formation of polymer frameworks of higher dimensionality through the loss of terminal ancillary ligands. Thus, for example, Wood et al. [52] have found a condensed 3D structure for [Mn(TMA)] [TMA = trimesate (benzene-1,3,5-tricarboxylate)], whereas a discrete molecular complex $[Mn(TMA\text{-}H_2)_2(H_2O)_4]$ is formed at room temperature [53]. Hence, the use of synthetic methods, such as the reaction of metallocenes with molten-ligands [54], and those involving solvothermal chemistry [55], have been used in attempts to form higher dimensionality frameworks.

Connectivity is an influential concept that describes the way a set of points connects to build a lattice that is infinite in one to three dimensions, like a crystal [56]. In two dimensions, there are only three regularly connected nets [57]. In this case "regular" means a network that not only has the same number of neighbours at each site, but where there is only one type of polyhedron in the net. For 3-connected planar nets, there is a hexagonal arrangement, while the 4-connected one corresponds to a net

made up of quadrilaterals (not necessarily squares) and regular 6-connected nets are an array of triangles (not necessarily equilateral). The most symmetrical forms of these three regular networks are shown in Figure 1.6.

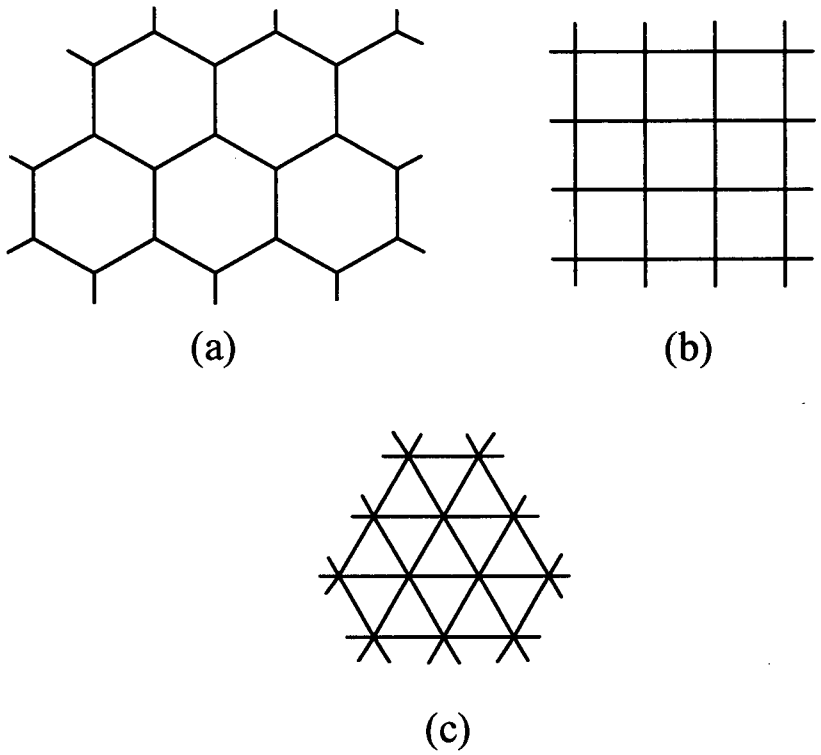

Figure 1.6 The three regular planar nets. (a) 3-, (b) 4- and (c) 6-connected.

It has become more evident that connectivity (i.e. the number and arrangement of interaction pathways between neighbouring centres with localized spins) is critical in generating long-range ordered systems. Since the interaction mechanism between spins

connected through a chemical bonding pathway is superexchange, it is not only the connectivity between atoms that should be considered, but also connectivity between orbitals. Throughout this thesis, the concept of connectivity has been utilized for a better understanding of the relationship between extended structures and magnetic properties in several compounds studied.

Ferromagnetic interactions do not necessarily lead to long-range ferromagnetic ordering. The central point is that such long-range magnetic ordering is rigorously impossible for a system consisting of isolated molecules (zero-dimensional), or of isolated chains (one-dimensional). It may occur for a system consisting of isolated layers (two-dimensional), provided that the spins are not strictly isotropic. On the contrary, long-range magnetic ordering is the normal behaviour of a three-dimensional spin network. Therefore, the design of a molecule-based magnet requires one to create spin interactions along the three directions of space. Furthermore, these interactions must be either ferromagnetic, antiferromagnetic between non-equivalent spin lattices (ferrimagnetism), or as determined in this work, canted antiferromagnetic leading to weak ferromagnetism.

1.3 COORDINATION POLYMERS

A coordination polymer may be defined as a material consisting of metal ions linked by coordinate bonds by mono-atomic or poly-atomic species forming an

extended structure. About 30 years ago, the main interest in coordination polymers depended mainly on the expectation of increased thermal stability for the materials. Over the last 10 years or so, the properties of ordered infinite aggregates of metal ions, connected by bridging ligands, have come to the fore as a subject for synthetic study. As in classical coordination chemistry the local electronic structure at the metal ion remains important but the connectivity of the lattice and the nature of the bridging groups tuning the inter-metallic interactions are essential in determining the properties of the bulk material.

The increasing interest in the area of coordination polymers has been motivated by the ability of the metal–ligand coordination to provide a facile approach to the controlled assembly of one-, two- and three-dimensional extended solids. This strategy presents an excellent opportunity for the construction of functional materials with interesting properties such as, second-order non-linear optical [58], electronic [59], magnetic [60], inclusion [61], and catalytic properties [62].

A general problem in the characterization of coordination polymers arises because of the extreme intractability of many of these of materials, and the consequent lack of available structural information. In addition, owing to the difficulty of obtaining single crystals of these materials, relatively few X-ray structure determinations have been carried out on coordination polymers, necessitating the use of indirect methods of structural characterization.

1.4 DIAZOLES AND DIAZOLATES

Diazoles are five-membered, aromatic, two nitrogen-containing heterocyclic molecules. Among the best known of these compounds are the 1,2-diazole, pyrazole, and the 1,3-diazole, imidazole, which are shown in Figure 1.7. The role of diazoles and their anions (diazolates) as ligands in coordination chemistry is well documented by several reviews published on this topic [63 -65].

(a) (b)

Figure 1.7 Structures of pyrazole (a), and imidazole (b).

From the point of view of molecular architecture, the most important characteristic of the diazolates is the way they bridge metal centres. Both, 1,2-diazolates and 1,3-diazolates act as exo-bidentate ligands; however, while pyrazolates generally form double ligand bridges between metals, imidazolates form only single-ligand

bridges [66] (Figure 1.8). This difference in the coordination modes of these two diazolates can be explained by the steric hindrance imposed by the CH group in the 2-position between the two nitrogens in the 1,3-diazolate (i.e., imidazolate). As a consequence, binary transition-metal imidazolate compounds are typically 3-D coordination polymers, whereas binary transition-metal pyrazolates have linear chain 1-D extended structures [67, 68] (Figure 1.8). Another important property of diazolate polymers is the conjugation of electronic density throughout their structures, This is an important characteristic of these ligands in terms of their ability to mediate magnetic exchange between paramagnetic centers [68].

As a consequence of their structural characteristics, paramagnetic transition metal pyrazolate and imidazolate polymers exhibit different spin coupling behaviours. Thus, while metallic pyrazolate-bridged polymers generally exhibit antiferromagnetic coupling due to antiparallel alignment of their spins (Figure 1.8 (top)), metallic imidazolate-bridged polymers possess a canted-spin structure resulting from an imperfect antiparallel alignment of the spins (Figure 1.8 (bottom)). As previously mentioned, canted-spin antiferromagnetism leads to weak ferromagnetism at low temperatures [19]. Hence, the 3-D long-range magnetic ordering exhibited by several paramagnetic transition-metal imidazolate polymers studied in this thesis, classify them as molecule-based magnets.

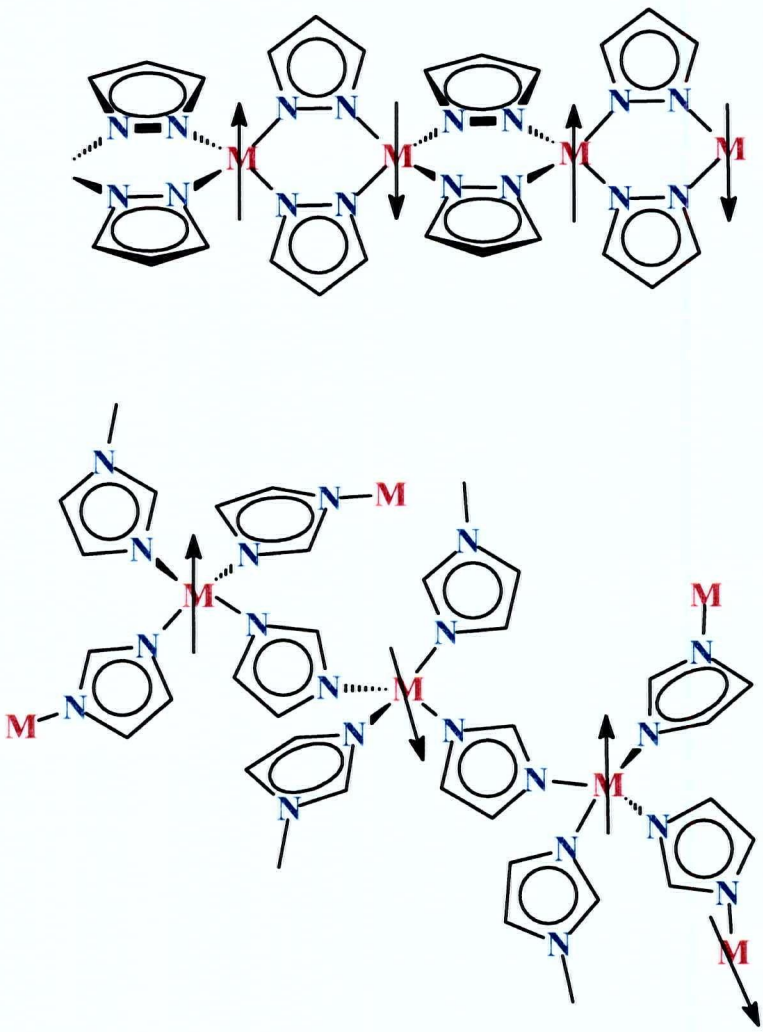

Figure 1.8 Schematic representation of different bridging modes for pyrazolate (1,2-diazolate) (top) and imidazolate (1,3-diazolate) (bottom) metal complexes. Spin orientations (arrows) are also illustrated as expected for the two different structural motifs.

1.5 PHYSICAL METHODS OF CHARACTERIZATION

This section is intended to give a brief description of the principles and general usefulness of the main methods of characterization utilized in this thesis. References to detailed reviews on these techniques are given in the appropriate sections.

DC magnetic susceptibility, thermal gravimetric analysis, X-ray powder diffraction, UV-Vis-NIR spectroscopy and IR spectroscopy studies were performed by the author. AC magnetic susceptibility and Mössbauer spectroscopy studies were performed by Prof. William M. Reiff at the Department of Chemistry of Northeastern University, Boston, Mass., USA. X-ray single crystal diffraction studies were carried out by Dr. Steven J. Rettig and Dr. Brian O. Patrick of this Department. Mr. Peter Borda of this Department performed the elemental analyses. Experimental details for most of the physical methods of characterization employed in this work are given in Chapter 9, section 9.3.

1.5.1 MAGNETIC SUSCEPTIBILITY DETERMINATION

The magnetic properties of the materials investigated here were mainly studied by DC and AC magnetization measurements. Classical methods to measure magnetization are based on the force acting on a sample when it is placed into an

inhomogeneous magnetic field or on the total electromotive force induced in a pick-up coil when the sample is moved in a constant magnetic field.

When an isotropic paramagnetic material is placed in an inhomogeneous magnetic field, a displacement force is applied on the sample drawing it into a region of higher field. Since the displacement force depends on the both magnetization and field gradient, measurement of the force gives direct information on the magnetic susceptibility of a material. These are the fundamentals of the force methods, such as the Gouy method, [69] the Faraday method [70, 71], and the alternating force magnetometer [72, 73].

Alternatively, the change in magnetic flux density that results from placement of the material in a magnetic field may be examined by inductive methods. If a sample is inserted into an induction detection coil, then a change in the voltage is induced in this coil associated with the insertion of the sample into the detection coil. The strength of the induced voltage is given by the equation

$$v = \frac{\mu N^2 A}{S} \frac{di}{dt}$$

where N is the number of turns of wire, A is the cross-sectional area, S is the length of the coil, and di/dt is the frequency of current oscillation. The quantity μ is the

permeability of the material within the coil and is related to the magnetic susceptibility by the equation

$$\mu = 1 + 4\pi\chi$$

The general inductive response described in the first equation is the basis of several techniques that measure magnetic susceptibility, such as the vibrating sample magnetometer [74], AC susceptometer [75, 76], and superconducting susceptometer (SQUID) [77 - 82].

In DC (direct current) measurements, a static field, H_0, is applied, which induces a magnetization, M. In AC (alternating current) measurements, an oscillating field, H_1, is applied. Thus, the applied magnetic field can be defined as consisting of a static component H_0 and an oscillating component H_1, then the magnetic field at any time, t, can be written as

$$H(\mathrm{t}) = H_0 + H_1 \cos(\omega \mathrm{t})$$

where ω is the period of oscillation.

The resulting magnetization of a sample in the oscillating magnetic field may be written as

$$M(\mathrm{t}) = M_0 + M_1 \cos(\omega \mathrm{t} - \varphi)$$

where φ is the phase angle by which the magnetization lags the oscillating component of the magnetic field. It can be then written

$$M(t) = \chi_0 H_0 + \chi' H_1 \cos(\omega t) + \chi'' H_1 \sin(\omega t)$$

where

$$\chi_0 = \frac{M_0}{H_0} \qquad \chi' = \frac{M_1 \cos(\varphi)}{H_1} \qquad \chi'' = \frac{M_1 \sin(\varphi)}{H_1}$$

and χ' and χ'' depend on the frequency and magnitude of the oscillating field. Hence, the AC magnetic susceptibility is determined from its two components, the in-phase (or real) component, χ', and the out-of-phase susceptibility (or imaginary) component, χ''. The in-phase susceptibility is an initial susceptibility with the same phase as the oscillating field. The out-of-phase susceptibility is related to the phase delay with respect to the oscillating field in the magnetically ordered phase. The presence of a non-zero χ'' response is characteristic of a magnet [83].

1.5.2 X-RAY DIFFRACTION

Currently the most important method for determining molecular structure is single crystal X-ray diffraction. An X-ray diffraction experiment consists of placing a crystal in a monochromatic X-ray beam and then measuring the position and intensity

of the diffracted (scattered) rays [84]. This is also the most widely used method to obtain accurate structural information about bond lengths and angles. The necessity of a single crystal to apply this technique precluded the in-depth structural characterization of several coordination polymers obtained as microcrystalline powders in this study. Nonetheless, several key structures were, in fact, obtained here by this method.

X-ray powder diffraction [85] is used to get structural information on microcrystalline powders; however, the information that can be obtained from a powder diffractogram is much more limited than that from single crystal X-ray diffraction. In this work, the powder diffraction patterns obtained are used to determine isomorphism between analogous compounds, and this is particularly useful when the molecular structure of one of the compounds is known.

1.5.3 SPECTROSCOPIC METHODS

1.5.3.1 INFRARED

Infrared (IR) spectroscopy involves direct absorption of radiation that can only occur when the vibrational motion in a molecule involves some change in its dipole moment. If this happens, a vibration is said to be infrared active. This very useful technique [86] provides, among other structural characteristics in a material, immediate information on the different chemical moieties present. IR spectroscopy was useful for

determining the presence or absence of neutral azoles in the compounds prepared in this work.

1.5.3.2 UV-VIS-NIR

Electronic spectroscopy of transition metal complexes can provide useful information about the metal chromophore geometry [87]. This was helpful in the current work primarily when microcrystalline samples of the compounds were obtained. Hence, electronic spectroscopy was used as an indirect method for structural characterization of some of the compounds obtained here.

1.5.3.3 NMR

Due to the paramagnetic nature and solubility properties of the main compounds synthesized here, this very powerful structural characterization tool [88, 89] had limited use in the present research. NMR was utilized here primarily to confirm the structure, and purity, of some ligand precursors.

1.5.3.4 MÖSSBAUER

The discovery of the Mössbauer effect (Nuclear Gamma Resonance (*ngr*) spectroscopy) in 1958 [90] has led to an elegant and welcome spectroscopic technique

for direct microscopic observation of single ion effects and cooperative magnetic behavior in solids. Information on the type of magnetism and the onset of magnetic ordering (T_c or T_N), can be obtained with this technique. The Mössbauer effect experiment is based on the recoil free emission and subsequent recoil free, resonant absorption of low energy gamma rays (Eγ generally < 100 kev) in the solid state for identical isotopes of a given element. The Mössbauer spectra of magnetic materials frequently show interesting features in the critical region near magnetic ordering transitions [91]. Hence, the onset of nuclear Zeeman splitting resulting from the growth of internal hyperfine fields owing to exchange fields and long-range magnetic ordering can be observed directly in Mössbauer effect spectra of appropriate metal nuclides, e.g. Fe-57 [92].

All the iron(II) imidazolate polymers obtained in this thesis were evaluated by Mössbauer spectroscopy studies. These studies were performed in order to confirm the presence of a magnetic transition in the compounds as well as the determination of the critical temperature, T_c, at which their long-range magnetic ordering occurs. Also this spectroscopic technique was utilized to further identify the different coordination geometries found in the iron(II) imidazolate type compounds. In addition, evidence of structural phase transitions occurring in one of the compounds studied was obtained from Mössbauer spectroscopy studies.

1.5.4 THERMAL GRAVIMETRIC ANALYSIS (TGA)

By monitoring the thermal decomposition of a material, additional information about its composition, and the thermal stability of a particular component of the material can be determined. In a typical experiment, the sample is placed in a very sensitive microbalance and the weight of the sample is monitored as the temperature is increased [93]. The programming capabilities of modern instrumentation involving this technique were also used here for the preparation of a coordination polymer, by thermal elimination of neutral molecules from precursor (Chapter 4, section 4.2.2.1).

1.5.5 ELEMENTAL ANALYSIS

As an essential tool this technique provides the relative percentages of analyzed elements from which an empirical formula can be determined [94]. Purity and the composition of all the compounds described in this thesis were assessed by this technique. This technique was particularly important in the initial characterization of microcrystalline coordination polymers since spectroscopic techniques, such as IR, did not provide enough composition/structural information.

1.6 OBJECTIVES AND ORGANIZATION OF THIS THESIS

The synthesis and structural and magnetic characterization of several paramagnetic transition metal diazolate polymers was carried out in the present thesis with the main purpose of contributing to fundamental understanding in the growing field of molecule-based magnets. Previous studies of compounds having mainly pyrazolate as the bridging ligand, established the ability of diazolate bridging ligands to promote magnetic interaction between paramagnetic transition metal ions [68, 95 - 98]. In the current work, new transition metal diazolate polymers, mainly with imidazolate type bridging ligands, were synthesized and found to have structures with one-, two- and three-dimensional frameworks. Hence, one aim of this work was achieved by correlating the magnetic properties of the compounds studied with their different structural dimensionalities. In this regard, the iron(II) diazolate polymers prepared here were the most successfully studied of the different metal systems because they were formed as macroscopic crystalline materials in a form suitable for single crystal X-ray diffraction characterization. Nevertheless, related cobalt(II), nickel(II) and copper(II) imidazolate systems, which were obtainable only as microcrystalline powders, were also studied extensively since they were found to have magnetic properties that also characterize them as molecule-based magnets.

Another pursued objective, the comparison of the magnetic properties of isostructural systems possessing different transition metal ions was also possible. Thus,

2-D and 3-D coordination polymers of iron(II) and cobalt(II) isostructural systems provided a unique opportunity to study the influence of the d^n electronic configuration on the magnetic properties of molecule-based magnets.

This thesis is structured in nine Chapters and an Appendix. Chapter 1 has introduced concepts and provided general information about the different topics involved in this work. In addition, a brief description of the physical methods of characterization has been presented. Chapter 2 concerns the characterization of polybis(pyrazolato)iron(II), a one-dimensional material showing weak antiferromagnetic exchange and no long-range magnetic order. Chapters 3 to 7 describe the synthesis and structural and magnetic characterization of several new imidazolate-based magnetic materials most of which are shown to exhibit properties of molecule-based magnets at low temperature. A binary iron(II) imidazolate (and its cobalt(II) analogue) with a novel 3-D single diamondoid structure is reported in Chapter 3. Binary imidazolates of Co(II), Ni(II) and Cu(II) are described in Chapter 4. Chapters 5 and 6 describe compounds which incorporate neutral "capping ligands" and which have 2-D extended structures, a motif never before seen for metal imidazolate polymers. A rare example of a 1-D chain polymer exhibiting long-range magnetic ordering is described in Chapter 7. In Chapter 8, a general summary of this work and suggestions for future work are provided. Lastly, Chapter 9 provides experimental details of the syntheses and the methods utilized in the physical characterizations of the compounds studied in this

dissertation. Crystallographic data, and selected bond distances and bond angles for all the macro-crystalline compounds studied here, are provided in the Appendix.

References

1. O. Kahn. *Molecular Magnetism*. VCH. New York. (1993).

2. D. Gatteschi. *Adv. Mat.* **6**, 635 (1994).

3. P. W. Selwood. *Magnetochemistry*. Interscience. New York. 1956.

4. A. P. Long, T. D. Clark, and R. J. Prance. *Rev. Sci. Instrum.* **51**, 8 (1980).

5. J. S. Miller, and A. J. Epstein. *Angew. Chem. Int. Ed. Engl.* **33**, 385 (1994).

6. P. W. Anderson, in *Magnetism*. G. T. Rado, and H. Suhl. Eds. Vol. 1. Academic Press. New York. 1963.

7. A. P. Ginsberg. *Inorg. Chim. Acta, Rev.* **5**, 45 (1971).

8. C. J. O'Connor. *Prog. Inorg. Chem.* **29**, 203 (1982). p. 238.

9. L. K. Thompson, S. S. Tandon, M. E. Manuel, M. K. Park, and M. Handa in *Molecule-based Magnetic Materials*. M. M. Turnbull, T. Sugimoto and L. K. Thompson. Eds. ACS symposium series. Washington. 1996.

10. F. Palacio, F. J. Lazaro, and A. J. van Duyneveldt. *Mol. Cryst. Liq. Cryst.* **176**, 289 (1989).

11. O. Kahn. *Acc. Chem. Res.* **33** (10) 647 (2000).

12. C. J. O'Connor. *Prog. Inorg. Chem.* **29**, 203 (1982). p. 205.

13. O. Kahn. *Molecular Magnetism*. VCH. New York. (1993). p. 1.

14. L. Carlin. *Magnetochemistry*. Springer. Berlin. 1986. pp. 5, 11, 25.

15. J. S. Miller, and A. J. Epstein. *Angew. Chem. Int. Ed. Engl.* **33**, 385 (1994). p. 389.

16. O. Kahn. *Molecular Magnetism*. VCH. New York. (1993). p. 11.

17. J. S. Miller, and A. J. Epstein. *Chem. & Eng. News*, **73**, (40), 30 (1995).

18. M. Cohen. *Advancing Materials Reasearch.* P. A. Psaras and H. D. Langford. National Academy Press. Washington, DC. USA. 1987. p. 91.

19. T. Moriya, in *Magnetism.* G. T. Rado, and H. Suhl. Eds. Vol. 1. Academic Press. New York. 1963.

20. O. Kahn. *Molecular Magnetism.* VCH. New York. (1993). p.321.

21. F. Palacio, M. C. Morón, J. Pons, J. Casabó, K. E. Merabet, and R. L. Carlin. *Phys. Lett. A*, **135**, 231 (1989).

22. P. W. Anderson. *Phys. Rev.* **115**, 2 (1959).

23. Conference Proceedings in the Conference on Molecule-Based Magnets, J. S. Miller and A. J. Epstein. *Mol. Cryst. Liq. Cryst.*, **271** (1995).

24. O. Kahn. *Adv. Inorg. Chem.* **43**, 179 (1995).

25. H. H. Wickman, A. M. Trazzolo, H. J. Williams, G. W. Hull, and F. R. Merrit. *Phys. Rev.*, **155**, 563 (1967).

26. B. Mahan, and R. Myers, *University Chemistry.* Benjamin/Cummins. Menlo Park, CA, 1987; p 991.

27. K. Agawa, T. Inabe, U. Nagashima, and Y. Muruyama. *J. Chem. Soc., Chem. Commun.*, 1617 (1989).

28. R. Chiarelli, M. A. Novak, A. Rassat, and J. L. Tholance. *Nature* **363**, 147 (1993).

29. D. A. Eichhorn, D. C. Skee, W. E. Broderick, and B. M. Hoffman. *Inorg. Chem.* **32**, 491 (1993).

30. T. Malah, S. Thiebaut, M. Verdaguer, and P. Veillet. *Science*, **262**, 1554 (1993).

31. Proceedings of the Fifth International Conference on Molecule-Based Magnets, *Mol. Cryst. Liq. Cryst.* (Eds.: K. Itoh, J. S. Miller, K. Takui), **305-306** (1997).

32. J. S. Miller, J. C. Calabrese, A. J. Epstein, R. W. Bigelow, J. H. Zang, and W. M. Reiff. *J. Chem. Soc., Chem. Commun.*, 1026 (1986).

33. L. Carlin. *Magnetochemistry.* Springer. Berlin. 1986.

34. P. Day and I. D. Hall. *J. Chem. Soc.* (A), 2679 (1970).

35. F. E. Mabbs and D. J. Machin. *Magnetism and Transition Metal Chemistry.* Chapman and Hall. London. 1973.

36. A. Earnshaw. *Introduction to Magnetochemistry.* Academic Press. New York. 1968.

37. M. Gerloch. *Magnetism and Ligand Field Analysis.* Cambridge University Press. Cambridge. 1983.

38. J. S. Miller and A. J. Epstein. *Angew. Chem. Int. Ed. Engl.*, **106**, 399 (1994).

39. A. L. Buchachenko. *Russ. Chem. Rev.* **59**, 307 (1990).

40. R. L. Carlin and A. J. van Duyneveldt. *Magnetic Properties of Transition Metal Compounds.* Springer. Berlin. 1986.

41. C. J. O'Connor. Ed. *Research Frontiers in Magnetochemistry.* World Scientific. Songapore. 1993.

42. D. H. Martin. *Magnetism in Solids.* MIT Press. Cambridge. 1967.

43. J. Hu, T. W. Odom, and C. M. Lieber. *Acc. Chem. Res.* **32**, 435 (1999).

44. J. Rouxel. Ed. *Crystal Chemistry and Properties of Materials with Quasi-One-Dimensional Structures.* Reidel. Boston (1986).

45. C. M. Lieber, J. Liu, and P. E. Sheehan. *Angew. Chem., Int. Ed. Engl.* **35**, 686 (1996).

46. M. Fujita, Y. J. Kwon, S. Washizu, and K. Ogura. *J. Am. Chem. Soc.* **119**, 2861 (1994).

47. R. Pech, and J. Pickardt. *Acta Crystallogr.* **C44**, 992 (1988).

48. B. F. Abrahams, B. F. Hoskins, D. M. Michail, and R. Robson. *Nature.* **369**, 727 (1994).

49. O. M. Yaghi, G. Li, and H. Li. *Nature.* **378**, 703 (1995).

50. R. W. Gable, B. F. Hoskins, and R. Robson. *J. Chem. Soc. Chem. Commun.* 1697 (1990).

51. S. Subramanian, and M. Zaworotko. *Angew. Chem. Int. Ed. Engl.* **34**, 2127 (1995).

52. S. O. H. Gutschke, A. M. Slawin, and P. T. Wood. *J. Chem. Soc. Chem. Commun.* 823 (1996).

53. S. S. -Y. Chui, S. M. –F, Lo, J. P. H. Charmant, A. G. Orpen, and I. D. Williams. *Science.* **283**, 1148 (1999).

54. Rettig, S. J.; Storr, A.; Summers, D. A.; Thompson, R. C.; Trotter, J. *J. Amer. Chem. Soc.* **119**, 8675 (1997).

55. D. J. Price, A. K. Powell and P. T. Wood. *J. Chem. Soc., Dalton Trans.*, 3566, 2000.

56. P. Day. *Coord. Chem. Rev.* **190-192**, 827 (1999).

57. A. F. Wells, *Structural Inorganic Chemistry*, 4th ed., Oxford, Clarendon Press. 1975, pp. 70-74.

58. W. Lin, O. R. Evans, R.-G. Xiong, and Z. Wang. *J. Am. Chem. Soc.* **120**, 13272 (1998).

59. K. Sinzger, *et. al. J. Am. Chem. Soc.* **115**, 7696 (1993).

60. W. R. Entley, and G. S. Girolami. *Inorg. Chem.* **33**, 5165 (1994).

61. C. Janiak. *Angew. Chem., Int. Ed. Engl.* **36**, 1431 (1997).

62. M. Fujita, Y. J. Kwon, S. Washizu, and K. Ogura. *J. Am. Chem. Soc.* **116**, 1151 (1994).

63. H. C. Freeman. *Adv. Protein Chem.* **22**, 257 (1967).

64. S. Trofimenko. *Prog. Inorg. Chem.* **34**, 115 (1986).

65. G. La-Monica and G. A. Ardizzoia. *Prog. Inorg. Chem.* **46**, 151 (1997).

66. S. J. Rettig, A. Storr, D. A. Summers, R. C. Thompson, and J. Trotter. *Can. J. Chem.* **77**, 425 (1999).

67. M. K. Ehlert, S. J. Rettig, A. Storr, R. C. Thompson, and J. Trotter. *Can. J. Chem.* **67**, 1970 (1989).

68. M. K. Ehlert, A. Storr, D. A. Summers, and R. C. Thompson. *Can. J. Chem.* **75**, 491 (1997).

69. C. J. O'Connor, in *Molecule-based Magnetic Materials*. M. M. Turnbull, T. Sugimoto and L. K. Thompson. Eds. ACS symposium series. Washington. 1996. p. 45.

70. D. A. Cruse and M. J. Gerloch. *J. Chem. Soc. Dalton Trans.* **152**, 1977.

71. R. T. Lewis. *Rev. Sci. Instrum.* **42**, 31 (1971).

72. R. Reeves. *J. Phys. E.* **5**, 547 (1972).

73. C. J. O'Connor, in *Molecule-based Magnetic Materials*. M. M. Turnbull, T. Sugimoto and L. K. Thompson. Eds. ACS symposium series. Washington. 1996. p. 47.

74. S. Foner. *Rev. Sci. Instrum.* **30**, 548 (1959).

75. R. L. Carlin, K. O. Joung, A. Paduan-Filho, C. J. O'Connor, and E. J. Sinn. *J. Phys. C.* **12**, 293 (1979).

76. H. A. Groenendljk, A. J. van Deyneveldt, and R. D. Willet. *Physica.* **101B**, 320 (1980).

77. R. C. Jacklevic, J. Lambe, A. H. Silver, and J. E. Marcereau. *Phys. Rev. Lett.* **12**, 159 (1964).

78. B. S. Jr. Deaver, T. J. Bucelot, and J. J. Finney, in *Future Trends in Superconducting Electronics*. AIP Conference Proceedings No. 44. Charlotesville, VA. 1978. B. Deaver, C. Falco, J. Harris, and S. Wolf. Eds. AIP. New York. 1978.

79. Quantum Design Corporation. San Diego, CA 92121.

80. P. A. Salyer and L. W. ter Haar, in *Molecule-based Magnetic Materials*. M. M. Turnbull, T. Sugimoto and L. K. Thompson. Eds. ACS symposium series. Washington. 1996.

81. J. A. Bertrand, E. Fujita, and D. G. Derveer. *Inorg. Chem.* **19**, 2022 (1980).

82. W. G. Jenks, S. S. H. Sadeghi, and J. P. Jr. Wikswo. *J. Phys. D: Appl. Phys.* **30** (3), 293 (1997).

83. O. Kahn, J. Larinova, and J. V. Yakhmi. *Chem. Eur. J.* **5** (12) 3443 (1999).

84. M. F. Ladd and R. A. Palmer. *Structure Determination by X-ray Crystallography*. Plenum Press. New York. 1988.

85. L. V. Azaroff and M. J. Buerger. *The Powder Method in X-ray Crystallography*. McGraw-Hill. New York. 1958.

86. K. Nakamoto. *Infrared Spectra of Inorganic and Coordination Compounds*. Wiley-Interscience. New York. 1969.

87. A. P. B. Lever. *Inorganic Electronic Spectroscopy*. Elsevier. Amsterdam. 1984.

88. J. W. Akitt. *NMR and Chemistry*. Chapman and Hall. London. 1983.

89. J. K. M. Sanders, E. C. Constable, and B. K. Hunter. *Modern nmr Spectroscopy: A Workbook of Chemical Problems*. Oxford. Toronto. 1989.

90. D. P. E. Dickson and F. J. Berry. Eds. *Mössbauer Spectroscopy*. Cambridge University Press. Cambridge. 1986.

91. N. N. Greenwood and T. C. Gibb. *Mössbauer Spectroscopy*. Chapman and Hall. London. 1971.

92. W. M. Reiff. *Mol. Cryst. Liq. Cryst.* **176**, 391 (1989).

93. A. R. West. *Solid-state Chemistry and its Applications*. John Wiley & Sons. New York. 1984.

94. T. S. Ma and R. C. Rittner. *Modern Organic Elemental Analysis*. Marcel Decker Inc. New York. 1979.

95. M. K. Ehlert, S. J. Rettig, A. Storr, R. C. Thompson, and J. Trotter. *Can. J. Chem.* **68**, 1494 (1990).

96. M. K. Ehlert, S. J. Rettig, A. Storr, R. C. Thompson, and J. Trotter. *Can. J. Chem.* **69**, 432 (1991).

97. M. K. Ehlert, S. J. Rettig, A. Storr, and R. C. Thompson. *Can. J. Chem.* **70**, 1121 (1992).

98. M. K. Ehlert, S. J. Rettig, A. Storr, and R. C. Thompson. *Can. J. Chem.* **71**, 1412 (1993).

Chapter 2 POLYBIS(PYRAZOLATO)IRON(II). A ONE-DIMENSIONAL MATERIAL SHOWING WEAK ANTIFERROMAGNETIC EXCHANGE

2.1 INTRODUCTION

Metal coordination complexes with one-dimensional structures have long been investigated as materials with unusual properties. Molecule-based ferromagnets, electrical conductors, and nonlinear optical materials represent several potential applications of one-dimensional coordination polymers. Several studies have demonstrated that it is possible to modify the bulk magnetic, electronic, and optical properties of such materials [1-3]. Compared with high-dimensional materials, one-dimensional molecule-based magnetic materials sometimes have larger anisotropy favoring hard magnetic materials (stronger coercive field and larger hysteresis loop) [4].

Coordination compounds containing pyrazoles or pyrazolates as terminal or bridging ligands to transition metals have been extensively studied. Reviews such as those authored by Trofimenko [5, 6] and La Monica and Ardizzoia [7] give a good account of the development and importance of this field in coordination chemistry. The ability of pyrazolates to form double bridges between transition metal ions and 1-D extended chain structures in which the metal ions are antiferromagnetically coupled via

the ligands has been well documented in previous research on binary M(II) pyrazolates (M = Mn, Co, Ni, or Cu) [8-11].

While iron(II) pyrazolate complexes or polymers are relatively rare, the synthesis of iron pyrazolate polymers, $[Fe(pz)_2]_x$ and $[Fe(pz)_3]_x$, appeared in 1968 [12]. The work involved reacting pyrazole with $Fe(CO)_5$ or $[CpFe(CO)_2]_2$ in benzene or toluene solvent. Only the elemental analysis of the polymeric compounds was reported without further characterization. The extensive characterization of the 1-D polymer, $[Fe(pz)_2]_x$, described here, is important for further discussion of other azolate transition metal polymers studied in this thesis. This model compound, $[Fe(pz)_2]_x$, has permitted the determination of the main structural differences between the 1,2 and 1,3-diazolate bridging motifs as well as permitted a better understanding of the influence of structure on the different magnetic behaviors observed.

2.2 RESULTS AND DISCUSSION

2.2.1 SYNTHESIS AND PHYSICAL PROPERTIES

Details of the synthesis employed for $[Fe(pz)_2]_x$ are given in Chapter 9, section 9.2.1.1. In this approach, which was used previously to obtain other iron(II) azolate polymers [13], ferrocene was reacted with an excess of pyrazole under inert atmosphere conditions. The product was isolated as red brown air-sensitive crystals. In this synthetic "metallocene" approach, the formation of the polymer involves an acid-base reaction in

which the pyrazole NH proton is transferred to a Cp ring of ferrocene. The resulting pyrazolate binds to the iron ion liberating cyclopentadiene, in the process:

$$x(FeCp_2) + xs(pzH) \longrightarrow [Fe(pz)_2]_x + 2x(CpH)$$

The reaction of metallocenes with molten imidazoles has been a successful method for the preparation of divalent transition metal imidazolate coordination polymers. Often, when ferrocene is involved in this type of reaction, single crystals of the coordination polymers are obtained [13, 14]. Here, the reaction of ferrocene with pyrazole produced the polymeric Fe(II) material, $[Fe(pz)_2]_x$, in needle-like crystalline form suitable for single crystal X-ray diffraction studies.

2.2.2 SINGLE-CRYSTAL X-RAY DIFFRACTION CHARACTERIZATION

A section of the extended structure of $[Fe(pz)_2]_x$ is shown in Figure 2.1. Selected crystallographic data, atom coordinates, bond lengths and bond angles appear in Appendix I, Tables I-1 and I-2. In this coordination polymer iron ions are linked by double pyrazolate bridges in the structure generating tetrahedral FeN_4 metal chromophores and extended 1-D chains. The double pyrazolate bridge between the Fe ions generates a linear chain structure (Figure 2.1). A projection of the structure down the *c* axis is shown in Figure 2.2. This type of structure has been determined by X-ray crystallography previously for $[Cu(pz)_2]_x$ [8].

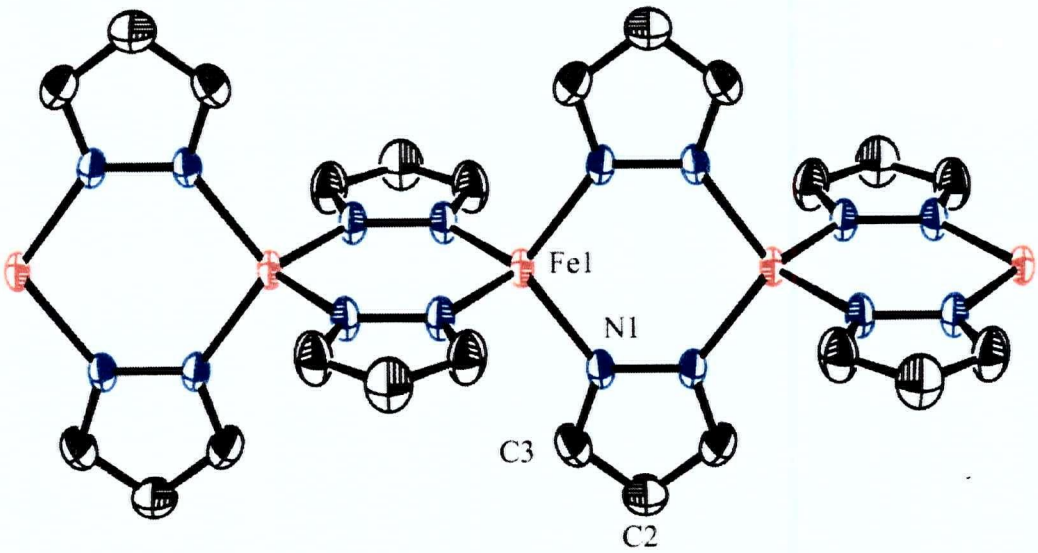

Figure 2.1. Section of the polymer chain of $[Fe(pz)_2]_x$ showing the atom numbering scheme. Hydrogen atoms are omitted. (50 % probability thermal ellipsoids shown).

The Fe(1)—N(1) bond distance of 2.07(1) Å is normal for an iron(II) azolate system [13, 14]. The N(1)—Fe(1)—N(1) bond angles, which range from 108.93(9) to 110.27(9)° are remarkably close to the value for a regular tetrahedron. The corresponding angles for the copper(II) analogue, for example, lie in the range 94.3(1) to 139.5(1)° [8].

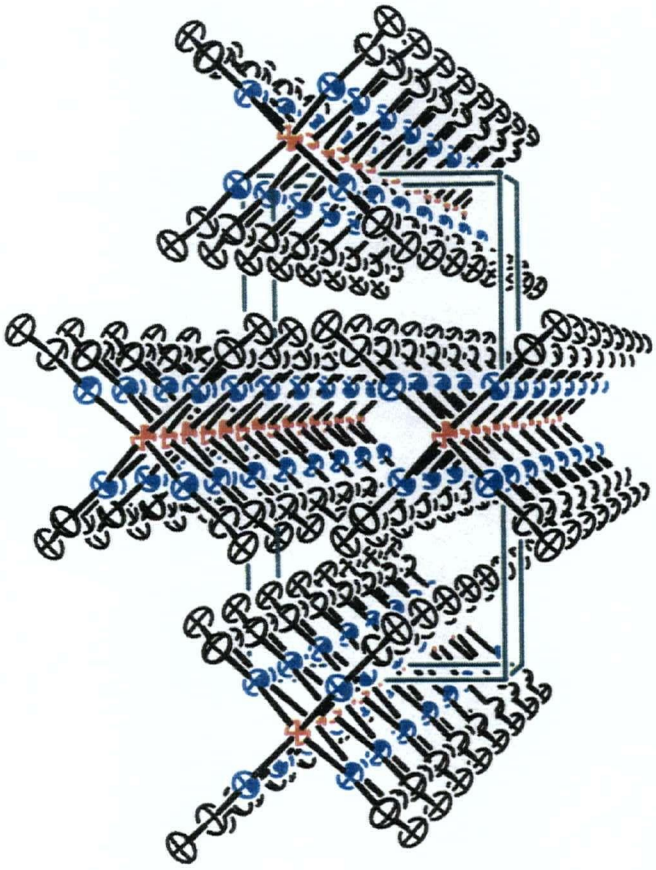

Figure 2.2. View looking almost down the *c* axis in the structure of $[Fe(pz)_2]_x$. (50 % probability thermal ellipsoids shown).

2.2.3 INFRARED SPECTROSCOPY

Infrared spectroscopy was utilized to ensure that no neutral pyrazole molecules were present in the polymeric structure of $[Fe(pz)_2]_x$. The sharp and intense band at ~ 3380 cm^{-1}, expected for neutral pyrazole (N-H stretch), was absent in the IR spectrum of this compound. Assignments of the vibrational spectrum of the pyrazolate ion were made previously [15].

2.2.4 MAGNETIC BEHAVIOR

DC magnetic susceptibility measurements were made on powdered samples of $[Fe(pz)_2]_x$ at an applied field of 10 000 G over the temperature range 2 to 300 K. Plots of χ and μ_{eff} against T are given in Figure 2.3. Although no maximum is observed in the susceptibility plot, the decrease in μ_{eff} with decreasing temperature (4.8 μ_B at 300 K; 1.75 μ_B at 2 K), suggests antiferromagnetic coupling, albeit very weak.

In an attempt to quantify the magnitude of the antiferromagnetic exchange in this system the magnetic data were fitted to a model appropriate for a 1-D compound. Accordingly, fits of the susceptibility data to the isotropic Heisenberg model for antiferromagnetically coupled linear chains developed by Weng [16] and Hiller *et al.* [17] were examined. To obtain a satisfactory fit it was necessary to include a term in the

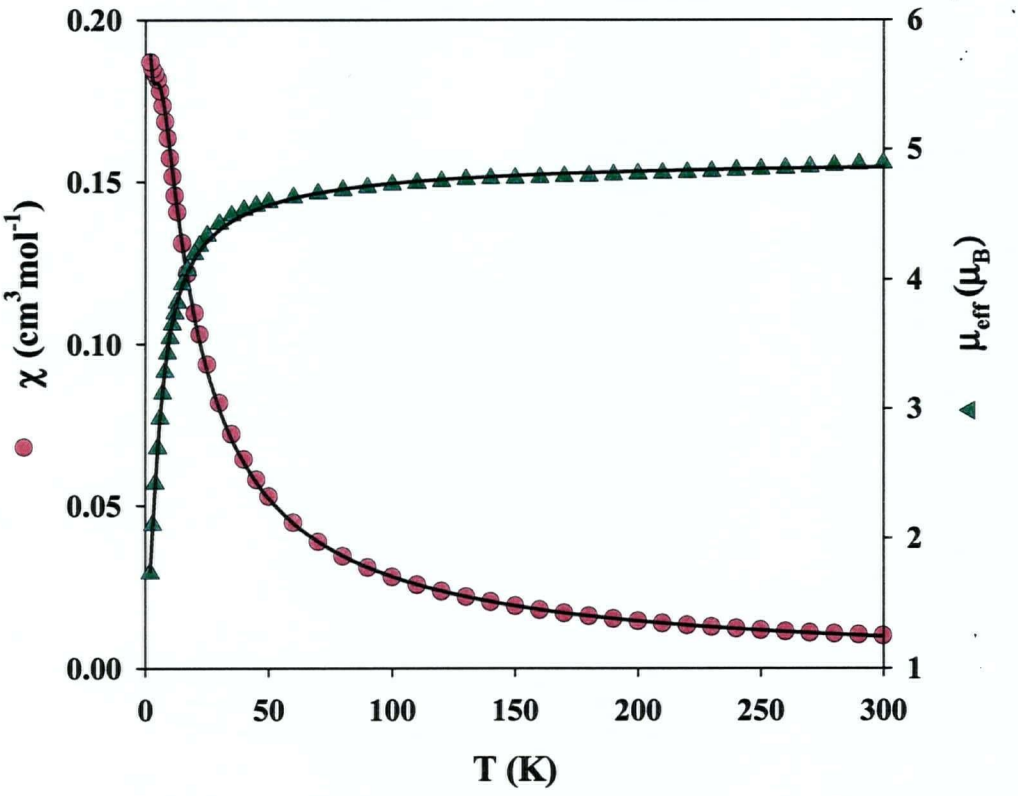

Figure 2.3 χ and μ_{eff} versus temperature plot at 10 000 G for $[Fe(pz)_2]_x$. Lines are from theory as described in the text.

expression to accommodate a fraction *P* of the iron ions present as a structural paramagnetic impurity. The necessity of allowing for paramagnetic impurity in analyzing magnetic data of antiferromagnetically coupled systems is not uncommon, as was found

to be the case in analyzing the magnetic properties of the copper(II) analogue [8]. The modified expression used was:

$$\chi = (1-P)\left(Ng^2\beta^2/kT\right)\left[\frac{2+71.938x^2}{1+10.482x+955.56x^3}\right]+P(2Ng^2\beta^2/kT)$$

where $x = |J|/kT$, J is the exchange coupling constant, and g is the Landé factor.

In the least squares fitting procedure used, the function minimized, F, was:

$$F=\left[\frac{1}{n}\sum_{i=1}^{n}\left[\frac{\chi^i{}_{calc}-\chi^i{}_{obs}}{\chi^i{}_{obs}}\right]^2\right]^{1/2}$$

where n = the number of data points.

The value of F provides a measure of the goodness of fit. Employing g, J (the exchange coupling parameter) and P as variable parameters the best fit of experiment to theory was obtained for $g = 2.01$, $-J = 0.591(5)$ cm^{-1} and $P = 0.033(2)$ with $F = 0.011$.

The solid lines shown in Figure 2.3 were calculated from theory employing these best fit parameter values and provide a visual indication of the goodness of fit. Clearly the magnetic properties of $[Fe(pz)_2]_x$ are well described by the model used.

The antiferromagnetic coupling in $[Fe(pz)_2]_x$ is judged to be weak, based on the absence of a detectable maximum in the χ versus T plot above 2 K and on the small value of the exchange coupling constant. To put the magnitude of the exchange observed here in some perspective it is necessary to compare it with that recorded for linear chain pyrazolates of other metals. To compare the magnitude of coupling in systems of different spin, rather than comparing J values it is appropriate to compare $|4JS^2|$ values [18]. For $[Fe(pz)_2]_x$ this is 9.4 cm^{-1}, a value significantly smaller than the 78 cm^{-1} of the copper(II) analogue [8].

In an earlier summary of $|4JS^2|$ values for Ni(II), Mn(II), Cu(II) and Co(II) linear chain pyrazolates it was observed that the strength of coupling appears related to the total number of *d* electrons in the system, suggesting that covalency of the metal – ligand bonds is an important factor [19]. Consistent with this, the $|4JS^2|$ value of $[Fe(pz)_2]_x$ is close to the range 10 to 50 cm^{-1} observed in Mn(II) systems and clearly outside the range 58 to 105 cm^{-1} observed in Cu(II) systems [19].

2.3 SUMMARY AND CONCLUSIONS

Polybis(pyrazolato)iron(II), $[Fe(pz)_2]_x$, has an extended chain 1-D structure in which iron ions are doubly bridged by pyrazolate ligands. The compound exhibits weak antiferromagnetic interactions. The magnetic susceptibility data were fit to a Heisenberg

model for chains of antiferromagnetically coupled $S = 2$ metal centers, yielding the magnetic parameters $-J = 0.591(5)$ cm^{-1} and $g = 2.01$.

In characterizing polybis(pyrazolato)iron(II), $[Fe(pz)_2]_x$, as a 1-D linear chain polymer which incorporates double azolate bridges and which exhibits weak antiferromagnetic exchange mediated by the bridging ligands, the work confirms that the structural motif and consequent magnetic properties, that characterize binary metal pyrazolates of other metals, extend to iron(II) systems.

As mentioned previously, the analysis made here for $[Fe(pz)_2]_x$ will be useful in establishing a better understanding of the different structures, structural dimensionalities, and magnetic properties of the other transition metal azolate polymers presented in the following Chapters of this thesis.

References

1. C. T. Chen and K. S Suslick. *Coord. Chem. Rev.* **128**, 293 (1993).

2. O. Kahn. *Molecular Magnetism*. VCH. New York. 1993.

3. J. S. Miller. Ed. *Extended Linear Chain Compounds*. Vol. 3.Plenum. New York, 1982.

4. P. Delahes and M. Drillon. Eds. *Organic and Inorganic Linear Dimensional Crystalline Materials*. NATO: New York, 1989.

5. S. Trofimenko. *Chem. Rev.* **72**, 497 (1972).

6. S. Trofimenko. *Prog. Inorg. Chem.* **34**, 115 (1986).

7. G. La-Monica and G. A. Ardizzoia, *Prog. Inorg. Chem.* **46**, 151 (1997).

8. M. K. Ehlert, S. J.Rettig, A. Storr, R. C. Thompson, and J. Trotter. *Can. J. Chem.* **67**, 1970 (1989).

9. M. K. Ehlert, S. J.Rettig, A. Storr, R. C. Thompson, and J. Trotter. *Can. J. Chem.* **69**, 432 (1991).

10. M. K. Ehlert, S. J.Rettig, A. Storr, R. C. Thompson, F. W. B. Einstein, and R. J. and Batchelor. *Can. J. Chem.* **71**, 331 (1993).

11. M. K. Ehlert, A. Storr, and R. C. Thompson. *Can. J. Chem.* **71**, 331 (1993).

12. F. Seel, and V. Sperber. *Angew. Chem. Int. Ed.* **7**, 70 (1968).

13. S. J. Rettig, A. Storr, D. A. Summers, R. C. Thompson, and J. Trotter. *J. Amer. Chem. Soc.* **119**, 8675 (1997).

14. S. J. Rettig, A. Storr, D. A. Summers, R. C. Thompson, and J. Trotter. *Can. J. Chem.* **77**, 425 (1999).

15. J. G. Voss; and W. L. Groeneveld. *Inorg. Chim. Acta*. **24**, 173 (1978).

16 C. H. Weng, Doctor of Philosophy Thesis, Carnegie-Mellon University, 1968.

17. W. Hiller, J. Strahle, A. Datz, M. Hanack, W. F. Hatfield, and P. Gutlich. *J. Am. Chem. Soc.* **106**, 329. (1984).

18. S. L. Lambert, and D. N. Hendrickson. *Inorg. Chem.* **18**, 2683 (1979).

19. A. Storr, D. A. Summers, and R. C Thompson. *Can. J. Chem.* **76**, 1130 (1998).

Chapter 3 *POLYBIS(4-AZABENZIMIDAZOLATO) IRON(II) AND COBALT(II). 3-D SINGLE DIAMONDOID MATERIALS EXHIBITING WEAK FERROMAGNETIC ORDERING*

3.1 INTRODUCTION

As described in Chapter 1, the ability of diazolate ligands to bridge metal ions and to mediate magnetic interactions between paramagnetic centers has been well documented [1-3]. Studies on binary copper(II), cobalt(II) nickel(II) and manganese(II) [4-9] and iron (II) (Chapter 2) pyrazolates show that the 1,2 positioning of the nitrogen atoms in the ligands leads to polymeric 1-D linear chain structures with double azolate bridges and antiferromagnetically coupled metal centers. In contrast, it has been suggested that the 1,3 positioning of the donor nitrogens in imidazolate ligands results in steric constraints which prevent the formation of double azolate bridges between metal ions [10]. These imidazolate ligands characteristically singly bridge metals leading to higher dimensional, 2-D or 3-D, structures often possessing interesting long-range magnetic interactions. This structural motif is exhibited by $[Fe_3(imid)_6(imidH)_2]_x$ (where imidH = imidazole), a compound in which iron(II) ions are singly bridged by imidazolate ligands in an extended 3-D lattice [10].

Magnetic studies on $[Fe_3(imid)_6(imidH)_2]_x$ revealed antiferromagnetic coupling at higher temperatures but long-range ordering and weak ferromagnetism at lower temperatures. The use of 2-methylimidazolate as the bridging ligand in an analogous reaction led to an entirely different 3-D material, $[Fe(2\text{-meimid})_2 \cdot 0.13Cp_2Fe]_x$ (2-meimid = 2-methylimidazolate and Cp = cyclopentadienyl) [11], which again was found to exhibit properties characteristic of molecule-based magnets at low temperatures. In expanding these studies we decided to try to prepare a 3-D Fe(II) polymer using 4-azabenzimidazole as a precursor of the 4-azabenzimidazolate ion. Compared to imidazolate or 2-methylimidazolate, this ligand has an extra nitrogen, the 4-aza nitrogen, with potential to be coordinated to a metal ion. We were curious to know if this nitrogen would get involved in the coordination of the metal ion. Another interesting difference, compared to imidazolate or 2-methylimidazolate, is the additional bulkiness that the 4-azabenzimidazolate ligand provides. Hence we were also interested in what effect the steric hindrance in the ligand would have on the structural dimensionality of the polymeric product.

The direct reaction between ferrocene and excess molten 4-azabenzimidazole yields amber-green crystals of polybis(4-azabenzimidazolato)iron(II), $[Fe(4\text{-abimid})_2]_x$. Single crystal X-ray diffraction studies reveal that in $[Fe(4\text{-abimid})_2]_x$ the 4-aza nitrogen is not involved in coordination to the metal, the 4-azabenz-substituent serving instead to create sufficient steric bulk in the imidazolate moiety to generate a unique 3-D diamond-like (diamondoid) extended lattice. The diamond-like structure in coordination

polymers has attracted the attention of synthetic and materials chemists for some time now. They provide examples of 3-D "scaffolding-like materials" of potential practical importance [12, 13] and they are part of supramolecular chemistry and the emerging cross-disciplinary field of crystal engineering [14, 15]. Since the work of Kinoshita *et al.*, [16] on bis(adiponitrilo)copper(I) nitrate, there have been a number of papers devoted to this particular molecular motif [17-25]. The title compound, $[Fe(4\text{-}abimid)_2]_x$, is the first to be reported with a totally covalent, non-interpenetrating (single) diamond-like network, exhibiting spontaneous magnetization at low temperatures.

The need to explore factors affecting characteristic properties of molecule-based magnets, such as coercivity, has been recently addressed [26]. To explore the effects of altering the d^n configuration, polybis(4-azabenzimidazolato)cobalt(II), $[Co(4\text{-}abimid)_2]_x$, has also been synthesized and characterized here. Evidence indicates that the polymer $[Co(4\text{-abimid})_2]_x$ is isomorphous, and probably isostructural, with the polymer $[Fe(4\text{-abimid})_2]_x$. Although $[Co(4\text{-abimid})_2]_x$ also exhibits the properties of a molecule-based magnet its critical temperature, as well as coercive field and remnant magnetization at 4.8 K are all distinctly different from those of $[Fe(4\text{-abimid})_2]_x$.

An article regarding the structural and magnetic properties of the compounds described in this chapter has been published recently [27].

3.2 RESULTS AND DISCUSSION

3.2.1 SYNTHESES, STRUCTURES AND PHYSICAL MEASUREMENTS

The reaction of metallocenes with molten azoles has been utilized as an effective method for preparing divalent metal azolate polymers, often in macroscopic crystalline form [10, 11]. In the present work the reaction between ferrocene and excess molten 4-azabenzimidazole has afforded a polymeric Fe(II) material, $[Fe(4\text{-abimid})_2]_x$, in macroscopic crystalline form. While, the reaction of cobaltocene with the same molten ligand generated the Co(II) material, $[Co(4\text{-abimid})_2]_x$, as a microcrystalline powder. Details about these syntheses are in Chapter 9, sections 9.2.1.3 and 9.2.2.6, respectively.

$[Fe(4\text{-abimid})_2]_x$, was obtained in crystalline form suitable for single crystal X-ray diffraction studies. Crystallographic data for $[Fe(4\text{-abimid})_2]_x$, appear in Appendix I, Table I-3. Selected bond lengths and bond angles are shown in Appendix I, Table I-4. The repeat unit of $[Fe(4\text{-abimid})_2]_x$ is shown in Figure 3.1 and a stereoscopic view of a segment of the structure is shown in Figure 3.2. The structure consists of iron(II) ions linked by single 4-azabenzimidazolate bridges bridging through the 1,3 nitrogens giving a 3-D extended array. Coordination of the 4-aza nitrogen is not observed. The bond distances between Fe and the four nitrogen atoms in the tetrahedral chromophore are: Fe(1)—N(1) = 2.030 Å, Fe(1)—N(2) = 2.046 Å, Fe(1)—N(4) = 2.044 Å, and Fe(1)—N(5) = 2.034 Å. These values are within the expected Fe—N bond distances for

tetrahedral iron(II) imidazolate complexes [10, 11]. The N—Fe(1)—N bond angles range from 102.10° to 118.24°, which correspond to angles typically obtained for FeN_4 chromophores having a distorted tetrahedral geometry [10, 11]. Fused rings of six

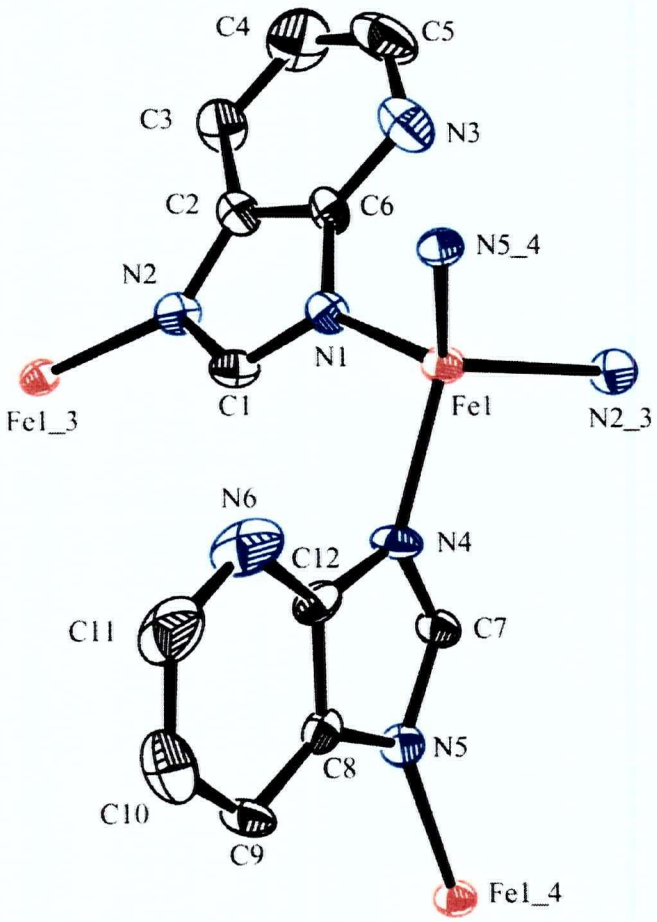

Figure 3.1 View of the repeat unit of $[Fe(4\text{-abimid})_2]_x$ and atom numbering scheme (33% probability thermal ellipsoids). Hydrogen atoms are omitted.

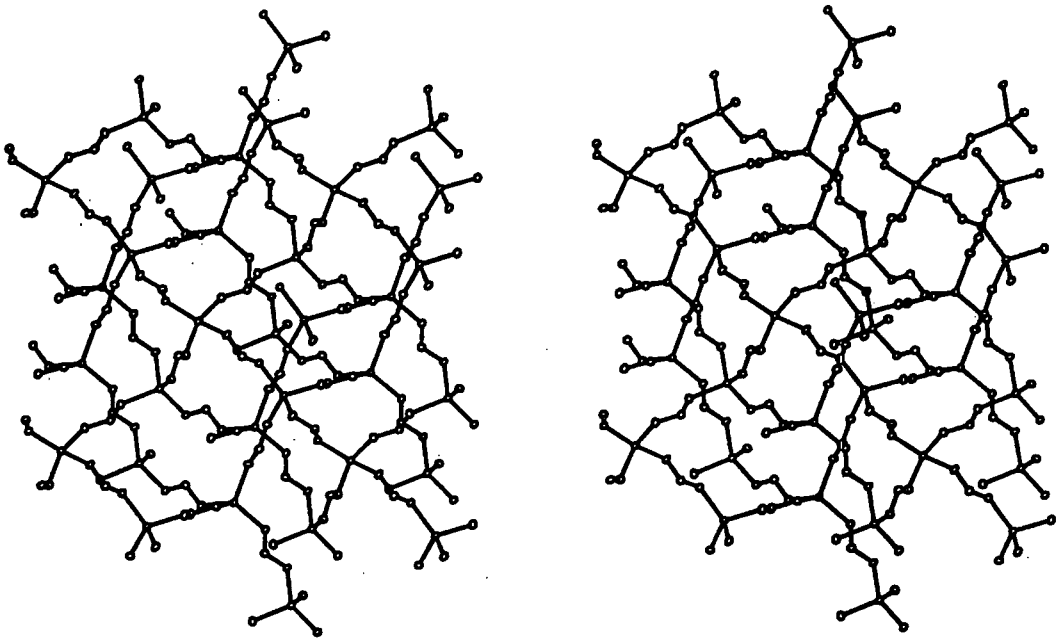

Figure 3.2 Stereoscopic view of a section of the diamond-like framework of $[Fe(4\text{-abimid})_2]_x$. For clarity only the iron ions and the bridging N–C–N atoms of the imidazolate rings are shown.

distorted-tetrahedral iron centers form a unique covalently bonded diamond-like framework. This framework can be viewed easily in the iron ion connectivity diagram shown in Figure 3.3. Further views of this structure looking down the *b* axis of the unit cell are shown in Figures 3.4 and 3.5.

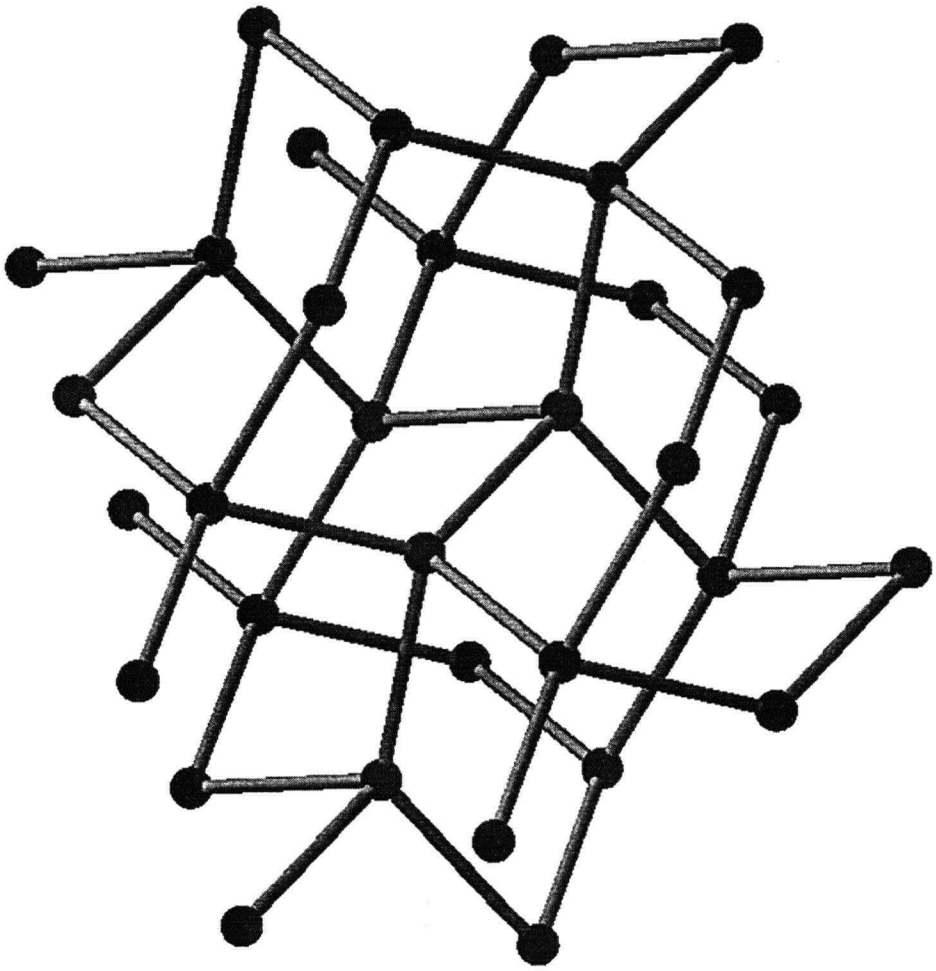

Figure 3.3 Iron ion connectivity diagram for a section of $[Fe(4\text{-abimid})_2]_x$.

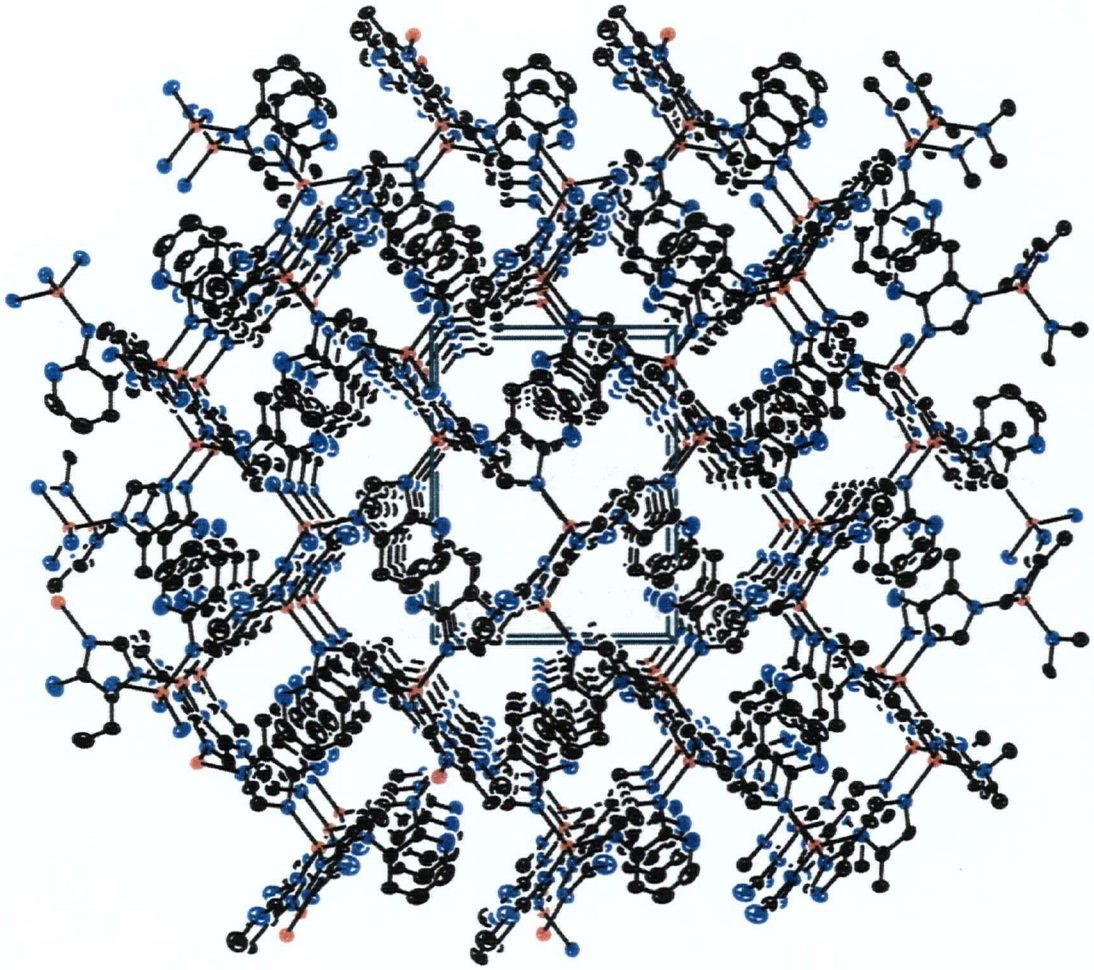

Figure 3.4 View of $[Fe(4\text{-abimid})_2]_x$ looking down the *b* axis. Notice the voids being occupied by the 4-azabenzene part of the ligand.

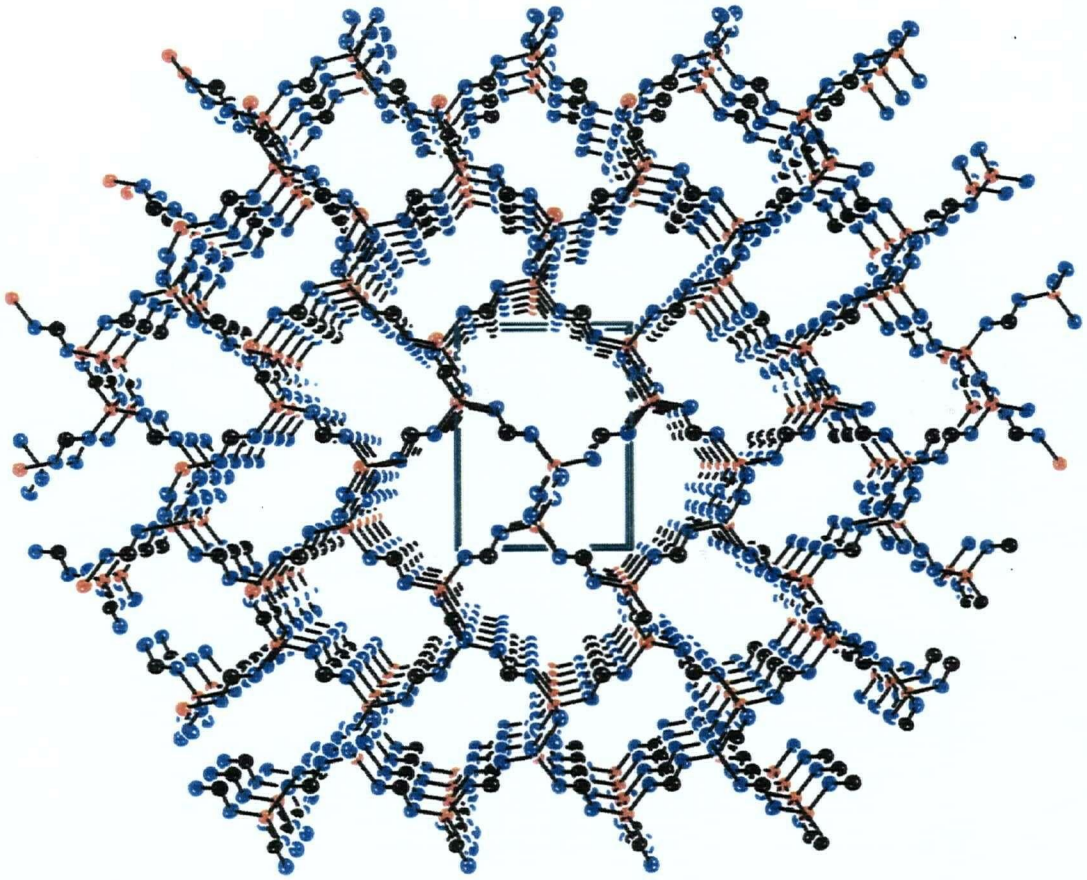

Figure 3.5 View of $[Fe(4\text{-abimid})_2]_x$ looking down the *b* axis. For clarity only the iron ions and the bridging N-C-N are shown.

Although coordination polymers with diamond-like structures have been reported before [17-25, 28], none of them involve iron(II). Moreover, most of these materials present different degrees of interpenetration in their diamond-like arrays. In contrast, $[Fe(4\text{-abimid})_2]_x$ consists of a single, non-interpenetrating, diamond-like framework.

There are few examples of molecular compounds showing a single diamond-like motif. One of the most interesting studies of such structures was done by Hoskins and Robson [12], who employed large counter ions, such as $N(CH_3)_4^+$ in $[N(CH_3)_4][Cu^IZn^{II}(CN)_4]$, and BF_4^- in Cu^I[4,4',4'',4'''-tetracyanotetraphenylmethane]$BF_4 \cdot xC_6H_5NO_2$, to block the adamantane-like cavities and prevent interpenetration. The latter compound also contains molecules of nitrobenzene occupying the cavities. Another example of a single diamond-like framework was obtained in this laboratory [29]. The compound poly-bis(μ-2,5-dimethylpyrazine)copper(I) hexafluorophosphate has a cationic diamond-like lattice where the PF_6^- ions occupy positions in the lattice cavities. It should be noted that these reported single diamond-like structures have ionic lattices with counter ions occupying positions within the extended lattice, thus preventing interpenetration. Therefore, $[Fe(4\text{-abimid})_2]_x$ is the first example of a totally covalent coordination complex having a single diamond-like framework.

Extended non-diamondoid 3-D networks in compounds incorporating iron(II) and bridging imidazolate ligands have been observed before [10, 11]. The 2-methylimidazolate iron(II) polymer has a complex 3-D network of linear channels in which ferrocene molecules, utilized in the synthesis of the material, are trapped [11]. This contrasts with the situation seen for $[Fe(4\text{-abimid})_2]_x$ in which there is a single non-interpenetrating diamond-like lattice with nothing trapped in the lattice cavities, a consequence, presumably, of the steric bulk of the 4-azabenz-substituent (Figure 3.5).

By employing cobaltocene instead of ferrocene, and following the same synthetic procedure as described for $[Fe(4\text{-abimid})_2]_x$, an analogous cobalt(II) compound, $[Co(4\text{-abimid})_2]_x$, was obtained in microcrystalline form, and its X-ray diffraction powder pattern was determined. The powder pattern for $[Fe(4\text{-abimid})_2]_x$ was calculated, for comparison with the experimentally determined one for $[Co(4\text{-abimid})_2]_x$, employing the program Powdercell [30]. The X-ray powder diffractogram of $[Co(4\text{-abimid})_2]_x$, corresponds well with that calculated from the single-crystal data of $[Fe(4\text{-abimid})_2]_x$ (Figure 3.6) indicating the two materials are isomorphous. Indexing the powder data [31] for $[Co(4\text{-abimid})_2]_x$ gave an orthorhombic unit cell with lattice parameters a = 9.72, b = 10.37 and c = 12.45 Å, in close agreement with those of $[Fe(4\text{-abimid})_2]_x$ (a = 9.65, b = 10.34 and c = 12.46 Å) (Appendix I, Table I-3.).

Evidence in support of the fact the iron and cobalt compounds are isostructural in addition to being isomorphous comes from spectroscopic studies. The electronic spectrum of $[Co(4\text{-abimid})_2]_x$ shows two principal absorption regions at around 1125 (broad), and between 580 nm to 540 nm (Figure 3.7). These bands can be assigned to the $^4A_2 \rightarrow {}^4T_1(F)$ and $\rightarrow {}^4T_1(P)$ transitions, respectively, for tetrahedral cobalt(II) [32, 33]. The latter band seems to consist of two bands, one of them split. This complexity may result from transitions to doublet excited states occurring in this region [34]. Hence, complex envelopes in the visible region are generally observed for tetrahedral Co(II) chromophores [34]. It is also important to notice that, due to the strong bands

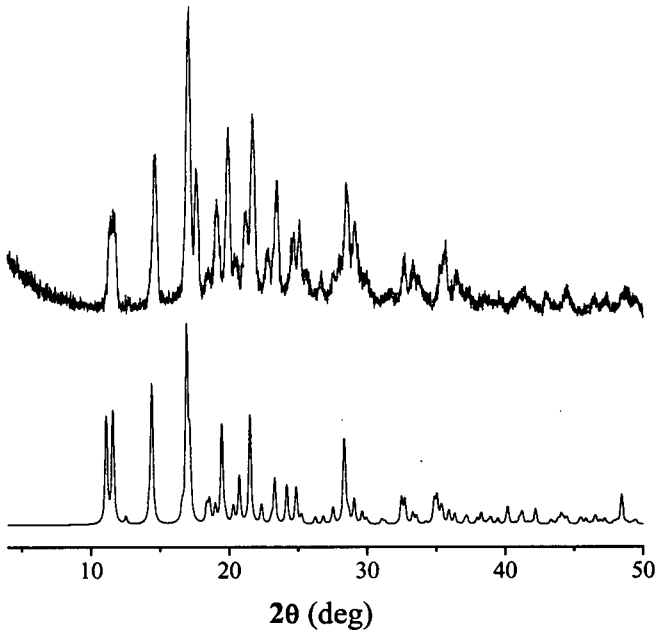

Figure 3.6 X-ray powder diffractograms of $[Co(4\text{-abimid})_2]_x$ (top, experimental) and $[Fe(4\text{-abimid})_2]_x$ (bottom, calculated).

arising presumably from charge transfer in the lowest wavelength region of the spectrum, the bands in the 540 - 580 nm region are not as well defined as usual for tetrahedral Co(II) compounds (See Chapter 4, section 4.2.2.1). Interesting also is the presence of another band at around 1750 nm, which appears very weakly in the higher-concentration mull spectrum (Figure 3.7). This low energy band corresponds to the $^4A_2 \rightarrow {}^4T_2$ transition. This band typically appears in the 1000-2000 nm region in the

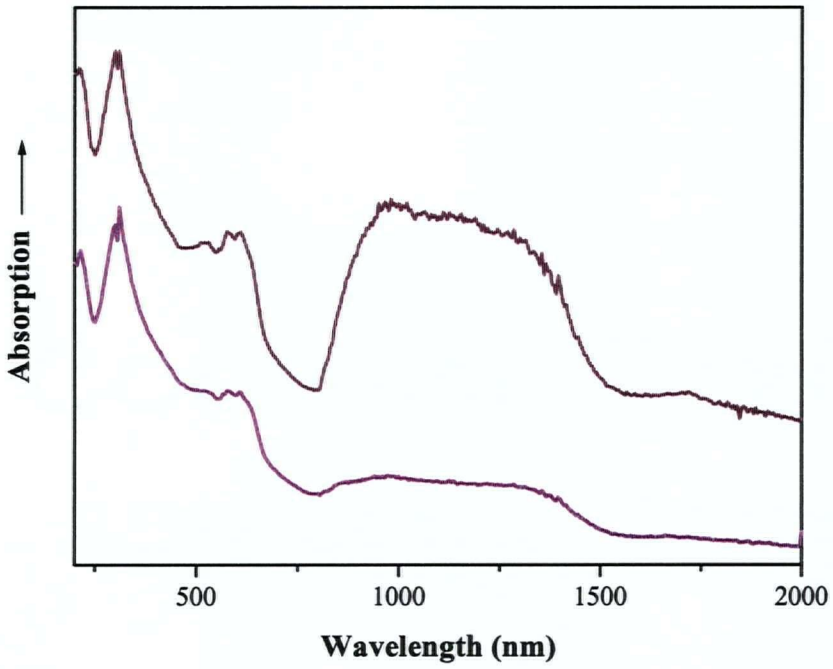

Figure 3.7 Electronic spectra of $[Co(4\text{-abimid})_2]_x$ at two different mull concentrations.

tetrahedral Co(II) compounds, but is often too weak to be observed [33]. Comparison of the spectral data with the corresponding Tanabe-Sugano diagram for d^7 tetrahedral systems [35], shows that these transitions are consistent with Dq and B values of 541 cm^{-1} and 731 cm^{-1} respectively. In summary, the electronic spectra of $[Co(4\text{-abimid})_2]_x$ is consistent with tetrahedrally coordinated cobalt centers, and a structure akin to that of the iron compound. Further support that the compounds are isomorphous comes from infrared spectroscopy. The infrared spectra of $[Fe(4\text{-abimid})_2]_x$ and $[Co(4\text{-abimid})_2]_x$ show very similar vibrational bands at almost identical frequencies.

The 3-D diamond-like structure seems to confer high thermal stability on both $[Fe(4\text{-abimid})_2]_x$ and $[Co(4\text{-abimid})_2]_x$, as shown by thermal gravimetric analysis (TGA) (Figure 3.8). $[Fe(4\text{-abimid})_2]_x$ is thermally stable to 402 °C. Decomposition with continuous weight loss occurs from 402 to 476 °C with a total weight loss of 70% of the initial mass. No additional loss of mass was observed up to the maximum temperature reached of 800 °C. $[Co(4\text{-abimid})_2]_x$ is thermally more robust than $[Fe(4\text{-abimid})_2]_x$, and it does not show significant weight loss until the temperature exceeds ~ 600 °C. This material shows a gradual weight loss amounting to 50 % of the initial mass over the temperature range of ~ 600 °C to 800 °C.

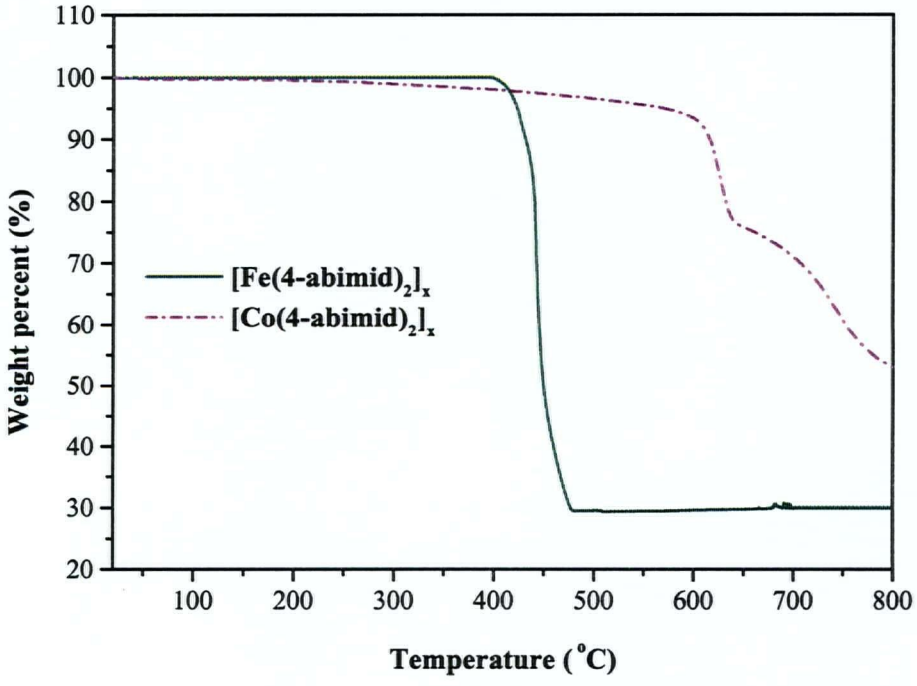

Figure 3.8 TGA plots for $[Fe(4\text{-abimid})_2]_x$ and $[Co(4\text{-abimid})_2]_x$.

3.2.2 MAGNETIC PROPERTIES

Magnetic susceptibilities of a powdered sample of $[Fe(4\text{-abimid})_2]_x$ were measured at a field of 500 G from 2 to 300 K. Figure 3.9 presents the χ versus T and χT versus T data obtained below 150 K. The value of χT decreases smoothly with temperature from the value 3.38 cm^3Kmol^{-1} at 300 K (corresponding to $\mu_{eff} = 5.20\ \mu_B$) to a low of 1.60 cm^3Kmol^{-1} just above a critical temperature, T_c, of 21 K. Below T_c, χT increases abruptly to a maximum value of 32.8 cm^3Kmol^{-1} at 14 K before decreasing again with temperature to 6.10 cm^3Kmol^{-1} at 2 K. The magnetic transition at T_c is also observed in the χ versus T plot (Figure 3.9). The magnetic susceptibility, which decreases smoothly with decreasing temperature below 300 K, rises abruptly (below T_c), as the temperature decreases before leveling off and approaching a saturation value.

This magnetic behavior exhibited by $[Fe(4\text{-abimid})_2]_x$ is similar to that reported for $[Fe_3(imid)_6(imidH)_2]_x$ [10] and $[Fe(2\text{-meimid})_2 \cdot 0.13Cp_2Fe]_x$ [11]. It suggests antiferromagnetic coupling in which perfect antiparallel alignment of spins on neighboring metal ions does not occur due to canting of spins. This leads to a residual spin on the metal centers as the temperature is lowered. Long-range ferromagnetic ordering of these spins below T_c generates a ferromagnetic transition.

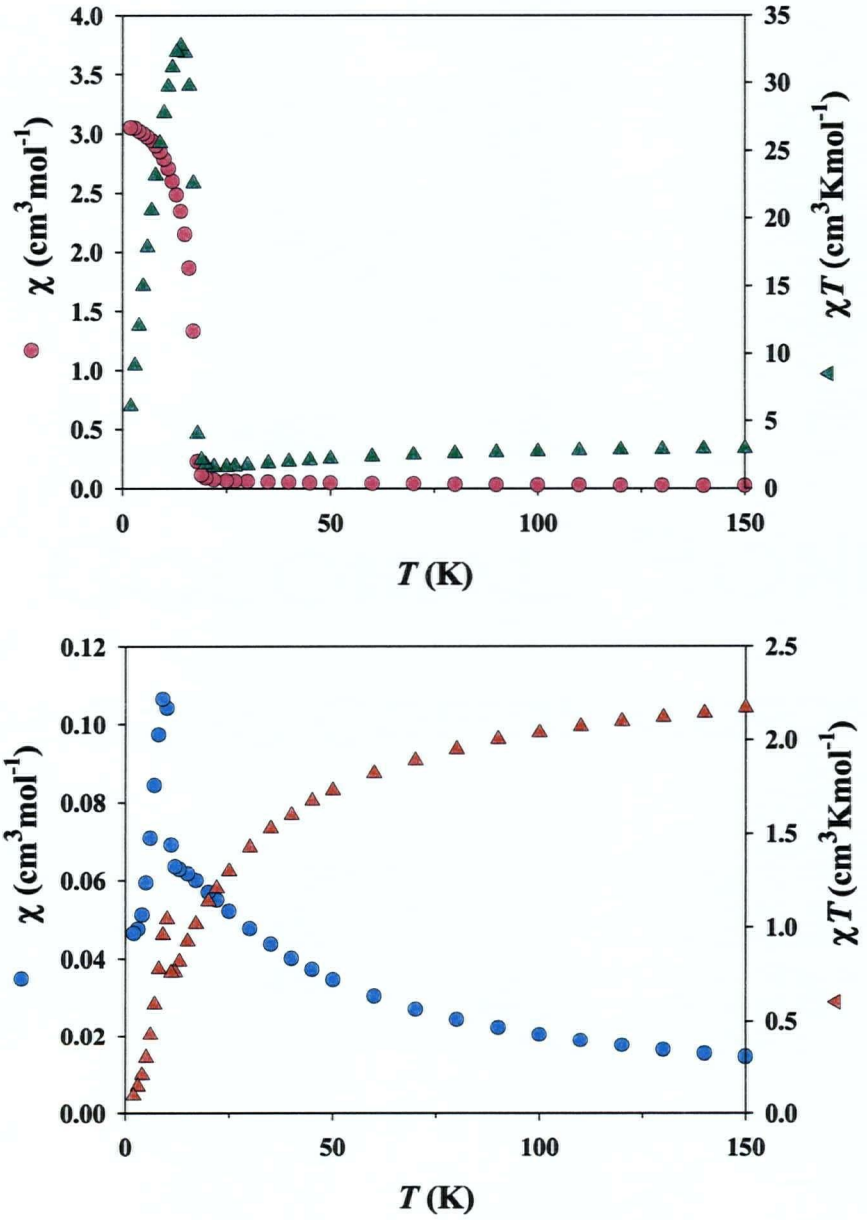

Figure 3.9 χ and χT versus T plots at 500 G for $[Fe(4\text{-abimid})_2]_x$ (top) and $[Co(4\text{-abimid})_2]_x$ (bottom).

The magnetization versus field plots at three temperatures, shown in Figure 3.10, reflect this anomalous magnetic behavior. The plot is linear at 35 K and extrapolates to zero magnetization at zero applied field while at 10 and 4.8 K (below T_c) the plots extrapolate to give a net magnetization at zero applied field. These results confirm that $[Fe(4\text{-abimid})_2]_x$ exhibits long-range ferromagnetic order below T_c. Cycling the applied field between +55 000 and –55 000 G at 4.8 K generates a hysteresis loop, the central portion of which is shown in Figure 3.11. From this is obtained a remnant magnetization of 2100 cm^3Gmol^{-1} and a coercive field of 80 G. This hysteresis magnetization result provides conclusive evidence that $[Fe(4\text{-abimid})_2]_x$ behaves as a magnet at low temperatures.

A spin-canted structure for $[Fe(4\text{-abimid})_2]_x$ is supported by the fact that the highest magnetization reached, 6690 cm^3Gmol^{-1}, (at 4.8 K and 55 000 G) is significantly smaller than the theoretical saturation value of 22 300 cm^3Gmol^{-1} [36]. Further evidence for a canted spin structure comes from the structural data of $[Fe(4\text{-abimid})_2]_x$ which show a feature observed before in this type of system, that is a systematic alternation of the relative orientation of neighboring metal chromophores [10, 11]. As a measure of this the dihedral angles between the N(1)–Fe(1)–N(5) planes on adjacent, symmetry related, iron centers was examined. On every iron center, the N(1)–Fe(1)–N(5) plane forms dihedral angles of 75.4° with the corresponding planes on two of its nearest neighbors and angles of 172.5° with the corresponding planes on the other two neighbors.

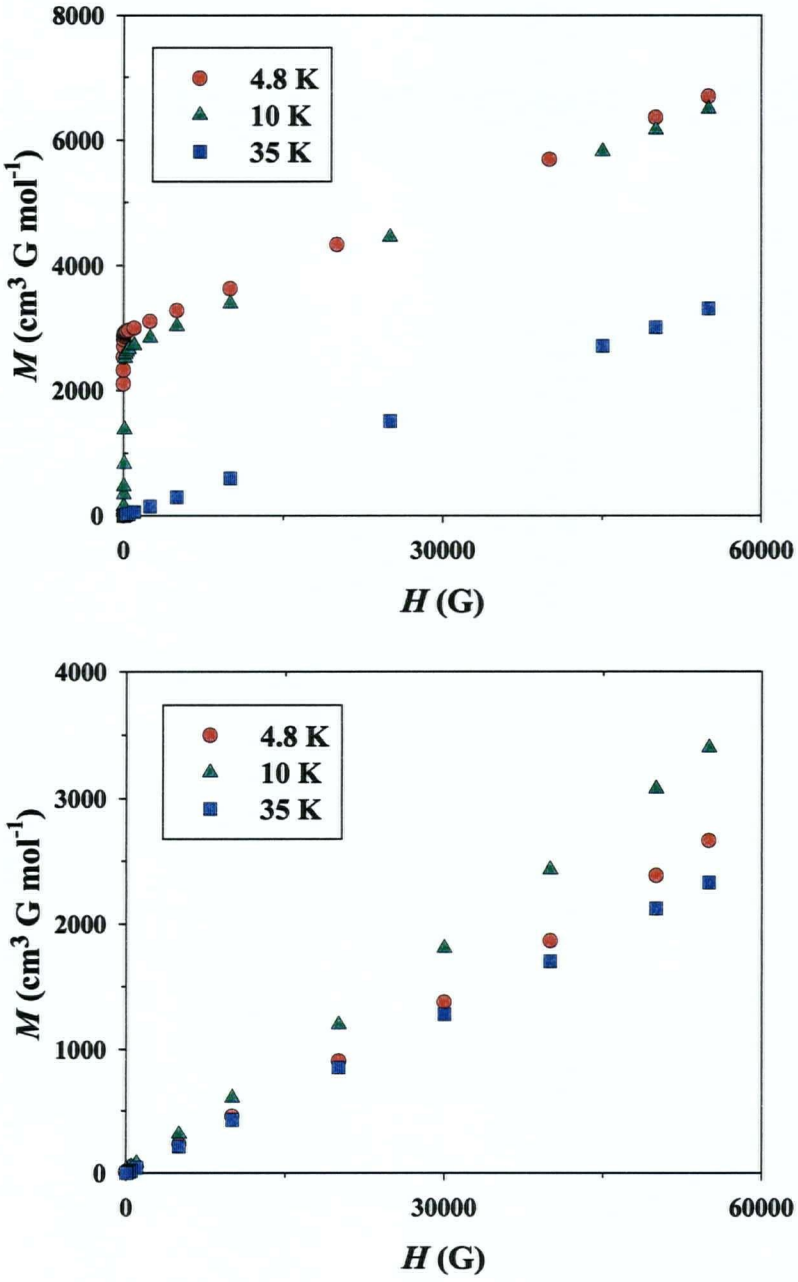

Figure 3.10 Magnetization versus applied field plots at different temperatures for $[Fe(4\text{-abimid})_2]_x$ (top) and $[Co(4\text{-abimid})_2]_x$ (bottom).

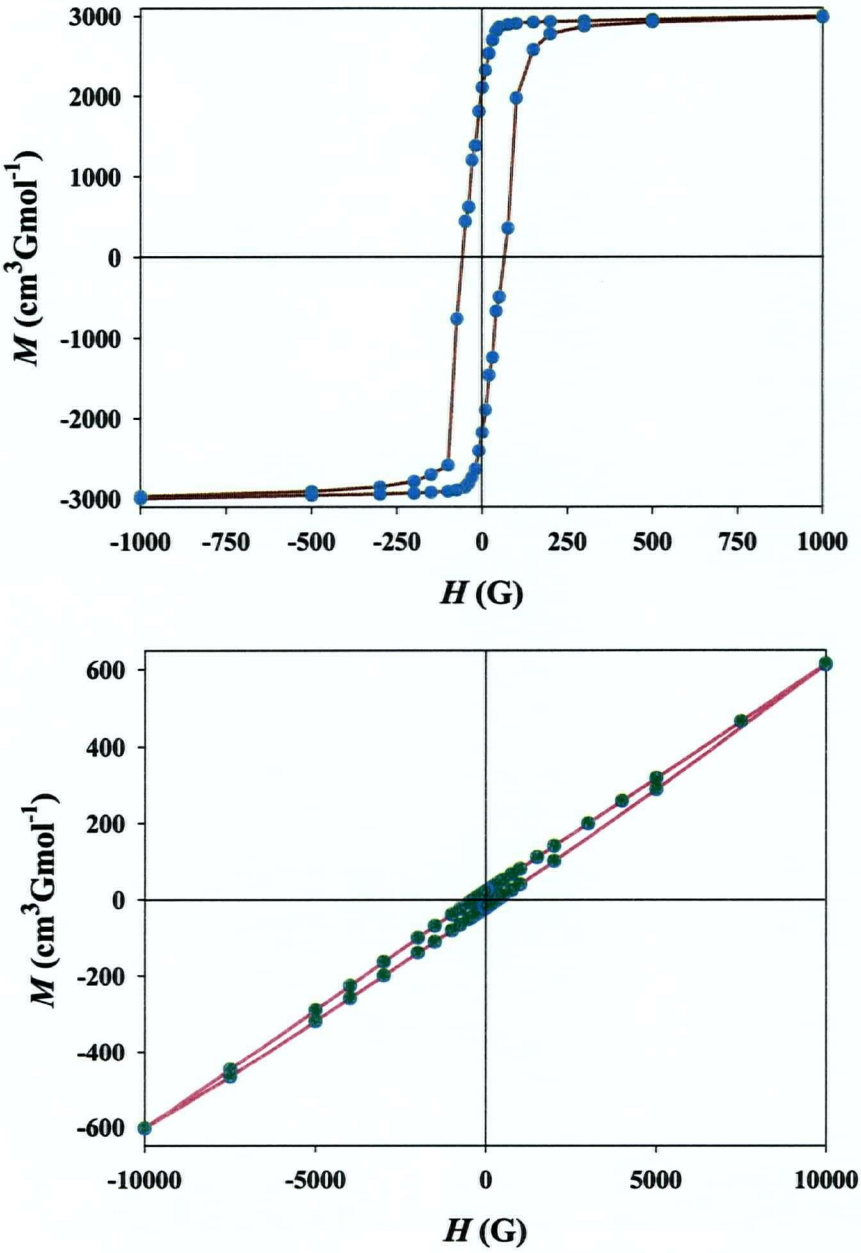

Figure 3.11 Magnetic hysteresis plots at 4.8 K for $[Fe(4\text{-abimid})_2]_x$ (top) and at 10 K for $[Co(4\text{-abimid})_2]_x$ (bottom).

The extent of the spin canting can be estimated by extrapolating the plot of magnetization (M) versus applied field (H) obtained at 4.8 K (Figure 3.10) to $H = 0$. This extrapolation gives a saturated moment ($M_s(0)$) of ~ 2650 cm^3Gmol^{-1} for $[Fe(4\text{-}abimid)_2]_x$. From this, an estimation of the spin canting angle, γ, can be obtained using the following equation [37]

$$\gamma = \tan^{-1}\left(\frac{M_S(0)}{Ng\mu_B S}\right)$$

Hence, the canting angle for $[Fe(4\text{-}abimid)_2]_x$ is calculated to be $\gamma \sim 7°$.

In the earlier study on the related $[Fe(2\text{-}meimid)_2 \cdot 0.13Cp_2Fe]_x$, it was observed that the ferromagnetic ordering appears to be repressed by the applied field [11]. The same situation, arising presumably through saturation effects, pertains to $[Fe(4\text{-}abimid)_2]_x$. Plots of χT and χ versus T (2 to 150 K range) obtained at 10 000 G are shown in Figure 3.12. Although the ferromagnetic transition is still observed at this applied field, the maximum in χT and the saturation value of χ are both smaller than observed at an applied field of 500 G.

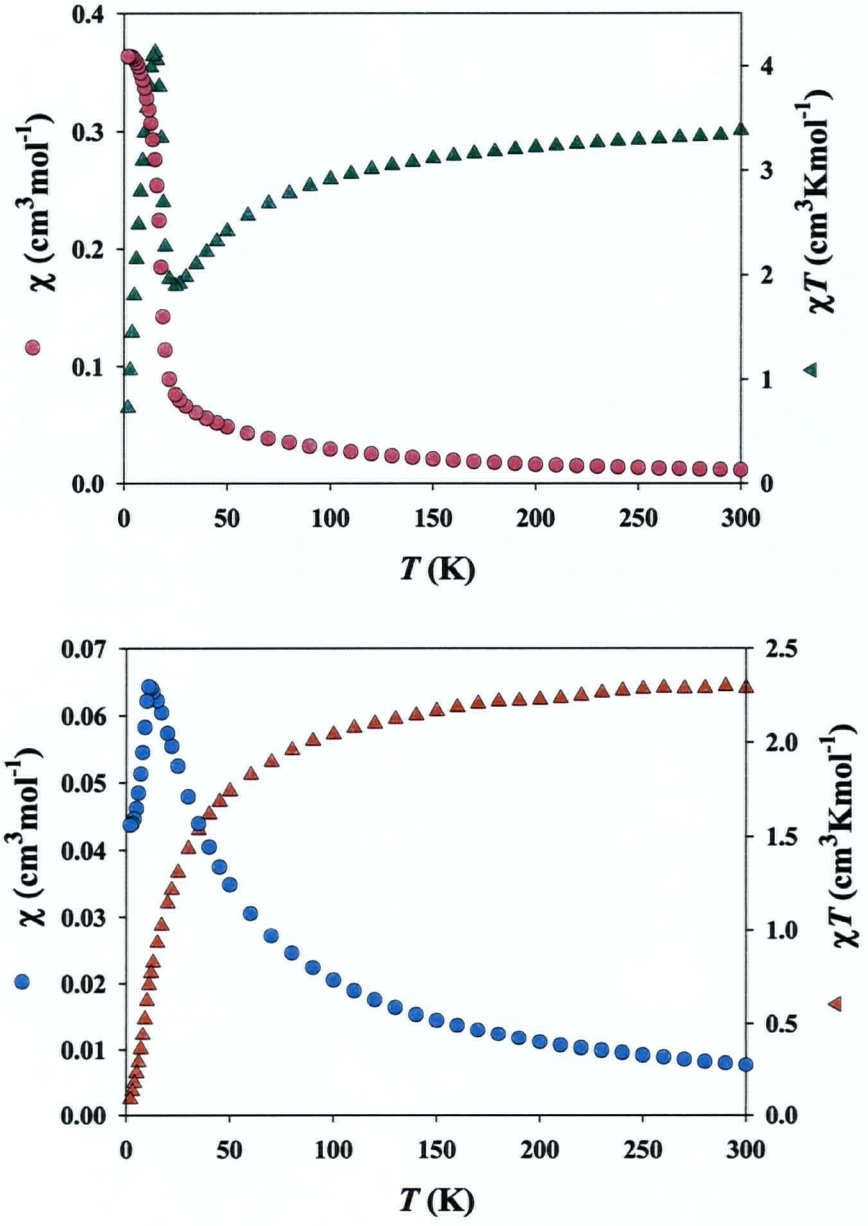

Figure 3.12 χ and χT versus T plots at 10 000 G for $[Fe(4\text{-abimid})_2]_x$ (top) and $[Co(4\text{-abimid})_2]_x$ (bottom).

In addition to DC measurements, the magnetic susceptibility was determined in an applied AC field of 1 G at 125 Hz for $[Fe(4\text{-abimid})_2]_x$ and the resulting data are consistent with long-range ferromagnetic order. An extremely sharp peak in the real part of the AC susceptibility, χ', at 17.27 K is further confirmation of the spontaneous magnetization exhibited by this compound (Figure 3.13). An out-of-phase component (imaginary), χ'', characteristic of a non-compensated moment is present also with a peak at 17.23 K (Figure 3.13). These peak maxima in χ' and χ'' provide more accurate measures of T_c [38] than DC magnetic susceptibility studies (*vide supra*) which indicate the critical temperature to be 21 K.

The magnetic properties of $[Co(4\text{-abimid})_2]_x$ suggest that it too can be classified as a spin canted low temperature molecule-based magnet. As for $[Fe(4\text{-abimid})_2]_x$, χT measured at an applied field of 500 G decreases with decreasing temperature from 2.30 cm^3Kmol^{-1} at 300 K (corresponding to $\mu_{eff} = 4.29\ \mu_B$) to a critical temperature $T_c = 11$ K. Below 11 K it increases abruptly, signaling the onset of long-range ferromagnetic ordering (Figure 3.9). Because of the very small remnant magnetization present in $[Co(4\text{-abimid})_2]_x$ the magnetization versus field plots shown in Figure 3.10 do not clearly display the net magnetization at zero applied field for the data obtained below T_c. The non-linearity of the plots obtained at 4.8 and 10 K is, however, evident. The highest magnetization measured for $[Co(4\text{-abimid})_2]_x$ was 3469 cm^3Gmol^{-1} at 10 K and 55 000 G. This is significantly lower than the theoretical saturation value of 16 766

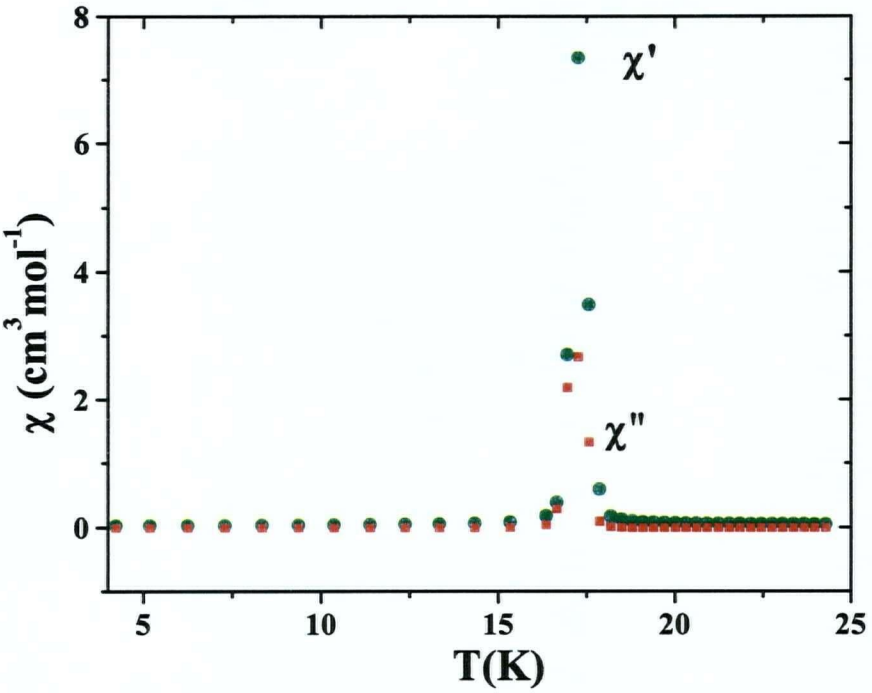

Figure 3.13 AC susceptibility of [Fe(4-abimid)2]x; H_{ac} = 1 G, f = 125 Hz

cm^3Gmol^{-1} for a S = 3/2 system [36], again consistent with spin canting providing the source of the residual spin at low temperatures. The canting angle for $[Co(4\text{-abimid})_2]_x$ was estimated to be very small (~ 0.1°) employing the method described above for the iron analogue.

The χ versus T plot for $[Co(4\text{-abimid})_2]_x$ is somewhat different from that observed for $[Fe(4\text{-abimid})_2]_x$ (Figure 3.9). For $[Co(4\text{-abimid})_2]_x$, the susceptibility shows an incipient maximum just above T_c and the expected abrupt rise below T_c;

however, as the temperature is lowered further, instead of showing saturation, as in $[Fe(4\text{-abimid})_2]_x$, χ passes through a maximum at 9 K and then decreases in value as the temperature is lowered further to 2 K (Figure 3.9). This type of behavior, which suggests the loss of long-range ferromagnetic order at the lowest temperatures, was observed previously for another cobalt(II) spin-canted molecule-based magnet, polybis(formamide)bis(μ-formato)cobalt(II) [39]. In this earlier study it was observed that for the formate compound this disruption of long-range order is not seen at lower applied fields. This prompted us to examine the susceptibility versus temperature behavior of $[Co(4\text{-abimid})_2]_x$ at applied fields below and above 500 G. Plots of χ versus T obtained at applied fields ranging from 50 to 10 000 G in the temperature range 2 – 25 K are shown in Figure 3.14. Above T_c the susceptibilities are essentially field independent. Below T_c, at fields of 50, 100 and 500 G there is an abrupt rise in χ signaling ferromagnetic ordering. At all three of these fields the susceptibility on further cooling passes through a maximum, the magnitude of which increases with decreasing applied field strength, consistent with earlier observations that ferromagnetic ordering in such systems appears to be repressed by applied fields. At the largest field studied, 10 000 G, there is no evidence of long-range ferromagnetic ordering as the susceptibility simply passes through a single maximum at about 10 K, indicative of the antiferromagnetic coupling. This is more clearly seen in Figure 3.12 which also shows that there is no magnetic anomaly in the χT plot for $[Co(4\text{-abimid})_2]_x$ at 10 000 G. In Figure 3.12, the susceptibility for $[Co(4\text{-abimid})_2]_x$ is seen to approach a constant value of ~ 0.043 cm^3mol^{-1} at the lowest temperatures, a consequence, presumably, of the spin

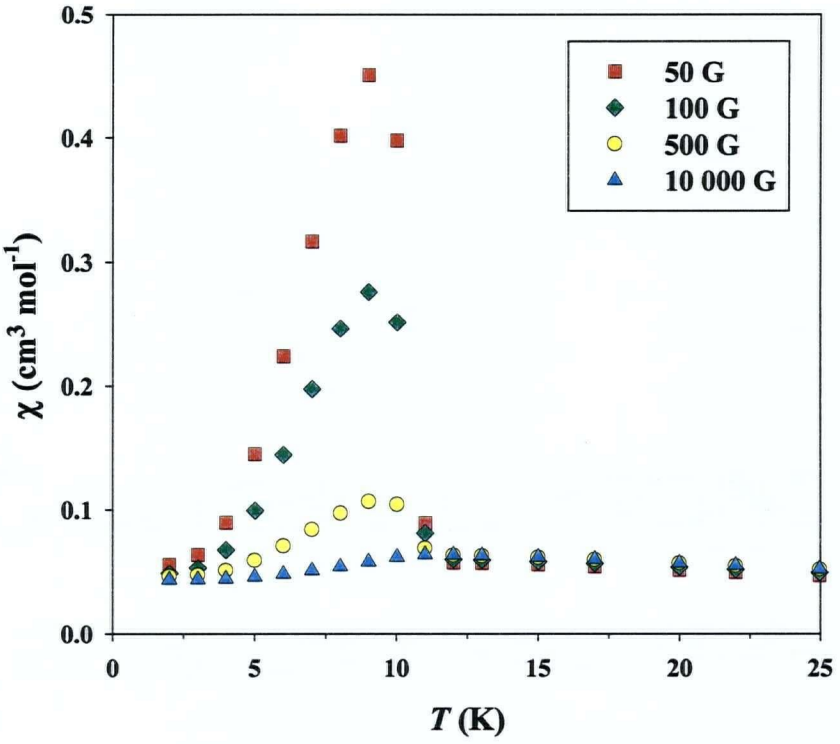

Figure 3.14 χ versus T plots for $[Co(4\text{-abimid})_2]_x$ at 50, 100, 500 and 10 000 G.

canting. At 2 K this χ value corresponds to an effective magnetic moment of 0.83 μ_B. At the three lowest fields studied, where ferromagnetic ordering is seen, the susceptibilities decrease below 9 K and, in all cases, approach at the lowest temperature studied the same value as that recorded at 10 000 G (Figure 3.14). There is no simple explanation for this apparent loss in ferromagnetic order at low temperatures. The cause could be at the single-ion level. The $^4A_2$ electronic ground state of tetrahedral cobalt(II) is subject to zero-field splitting and if this is large enough significant changes in the

population of zero-field split levels at low temperatures could affect the exchange. The significance of this factor will depend of course on the magnitude of the zero-field splitting. This may account for the fact that, although the ^5E ground state of tetrahedral iron(II) is also subject to zero-field splitting, loss in ferromagnetic ordering at low temperatures is not seen for the iron analogue, $[Fe(4\text{-abimid})_2]_x$.

A consequence of the phenomenon just discussed for the cobalt compound, $[Co(4\text{-abimid})_2]_x$, is that its hysteresis properties measured below T_c depend significantly on temperature. Measured at 10 K the hysteresis plot (central portion shown in Figure 3.11) yields M_{rem} = 22 cm^3Gmol^{-1} and H_{coer} = 400 G while at 4.8 K (the temperature at which the hysteresis behaviour was measured for $[Fe(4\text{-abimid})_2]_x$) M_{rem} = 6 cm^3Gmol^{-1} and H_{coer} = 100 G.

AC magnetic susceptibility measurements determined for $[Co(4\text{-abimid})_2]_x$ show this compound has a non magnetic ground state (Figure 3.15). In contrast to the AC susceptibility behaviour of $[Fe(4\text{-abimid})_2]_x$ (Figure 3.13), the cobalt analogue displays just a discontinuity on the real component of the susceptibility, χ', at 11 K (Figure 3.15). The imaginary component, χ'', does not show a maximum. This result is not totally inconsistent with the DC susceptibility study which clearly indicated a loss in ferromagnetic order at low temperatures for $[Co(4\text{-abimid})_2]_x$. In order to further investigate this behavior, the AC susceptibility measurements were done with application of a small DC field. It was expected that the presence of a low DC magnetic

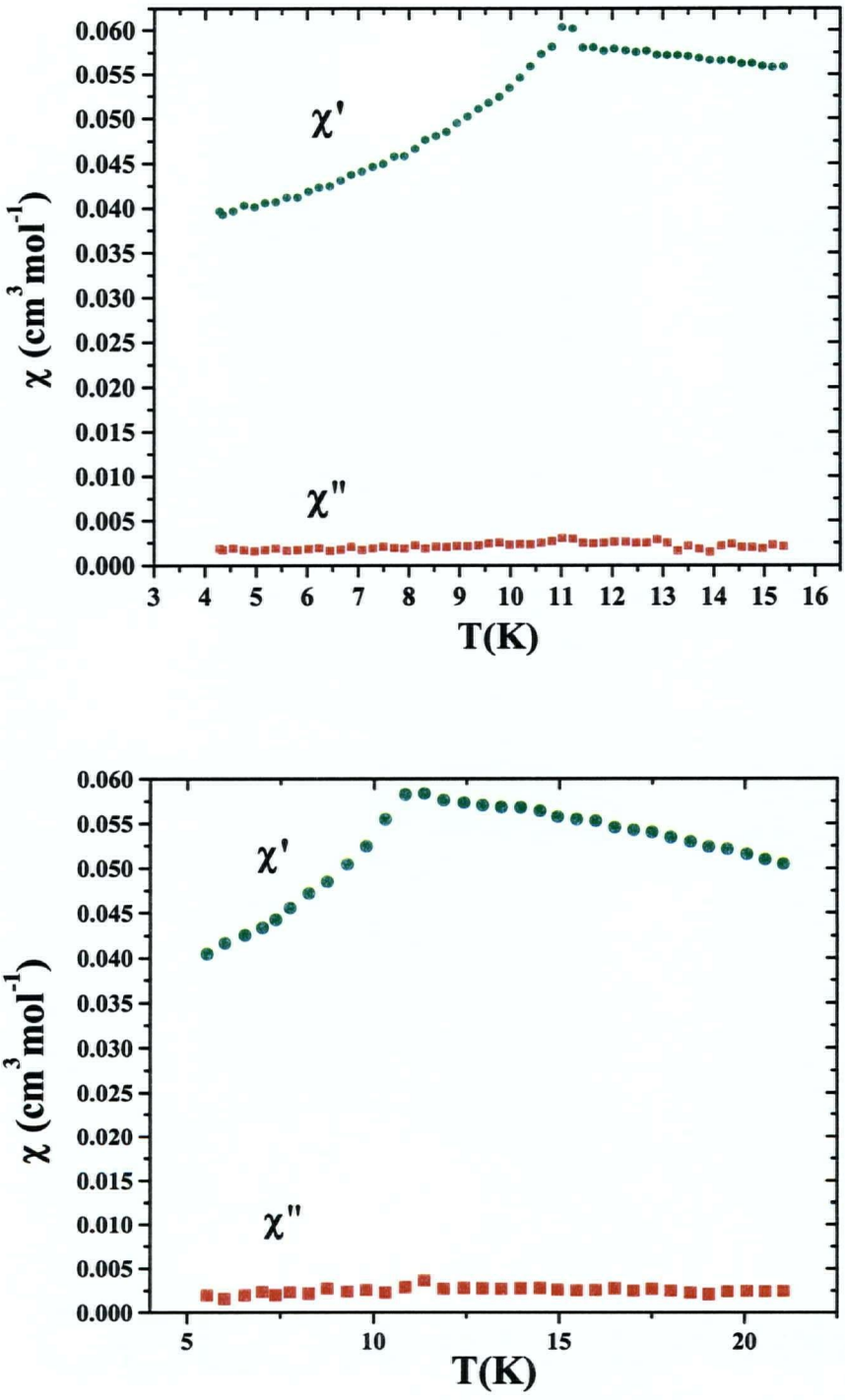

Figure 3.15 AC susceptibility for $[Co(4\text{-abimid})_2]_x$; H_{AC} = 1 G, f = 125 Hz (top) and H_{AC} = 1 G, H_{DC} = 20 G, f = 125 Hz (bottom).

field (20 G) would help to reveal the magnetic transition in the AC susceptibility study of $[Co(4\text{-abimid})_2]_x$. As can be seen in Figure 3.15 the application of the small DC field had basically no effect on the AC susceptibility behaviour.

Hence, in concordance with the magnetic studies discussed above it was found that, although $[Co(4\text{-abimid})_2]_x$ also exhibits the properties of a molecule-based magnet its critical temperature, as well as coercive field and remnant magnetization at 4.8 K are all markedly different from those exhibited by $[Fe(4\text{-abimid})_2]_x$.

3.2.3 MÖSSBAUER SPECTROSCOPY

The Mössbauer spectrum of $[Fe(4\text{-abimid})_2]_x$ shows a single quadrupole split doublet at 77.3 K (Figure 3.16) corresponding to a single tetrahedral site, and consistent with the structure determined single crystal X-ray diffraction studies (Figure 3.1). The isomer shift of about 0.83 mm s^{-1} at 77.3 K is typical of a tetrahedral ferrous chromophore [40] whereas the quadrupole splitting of 3.01 mm s^{-1} indicates a large low symmetry ligand field component lifting the degeneracy of the nominal ^5E ground state of regular T_d symmetry [41]. This single, sharp, narrow line-width doublet is maintained down to 18.5 K (Figure 3.17). At a temperature of about 18 K magnetic hyperfine splitting occurs signaling the onset of long-range magnetic order. This is consistent with the findings of the magnetization experiments discussed above and the

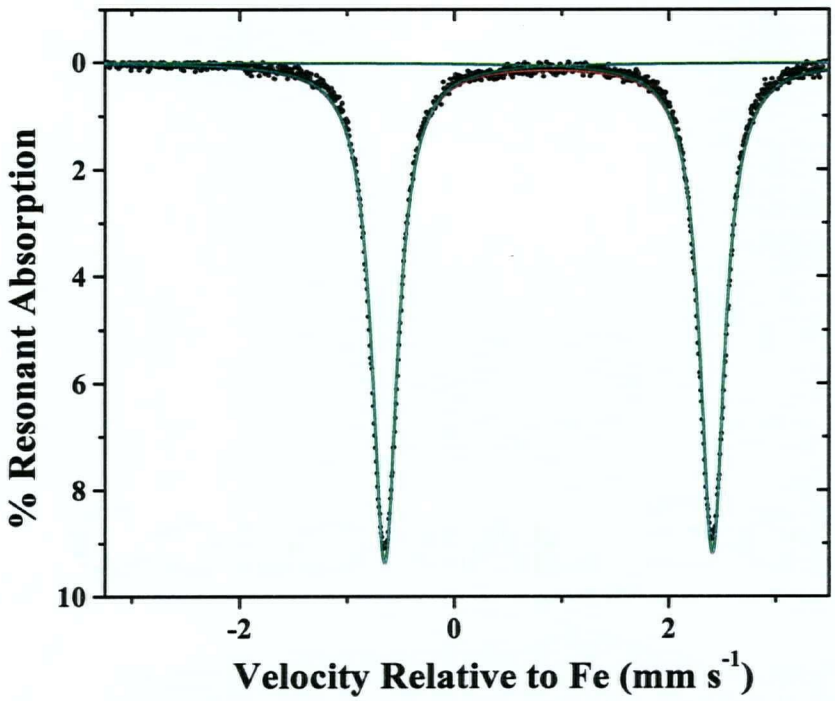

Figure 3.16 Mössbauer spectrum of $[Fe(4\text{-abimid})_2]_x$ at 77.3 K.

temperature is in good agreement with the ones determined by the DC and AC susceptibility measurements (21 K and 17.27 K respectively). For a unique Fe(II) site the number of hyperfine lines should be six. Careful examination of the spectra, particularly the one at 4.3 K (Figure 3.17), reveals more than six lines suggesting the presence of at least two unique iron sites. This is not in agreement with the higher temperature X-ray diffraction structure and suggest a structural phase change at low temperatures. A low temperature X-ray diffraction structure determination for $[Fe(4\text{-abimid})_2]_x$ (below 18 K) is needed to confirm this finding.

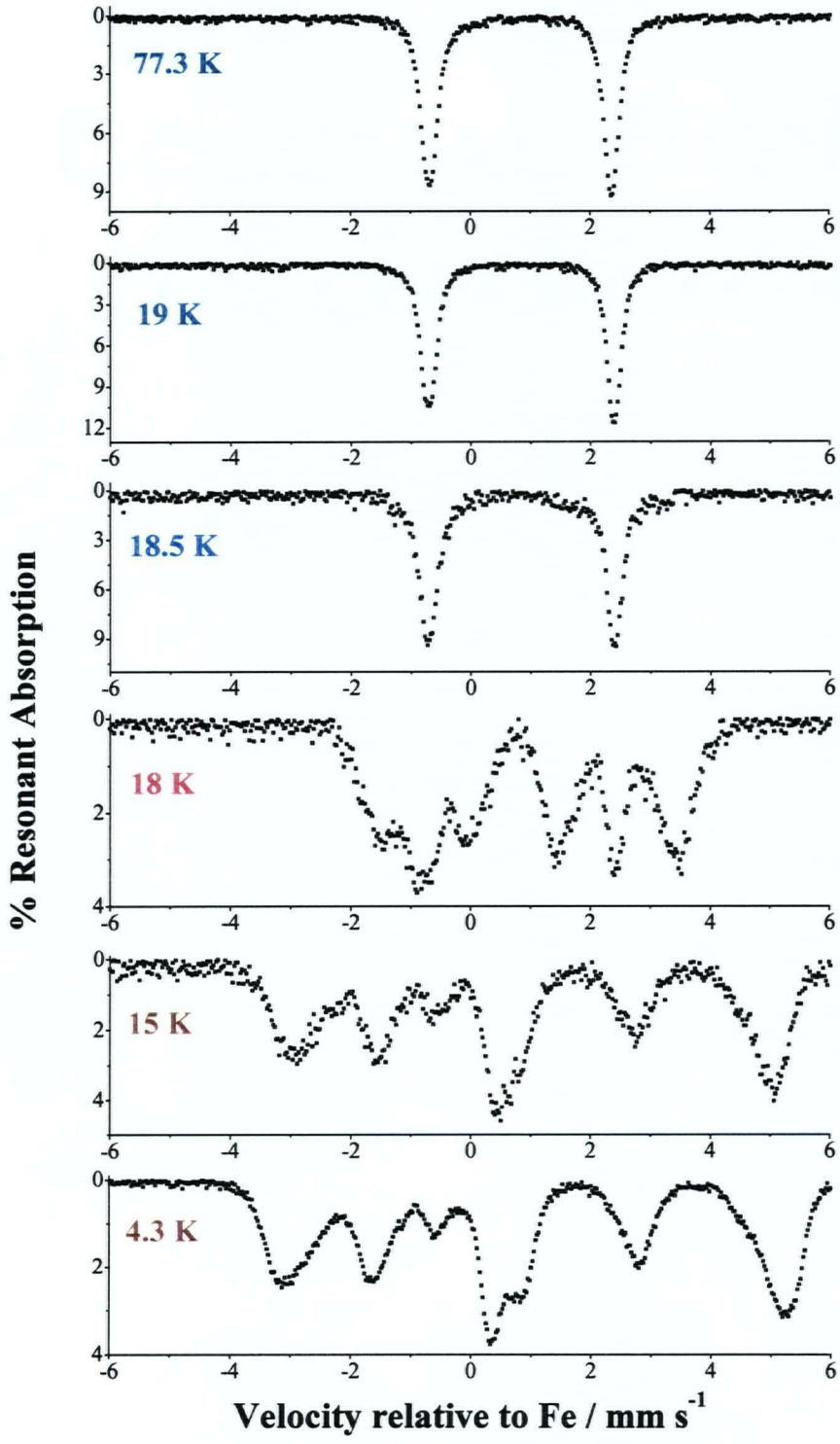

Figure 3.17 Selected Mössbauer spectra for $[Fe(4\text{-abimid})_2]_x$ at various temperatures

3.3 SUMMARY AND CONCLUSIONS

$[Fe(4\text{-abimid})_2]_x$ and $[Co(4\text{-abimid})_2]_x$ provide the first examples of isomorphous and presumably isostructural molecule-based magnets of two different metals. The objective in comparing two such materials was to examine the effect on the magnetic properties of changing the d^n configuration of the metal. In both $[Fe(4\text{-abimid})_2]_x$ and $[Co(4\text{-abimid})_2]_x$ the metal is in a pseudo-tetrahedral geometry. In terms of single ion effects there is no first-order orbital contribution to the magnetic moment in either case [42] and the primary difference lies in the spin contributions, S = 2 for $[Fe(4\text{-abimid})_2]_x$ and S = 3/2 for $[Co(4\text{-abimid})_2]_x$. This may, partly at least, contribute to the smaller remnant magnetization observed for $[Co(4\text{-abimid})_2]_x$ (6 cm^3Gmol^{-1} at 4.8 K and 22 cm^3Gmol^{-1} at 10 K) compared to that for $[Fe(4\text{-abimid})_2]_x$ (2100 cm^3Gmol^{-1} at 4.8 K). It seems likely, however, that the degree of spin canting, calculated and described above to be very small for the cobalt compound, would be much more important in this regard. The coercive fields are not as remarkably different in the two materials. This quantity, defined as the applied field required to return the magnetization of the sample to zero, is 80 G (at 4.8 K) for $[Fe(4\text{-abimid})_2]_x$ and 100 G at 4.8 K (400 G at 10 K) for $[Co(4\text{-abimid})_2]_x$. In terms of hysteresis behavior another characteristic property is the range of applied fields over which the magnetization of the sample is dependent on the history of the field sweep (increasing or decreasing). In this regard the samples are quite different. For $[Fe(4\text{-abimid})_2]_x$ this field range is approximately ±1 000G at 4.8 K while for $[Co(4\text{-abimid})_2]_x$ it is about ±10 000 G at

10 K. At 4.8 K the magnetization of $[Co(4\text{-abimid})_2]_x$ is dependent on the history of the field sweep over the entire range of fields studied. Finally it is noticeable that below T_c ferromagnetic ordering persists at higher applied fields for $[Fe(4\text{-abimid})_2]_x$ than for $[Co(4\text{-abimid})_2]_x$ and that the apparent loss in order at low temperatures and all fields exhibited by $[Co(4\text{-abimid})_2]_x$ is not observed for $[Fe(4\text{-abimid})_2]_x$. On the basis of this single study it would be dangerous to draw general conclusions. To establish the generality of such findings investigation of other isomorphous pairs of iron and cobalt compounds is required. Also to better understand the detailed aspects of the magnetic properties of both compounds single crystal and powder X-ray diffraction studies at He temperatures are needed. Ideally, neutron diffraction experiments would also be very useful. The difficulty here is that larger single crystals of the iron(II) compound are required and, since presence of hydrogen atoms interfere in the neutron diffraction results, a deuterated $[Fe(4\text{-abimid})_2]_x$ would need to be prepared [43, 44].

References

1. M. K. Ehlert, S. J. Rettig, A. Storr, R. C. Thompson, and J. Trotter. *Can. J. Chem.* **67**, 1970 (1989).

2. M. A. Martinez-Lorente, V. Petrouleas, R. Poinsot, J. P. Tuchagues, J. M. Savariault, and M. Drillon. *Inorg. Chem.* **30**, 3587 (1991).

3. M. K. Ehlert, S. J. Rettig, A. Storr, R. C. Thompson, and J. Trotter. *Can. J. Chem.* **68**, 1444 (1990).

4. M. K. Ehlert, S. J. Rettig, A. Storr, R. C. Thompson, and J. Trotter. *Can. J. Chem.* **68**, 1494 (1990).

5. M. K. Ehlert, S. J. Rettig, A. Storr, R. C. Thompson, and J. Trotter. *Can. J. Chem.* **69**, 432 (1991).

6. M. K. Ehlert, S. J. Rettig, A. Storr, and R. C. Thompson. *Can. J. Chem.* **70**, 1121 (1992).

7. M. K. Ehlert, S. J. Rettig, A. Storr, and R. C. Thompson. *Can. J. Chem.* **71**, 1412 (1993).

8. Ehlert, M. K.; Rettig, S. J.; Storr, A.; Thompson, R. C.; Einstein, F. W. B.; Batchelor, R. J. *Can. J. Chem.* **71**, 331 (1993).

9. M. K. Ehlert, A. Storr, D. A. Summers, and R. C. Thompson. *Can. J. Chem.* **75**, 491 (1997).

10. S. J. Rettig, A. Storr, D. A. Summers, R. C. Thompson, and J. Trotter. *J Amer. Chem. Soc.* **119**, 8675 (1997).

11. S. J. Rettig, A. Storr, D. A. Summers, R. C. Thompson, and J. Trotter. *Can. J. Chem.* **77**, 425 (1999).

12. B. F. Hoskins and R. Robson. *J. Amer. Chem. Soc.* **112**, 1546 (1990).

13. L. R. MacGillivray, S. Subramanian, and M. J. Zaworotko. *J. Chem. Soc. Chem. Commun.* 1325 (1994).

14. M. Ward. *Chemistry in Britain.* September, 52 (1998).

15. M. Munakata, L. P. Wu, and T. Kuroda-Sowa. *Adv. Inorg. Chem.* **46**, 173 (1999).

16. Y. Kinoshita, I. Matsubara, T. Higuchi and Y. Saito. *Bull. Chem. Soc. Jpn.* **34**, 1221 (1959).

17. O. Ermer. *Adv. Mater.* **3**, 608 (1991).

18. B. F. Abrahams, M. J. Hardie, B. F. Hoskins, R. Robson, and G. A. Williams. *J. Am. Chem. Soc.* **114**, 10641 (1992).

19. O. M. Yaghi, D. A. Richardson, G. Li, E. Davis, and T. L. Groy, *Mater. Res. Soc. Symp. Proc., 371 (Advances in Porous Materials)*, **15**, 1995.

20. T. Vossmeyer, G. Reck, L. Katsikas, E. T. K. Haupt, B. Schulz, and H. Weller. *Science.* **267**, 1476 (1995).

21. T. Kuroda-Sowa, M. Yamamoto, M. Munakata, M. Seto, and M. Maekawa. *Chem. Lett.*, 349 (1996).

22. T. Kuroda-Sowa, T. Horino, M. Yamamoto, Y. Ohno, M. Maekawa, and M. Munakata. *Inorg. Chem.* **36**, 6382 (1997).

23. S. Lopez, M. Kahraman, M. Harmata, and S. W. Keller. *Inorg. Chem.* **36**, 6138 (1997).

24. S. M. Stalder and A. P. Wilkinson. *Chem. Mater.* **9**, 2168 (1997).

25. E. Siebel, A. M. A. Ibrahim, and R. D. Fischer. *Inorg. Chem.* **38**, 2530 (1999).

26. M. G. F. Vaz, L. M. M. Pinheiro, H. O. Stumpf, A. F. C. Alcântara, S. Golhen, L. Ouahab, O. Cador, C. Mathonière, and O. Kahn. *Chem. Eur. J.* **5**, 1486 (1999).

27. S. J. Rettig, V. Sánchez, A. Storr, R. C. Thompson, and J. Trotter. *J. Chem. Soc., Dalton Trans.* 3931 (2000).

28. W. Choe, Y.-H. Kiang, Z. Xu, and S. Lee. *Chem. Mater.* **11**, 1776 (1999).

29. T. Otieno, S. J. Rettig, R. C. Thompson, and J. Trotter. *Inorg. Chem.* **32**, 1607 (1993).

30. PowderCell, version 2.3, W. Krauss and G. Nolze, Federal Institute for Materials Research and Testing (BAM). Berlin, 1997.

31. R. Shirley, *The CRYSFIRE System for Automatic Powder Indexing: User's Manual*, The Lattice Press, Guildford, 1999; J. W. Visser, *J. Appl. Crystallogr.* **2**, 89 (1969).

32. A. M. Vecchio-Sadus. *Transition Met. Chem.* **20**, 46 (1995).

33. M. K. Ehlert, A. Storr and R. C. Thompson. *Can. J. Chem.* **71**, 1412 (1993).

34. F. A. Cotton and G. Wilkinson. *Advanced Inorganic Chemistry. A Comprehensive Text.* 4th Edition. Wiley-Interscience. New York. 1980. pp. 770-772.

35. Y. Tanabe and S. Sugano. *J. Phys. Soc. Jpn.* **9**, 753 (1954).

36. R. L. Carlin, *Magnetochemistry.* Springer-Verlag. Berlin. 1986. pp. 7-9.

37. F. Palacio, M. Andres, R. Horne, and A. J. van Duyeneveldt. *J. Magn. Magn. Mater.* **54-57**, 1487 (1986).

38. O. Kahn. *Acc. Chem. Res.* **33** (10) 647 (2000).

39. S. J. Rettig, R. C. Thompson, J. Trotter and S. Xia. *Inorg. Chem.* **38**, 1360 (1999).

40. B. W. Dockum and W. M. Reiff. *Inorg. Chim. Acta.* **120**, 61 (1986).

41. N. N. Greenwood and T. C. Gibb. Mössbauer Spectroscopy. Chapman and Hall Ltd. London. 1971.

42. B. N. Figgis and M. A. Hitchman, *Ligand Field Theory and Its Applications.* Wiley-VCH. New York. 2000.

43. J. L. Manson, Q. Huang, J. W. Lynn, H-J. Koo, M-H. Wahngbo, R. Bateman, T. Otsuka, N. Wada, D. N. Argyriou, and J. S. Miller. *J. Am. Chem. Soc.* **123**, 162 (2001).

44. C. Hardacre, J. D. Holbrey, and S. E. J. McMath. *J. Chem. Soc. Chem. Commun.* 367 (2001).

Chapter 4 BINARY IMIDAZOLATES OF COBALT(II), NICKEL(II), AND COPPER(II)

4.1 INTRODUCTION

As previously stated, the non-centrosymmetric M-L-M exchange pathway provided by single-bridging 1,3-diazolate ligands (Chapter 1, section 1.4) appears to be a key factor in generating spin canting and weak ferromagnetism in $[Fe_3(imid)_6(imidH)_2]_x$ [1], $[Fe(2\text{-meimid})_2 \cdot 0.13Cp_2Fe]_x$ [2], and $[Fe(4\text{-abimid})_2]_x$ (Chapter 3). The phenomenon should not be restricted to coordination polymers of iron(II). This fact, coupled with the observation that the iron centers involved in the primary exchange pathways in the above systems are tetrahedrally coordinated, a common geometry for cobalt(II), prompted interest in broadening the investigation to include the magnetic properties of related cobalt systems. This work was later extended to the nickel and copper imidazolate systems.

4.2 COBALT(II) IMIDAZOLATE POLYMERS

4.2.1 INTRODUCTION

Reported here are the synthesis, structural studies and magnetic properties of five cobalt systems: $[Co(imid)_2]_x$, $[Co(2\text{-meimid})_2]_x$, $[Co(4\text{-meimid})_2]_x$, $[Co(benzimid)_2]_x$

(benzimid = benzimidazolate), and $[Co_3(imid)_6(imidH)_2]_x$. $[Co(imid)_2]_x$ has been reported previously and its structure determined by single crystal X-ray diffraction studies [3]. We had hoped to determine the molecular structures of the other cobalt(II) imidazolates studied here; unfortunately, in spite of utilizing a synthetic route which has been very successful in obtaining single crystals of related iron(II) imidazolate polymers [1, 2], it was not possible to obtain macroscopic single crystals of these Co(II) compounds. In the present work we were, however, able to show by X-ray powder diffraction studies that $[Co_3(imid)_6(imidH)_2]_x$, is isomorphous, and presumably isostructural, with the iron analogue. The latter has an extended 3-D lattice structure [1]. $[Co(2\text{-meimid})_2]_x$, $[Co(4\text{-meimid})_2]_x$ and $[Co(benzimid)_2]_x$, have been reported previously [4-6] and although definitive structures of these compounds remain elusive, spectroscopic and thermal analysis data described below attest to their polymeric nature.

$[Co(imid)_2]_x$ was chosen to be investigated, in particular, because its structure is known and because previous magnetic measurements were conducted at high temperatures only [3, 6]. Of the other four compounds only $[Co(benzimid)_2]_x$ has been subjected to magnetic studies previously, again only at high temperatures [7]. New magnetization studies to cryogenic temperatures on the five cobalt systems are reported here. All five compounds show the presence of antiferromagnetic exchange, and three of them, $[Co(imid)_2]_x$, $[Co(benzimid)_2]_x$ and $[Co_3(imid)_6(imidH)_2]_x$ show clear transitions below critical temperatures, T_c, to low-temperature long-range ferromagnetically ordered states.

4.2.2 RESULTS AND DISCUSSION

4.2.2.1 SYNTHESES, PHYSICAL, THERMAL AND STRUCTURAL CHARACTERIZATION

$[Co(imid)_2]_x$, was prepared by reacting cobalt(II) nitrate hexahydrate with an excess of imidazole in water (Chapter 9, section 9.2.2.1). This method yields a purple microcrystalline powder. A method involving basic conditions and another, an electrochemical procedure, have been reported in the literature [3, 4-6]. $[Co(imid)_2]_x$ was also produced in the present study by thermal decomposition of $[Co_3(imid)_6(imidH)_2]_x$, at ~ 325 °C, at which temperature the loss of the neutral imidazole molecules occurs (*vide infra*).

The methods described for the synthesis of $[Co(2\text{-meimid})_2]_x$, $[Co(4\text{-meimid})_2]_x$, and $[Co(benzimid)_2]_x$ (Chapter 9, sections 9.2.2.2 through 9.2.2.4), also led to purple microcrystalline materials and efforts to produce samples suitable for single crystal X-ray studies were unsuccessful. The structure of $[Co(imid)_2]_x$, was determined previously by X-ray crystallography [3]. This crystalline form of the compound displays tetrahedrally coordinated cobalt(II) ions. It is a 3-D polymer consisting of fused puckered rings of four tetrahedrally coordinated cobalt(II) ions linked by single-bridging imidazolates. A representation of the asymmetric unit of $[Co(imid)_2]_x$ is shown in Figure 4.1. This illustration was obtained employing the software Powdercell [8] using the crystallographic data previously reported [3].

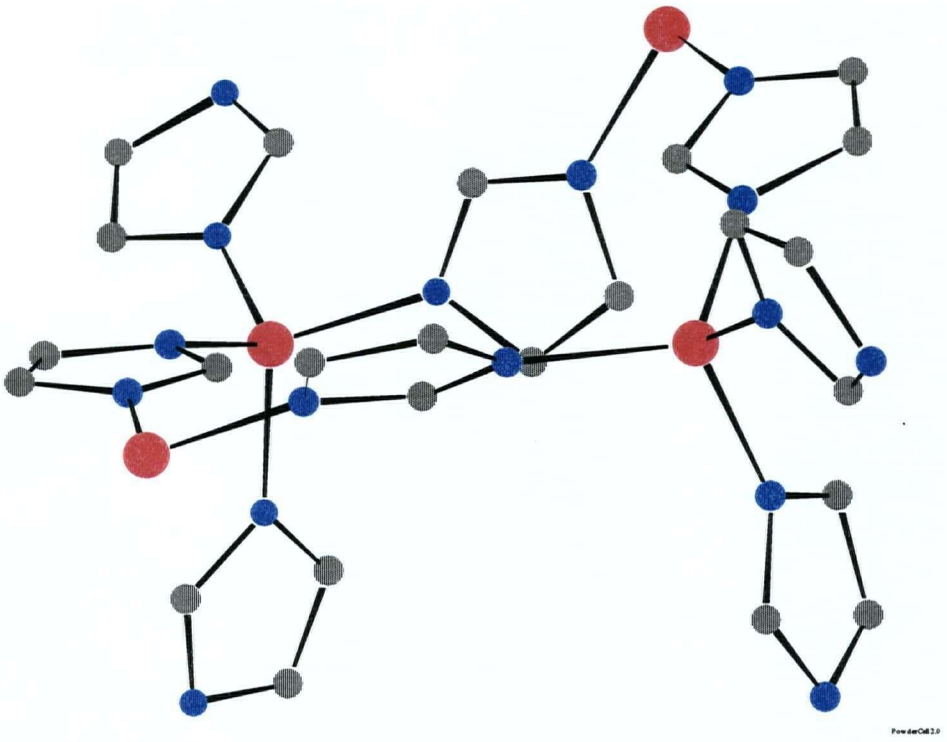

Figure 4.1 Asymmetric unit of $[Co(imid)_2]_x$. View looking down the c axis. Hydrogen atoms are omitted.

Although the exact structures of $[Co(2\text{-meimid})_2]_x$, $[Co(4\text{- meimid})_2]_x$, and $[Co(benzimid)_2]_x$ remain unknown the polymeric nature of the materials is indicated by their physical properties, which to some extent resemble those determined for $[Co(imid)_2]_x$. All four of these compounds are stable both in air and in contact with moisture. They are insoluble in water and common organic solvents; they are nonvolatile, and thermally robust, and they decompose when treated with concentrated mineral acids. Thermal gravimetric analyses of these materials show no mass loss due to thermal

decomposition or sublimation below 200 °C and at higher temperatures the compounds present similar thermal decomposition behaviors with no significant weight loss till temperatures above 400 °C are reached (Figure 4.2). $[Co(benzimid)_2]_x$ is the most thermally robust of the four compounds in that there is no indication of thermal decomposition below 600 °C for this material.

The electronic spectra of $[Co(imid)_2]_x$, $[Co(2\text{-}meimid)_2]_x$, $[Co(4\text{-}meimid)_2]_x$, and $[Co(benzimid)_2]_x$ are very similar (Figure 4.3). They show two intense d-d transition bands, the first one centered (determined visually) around 1110 - 1130 nm (broad and structured), and the second one observed between 570 - 590 nm, the latter with a shoulder at about 520 –540 nm. These can be tentatively assigned to the $^4A_2 \rightarrow {}^4T_1(F)$ and $^4A_2 \rightarrow {}^4T_1(P)$ transitions, respectively, of (distorted) tetrahedral cobalt(II) [9]. The absorptions seen at the lowest wavelengths (Figure 4.3) arise from charge transfer transitions. An expected third d-d band due to the $^4A_2 \rightarrow {}^4T_2$ transition, expected in the 1500 - 2500 nm region, is usually too weak and broad, to be clearly identified in spectra of mulls of the type studied here. Nevertheless, this third band is just apparent in the spectra of $[Co(imid)_2]_x$, $[Co(4\text{-}meimid)_2]_x$ and $[Co(benzimid)_2]_x$ between 1750 to 2020 nm. Using average band wavelengths of 580nm and 1120 nm, Dq and B parameters of 525 cm^{-1} and 700 cm^{-1}, respectively, were calculated using the appropriate Tanabe-Sugano correlation diagram [10]. These values of Dq and B are in close agreement with those reported previously for other tetrahedral Co(II) imidazolate and pyrazolate complexes [6, 11].

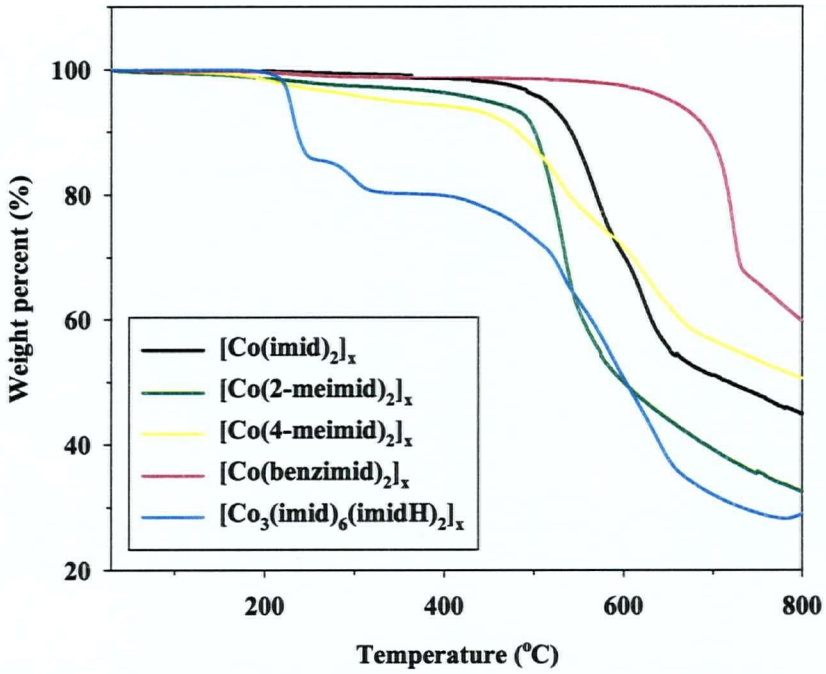

Figure 4.2 TGA plots for compounds $[Co(imid)_2]_x$, $[Co(2\text{-}meimid)_2]_x$, $[Co(4\text{-}meimid)_2]_x$, $[Co(benzimid)_2]_x$, and $[Co_3(imid)_6(imidH)_2]_x$.

Using these Dq and B values the $^4A_2 \rightarrow {}^4T_2$ transition is predicted to appear at ~ 5250 cm^{-1} (~ 1904 nm), which is within the wavelength range where the very weak, broad, absorption was observed in some of the spectra (*vide supra*). Electronic spectral data for all four of these compounds have been reported previously [6, 7, 12]. Previous studies [6] on the diffuse reflectance spectra of $[Co(imid)_2]_x$ and $[Co(4\text{-}meimid)_2]_x$ reported the

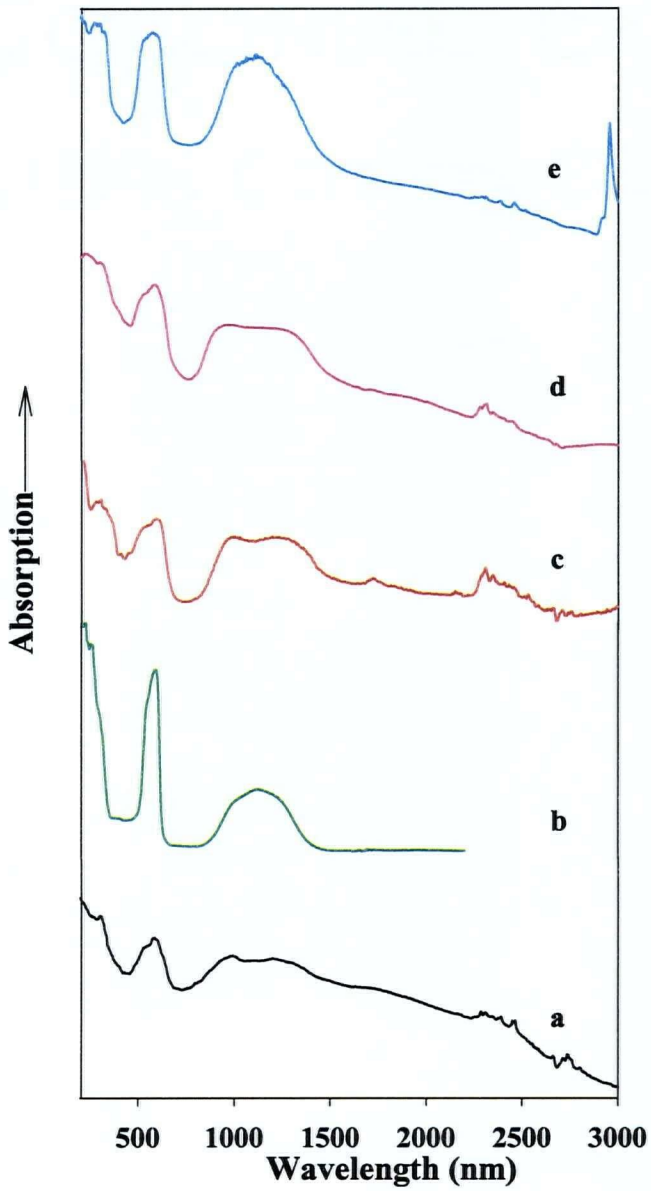

Figure 4.3 UV-Vis-NIR spectra for compounds $[Co(imid)_2]_x$, (a); $[Co(2\text{-}meimid)_2]_x$, (b); $[Co(4\text{-}meimid)_2]_x$, (c); $[Co(benzimid)_2]_x$, (d); and $[Co_3(imid)_6(imidH)_2]_x$, (e).

presence of bands at 1840 and 2290 nm for $[Co(imid)_2]_x$, and 1860, 1990 and 2280 nm for $[Co(4\text{-}meimid)_2]_x$). These are likely components of the $^4A_2 \rightarrow {}^4T_2$ transition seen only very weakly in the spectra studied here. An earlier electronic spectroscopy study [7] on $[Co(benzimid)_2]_x$, using both reflectance and mull methods, reported the observation of only the two major d-d transitions, with the mull spectrum bands at 1150 and 595 nm (a shoulder at ~540 nm). Hence, the spectra shown in Figure 4.3 are in general agreement with the earlier work which also concluded that these compounds have structures incorporating tetrahedrally coordinated cobalt(II) centers. The absence of a $\nu_{N\text{-}H}$ stretching vibration in these electronic spectra and in the infrared spectra of these complexes (see the discussion below concerning the observation of this band in $[Co_3(imid)_6(imidH)_2]_x$) is indicative of the absence of neutral imidazole in these materials [1].

The X-ray powder diffractogram of a sample of $[Co(imid)_2]_x$ synthesized in this work agrees well with that calculated [8] from single crystal X-ray diffraction data reported for the same compound [3] (Figure 4.4). Indexing the X-ray powder diffractogram using the program Celref [13] yields calculated lattice parameters of a = 22.834, b = 22.834 and c = 12.983 Å. These values are very similar to those reported for the same compound in the previous study (a = 22.872, b = 22.872, c = 12.981 Å) [3]. We conclude that $[Co(imid)_2]_x$ synthesized in the present work is the same as that reported earlier [3].

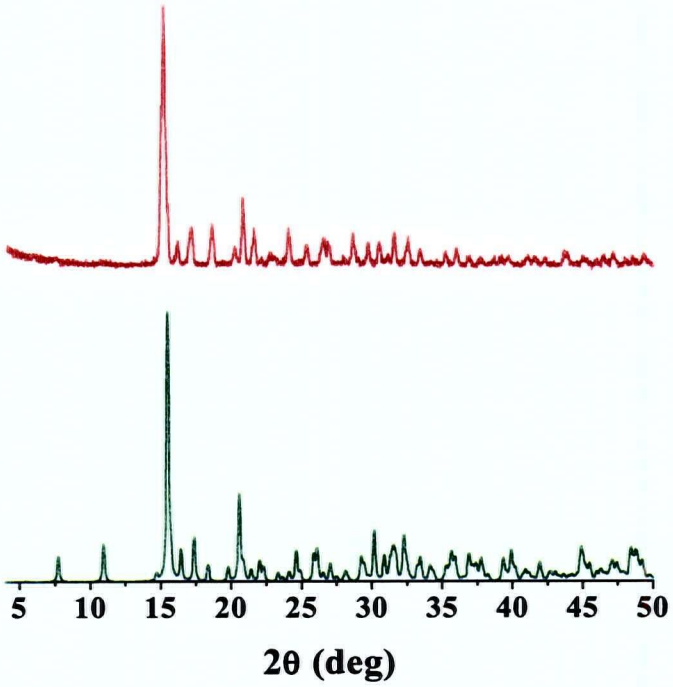

Figure 4.4 X-ray powder diffractograms of $[Co(imid)_2]_x$ (top, experimental; bottom, calculated).

Unfortunately, relatively little structural information was obtained from the powder X-ray diffraction studies of the other three cobalt compounds. The X-ray powder diffraction patterns for $[Co(2\text{-meimid})_2]_x$ and $[Co(benzimid)_2]_x$ are shown in Figure 4.5. From these diffractograms it can be seen that these compounds are not isomorphous with each other, nor with $[Co(imid)_2]_x$. A very poor diffraction pattern with no detectable peaks, characteristic of an amorphous solid, was obtained for $[Co(4\text{-meimid})_4]_x$.

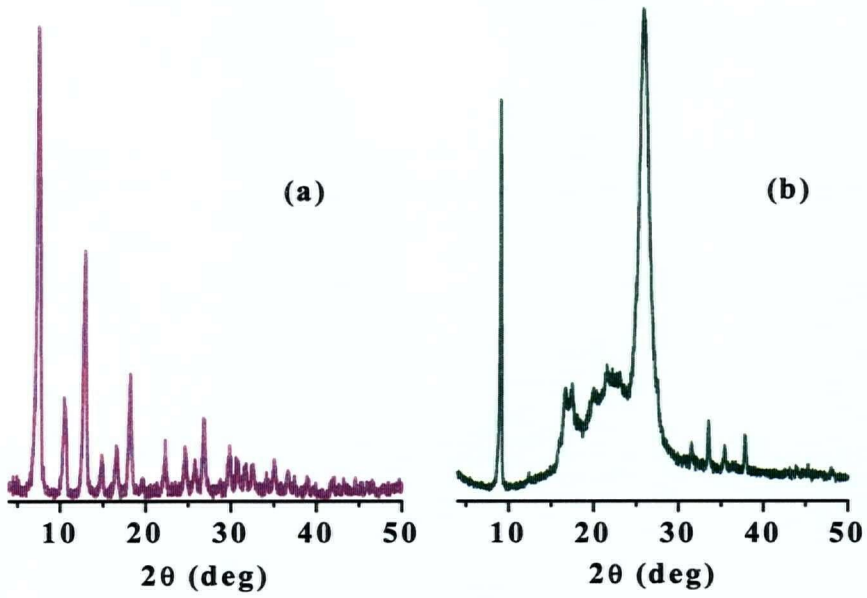

Figure 4.5 X-ray powder diffractograms of $[Co(2\text{-meimid})_2]_x$ (a) and $[Co(benzimid)_2]_x$ (b).

In summary, concerning structures, the similarities in stoichiometry and physical and spectroscopic properties of $[Co(imid)_2]_x$, $[Co(2\text{-meimid})_2]_x$, $[Co(4\text{-meimid})_2]_x$, and $[Co(benzimid)_2]_x$ strongly support the conclusion that, as known definitively for $[Co(imid)_2]_x$, all have extended structures with tetrahedrally coordinated metal centers and singly bridging azolate ligands.

In an earlier study [1] the synthesis of a new molecule-based magnet, $[Fe_3(imid)_6(imidH)_2]_x$, by the reaction of ferrocene with excess molten imidazole, was reported. The same reaction, employing cobaltocene in place of ferrocene, yields the analogous cobalt compound, $[Co_3(imid)_6(imidH)_2]_x$, as a microcrystalline powder (Chapter 9, section 9.2.2.5). The X-ray powder diffractogram of $[Co_3(imid)_6(imidH)_2]_x$ coincides well with that calculated (employing single crystal X-ray diffraction data [1] and the program PowderCell, [8]), for $[Fe_3(imid)_6(imidH)_2]_x$ (Figure 4.6). Indexing the X-ray powder diffractogram of $[Co_3(imid)_6(imidH)_2]_x$ using the program Celref [13] yields calculated lattice parameters of a = 10.568, b = 12.964 and c = 10.634 Å. These are very similar to those of $[Fe_3(imid)_6(imidH)_2]_x$ (a = 10.591, b = 12.958, c = 10.617 Å) [1]. Additional evidence supporting the conclusion that the iron and cobalt compounds are isostructural in addition to isomorphous comes from spectroscopic studies on $[Co_3(imid)_6(imidH)_2]_x$. The X-ray determined structure of the iron compound shows the presence of both tetrahedral and octahedral metal centers, the additional coordination sites on the latter being filled by neutral imidazole molecules. The electronic spectrum of $[Co_3(imid)_6(imidH)_2]_x$ (Figure 4.3) shows the absorption bands assignable to the $^4A_2 \rightarrow {}^4T_1(F)$ and $^4A_2 \rightarrow {}^4T_1(P)$ transitions of tetrahedrally coordinated Co ions (see previous discussion). Transitions assignable to octahedral cobalt(II) centers are not observable; however, this is not too surprising in view of the fact they would be expected to be an order of magnitude or more weaker than the bands arising from the tetrahedral centers [14]. Evidence for neutral imidazole molecules (coordinated, presumably, to octahedral cobalt centers) in $[Co_3(imid)_6(imidH)_2]_x$ comes from the observation of a sharp peak at

2950 nm in the electronic spectrum (Figure 4.3) corresponding to the ν_{N-H} stretching vibration of neutral imidazole [1]. Finally we note that the infrared spectrum of

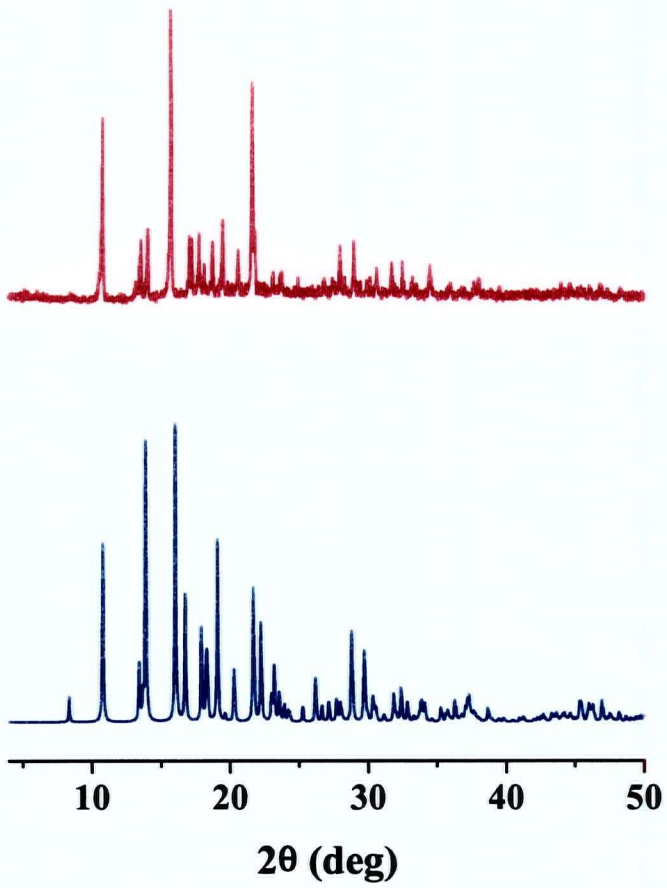

Figure 4.6 X-Ray powder diffractograms of $[Co_3(imid)_6(imidH)_2]_x$ (top, experimental) and $Fe_3(imid)_6(imidH)_2$ (bottom, calculated).

$[Co_3(imid)_6(imidH)_2]_x$ and the iron analogue are virtually identical exhibiting the same vibrational bands at almost the same frequencies. It can be concluded that $[Co_3(imid)_6(imidH)_2]_x$ has the same structure as the iron analogue [1]. In this structure, tetrahedrally coordinated metal ions are connected in chains by singly bridging imidazolate ions. The chains are cross-linked by octahedrally coordinated metal ions. Each tetrahedral center is linked to two others in the same chain and via octahedral centers to two additional chains. Each chain is linked to four different chains via the octahedral centers.

$[Co_3(imid)_6(imidH)_2]_x$ is nonvolatile and does not melt up to the temperature at which its thermal decomposition begins (208 °C). Thermal gravimetric analysis of the compound shows that it decomposes in several steps (Figure 4.2). Approximately 15% of the initial weight is lost between 208 and 255 °C. The next 4% is lost between 255 and 320 °C. This total weight loss of 19% corresponds to that expected for the loss of the neutral imidazole ligands. The remaining material has the same composition as $[Co(imid)_2]_x$. This is evidenced by the thermogravimetric data and by the experiment described in the experimental section in which a sample was retrieved from the TA instrument, after heating for 30 minutes at 325 °C, and subjected to elemental analysis. The rest of the thermolysis curve of $[Co_3(imid)_6(imidH)_2]_x$ above 320 °C parallels closely that of the authentic sample of $[Co(imid)_2]_x$, as expected.

4.2.2.2 MAGNETIC PROPERTIES

Magnetic susceptibility, χ, and magnetic moment, μ_{eff}, versus T data over the temperature range 2-300 K on powdered samples of the five cobalt compounds in an applied field of 10 000 G are shown in Figures 4.7 and 4.8, respectively. For all five

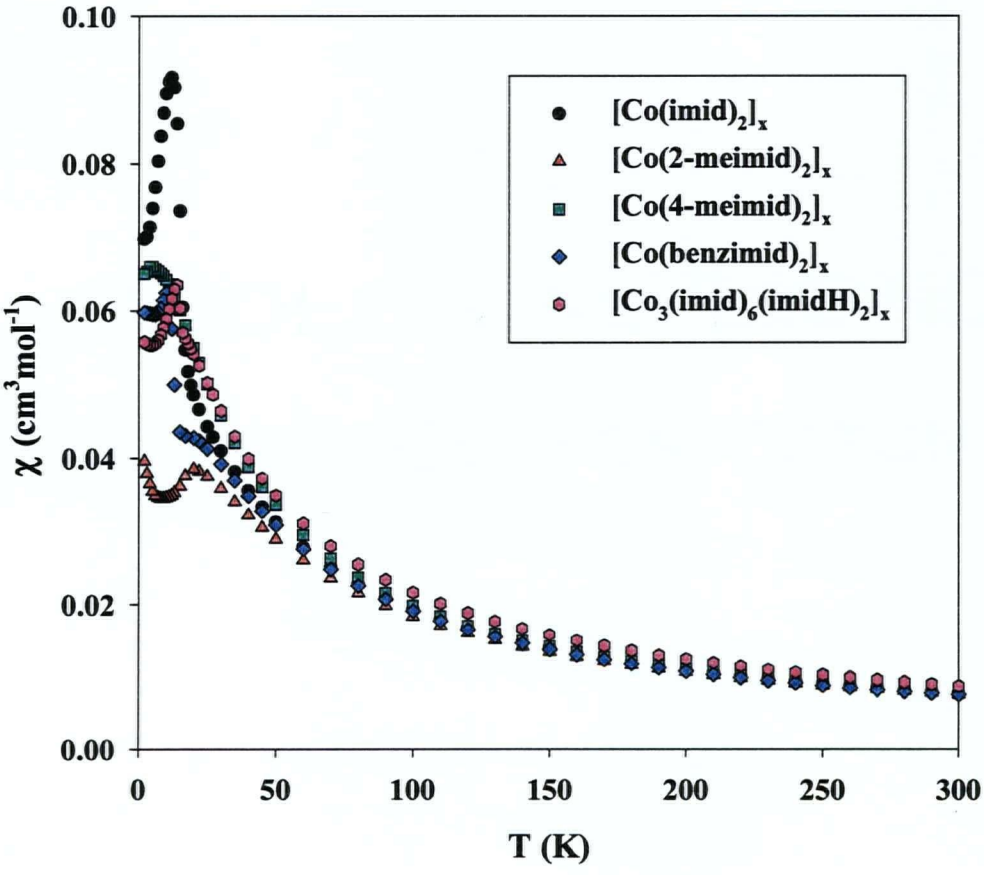

Figure 4.7 χ versus T plots at 10 000 G for compounds $[Co(imid)_2]_x$, $[Co(2\text{-}meimid)_2]_x$, $[Co(4\text{-}meimid)_2]_x$, $[Co(benzimid)_2]_x$, and $[Co_3(imid)_6(imidH)_2]_x$.

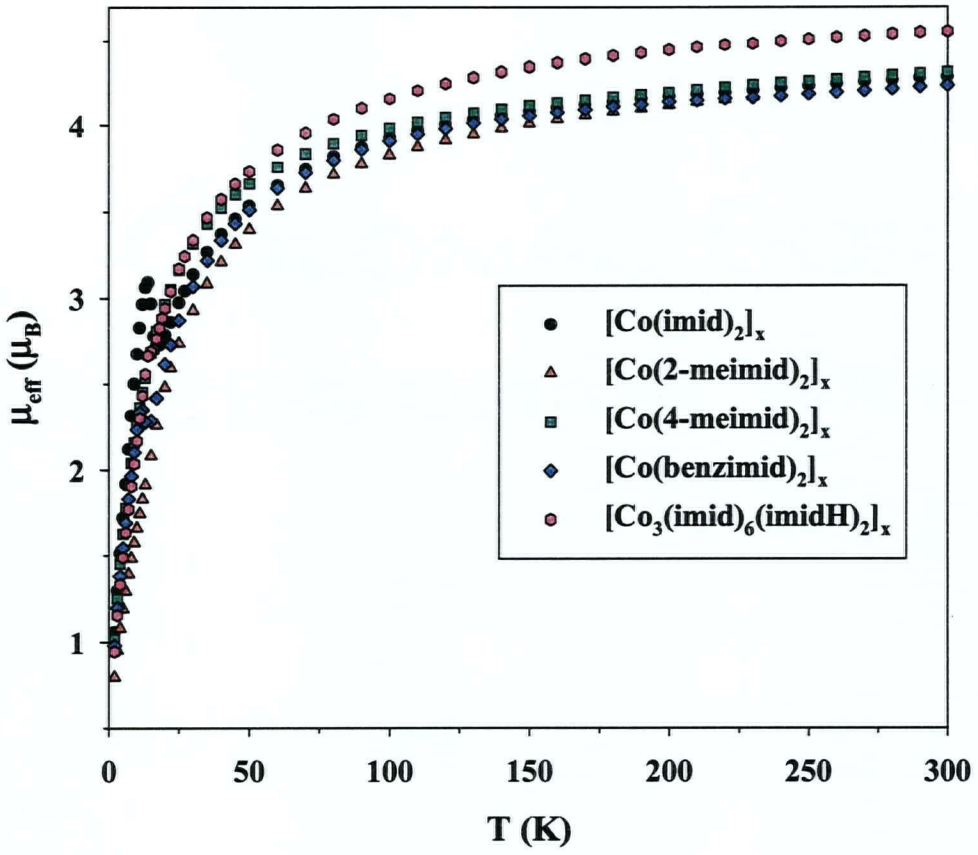

Figure 4.8 μ_{eff} versus T plots at 10 000 G for compounds [Co(imid)$_2$]$_x$, [Co(2-meimid)$_2$]$_x$, [Co(4-meimid)$_2$]$_x$, [Co(benzimid)$_2$]$_x$, and [Co$_3$(imid)$_6$(imidH)$_2$]$_x$.

compounds the magnetic moment decreases with decreasing temperature from a value above 4 μ_B at 300 K to a value below 1 μ_B at 2 K (Figure 4.8). This suggests antiferromagnetic coupling between magnetic centers, a conclusion further supported by the susceptibility data for [Co(2-meimid)$_2$]$_x$ and [Co(4-meimid)$_2$]$_x$ which show broad maxima at low temperatures. In contrast to the results for [Co(2-meimid)$_2$]$_x$ and [Co(4-meimid)$_2$]$_x$, the data for [Co(imid)$_2$]$_x$, [Co(benzimid)$_2$]$_x$ and [Co$_3$(imid)$_6$(imidH)$_2$]$_x$ show

clear evidence of magnetic anomalies in the region below 20 K. These are noticeable in both the μ_{eff} and χ plots, particularly in the former. The abrupt increase in χ suggests a transition to a ferromagnetic state for these compounds and since saturation effects caused by large applied fields can mask such behavior (See Chapter 3, section 3.2.2) the magnetic properties of all five compounds were examined at the lower applied field of 500 G. μ_{eff} and χ data at 500 G over the low temperature region (2-50 K) are shown in Figures 4.9 and 4.10, respectively. While the magnetic properties of $[Co(2\text{-meimid})_2]_x$ and $[Co(4\text{-meimid})_2]_x$ are virtually unchanged at this lower applied field, as expected where only short range antiferromagnetic interactions are involved, χ and μ_{eff} data of $[Co(imid)_2]_x$, $[Co(benzimid)_2]_x$ and $[Co_3(imid)_6(imidH)_2]_x$ are dramatically altered below the temperature of the anomaly. Below a critical temperature, T_c, (16 K, 13 K and 15 K for $[Co(imid)_2]_x$, $[Co(benzimid)_2]_x$ and $[Co_3(imid)_6(imidH)_2]_x$ respectively) μ_{eff} increases abruptly to a maximum value (7.84 μ_B at 9 K for $[Co(imid)_2]_x$, 5.59 μ_B at 10 K for $[Co(benzimid)_2]_x$, and 6.02 μ_B at 13 K for $[Co_3(imid)_6(imidH)_2]_x$) before decreasing again as the temperature decreases to 2 K (Figure 4.9). The magnetic transition at T_c is also seen clearly in the χ versus T plots (Figure 4.10). The susceptibility increases with decreasing temperature below 300 K and above T_c for $[Co(imid)_2]_x$, $[Co(benzimid)_2]_x$ and $[Co_3(imid)_6(imidH)_2]_x$. Below T_c the susceptibility rises abruptly as the temperature decreases before leveling off and approaching a saturation value for

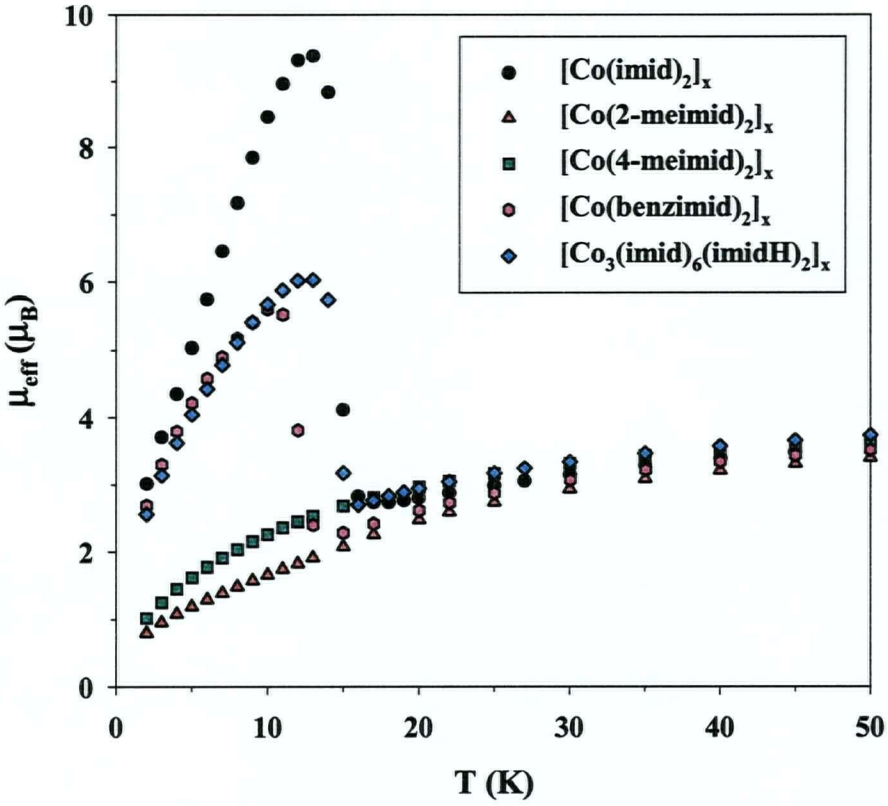

Figure 4.9 μ_{eff} versus T plots at 500 G for compounds [Co(imid)$_2$]$_x$, [Co(2-meimid)$_2$]$_x$, [Co(4-meimid)$_2$]$_x$, [Co(benzimid)$_2$]$_x$, and [Co$_3$(imid)$_6$(imidH)$_2$]$_x$.

[Co(benzimid)$_2$]$_x$ and [Co$_3$(imid)$_6$(imidH)$_2$]$_x$. The susceptibility of [Co(imid)$_2$]$_x$ maximizes at 11 K then decreases on cooling further before leveling off at the lowest temperatures studied (Figure 4.10). The magnetic behaviors of [Co(imid)$_2$]$_x$, [Co(benzimid)$_2$]$_x$ and [Co$_3$(imid)$_6$(imidH)$_2$]$_x$ indicate in all three compounds the presence

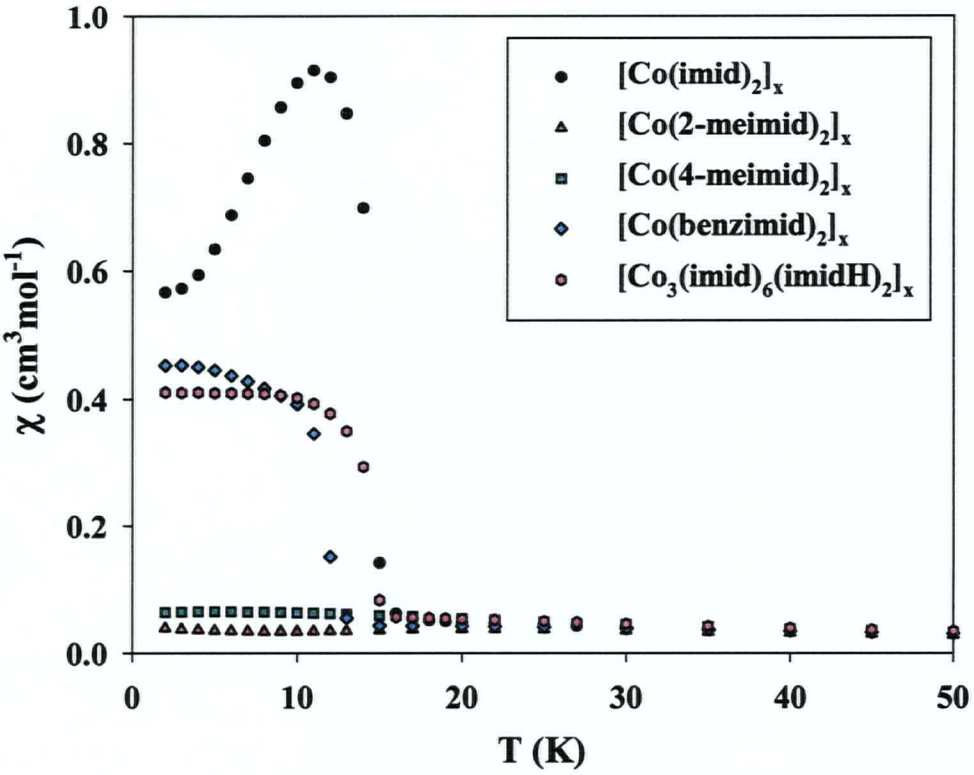

Figure 4.10 χ versus T plots at 500 G for compounds $[Co(imid)_2]_x$, $[Co(2\text{-}meimid)_2]_x$, $[Co(4\text{-}meimid)_2]_x$, $[Co(benzimid)_2]_x$, and $[Co_3(imid)_6(imidH)_2]_x$.

of antiferromagnetic coupling between paramagnetic centers as the primary exchange mechanism combined with a magnetic phase transition to a ferromagnetically ordered state at low temperatures. This magnetic behavior is very similar to that reported for $[Fe_3(imid)_6(imidH)_2]_x$ [1] $[Fe(2\text{-}meimid)_2.\ 0.13(FeCp_2)]_x$ [2] and $[Fe(4\text{-}abimid)_2]_x$ (Chapter 3), which suggests a form of canted-spin antiferromagnetic coupling leading to weak ferromagnetism at low temperatures, as discussed in Chapter 3, section 3.2.2. Weak

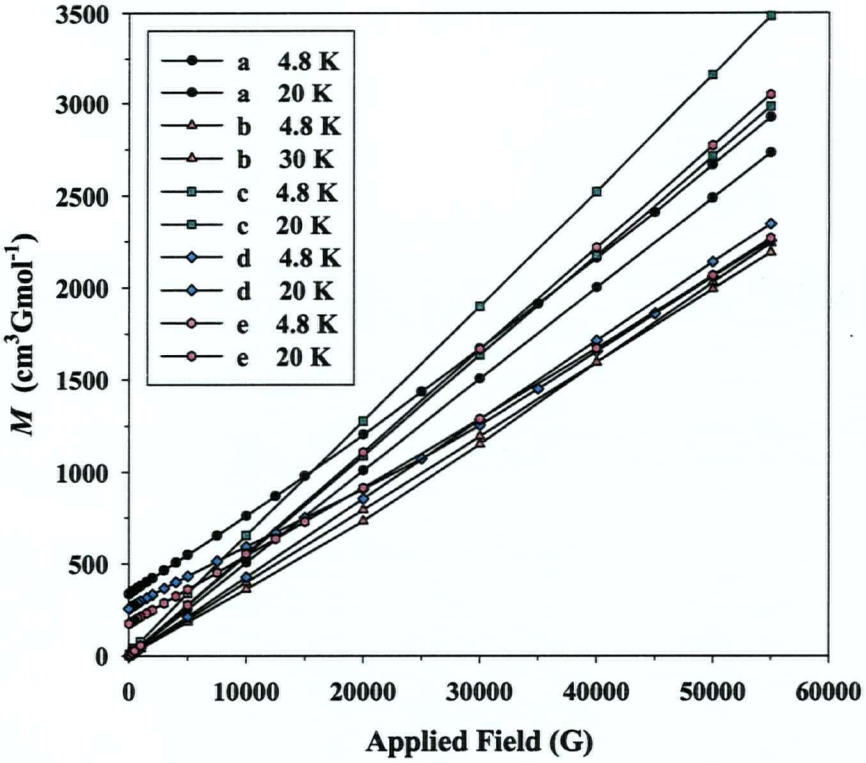

Figure 4.11 Magnetization versus applied field plots at different temperatures for compounds $[Co(imid)_2]_x$, (a); $[Co(2\text{-}meimid)_2]_x$, (b); $[Co(4\text{-}meimid)_2]_x$, (c); $[Co(benzimid)_2]_x$, (d); and $[Co_3(imid)_6(imidH)_2]_x$, (e).

ferromagnetism is also evident in the magnetization versus field plots at several temperatures for $[Co(imid)_2]_x$, $[Co(benzimid)_2]_x$ and $[Co_3(imid)_6(imidH)_2]_x$ (Figure 4.11). Plots of magnetization versus applied field for these compounds are linear above T_c and extrapolate to zero magnetization at zero applied field, while below T_c they show extrapolated net magnetization at zero field. In contrast, the data obtained at corresponding temperatures for $[Co(2\text{-}meimid)_2]_x$ and $[Co(4\text{-}meimid)_2]_x$ extrapolate to

zero magnetization at all temperatures studied (Figure 4.11). That $[Co(imid)_2]_x$, $[Co(benzimid)_2]_x$ and $[Co_3(imid)_6(imidH)_2]_x$ exhibit long-range ferromagnetic order and spontaneous magnetization below T_c is further illustrated by hysteresis studies. In these studies, the magnetization was measured as the applied field was cycled between +50 000 G and –50 000 G at 4.8 K. Preliminary hysteresis studies for these compounds showed evidence that the micro-crystals were aligning with the applied field, resulting in abnormal shapes of the hysteresis plots, as shown in Figure 4.12 (middle plot) for $[Co(benzimid)_2]_x$. These preliminary results prompted us to mull the sample in nujol to prevent the alignment of the micro-crystals with the applied field. The resulting hysteresis loops using nujol are shown in Figure 4.13. These loops give remnant magnetizations of 350, 280 and 200 cm^3 G mol^{-1} and coercive fields of 5500, 2500 and 2000 G for $[Co(imid)_2]_x$, $[Co(benzimid)_2]_x$ and $[Co_3(imid)_6(imidH)_2]_x$, respectively. A spin-canted structure, for $[Co(imid)_2]_x$, $[Co(benzimid)_2]_x$ and $[Co_3(imid)_6(imidH)_2]_x$ is also supported by the fact that their highest magnetizations measured were 2924, 2253 and 2267 cm^3Gmol^{-1}, respectively, at 4.8 K and 55 000 G. These values are considerably lower than the theoretical saturation magnetization value of 16 766 cm^3Gmol^{-1} for an S = 3/2 system [15].

Magnetic parameters for five cobalt(II) 1,3-diazolate compounds, including $[Co(imid)_2]_x$, $[Co(benzimid)_2]_x$ and $[Co_3(imid)_6(imidH)_2]_x$, which exhibit weak ferromagnetism are given in Table 4.1. The only parameter which is relatively constant in this group of compounds is the critical temperature which lies in the narrow range of 11

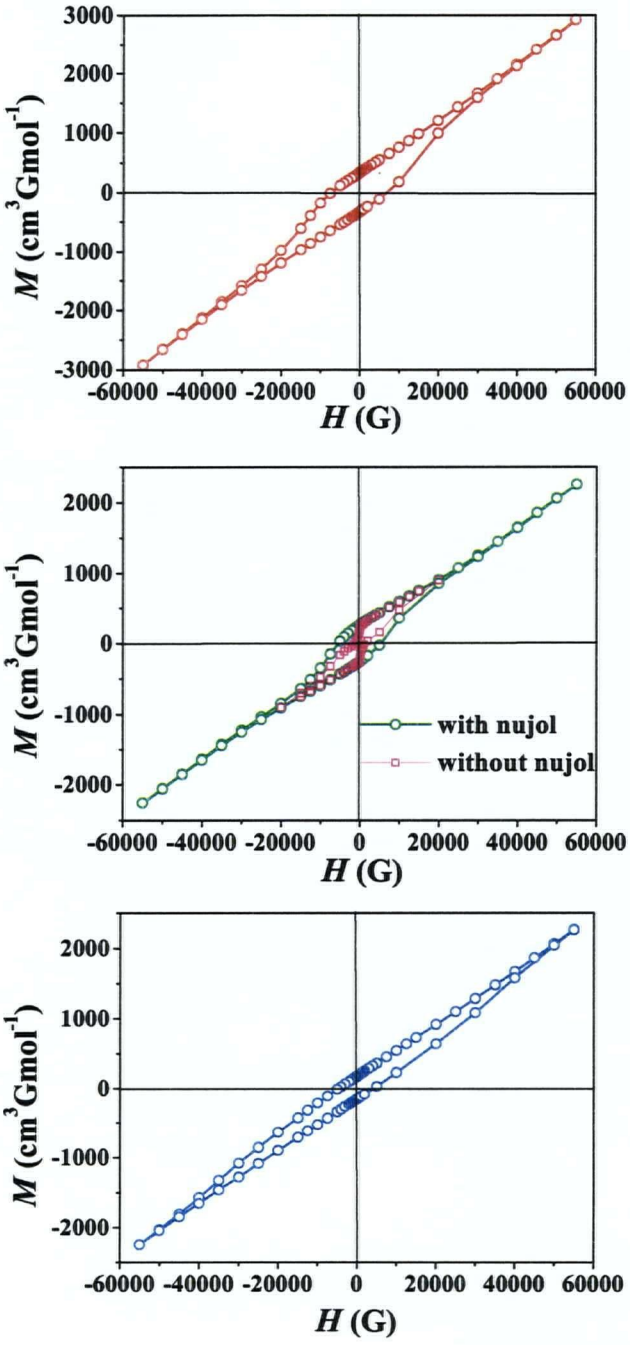

Figure 4.12 Magnetic hysteresis plots at 4.8 K for compounds $[Co(imid)_2]_x$, (top); $[Co(benzimid)_2]_x$, (middle); $[Co_3(imid)_6(imidH)_2]_x$, (bottom).

Table 4.1 Magnetic parameters for some cobalt(II) weak ferromagnets

Compound	T_c (K)	H_{coer} (G)	M_{rem} (cm^3Gmol^{-1})	Ref.
$Co(4\text{-abimid})_2$	11	400	22	Chapter 3
$Co_2(imid)_4(bipy)$	13	125	1900	Chapter 5
$Co(imid)_2$	16	6 620	334	This Chapter
$Co(benzimid)_2$	13	5 280	257	This Chapter
$Co_3(imid)_6(imidH)_2$	15	4 140	175	This Chapter

Abbreviations: imid = imidazolate, benzimid = benzimidazolate, 4-abimid = 4-azabenzimidazolate, bipy = 2,2'-bipyridine.

to 16 K. Single crystal X-ray diffraction studies on $[Co(imid)_2]_x$ [3], and powder diffraction studies on $[Co(4\text{-abimid})_2]_x$ (Chapter 3) show these compounds to have extended 3-D lattices with tetrahedral cobalt centers linked via singly-bridging azolates to four nearest neighbors. In spite of the structural similarities, they have significantly different magnetic properties, $[Co(imid)_2]_x$ being both a stronger magnet (larger remnant

magnetization) and a harder magnet (greater coercive field). The magnetic parameters of $Co(4\text{-abimid})_2$ have been discussed in some detail in Chapter 3. It is sufficient to point out here that in Chapter 3 it was concluded that the properties of cobalt(II) molecule-based magnets may be influenced significantly by single ion effects such as zero-field splitting. Differences in the magnitude of the zero-field splitting, in turn brought on by factors such as differences in the nature and degree of distortion of the CoN_4 chromophore, will cause significant differences in the populations of zero-field split levels at low temperatures with concomitant effects on the exchange and the magnetic properties. Unfortunately the number of compounds of this class with known structures is too small at this time to try to correlate magnetic parameters with detailed structural features.

In contrast to the behavior discussed above, $[Co(2\text{-meimid})_2]_x$ and $[Co(4\text{-meimid})_2]_x$ exhibit only short-range antiferromagnetic coupling. Plots of magnetic susceptibility, χ, and magnetic moment, μ_{eff}, versus T data in an applied field of 10 000 G are shown in Figure 4.7 and 4.8. A maximum at approximately 21 K is observed clearly in the magnetic susceptibility plot for $[Co(2\text{-meimid})_2]_x$. A paramagnetic impurity in this compound might be the cause of the small increase in magnetic susceptibility at the lowest temperatures studied (Figure 4.7). The maximum in the magnetic susceptibility plot of $[Co(4\text{-meimid})_2]_x$ is less noticeable since it appears at a very low temperature of 4 K (Figure 4.7). Antiferromagnetic behavior for these compounds is also apparent in the μ_{eff} versus T plots determined at 500 G (Figure 4.10). The magnetic moment decreases as

temperature is lowered. That these two polymers do not present a net magnetization at zero applied field is shown in their magnetization plots at two different temperatures which extrapolate to zero at zero applied field (Figure 4.11). In addition, magnetization studies at 4.8 K on these compounds, in which the applied field is cycled between +55 000 and – 55 000 G, reveal no evidence of significant hysteresis behavior (Figure 4.13). It is not possible to quantify the magnitude of the antiferromagnetic coupling in $[Co(2\text{-meimid})_2]_x$ and $[Co(4\text{-meimid})_2]_x$ due to the lack of a suitable model for $S = 3/2$ extended 3-D lattice systems.

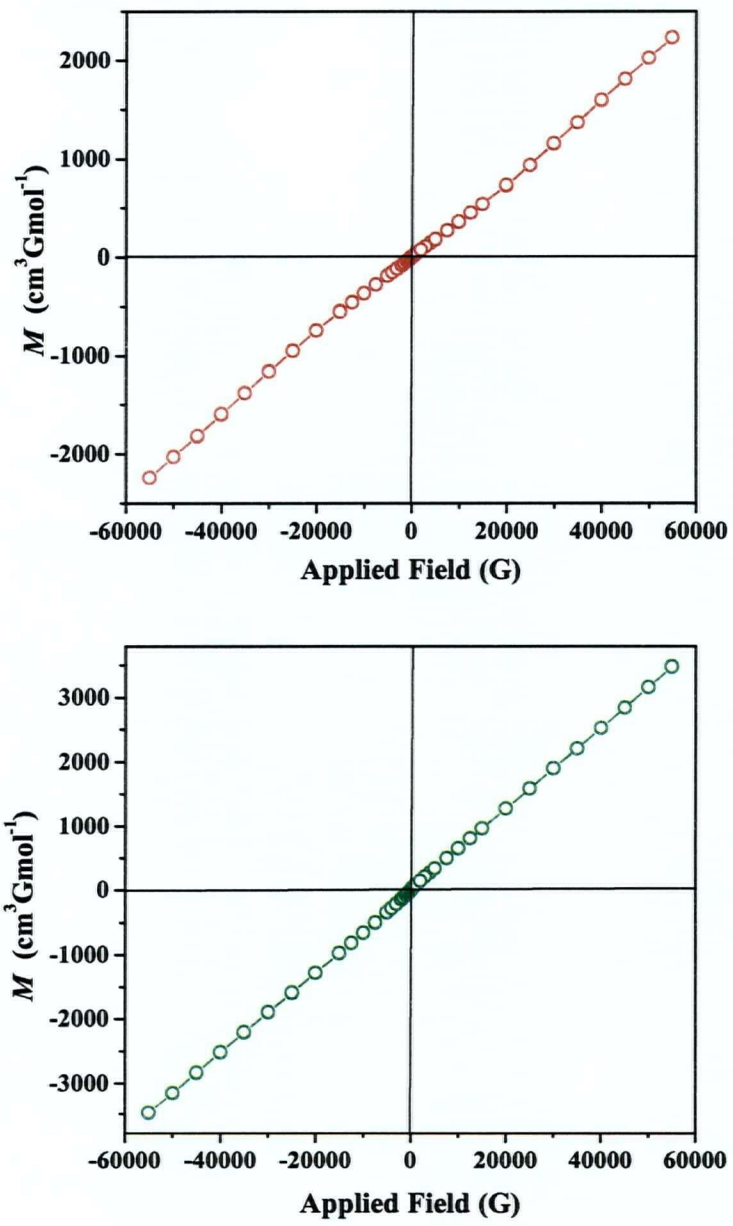

Figure 4.13 Magnetic hysteresis plots at 4.8 K for compounds $[Co(2\text{-meimid})_2]_x$, (top); and $[Co(4\text{-meimid})_2]_x$ (bottom).

4.3 A NICKEL(II) BENZIMIDAZOLATE POLYMER

4.3.1 INTRODUCTION

The magnetic properties of several 1-D nickel(II) pyrazolate polymers have been studied previously [16]. In those studies it was found that nickel(II) pyrazolates with a square planar chromophore geometry are diamagnetic, while those with tetrahedral geometry are paramagnetic and exhibit antiferromagnetic exchange coupling [17]. In contrast, few nickel(II) imidazolate polymers have been synthesized previously [6]. Those that have been made are square planar and diamagnetic [6]. None of the nickel(II) pyrazolate or imidazolate polymers reported has been obtained as macroscopic crystals suitable for single crystal X-ray diffraction studies.

In this section, a benzimidazolate complex of nickel(II) is examined. This microcrystalline material, $[Ni(benzimid)_2]_x$, was reported earlier [18] in a study which included some spectroscopic characterization. The magnetic properties of the compound were not studied in the earlier work. The magnetic studies presented here for $[Ni(benzimid)_2]_x$, show that this material behaves as a very weak ferromagnet at low temperatures. Therefore, $[Ni(benzimid)_2]_x$ is the first reported Ni(II) imidazolate-based compound that behaves as a molecule-based magnet.

Attempts to prepare other magnetically interesting Ni(II) imidazolate polymers, such as $[Ni(imid)_2]_x$ and $[Ni(4\text{-meimid})_2]_x$, were made, however, the materials obtained were found to be diamagnetic and for this reason were not investigated further.

4.3.2 RESULTS AND DISCUSSION

4.3.2.1 SYNTHESIS, STRUCTURAL, THERMAL AND PHYSICAL CHARACTERIZATION

$[Ni(benzimid)_2]_x$ was prepared, with some modifications, following the method outlined by Goodgame and Cotton [7]. In this method, a solution of benzimidazole in hot water was added to an aqueous solution of $Ni(NO_3)_2 \cdot 6H_2O$. The mixture was heated to boiling, and on cooling, a lavender precipitate formed. Details on this synthesis are given in Chapter 9, section 9.2.3.1.

This complex is stable both in air and in contact with moisture. It is insoluble in water and most organic solvents, nonvolatile and thermally robust. The UV-Vis-NIR spectrum of $[Ni(benzimid)_2]_x$ is shown in Figure 4.14. The spectrum, which has not been previously analyzed, consists of three main absorptions in the ranges of 1680-1700 nm (barely observable), 755-780 nm and 500-550 nm, which can be tentatively assigned to the following transitions, $^3T_1(F) \rightarrow {}^3T_2$, $^3T_1(F) \rightarrow {}^3A_2$, and $^3T_1(F) \rightarrow {}^3T_1(P)$, respectively. There is another absorption in the range 835-860 nm, which has been assigned previously to the spin-forbidden transition $^3T_1(F) \rightarrow {}^1T_2(D)$ [19]. These observable d-d

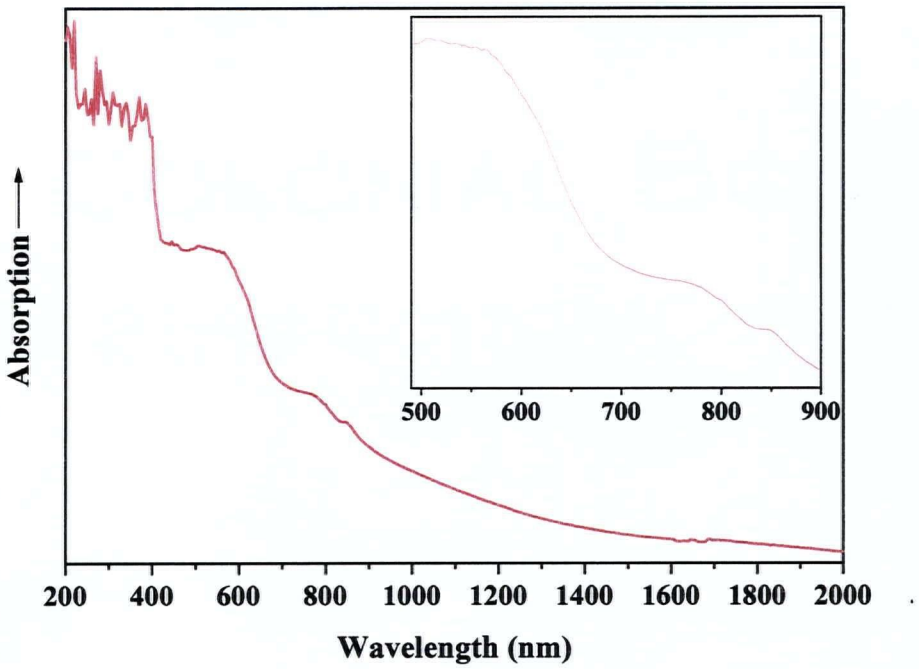

Figure 4.14 UV-visible-near-IR spectrum for $[Ni(benzimid)_2]_x$. Insert plot shows the two highest energy d-d transition bands.

transitions, three spin allowed and one spin forbidden, are expected for tetrahedral or distorted tetrahedral Ni(II) [20]. Using the two highest energy bands (770 nm and 525 nm), and the corresponding Tanabe-Sugano correlation diagram [10] for a d^8 tetrahedral system, Dq and B were calculated to be 711 cm^{-1} and 960 cm^{-1} respectively. In addition, strong charge transfer bands are seen in the region 200-400 nm.

The TGA plot for $[Ni(benzimid)_2]_x$ is shown in Figure 4.15. As can be seen there is no evidence of loss in mass due to thermal decomposition or sublimation at any temperature below ~ 450 °C. The TGA data suggest that two steps occur in the thermal decomposition of $[Ni(benzimid)_2]_x$. The first one involves a rapid lost of nearly 50 % of the initial mass of the sample between 450 °C and 612 °C. The second event is more gradual with an additional approximately 25 % of the initial mass being lost between 612 °C and 800 °C.

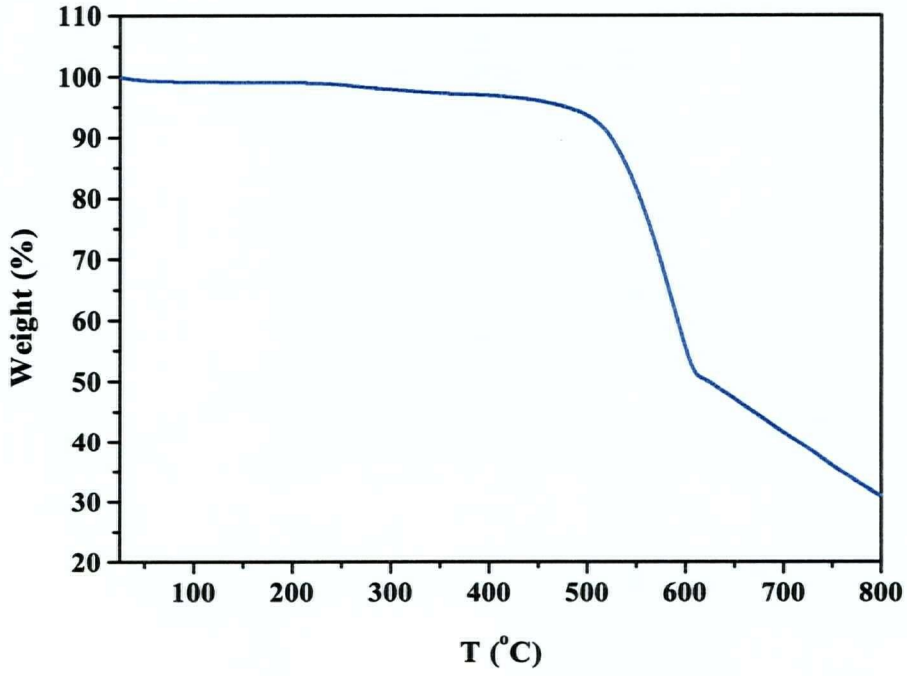

Figure 4.15 TGA plot for $[Ni(benzimid)_2]_x$.

Hence, according to the electronic spectroscopic and thermal characterization of $[Ni(benzimid)_2]_x$, this compound shows the physical properties of a coordination polymer and it, most likely, possesses metal ions with a tetrahedral coordination geometry, similarly to those found in $[Co(4\text{-}abimid)_2]_x$ (Chapter 3) or $[Co(imid)_2]_x$ (*vide supra*).

4.3.2.2 MAGNETIC PROPERTIES

Magnetic susceptibility and magnetic moment versus temperature data on powdered samples of $[Ni(benzimid)_2]_x$ in an applied field of 500 G are shown in Figure 4.16. The magnetic moment of $[Ni(benzimid)_2]_x$ decreases from 2.53 μ_B at 300 K decreases to 1.35 μ_B as the temperature is lowered to 2 K. This suggests antiferromagnetic coupling although confirmation of this, in the form of a maximum in the χ versus T plot, is not seen (Figure 4.16). Furthermore, no evidence for long-range ferromagnetic interaction as seen for the cobalt analogue, $[Co(benzimid)_2]_x$, is observed in this 500 G data. Nonetheless, the possibility that this nickel compound has a structure similar to that of the Co analogue (which exhibits magnetic properties of a molecule-based magnet) prompted us to investigate the magnetic properties of the nickel compound further.

Figure 4.17 shows the magnetization plots for $[Ni(benzimid)_2]_x$ at different

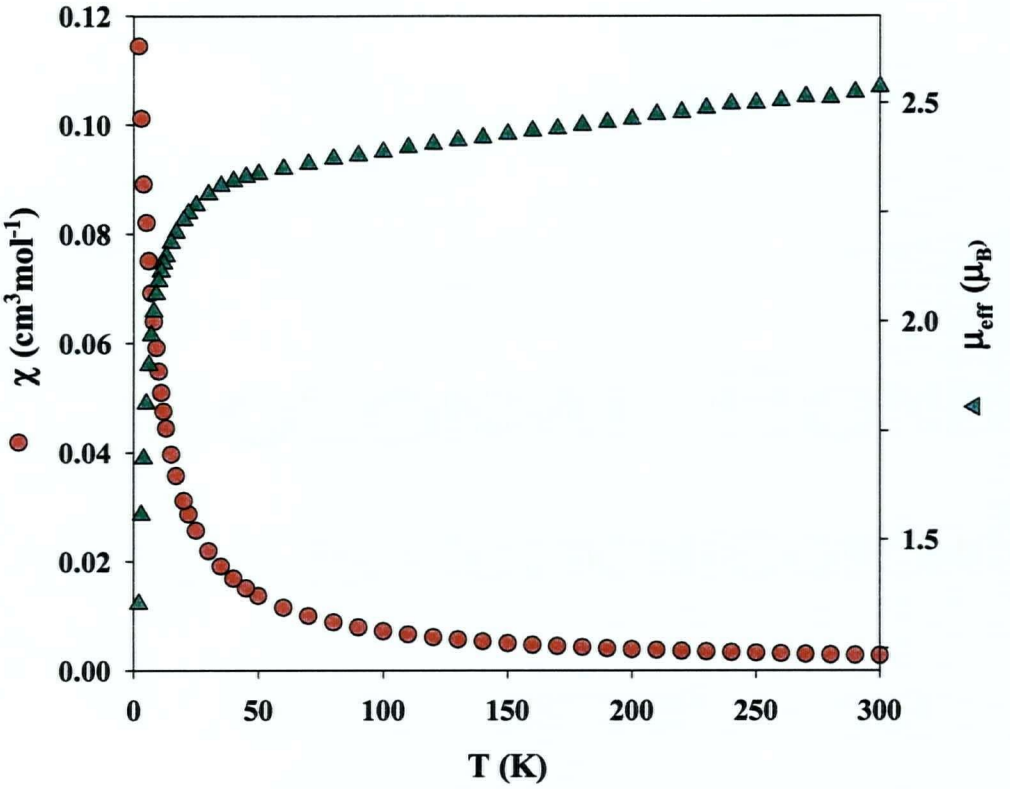

Figure 4.16 Plots of χ and μ_{eff} versus T for $[Ni(benzimid)_2]_x$.

temperatures. All the magnetization plots extrapolate to zero magnetization at zero field, except for the one determined at 4.8 K. In addition, except for the one determined at 4.8 K, all other magnetization plots in Figure 4.17 are linear. This result supports a possible long-range ferromagnetic ordering at temperatures ~ 4.8 K and below for $[Ni(benzimid)_2]_x$.

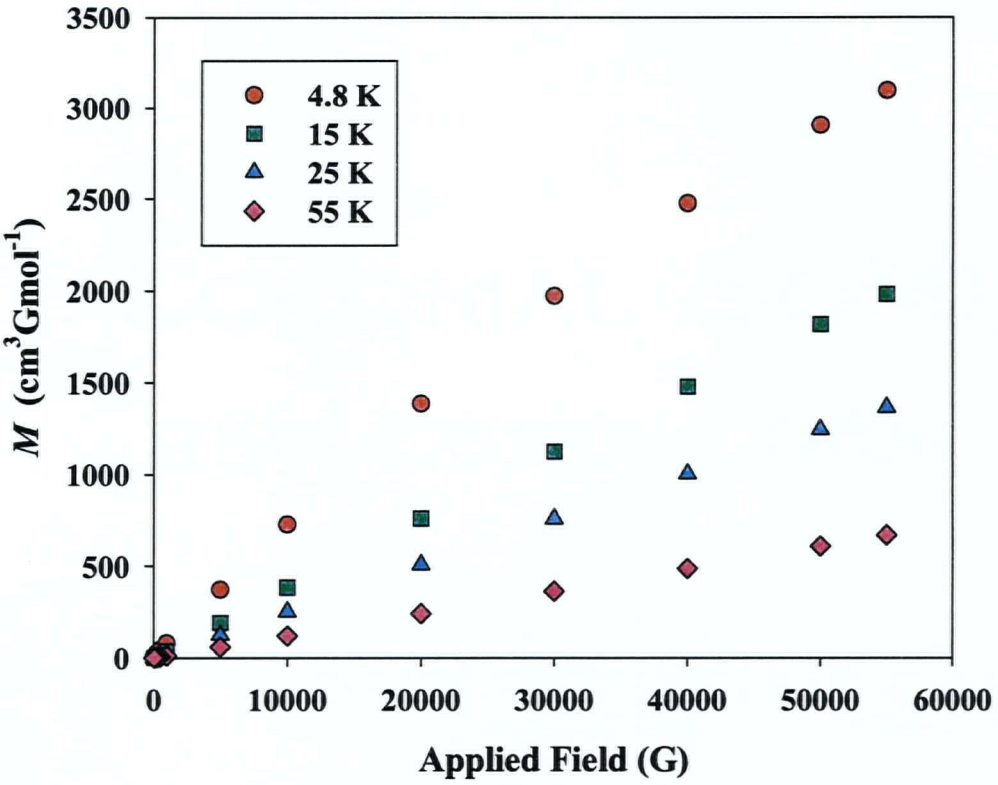

Figure 4.17 Magnetization versus applied field plots at different temperatures for $[Ni(benzimid)_2]_x$.

That $[Ni(benzimid)_2]_x$ exhibits long-range ferromagnetic order and spontaneous magnetization at ~ 4.8 K is further illustrated by a hysteresis study. Magnetization was measured as the applied field was cycled between +55 000 G and –55 000 G at 2 and 4.8 K. The resulting hysteresis loop at 2 K is shown in Figure 4.18. This loop gives a remnant magnetization of ~ 7 cm^3 G mol^{-1} and a coercive field of ~ 60 G for $[Ni(benzimid)_2]_x$ which characterize this compound as a very weak and soft molecule-based magnet.

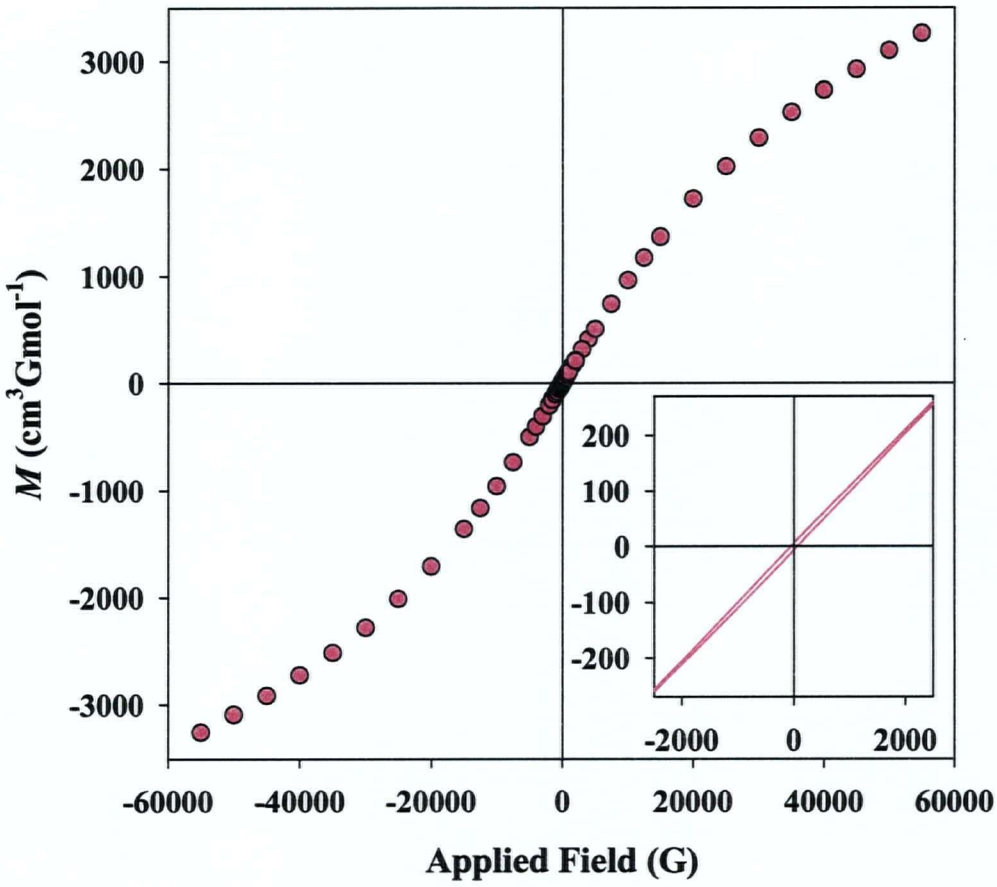

Figure 4.18 Magnetic hysteresis plot at 2 K for $[Ni(benzimid)_2]_x$. The insert plot shows a magnification of the central part of the hysteresis curve.

As was found for the cobalt analogue, $[Co(benzimid)_2]_x$, a spin-canted structure, for $[Ni(benzimid)_2]_x$, is also supported by the fact that the highest magnetization measured was 3089 cm^3Gmol^{-1} at 4.8 K and 55 000 G. This value is considerably lower

than the theoretical saturation magnetization value of 11 177 cm^3Gmol^{-1} expected for an $S = 1$ system [15].

To investigate further the possibility of a ferromagnetic ground state for $[Ni(benzimid)_2]_x$, DC magnetic susceptibility measurements at an applied field of 50 G were carried out on a sample of this polymer as follows: the sample was cooled in zero field to 2 K, a magnetic field of 50 G was applied and data were collected while warming the sample (zero-field-cooled magnetization - ZFCM); then, the sample was cooled in the same field (50 G) to 2 K, and data were collected in the warming mode (field-cooled magnetization – FCM); finally, the sample was cooled again to 2 K, in a field of 50 G, then the field is removed and data are collected while warming the sample (remnant magnetization – REM). The results of this data collection scheme are shown in Figure 4.19. The ZFCM data increases gradually to a maximum at ~ 6.5 K, then decreases slightly to increase again to a second maximum at ~ 2.5 K. The T_c value, determined as the first maximum on the ZFCM plot, is ~ 6.5 K,. When the applied field was switched off at 2 K a small remnant magnetization of ~ 0.95 cm^3Gmol^{-1} was found (in good agreement with the value of M_{rem} ~ 1 cm^3Gmol^{-1} obtained in the hysteresis study shown above). This M_{rem} decreased significantly on warming to 2.5 K then decreased further upon warming and vanished at ~ 5.5 K. $[Ni(benzimid)_2]_x$ exhibits another transition at ~ 2.5 K. The origin of this lower-temperature transition is not clear. A similar double transition has been recently observed in the ZFCM-FCM-REM studies in a 1-D

molecule-based ferrimagnet having Cu(II) and Mn(II) ions [20]. A possible source of this phenomenon was not discussed in this earlier report.

From these results it is evident that $[Ni(benzimid)_2]_x$ exhibits long-range ferromagnetic order at low temperatures, and that this material can be considered a molecule-based magnet.

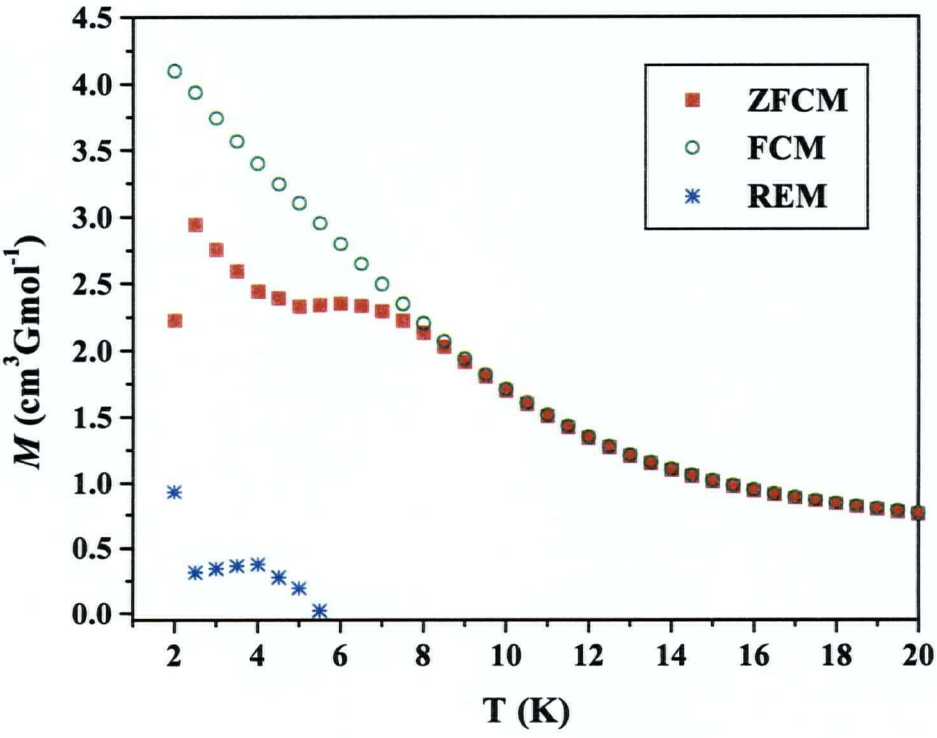

Figure 4.19 Zero-field cooling (ZFC) and field-cooling (FC) magnetization plots for $[Ni(benzimid)_2]_x$ at 50 G.

4.4 COPPER(II) IMIDAZOLATE POLYMERS

4.4.1 INTRODUCTION

Imidazolate-bridged copper(II) dimeric and oligomeric complexes have been actively studied [22-23] mainly to understand the factors determining the extent of coupling between two metal ions and to use these simple compounds as models for metalloenzymes that contain the same structural units [24, 25]. Several studies have already been reported in which structural data have been used to find useful correlations between structure and magnetic coupling [26-30]. On the contrary, structural and magnetic properties of imidazolate-bridged copper(II) polymers have not been extensively studied. A blue form of $[Cu(imid)_2]_x$ is the only compound of this family with a known molecular structure, and its magnetic properties have also been determined but only at temperatures between 80 – 300 K [31, 32].

In the present section, the synthesis, characterization, and low-temperature magnetic studies of $[Cu(imid)_2]_x$ and four other Cu(II) systems incorporating substituted imidazolate ligands: $[Cu(2\text{-meimid})_2]_x$, $[Cu(4\text{-meimid})_2]_x$, $[Cu(benzimid)_2]_x$, and $[Cu(4,5\text{-dichloroimid})_2]_x$, are discussed. None of the materials studied here was isolated in a form suitable for single crystal X-ray diffraction studies. Moreover, no definitive details on the structures of these compounds were obtained as neither the electronic spectra nor the X-ray powder diffractograms were particularly informative for these systems. Nonetheless,

as with most of the other compounds studied in this work, the compounds are considered to be polymeric based on solubility and thermal gravimetric studies.

With the exclusion of $[Cu(imid)_2]_x$ and $[Cu(4\text{-}meimid)_2]_x$, which showed only weak antiferromagnetic coupling, the other Cu(II) imidazolate polymers exhibited magnetic properties that classify them as weak low-temperature molecule-based magnets.

4.4.2 RESULTS AND DISCUSSION

4.4.2.1 SYNTHESES, STRUCTURAL, THERMAL AND PHYSICAL CHARACTERIZATION

Detailed descriptions of the syntheses of the copper(II) imidazolate complexes studied here, can be found in Chapter 9, sections 9.2.4.1 through 9.2.4.5. The molten ligand-copper shot method, which has been successfully used to obtain single crystals of binary copper(II) pyrazolates [33], was first tried in an attempt to obtain single crystals of the compounds; however, all attempts to produce macroscopic crystals were unsuccessful. Ultimately, the only compound prepared using this method was $[Cu(imid)_2]_x$, which was obtained as a dark blue powder. The other Cu(II) imidazolate compounds were prepared by wet methods which involved the use of copper shot with an ethanolic solution of the appropriate ligand or, the reaction of an appropriate salt of Cu(II) with the appropriate imidazolate in water. These synthetic procedures are modifications of previously reported methods [7, 34].

The five copper(II) compounds, $[Cu(imid)_2]_x$, $[Cu(2\text{-}meimid)_2]_x$, $[Cu(4\text{-}meimid)_2]_x$, $[Cu(benzimid)_2]_x$ and $[Cu(4,5\text{-}dichloroimid)_2]_x$, are stable both in air and in contact with moisture. They are insoluble in water and common organic solvents, nonvolatile and thermally robust. They decompose when treated with concentrated mineral acids.

Thermal gravimetric analyses of the five copper compounds show no mass loss due to thermal decomposition or sublimation below 180 °C. At higher temperatures the compounds present similar thermal decomposition behavior, showing a weight loss in three stages over the temperature range studied (Figure 4.20). $[Cu(benzimid)_2]_x$ is the most thermally robust of the five in that there is no indication of thermal decomposition below 320 °C. In general, the Cu(II) compounds are less thermally stable than the Co(II) imidazolates reported on above.

The absence of a $\nu_{N\text{-}H}$ stretching vibration in the electronic spectra (*vide infra*) and in the infrared spectra of these complexes (See the discussion above concerning the observation of this band in $[Co_3(imid)_6(imidH)_2]_x$) is indicative of the absence of neutral imidazole in these materials.

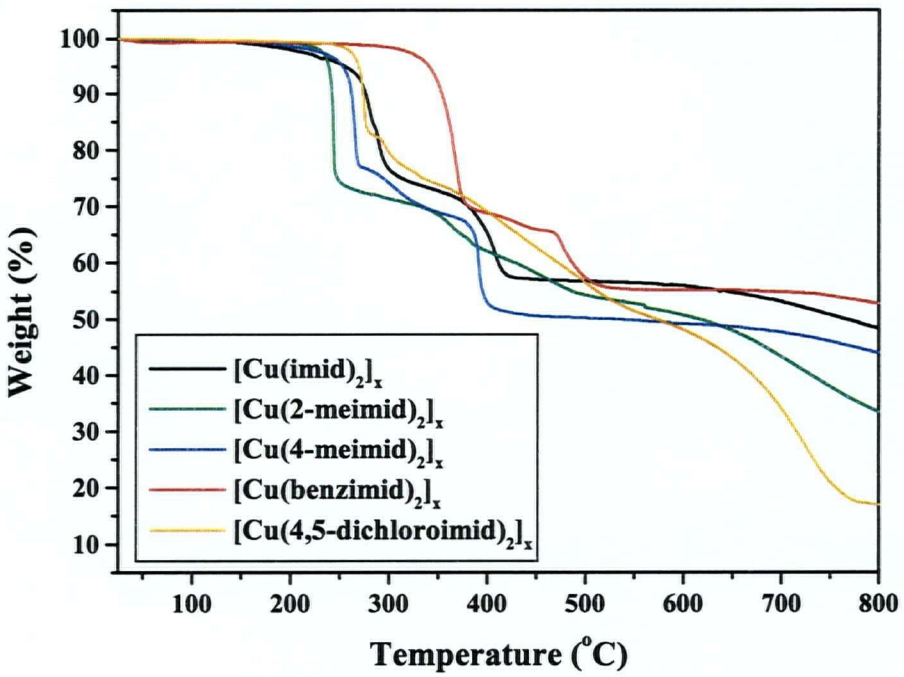

Figure 4.20 TGA plots for compounds $[Cu(imid)_2]_x$, $[Cu(2\text{-}meimid)_2]_x$, $[Cu(4\text{-}meimid)_2]_x$, $[Cu(benzimid)_2]_x$ and $[Cu(4,5\text{-}dichloroimid)_2]_x$.

The electronic spectra of the copper derivatives are shown in Figure 4.21 and a summary is presented in Table 4.2. In the NIR region, a band maximum is observed in the range 800 to 950 nm for $[Cu(imid)_2]_x$, $[Cu(4,5\text{-}dichloroimid)_2]_x$, $[Cu(benzimid)_2]_x$ and, less clear, for $[Cu(4\text{-}meimid)_2]_x$. All five compounds show bands around 550 – 600

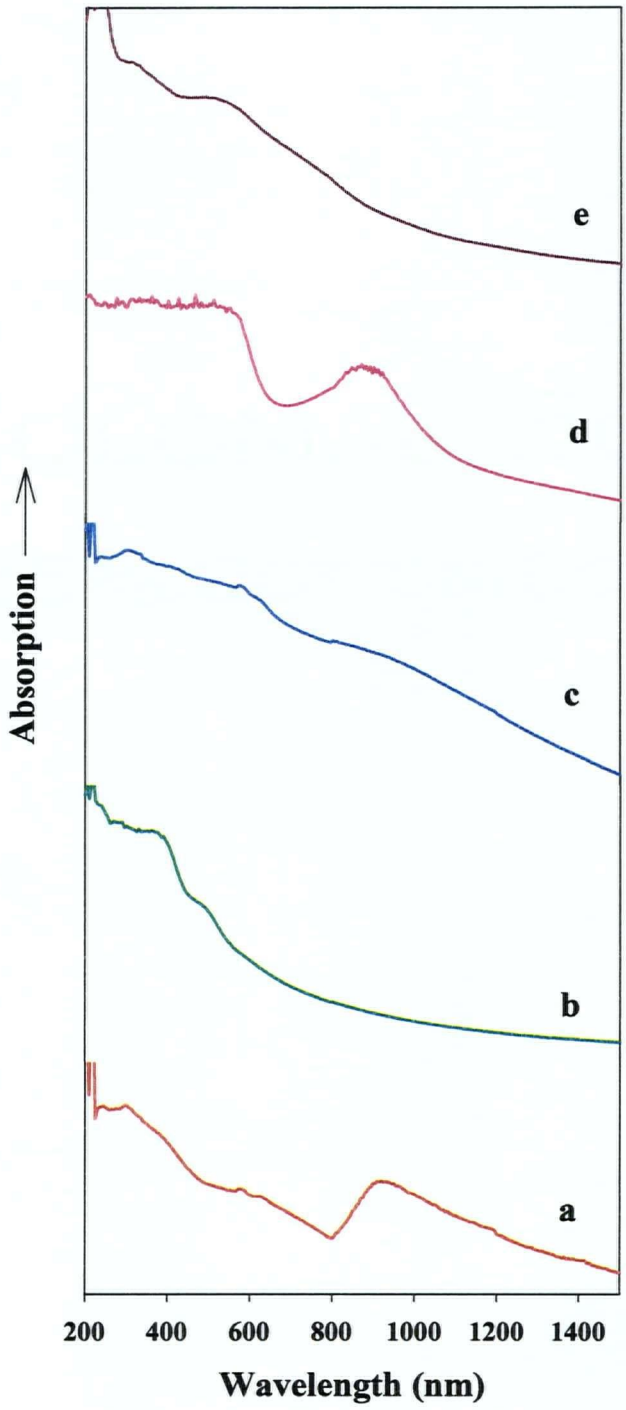

Figure 4.21 UV-Vis-NIR spectra for $[Cu(imid)_2]_x$, (a); $[Cu(2\text{-meimid})_2]_x$, (b); $[Cu(4\text{-meimid})_2]_x$, (c); $[Cu(benzimid)_2]_x$, (d); and $[Cu(4,5\text{-dichloroimid})_2]_x$, (e).

nm and 400 – 500 nm in the visible region although for $[Cu(4,5\text{-dichloroimid})_2]_x$ and $[Cu(benzimid)_2]_x$ the latter bands are somewhat obscured by intense bands in the UV region. All five compounds show bands assignable to charge-transfer in the 200 – 400 nm region.

Table 4.2 UV-Vis-NIR spectra of copper(II) imidazolates. Approximate wavelength values or regions (nm)

Compound	200 – 400 nm	400 – 500 nm	550 – 600 nm	800 – 950 nm
(a) imid	~ 200 - 300	~ 400	~ 600 (split)	~ 910
(b) 2-meimid	~ 200 - 380	~ 400 and 490	~ 600	None
(c) 4-meimid	~ 200 - 250	~ 400	600 (split)	~ 850 - 950
(d) benzimid	~ 200 - 400	?	~ 570	~ 890
(e) 4,5-diclimid	~ 200 - 290	?	~ 560	~ 800

According to Hathaway [35], complexes with CuN_4 chromophores that exhibit d-d bands in the 500 to 550 nm region are likely to have square-planar stereochemistries,

while bands in the 625 to 850 nm region are characteristic of compressed tetrahedral CuN_4 chromophores. These criteria for CuN_4 geometry have been used for related copper(II) pyrazolates [36] and pyrazolyl gallate systems [37]. As can be seen in Figure 4.21 and Table 4.2, the compounds studied here exhibit bands in wavelength regions corresponding to both chromophores. A mixture of two or more chromophore geometries is possible for these systems. As described above, one form of $[Cu(imid)_2]_x$ has been shown by single crystal X-ray diffraction studies to have both square-planar and distorted tetrahedral CuN_4 chromophores.

As previously mentioned, the crystal structure of a blue form of $[Cu(imid)_2]_x$ is known. Three magnetically different crystal modifications have been found for $[Cu(imid)_2]_x$ [31, 32], a blue modification (μ_{eff} = 1.57 μ_B at 293 K), a green modification (μ_{eff} = 1.62 μ_B at 303 K) and a brown modification (μ_{eff} = 1.46 μ_B at 303 K). The $[Cu(imid)_2]_x$ synthesized in the present work has a dark blue color, with a μ_{eff} = 1.54 μ_B at 300 K. The color of our compound and its high temperature magnetic properties suggested to us initially that we had prepared the blue form of the compound. The blue modification is the only one that has been studied by single crystal X-ray diffraction [32]. In this structure, imidazolato groups bridge Cu(II) ions to form chains, in which there is a systematic alternation of a Cu(II) ion with square planar coordination, followed by another Cu(II) ion in a flattened tetrahedral coordination. The chains are linked at the flattened tetrahedral Cu(II) ion so that the whole assembly forms a three-dimensional network [32]. A representation of the repeat unit of blue-$[Cu(imid)_2]_x$, and a stereoview

showing the 3-D structure of this polymer are shown in Figures 4.22 and 4.23, respectively. These views were achieved employing the software Powdercell [8] and using the crystallographic data previously reported [32].

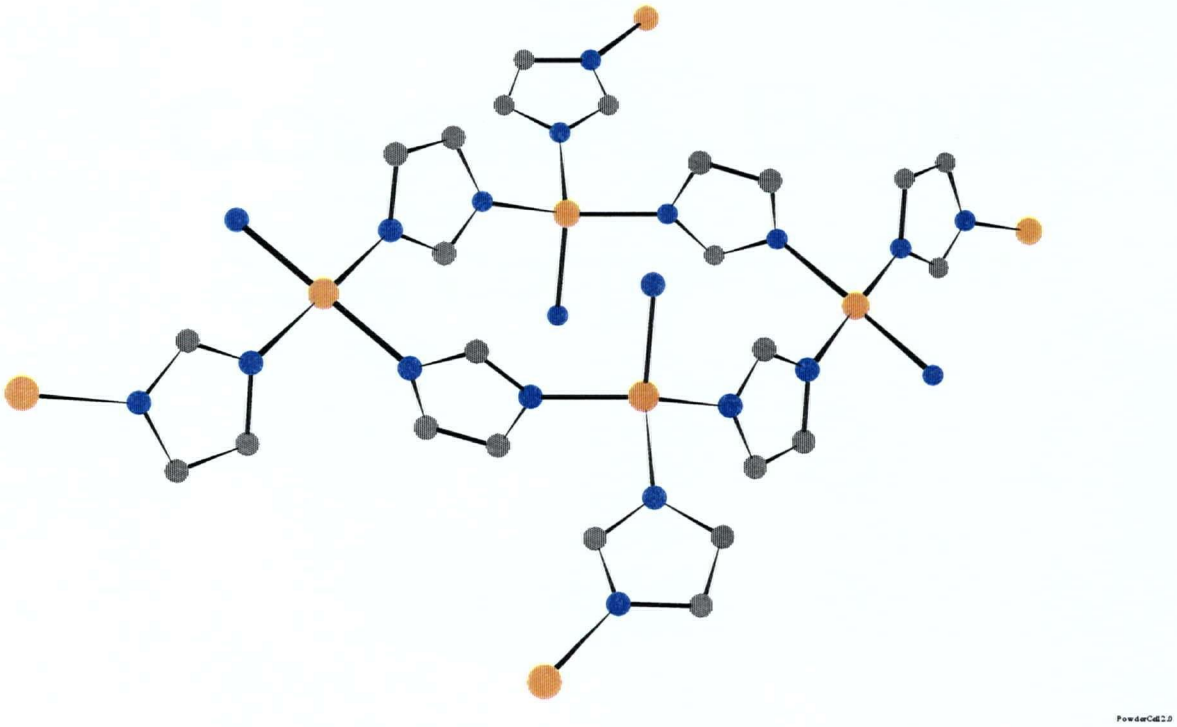

Figure 4.22 Repeat unit of blue-$[Cu(imid)_2]_x$. Hydrogen atoms are omitted.

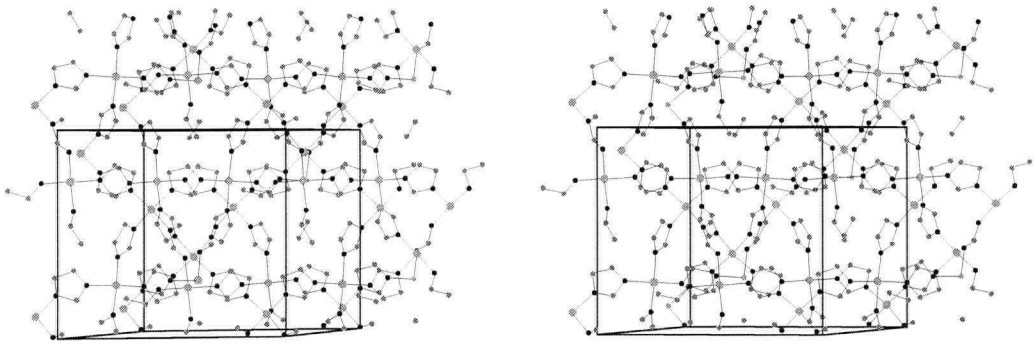

Figure 4.23 Stereoview of a section of blue-$[Cu(imid)_2]_x$ including the unit cell. Projection (001). No hydrogen atoms shown.

As shown in Figure 4.24, the experimental X-ray powder diffraction pattern of the sample of $[Cu(imid)_2]_x$ prepared in this thesis work does not coincide well with that calculated [8], employing single crystal X-ray diffraction data reported for the blue-$[Cu(imid)_2]_x$ [32]. This implies that the [Cu(imid)2]x synthesized in this work is not isomorphous with blue-$[Cu(imid)_2]_x$ [32]. The detailed structure of our compound remains unknown.

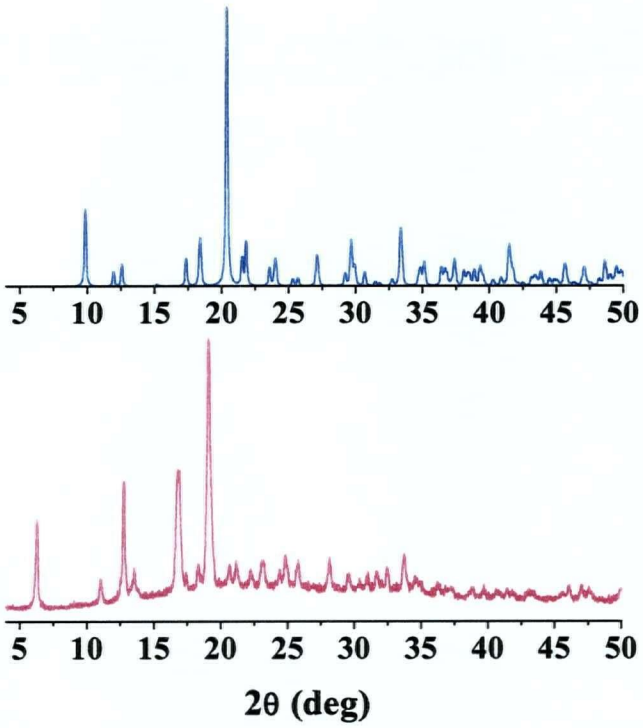

Figure 4.24 X-ray powder diffractograms of blue-$[Cu(imid)_2]_x$ (top, calculated) and $[Cu(imid)_2]_x$ prepared here (bottom, experimental).

The X-ray powder diffraction patterns for $[Cu(2\text{-meimid})_2]_x$, $[Cu(4\text{-meimid})_2]_x$, $[Cu(4,5\text{-dichloroimid})_2]_x$ and $[Cu(benzimid)_2]_x$, are shown in Figure 4.25. Each pattern is unique showing there is no isomorphism associated with the different copper systems. Interestingly, the patterns for the imid, 2-meimid and benzimid copper compounds are also different from those of the corresponding cobalt compounds (see Figures 4,4 and 4.5). In these studies we have found no examples of isomorphous pairs of copper(II) and

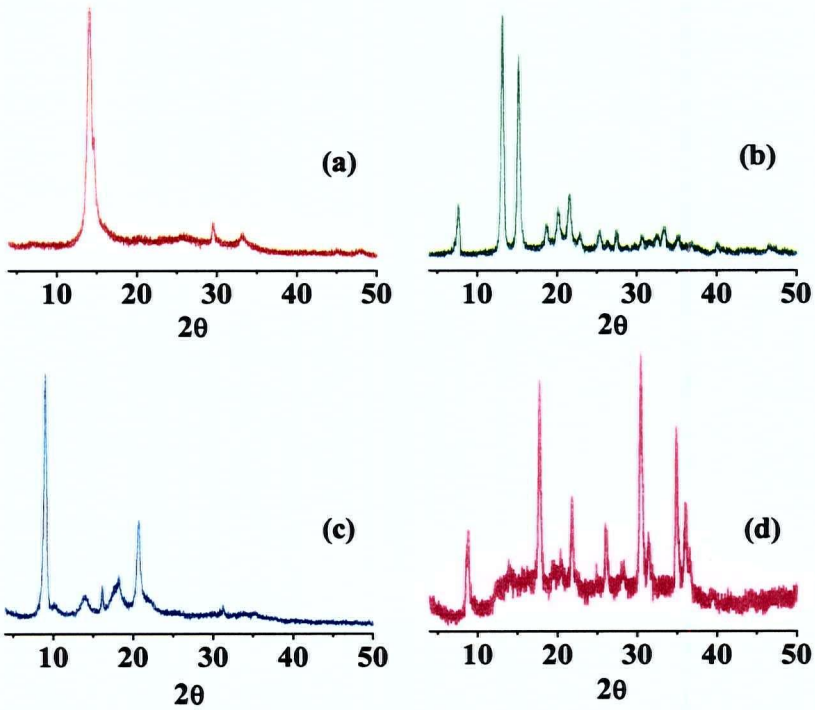

Figure 4.25 X-ray powder diffraction patterns of $[Cu(2\text{-meimid})_2]_x$, (a); $[Cu(4\text{-meimid})_2]_x$, (b); $[Cu(benzimid)_2]_x$, (c); and $[Cu(4,5\text{-dichloroimid})_2]_x$, (d).

cobalt(II) imidazolates. This contrasts sharply with the situation for iron(II) and cobalt(II) where we have discovered three examples of isomorphous pairs.

The structures of the copper(II) imidazolates studied here while likely involving 3-D connectivities of the type seen in blue-$[Cu(imid)_2]_x$ [32], appear to be somewhat unique. This may be caused by the presence of two or more different chromophores in the lattice as indicated by the electronic spectroscopy studies. At this point it is not possible to make a more conclusive statement regarding structures.

4.4.3 MAGNETIC PROPERTIES

Magnetic susceptibilities were measured at 10 000 G from 2 to 300 K for all five Cu(II) imidazolate compounds. Magnetic susceptibility, χ, and magnetic moment, μ_{eff}, versus T (2 to 100 K) data on powdered samples are shown in Figure 4.26 and 4.27, respectively.

All five compounds show broad maxima in their χ versus T plots over the 25 – 150 degree range indicating the presence of antiferromagnetic exchange. This is confirmed by the fact all five compounds show decreasing magnetic moments with decreasing temperature over this range. All five of the compounds exhibit an increase in χ at lower temperatures. The μ_{eff} versus T plot, in particular at low temperatures, clearly shows distinctive behavior for the five compounds. $[Cu(4\text{-meimid})_2]_x$ shows a decrease in

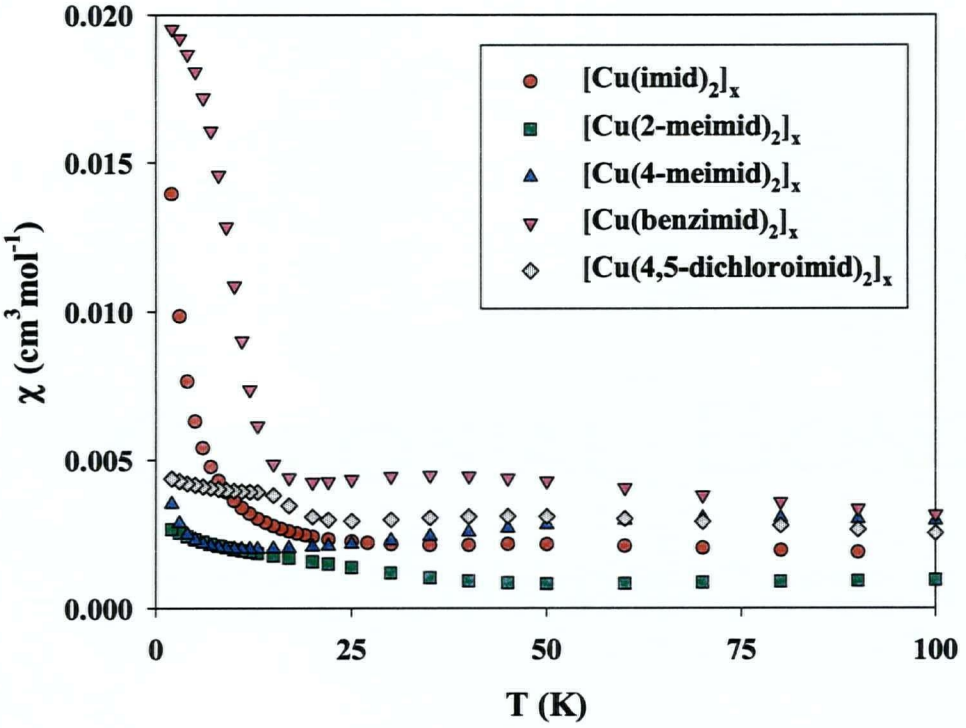

Figure 4.26 χ versus T plots at 10 000 G for $[Cu(imid)_2]_x$, $[Cu(2\text{-}meimid)_2]_x$, $[Cu(4\text{-}meimid)_2]_x$, $[Cu(benzimid)_2]_x$ and $[Cu(4,5\text{-}dichloroimid)_2]_x$.

μ_{eff} with decreasing temperature down to 2 K, consisted with antiferromagnetic exchange over the entire range studied. This is confirmed by the χ data obtained for this compound employing an applied field of 500 G. χ shows a broad maximum at ~ 75 K (Figure 4.28). The increase in χ, at the lowest temperatures studied seen in both the 10 000 and 500 G

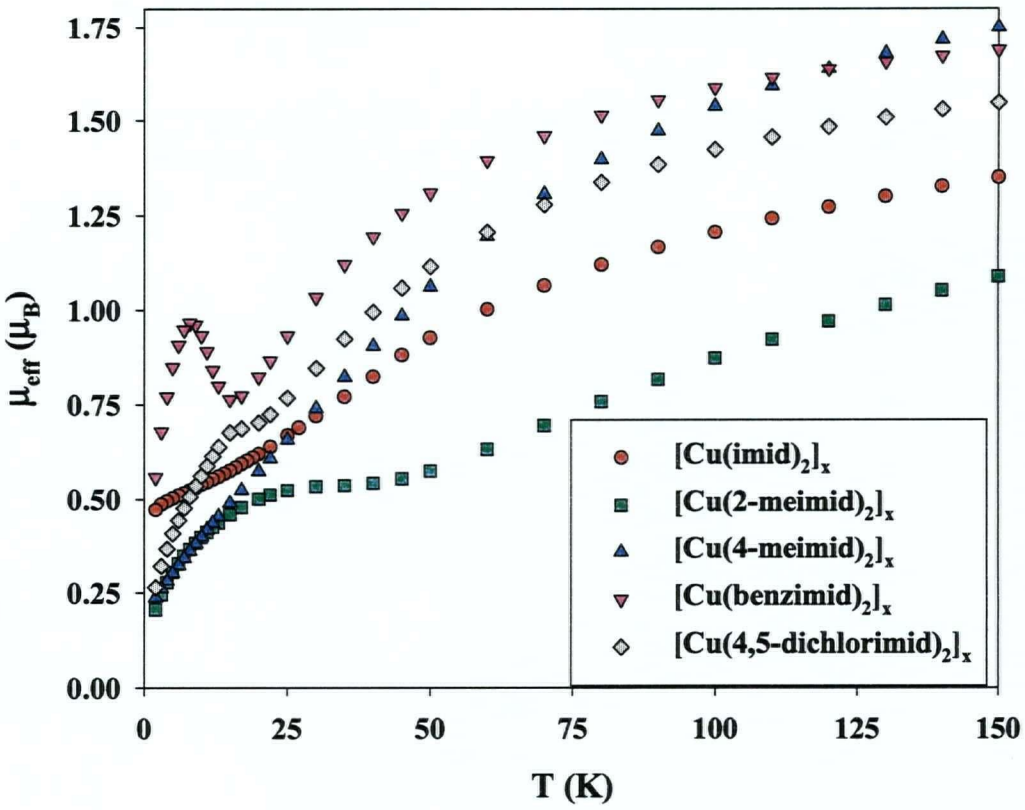

Figure 4.27 μ_{eff} versus T plots at 10 000 G for $[Cu(imid)_2]_x$, $[Cu(2\text{-}meimid)_2]_x$, $[Cu(4\text{-}meimid)_2]_x$, $[Cu(benzimid)_2]_x$ and $[Cu(4,5\text{-}dichloroimid)_2]_x$.

data is not large and likely arises from the presence of paramagnetic impurities.

The magnetic behavior of $[Cu(imid)_2]_x$ is similar to that of $[Cu(4\text{-}meimid)_2]_x$ with the exception that the "paramagnetic tail" in the χ plot is much more pronounced for this compound (Figure 4.26). As a result the μ_{eff} versus T plot shows a clear tendency to level

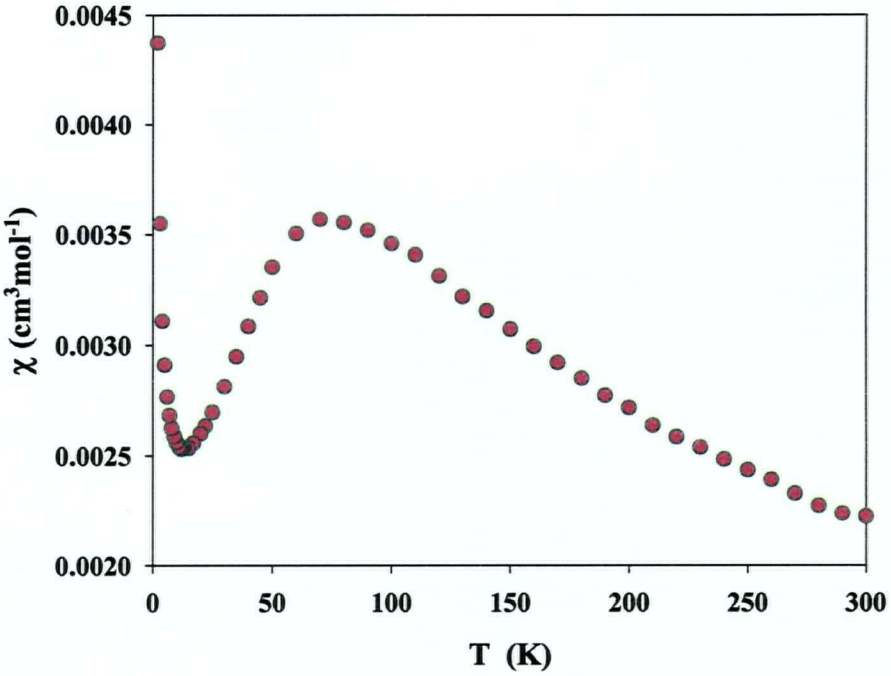

Figure 4.28 Plot of χ versus T for $[Cu(4\text{-meimid})_2]_x$ at 500 G.

off (smaller slope) below ~ 25 K. This suggests: (i) either a higher level of paramagnetic impurity in this material or, (ii) more complex behavior with a decrease in the strength of the antiferromagnetic coupling as the temperature is lowered or, (iii) a change in the magnetic exchange mechanism from primarily antiferromagnetic to primarily ferromagnetic coupling.

The other three compounds give clear evidence of a transition from antiferromagnetic to ferromagnetic exchange at low temperatures. This is clearly the case for $[Cu(benzimid)_2]_x$, which shows a magnetic anomaly at ~ 15 K below which μ_{eff} increases on decreasing the temperature before decreasing again below 8 K. Similar anomalies are less pronounced for $[Cu(4,5\text{-dichloroimid})_2]x$ and $[Cu(2\text{-meimid})_2]_x$ where the μ_{eff} values are seen just to level off on decreasing the temperature before decreasing again as the temperature is lowered (Figure 4.27).

To test for the presence (or absence) of long-range ferromagnetic order in these five copper systems we decided to undertake field-cooled (FC) and zero-field-cooled (ZFC) DC susceptibility measurements at a relatively low applied field of 50 G. The protocol for this consists of cooling the sample at zero field to 2.0 K, then, applying a magnetic field (50 G) the data are collected while the sample warms (ZFC data); the sample is then cooled in the field of 50 G to 2.0 K, and data are collected while warming the sample (FC data). The results of this data collection scheme are shown in Figures 4.29, 4.30, 4.31, 4.32, and 4.33, for $[Cu(benzimid)_2]_x$, $[Cu(2\text{-meimid})_2]_x$, $[Cu(4,5\text{-dichloroimid})_2]_x$, $[Cu(imid)_2]_x$, and $[Cu(4\text{-meimid})_2]_x$, respectively.

In a compound exhibiting long-range ferromagnetic ordering, the temperature-dependence of magnetization curves will show, generally, a break in the field-cooled magnetization (FCM) curve and a peak for the zero-field-cooled magnetization (ZFCM) curve at the onset of the magnetic transition (T_c). Also, the values of the ZFCM are

always lower than the FCM values at temperatures below the magnetic transition. Hence, these plots can provide one of the most accurate ways to determine the critical temperature (T_c) [38].

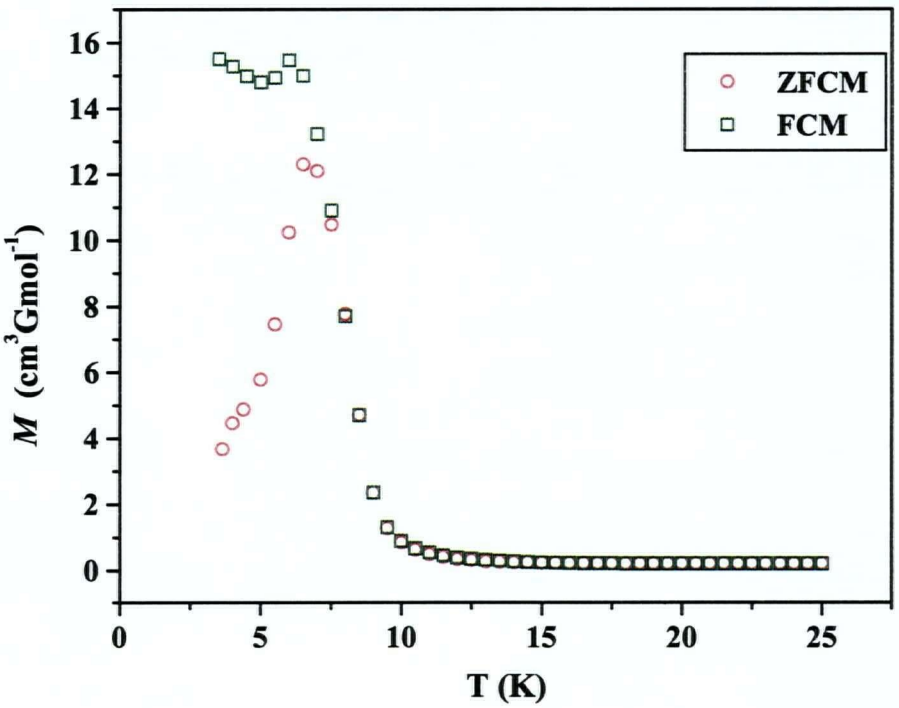

Figure 4.29 Zero-field cooling (ZFC) and field-cooling (FC) magnetization plots for $[Cu(benzimid)_2]_x$ at 50 G.

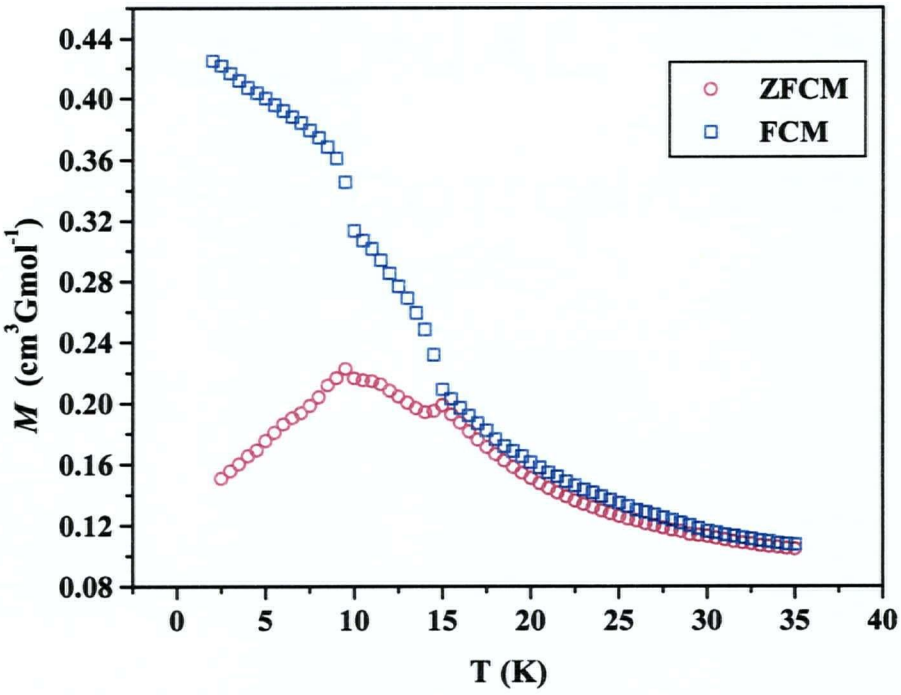

Figure 4.30 Zero-field cooling (ZFC) and field-cooling (FC) magnetization plots for $[Cu(2\text{-meimid})_2]_x$ at 50 G.

As can be seen in Figure 4.29, $[Cu(benzimid)_2]_x$ exhibits the FCM and ZFCM characteristics of a material showing long-range ferromagnetic order. The critical temperature (T_c) for this compound is determined to be ~ 8 K. Comparing the behavior of $[Cu(2\text{-meimid})_2]_x$ (Figure 4.30) and $[Cu(4,5\text{-dichloroimid})_2]_x$ (Figure 4.31) to that of $[Cu(benzimid)_2]_x$, it appears that these two polymers also exhibit long-range ferromagnetic order at low temperatures. Employing the maximum in the ZFCM plot as the measure of the critical temperature generates T_c values of ~ 15 K and ~ 14 K for

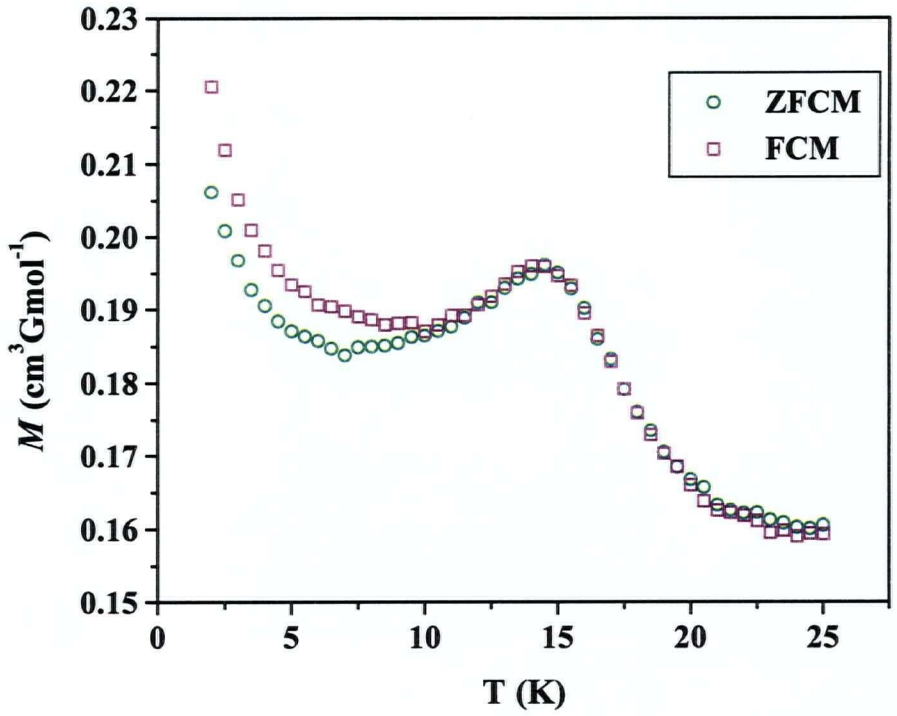

Figure 4.31 Zero-field cooling (ZFC) and field-cooling (FC) magnetization plots for $[Cu(4,5\text{-dichloroimid})_2]_x$ at 50 G.

$[Cu(2\text{-meimid})_2]_x$ and $[Cu(4,5\text{-dichloroimid})_2]_x$, respectively. $[Cu(2\text{-meimid})_2]_x$ shows a second maximum in its ZFCM plot at ~ 9 K. It is not at all clear what the origin is of this lower-temperature transition. A similar double transition appears in the ZFCM-FCM-REM studies carried out on $[Ni(benzimid)_2]_x$ and described earlier in this Chapter (section 4.3.2.2). Also, as mentioned earlier, a similar double transition has been recently reported in a 1-D molecule-based ferrimagnet involving Cu(II) and Mn(II) ions [20].

In contrast to the behavior just described, the studies on $[Cu(imid)_2]_x$ and $[Cu(4\text{-}meimid)_2]_x$ do not reveal peaks or large discontinuities in their ZFCM or FCM plots (Figures 4.32 and 4.33). For $[Cu(imid)_2]_x$ the ZFCM and FCM plots show only small discontinuities at around 15 K, the temperature at which the values of the FCM and ZFCM are the same following a warming mode (Figure 4.32). Interestingly, this compound shows a second minor anomaly at around 10 K. Similarly, the magnetization

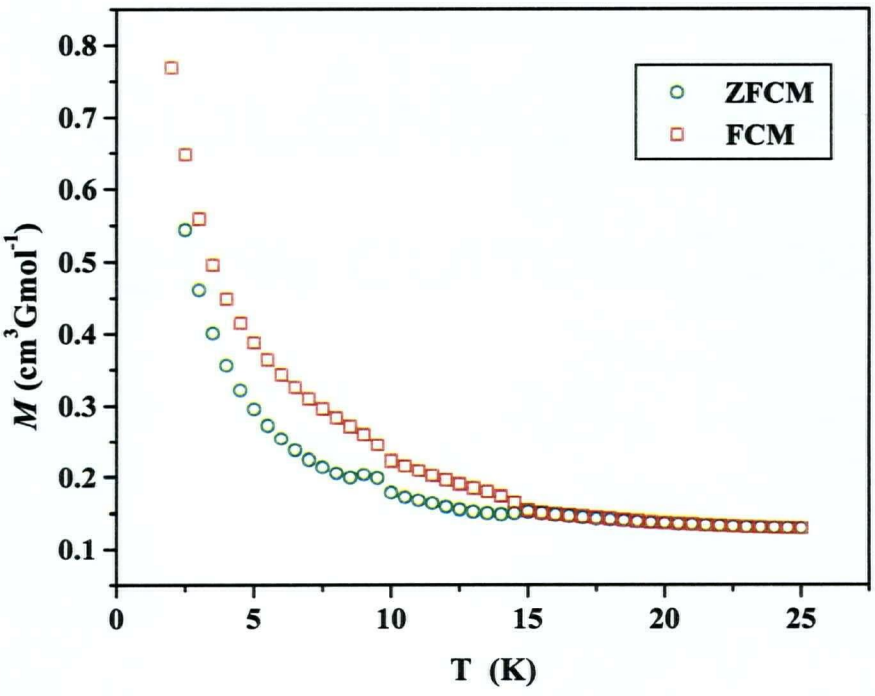

Figure 4.32 Zero-field cooling (ZFC) and field-cooling (FC) magnetization plots for $[Cu(imid)_2]_x$ at 50 G.

curves of $[Cu(4\text{-meimid})_2]_x$ have small breaks at around 15 K (Figure 4.33). In conclusion, $[Cu(imid)_2]_x$ and $[Cu(4\text{-meimid})_2]_x$ do not give evidence for long-range ferromagnetic order even in applied fields as low as 50 G. This is consistent with the conventional DC magnetization studies done at 500 and 10 000 G.

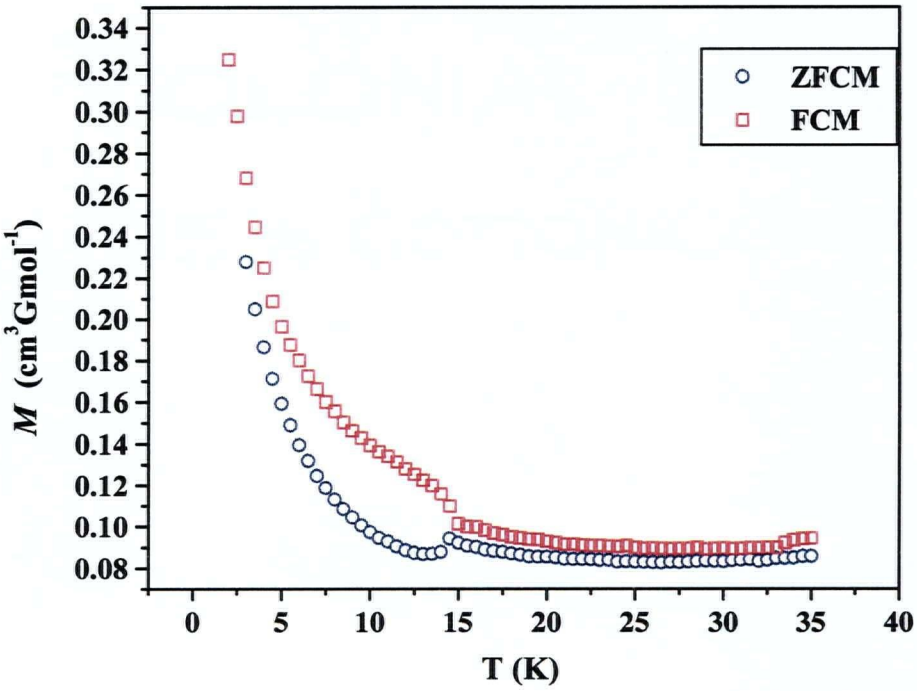

Figure 4.33 Zero-field cooling (ZFC) and field-cooling (FC) magnetization plots for $[Cu(4\text{-meimid})_2]_x$ at 50 G.

As described in earlier sections of this Chapter, hysteresis studies may be used to confirm the presence of long-range ferromagnetic order. Accordingly we examined the magnetization of all five copper compounds as the applied field was cycled between +55 000 G and –55 000 G at 4.8 K. The resulting hysteresis loops are shown in Figure 4.34. These loops give remnant magnetizations of 0.25, 6.0 and 0.02 cm^3 G mol^{-1} and coercive fields of 65, 45 and 4 G for $[Cu(2\text{-meimid})_2]_x$, $[Cu(benzimid)_2]_x$ and $[Cu(4,5\text{-dichloroimid})_2]_x$, respectively, which characterize these compounds as very soft molecule-based magnets.

In contrast, no well defined magnetic hysteresis was found, at 4.8 K, for $[Cu(imid)_2]_x$ and $[Cu(4\text{-meimid})_2]_x$, as shown in Figure 4.35. Thus, these two copper compounds cannot be regarded as molecule-based magnets.

A spin-canted structure, leading to residual spin at low temperatures, for $[Cu(2\text{-meimid})_2]_x$, $[Cu(benzimid)_2]_x$ and $[Cu(4,5\text{-dichloroimid})_2]_x$, is also supported by the fact that their highest magnetizations measured were 80, 347 and 251 cm^3Gmol^{-1}, respectively, at 4.8 K and 55 000 G. These values are considerably lower than the theoretical saturation magnetization value of 5588 cm^3Gmol^{-1} for an $S = 1/2$ system [15].

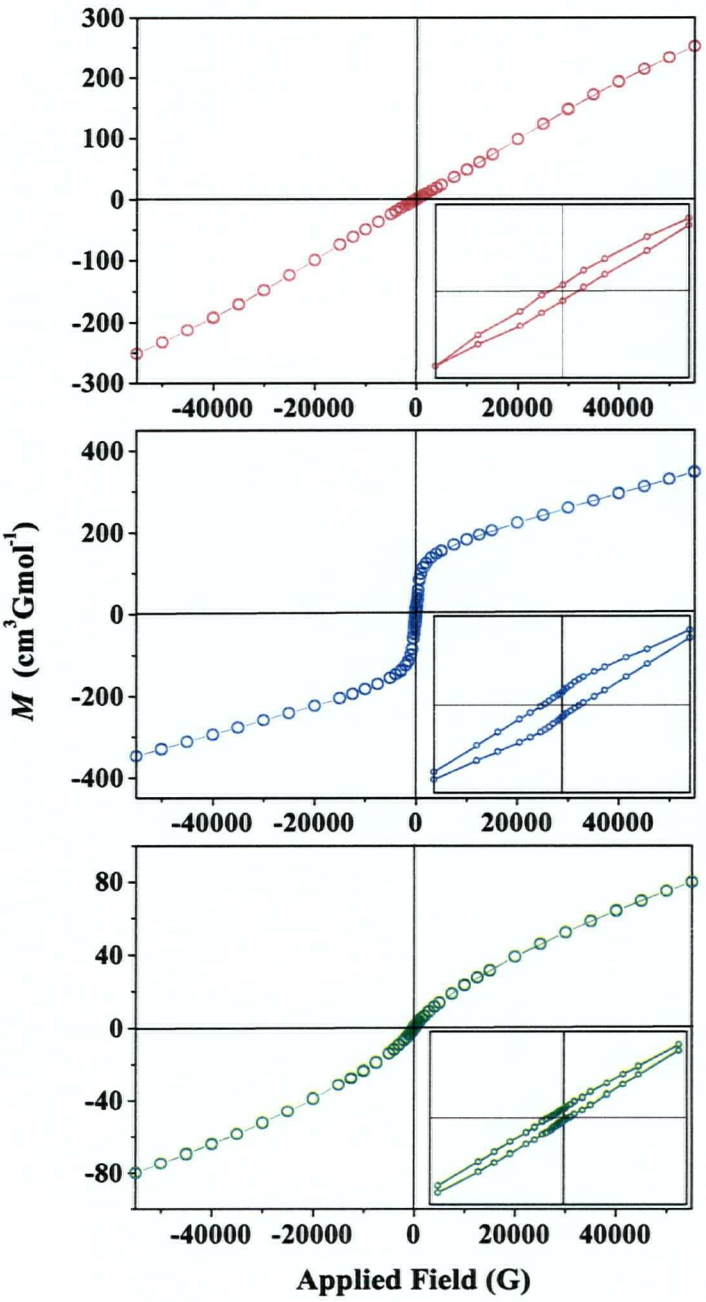

Figure 4.34 Magnetic hysteresis plots at 4.8 K for $[Cu(4,5\ dicloroimid)_2]_x$, (top); $[Cu(benzimid)_2]_x$, (middle); and $[Cu(2\text{-}meimid)_2]_x$, (bottom). The insert plots show magnifications of the central part of the hysteresis curves.

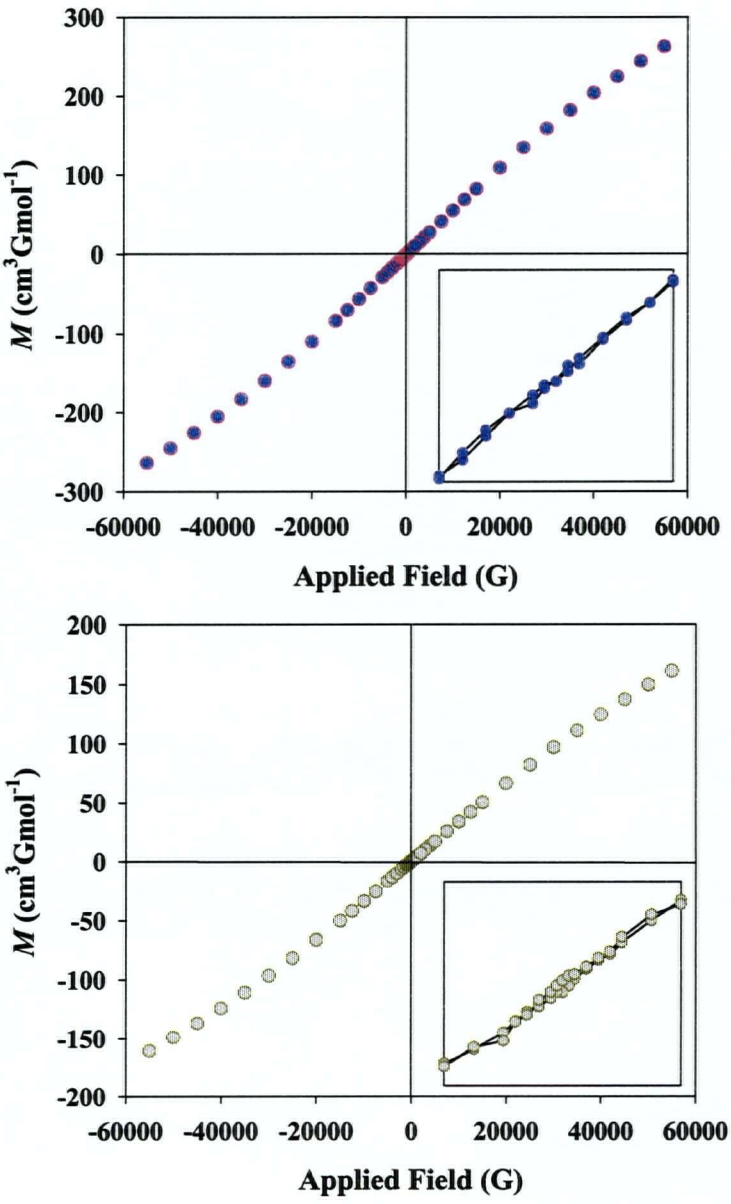

Figure 4.35 Magnetic hysteresis plots at 4.8 K for $[Cu(imid)_2]_x$, (top), and $[Cu(4\text{-meimid})_2]_x$, (bottom). The insert plots show magnifications of the central part of the hysteresis curves.

The magnetic behaviors of $[Cu(2\text{-meimid})_2]_x$, $[Cu(benzimid)_2]_x$ and $[Cu(4,5\text{-dichloroimid})_2]_x$, indicate in all three compounds the presence of antiferromagnetic coupling between paramagnetic centers as the primary exchange mechanism combined with a magnetic phase transition to a ferromagnetically ordered state at low temperatures. Therefore, these three copper compounds can be considered as molecule-based magnets. Again, this magnetic behavior is very comparable to that reported for $[Fe_3(imid)_6(imidH)_2]_x$ [1], $[Fe(2\text{-meimid})_2.\ 0.13(FeCp_2)]_x$ [2] and $[Fe(4\text{-abimid})_2]_x$ (Chapter 3), and the one observed previously in this Chapter for two Co(II) imidazolates and for the Co(II) and Ni(II) benzimidazolates.

4.5 SUMMARY AND CONCLUSIONS

Earlier studies, mainly on compounds of iron(II), led to the suggestion [1, 2] that azolate ligands which bridge through nitrogen atoms separated by one carbon in the heterocyclic ring will generate structures with single azolate bridges and extended arrays.

The work described in this Chapter indicates that, even though no new structures were determined by single crystal X-ray diffraction, this structural motif extends beyond compounds of iron(II) to include those of cobalt(II), nickel(II) and copper(II). Moreover, all of the systems studied in this Chapter show antiferromagnetic exchange coupling, mediated by the bridging imidazolate ligands, as the primary exchange process, and many, although not all, of the systems give evidence for a magnetic transition to long-

range ferromagnetic order at low temperatures. It appears that the phenomenon of spin-canting, a consequence of the non-centrosymmetric M–L–M exchange pathway provided by the single-bridging imidazolate ligands does indeed extend to metal systems other than iron(II).

It is not clear at this point why some, but not all, of the binary imidazolates of copper(II) and cobalt(II) show weak ferromagnetism. There appears to be no obvious ligand characteristic determining this. For example, while there is evidence for ferromagnetic order in the binary benzimidazolates of both cobalt and copper (nickel too, albeit very weak), the binary imidazolate of cobalt(II) shows low temperature order while that of copper(II) does not. In contrast, the 2-methylimidazolate of copper shows order and that of cobalt does not, while neither the cobalt nor the copper 4-methylimidazolate shows order.

It seems that the presence or absence of measurable long-range ferromagnetic order in imidazolate systems depends on structural details which in turn affect factors such as the degree of spin-canting. Less important is the d^n configuration of the metal center (other than that it be a paramagnetic configuration).

References

1. S. J. Rettig, A. Storr, D. A. Summers, R. C. Thompson, and J. Trotter. *J. Am. Chem. Soc.* **119**, 8675 (1997).

2. S. J. Rettig, A. Storr, D. A. Summers, R. C. Thompson, and J. Trotter. *Can. J. Chem.* **77**, 425 (1999).

3. V. M. Sturm, F. Brandl, D. Engel, W. Hoppe. *Acta Cryst.*, **B31**, 2369 (1975).

4. G. P. Brown, and S. Aftergut. *J. Polymer Sci.*, **A2**, 1839 (1964).

5. F. Seel, and J. Rodrian. *J. Organomet. Chem.*, **16**, 479 (1969).

6. A. M. Vecchio-Sadus. *Trans. Met. Chem.*, **20**, 46 (1995).

7. M. Goodgame, and F. A. Cotton. *J. Am. Chem. Soc.* **84**, 1543 (1962).

8. *PowderCell*, version 2.3, W. Krauss and G. Nolze, Federal Institute for Materials Research and Testing (BAM), Berlin, 1997.

9. F. A. Cotton, and G. Wilkinson. *Advanced Inorganic Chemistry*. Fourth Edition. John Wiley & Sons. New York. 1980. p. 770

10. Y. Tanabe and S. Sugano. *J. Phys. Soc. Jpn.* **9**, 753 (1954).

11. M. K. Ehlert, A. Storr, and R. C. Thompson. *Can. J. Chem.* **71**, 1412 (1993).

12. W. J. Eilbeck, F. Holmes, C. E. Taylor, and A. E. Underhill. *J. Chem. Soc. (A)*, 128 (1968).

13. *MGP-Suite of Programs for Interpretation of X-Ray Experiments*, by Jean Laugiert and Bernard Bochu, ENSP/Laboratoire des Matériaux et du Génie Physique. BP 46. 38042 Saint Martin d'Hères, France. http://www.inpg.fr/LMGP and htpp://www.ccp14.ac.uk/tutorial/lmgp/.

14. F. A. Cotton, and G. Wilkinson. *Advanced Inorganic Chemistry*. Fourth Edition. John Wiley & Sons. New York. 1980. p. 771.

15. R. L. Carlin. *Magnetochemistry*. Springer-Verlag. Berlin. 1986. pp. 7-9.

16. A. Storr, D. A. Summers, and R. C. Thompson. *Can. J. Chem.* **76**, 1130 (1998).

17. D. A. Summers. Ph. D. Thesis. The University of British Columbia. 1997.

18. M. M. Cordes and J. L. Walter. *Spectrochim. Acta.* **24**, 1421 (1968).

19. F. A. Cotton, and G. Wilkinson. *Advanced Inorganic Chemistry*. Fourth Edition. John Wiley & Sons. New York. 1980. p. 789.

20. N. Fukita, M. Ohba, T. Shiga, H. Okawa, and Y. Ajiro. *J. Chem. Soc., Dalton. Trans.* 64 (2001).

21. J. C. Dewan and S. J. Lippard. *Inorg. Chem.* **19**, 2079 (1980).

22. H. M. J. Hendricks, P. J. M. W. L. Birker, G. C. Vershoor, and J. Reedijk. *J. Chem. Soc., Dalton Trans.* 623 (1982).

23. C. Benelli, R. K. Bunting, D. Gatteschi, and C. Zanchini. *Inorg. Chem.* **23**, 3074 (1984).

24. J. A. Ibers and R. H. Holmes. *Science.* **209**, 223 (1980).

25. E. Colacio, J. M. Dominguez-Vera, M. Ghazi, R. Kivekäs, M. Klinga, and J. M. Moreno. *Inorg. Chem.* **37**, 3040 (1998).

26. J. T. Landrum, C. A. Reed, K. Hatano, and W. R. Scheidt. *J. Am. Chem. Soc.* **100**, 3232 (1978).

27. M. S. Haddad and D. N. Hendrickson. *Inorg. Chem.* **17**, 2636 (1978).

28. C. L. O'Young, J. C. Dewan, H. R. Lilenthal, and S. J. Lippard. *J. Am. Chem. Soc.* **100**, 7291 (1978).

29. G. Kolks, C. R. Frihart, P. K. Coughlin, and S. J. Lippard. *Inorg. Chem.* **20**, 2933 (1981).

30. G. Kolks, S. J. Lippard, J. V. Waszczak, and H. R. Lilienthal. *J. Am. Chem. Soc.* **104**, 717 (1982).

31. M. Inoue, M. Kishita, and M. Kubo. *Inorg. Chem.* **4**, 626 (1965).

32. H. C. Freeman. *Advan. Protein Chem.* **27**, 257 (1967).

33. M. K. Ehlert, S. J. Rettig, A. Storr, R. C. Thompson, and J. Trotter. *Can. J. Chem.* **67**, 1970 (1989).

34. G. P. Brown, S. Aftergut. *J. Polymer Sci.* **A2**, 1839 (1964).

35. B. J. Hathaway. *J. Chem. Soc. Dalton Trans.* 1196 (1972).

36. M. K. Ehlert, A. Storr, and R. C. Thompson. *Can. J. Chem.* **70**, 1121 (1992).

37. F. G. Herring, D. J. Patmore, and A. Storr. *J. Chem. Soc. Dalton Trans.* 711 (1975).

38. M. G. F. Vaz, L. M. M. Pinheiro, H. O. Stumpf, A. F. C. Alcântara, S. Golhen, L. Ouahab, O. Cador, C. Mathonière, and O. Kahn. *Chem. Eur. J.* **5**, 1486 (1999).

Chapter 5 TWO-DIMENSIONAL IRON(II) AND COBALT(II) IMIDAZOLATE POLYMERS EXHIBITING LONG-RANGE FERROMAGNETIC ORDERING

5.1 INTRODUCTION

It has already been suggested that steric constraints imposed by the 1,3 positioning of the nitrogens prevent double imidazolate bridging between metal centers [1]. One important consequence of the single azolate bridging in metal imidazolates has been the generation of extended structures with 3-D covalent connectivities (see Chapter 3). Another important characteristic property, not seen in corresponding pyrazolates (see Chapter 2), is that metal imidazolate polymers exhibit antiferromagnetic coupling above a critical temperature and long-range ferromagnetic ordering below that temperature, behavior that characterizes them as low temperature molecule-based magnets [1-3].

The work described in this Chapter achieves an important objective in the study of transition metal azolate polymers. It explores what effect significantly altering the extended structures of metal imidazolate systems would have on their magnetic properties. In the work described in this section, major structural modification has been achieved by incorporating 2,2'-bipyridine as a capping ligand in the compound

poly-2,2'-bipyridinetetrakis(imidazolato)diiron(II), $[Fe_2(imid)_4(bipy)]_x$. This material has a unique double layer 2-D extended lattice. Like the iron(II) 4-azabenzimidazolate system, $[Fe(4\text{-}abimid)_2)]_x$, (Chapter 3) it incorporates single imidazolate bridges and, moreover, it also exhibits long range ferromagnetic order and spontaneous magnetization at low temperatures. To see whether a similar structural modification is possible with other metals, the 2,2'-dipyridine complex of cobalt (II) imidazolate analogue was also investigated. Poly-2,2'-bipyridinetetrakis(imidazolato)dicobalt(II), $[Co_2(imid)_4(bipy)]_x$, was synthesized and was found to be isomorphous with $[Fe_2(imid)_4(bipy)]_x$. An investigation of the magnetic properties of the cobalt compound revealed that it too exhibits long range ferromagnetic order at low temperatures.

The polymer $[Fe_2(imid)_4(bipy)]_x$ is unique in that it exhibits two reversible structural phase transitions over the temperature range 2 to 300 K. These phase transitions, one of which exhibits thermal hysteresis, have been studied by both DC and AC susceptibility measurements, in addition to Mössbauer spectroscopy and X-ray crystallography.

Part of the material discussed in this chapter is currently in press.

5.2 POLY-2,2'-BIPYRIDINETETRAKIS(IMIDAZOLATO)DIIRON(II)

5.2.1 RESULTS AND DISCUSSION

5.2.1.1 SYNTHESIS, PHYSICAL AND THERMAL CHARACTERIZATION

The reaction of ferrocene with imidazole and excess molten 2,2'-bipyridine produced the polymeric material, $[Fe_2(imid)_4(bipy)]_x$, in macroscopic crystalline form, suitable for single crystal X-ray diffraction studies. Details of the synthesis of this compound are given in Chapter 9, section 9.2.1.2. $[Fe_2(imid)_4(bipy)]_x$ is moderately air-sensitive, it does not dissolve in common organic solvents and it is non-volatile. This latter characteristic is further supported by the thermal gravimetric analysis of $[Fe_2(imid)_4(bipy)]_x$. As shown in Figure 5.1, $[Fe_2(imid)_4(bipy)]_x$ does not start to decompose until ~ 250 °C. The TGA plot follows a two stage weight loss. The first major weight loss (~ 40 %) occurs between 250 °C and 335 °C, and the second one, with a weight loss of ~ 25 % of the initial weight, happens between 335 °C and 580 °C. No further weight loss of any significance occurs up to the highest temperature studied of 800 °C. The calculated weight loss for the dissociation of 2,2'-bipyridine is 29 %. However, the TGA plot does not show the expected plateau, corresponding to such an event which would lead to the formation of polybis(imidazolate)iron(II), $[Fe(imid)_2]_x$. It seems that this iron compound is very thermally unstable. This contradicts with the thermal properties of the analogue, $[Co(imid)_2]_x$, which can be obtained under the TGA analyser conditions from thermolysis of $[Co_3(imid)_6(imidH)_2]_x$ (see Chapter 4, section 4.2).

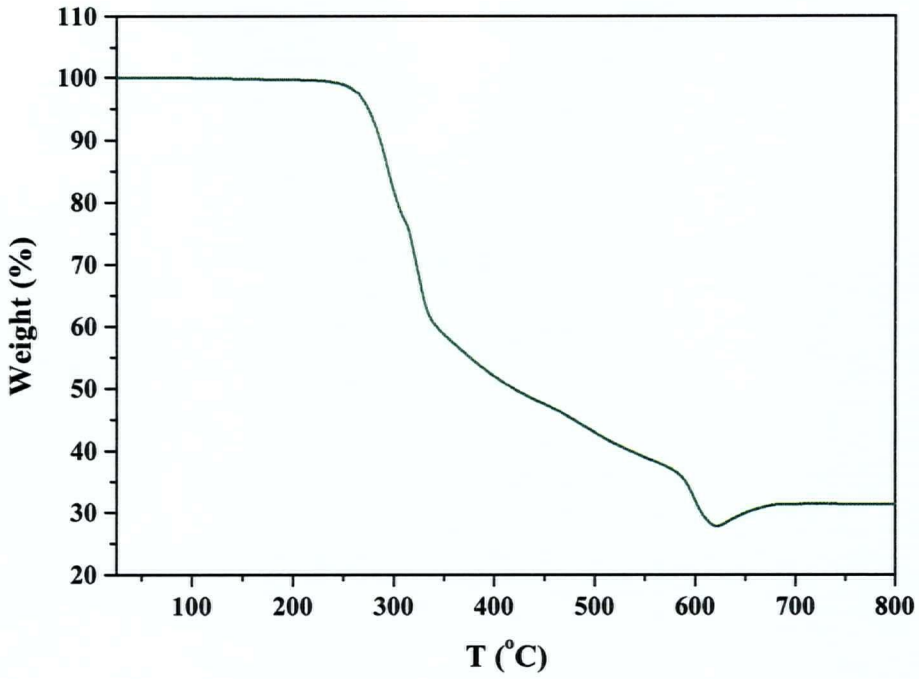

Figure 5.1 TGA plot for $[Fe_2(imid)_4(bipy)]_x$.

5.2.1.2 X-RAY DIFFRACTION STUDIES

Room temperature (294 K) X-ray diffraction studies revealed an extended structure involving double layer sheets of iron ions linked by single imidazolate bridges. As mentioned in the introduction, we have identified three different structural phases in this material and have labelled this high temperature phase the α-phase. Crystallographic data for $[Fe_2(imid)_4(bipy)]_x$ are shown in Appendix I, Table I-5. The repeat unit of the α-phase of $[Fe_2(imid)_4(bipy)]_x$ is shown in Figure 5.2.

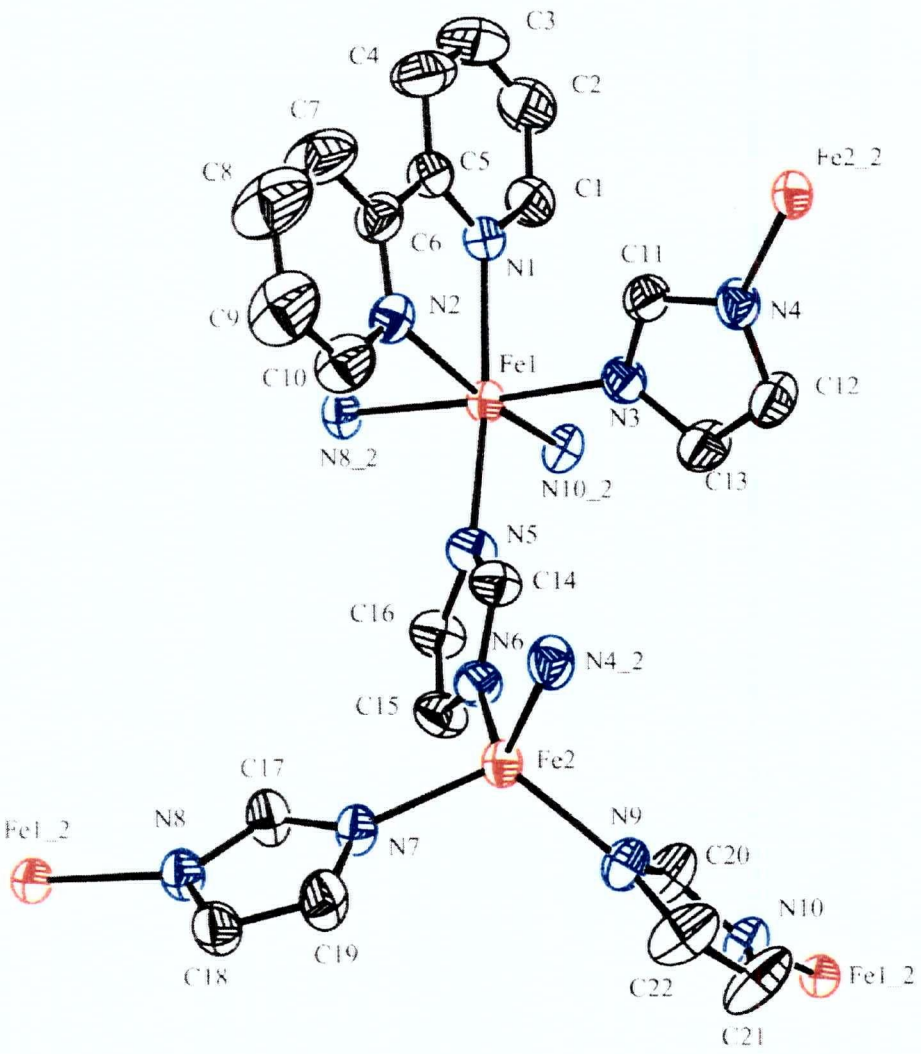

Figure 5.2 View of the repeat unit of $[Fe_2(imid)_4(bipy)]_x$ (α-phase, 294 K) and atom numbering scheme (33% probability thermal ellipsoids).

The capping of iron centres by 2,2'-bipyridine affects the dimensionality of this system, resulting in a 2-D polymer, as seen in Figures 5.3 and 5.4. Four- and six-coordinated Fe(II) ions alternate in the lattice, the latter ions being coordinated by bipy

ligands in addition to bridging imidazolates. Each tetrahedrally coordinated iron is bonded via the ligand to four octahedral irons with each of these bonded to four tetrahedral ones. The capping bipy ligands prevent bridging of metal centres in the third dimension and occupy space between the sheets, isolating the sheets from each other. By looking at the iron ion connectivity diagram (Figure 5.4), it can be seen that the connectivities between the two layers of a sheet form four-membered fused rings, while, the connectivities within the layers, top and bottom, form six-membered fused rings.

When DC magnetic susceptibility measurements were performed on $[Fe_2(imid)_4(bipy)]_x$, a major discontinuity was detected (*vide infra*) in the magnetic moment of this compound at around 135 K. Another discontinuity was also barely apparent at ~ 150 K. The latter was further confirmed by higher density DC susceptibility measurements (*vide infra*). These findings prompted the determination of the single-crystal X-ray structure of $[Fe_2(imid)_4(bipy)]_x$ at low temperatures to determine whether crystallographic phase transitions were involved. Subsequently, single crystal X-ray diffraction studies of $[Fe_2(imid)_4(bipy)]_x$ at ~ 143 K and ~ 113 K revealed two new structural phases.

These structural studies were carried out on different crystals of $[Fe_2(imid)_4(bipy)]_x$; therefore, in order to eliminate the possibility that these three different polymorphs were isolated from the room temperature synthesis, the unit cell of

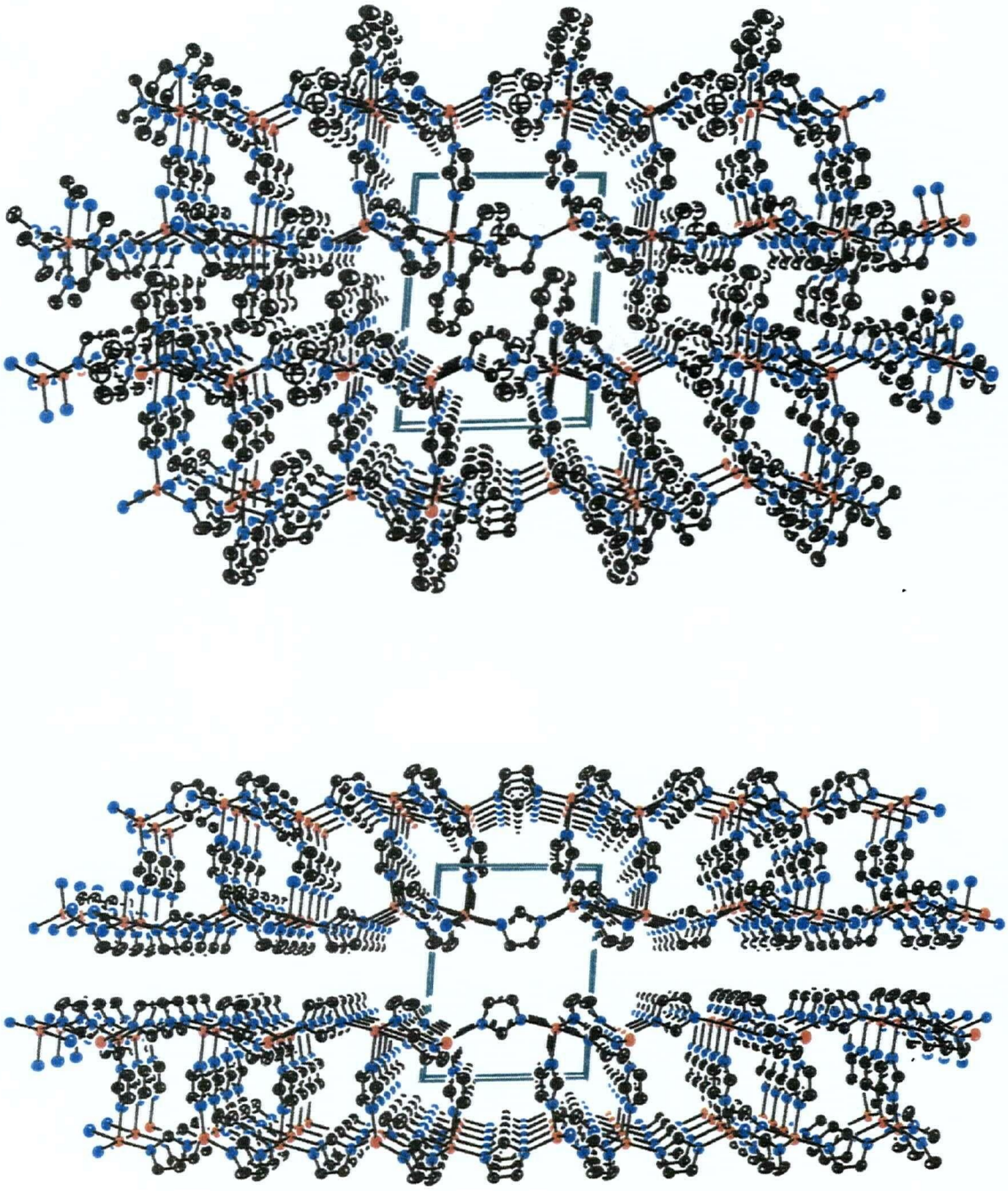

Figure 5.3 ORTEP diagrams of $[Fe_2(imid)_4(bipy)]_x$ (α-phase) looking down the *c* axis. In the bottom view, bipyridine ligands have been removed to reveal the double-layer sheet extended framework. (50 % probability thermal ellipsoids).

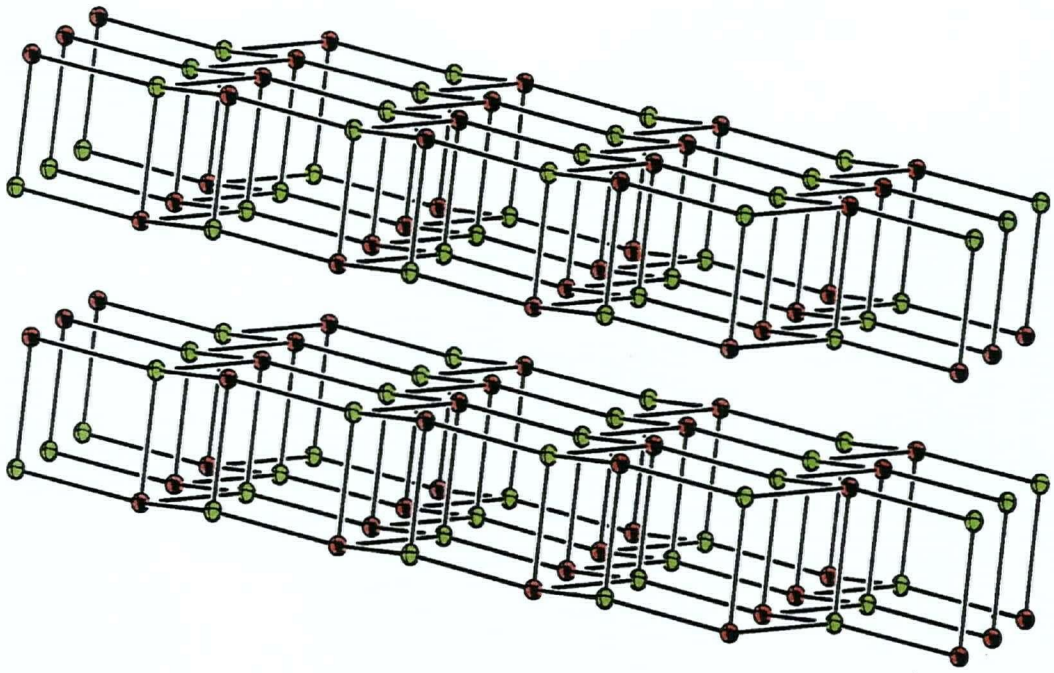

Figure 5.4 Iron ion connectivity diagram of a section of two double-layer sheets for the α-phase of $[Fe_2(imid)_4(bipy)]_x$. Octahedral iron (red), tetrahedral iron (green). View approximately looking down the *c* axis.

the crystal used for the lowest temperature (113 K) study was determined initially at 173 K. The unit cell at 173 K was found to be the same as that obtained at 294 K [a = 10.507(4), b = 13.730(4), c = 9.188(3) Å, α = 106.51(3), β = 108.32(3), γ = 80.84(3) deg, V = 1202.9(2), Å^3]. When the same crystal was cooled down from 173 to 113 K the unit cell parameters changed [a = 10.414(5), b = 13.508(5), c = 26.060(1) Å, α = 104.53(2), β = 93.892(2), γ = 100.512(2) deg, V = 3646.0(2), Å^3]. The phase with these

cell parameters is labelled the γ-phase. A similar procedure was utilized in determining the structure of $[Fe_2(imid)_4(bipy)]_x$ at ~ 143 K. A crystal of $[Fe_2(imid)_4(bipy)]_x$ was examined above 170 K and found to have the same cell parameters as those determined earlier at 294 K. The same crystal was then cooled to ~ 143 K and the cell parameters were determined and found to have changed [a = 17.1338, b = 18.5426, c = 23.6199 Å, α = 80.424, β = 75.364, γ = 80.826 deg, V = 7105.1(2) Å^3]. The phase with these cell parameters is labelled the β-phase.

The $P\bar{1}$ space group is retained in the three structures determined at 294 K (α-phase), 143 K (β-phase) and 113 K (γ-phase); therefore, there are no crystallographic transitions involved, but structural phase transitions are evident in $[Fe_2(imid)_4(bipy)]_x$.

That the volume of the unit cell in the γ-phase is three times larger than the one in the α-phase is due to the existence of six unique Fe(II) chromophores in the structure of the γ-phase, as shown by its asymmetric unit depicted in Figure 5.5. The FeN_6 cores involving the Fe(1), Fe(3) and Fe(5) sites in the γ-phase have been slightly modified compared to the octahedral Fe(1) site in the α-phase (Figure 5.2). The Fe(1)–N(9) and Fe(1)–N(10) bond lengths are 2.217(2) and 2.314(2) Å, respectively, compared to 2.262(2) and 2.299(2) Å, respectively, at 294 K. Selected bond lengths for the α- and γ-phases, are shown in Appendix I, Table I-6. The bond angles are also different at the two temperatures; for instance, the N(10)–Fe(1)–N(1) angle of 81.33(9)° at 113 K

corresponds to the N(2)–Fe(1)–N(3) angle of 88.99° at 294 K. As a consequence of the reduction in this angle the adjacent N(10)–Fe(1)–N(7) angle of 91.00(9)° at 113 K differs significantly from the corresponding N(2)–Fe(1)–N(8) angle of 83.61(9)° at 294 K.

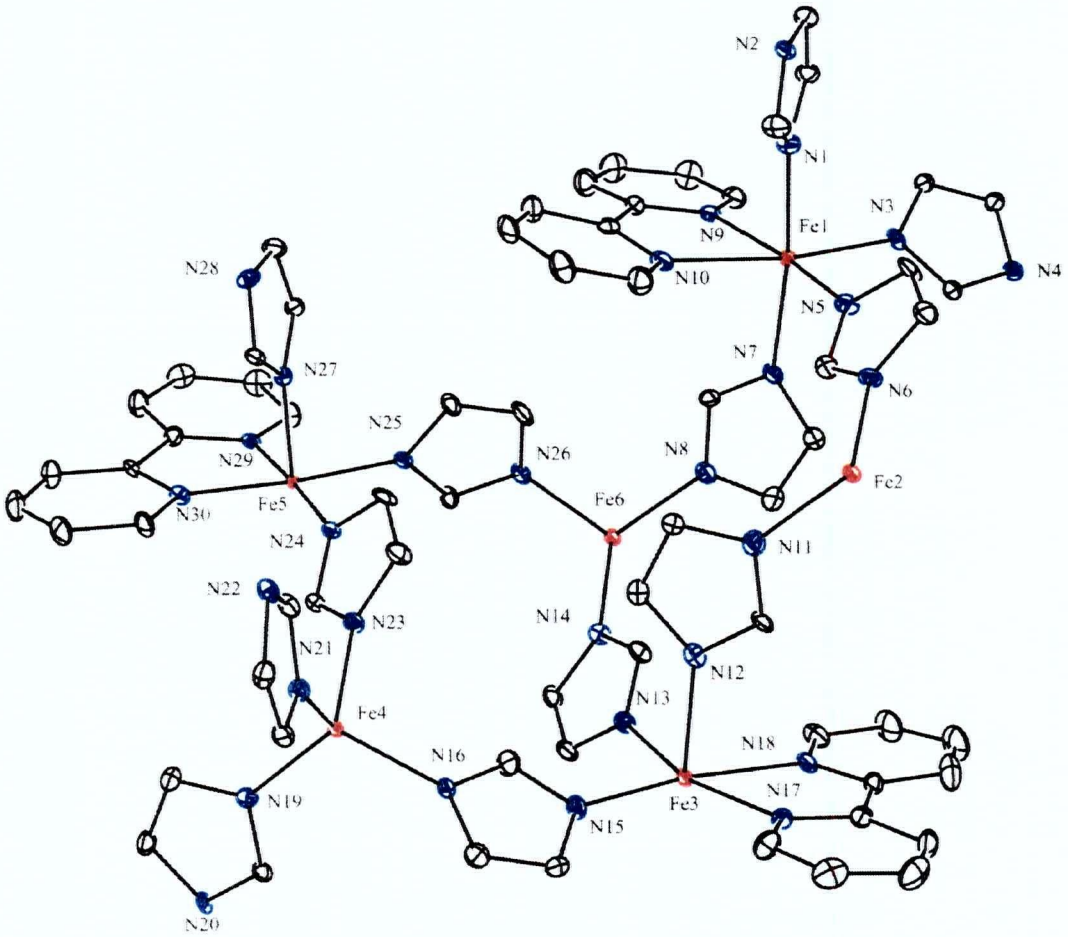

Figure 5.5 View of the asymmetric unit of $[Fe_2(imid)_4(bipy)]_x$ (γ-phase, 113 K) and atom numbering scheme (33% probability thermal ellipsoids).

Significant differences between the α- and γ- phases in bond lengths and angles involving the FeN_4 core are also seen. Fe(2)–N(6) is 2.019(2) Å at 113 K against 2.036(2) Å at 294 K. Furthermore, the N(2)–Fe(2)–N(4) bond angle is 107.4° at 113 K compared to the corresponding N(7)–Fe(2)–N(9) angle of 117.6° at 294 K. Selected bond angles for the α- and γ-phases of $[Fe_2(imid)_4(bipy)]_x$, are shown in Appendix I, Table I-7.

The similitude of the iron ion connectivity diagrams of the α- and γ-phases of $[Fe_2(imid)_4(bipy)]_x$ (Figures 5.4 and 5.6) show that the structural changes are relatively subtle. Nonetheless, these structural phase transitions were properly identified by DC and AC magnetic susceptibility measurements as well as Mössbauer spectroscopy as will be shown in subsequent sections. As previously mentioned, the *c* axis of the unit cell of the γ-phase is almost three times longer than that of the α-phase. This situation can be understood better by examining the octahedral iron centers in the connectivity diagrams of these phases (Figures 5.4 and 5.6, respectively). Hence, for the α-phase, looking approximately along the *c* axis, octahedral iron chromophores equivalent to that on the first row, can be found on the second and third rows shown (Figure 5.4). In contrast, in the γ-phase there are three different, and unique, octahedral iron chromophores in the first, second and third rows. The fourth row (not shown) is equivalent to the first. (Figure 5.6). As a consequence, the unit cell increases by approximately three times in volume compared to that of the α-phase (*vide supra*).

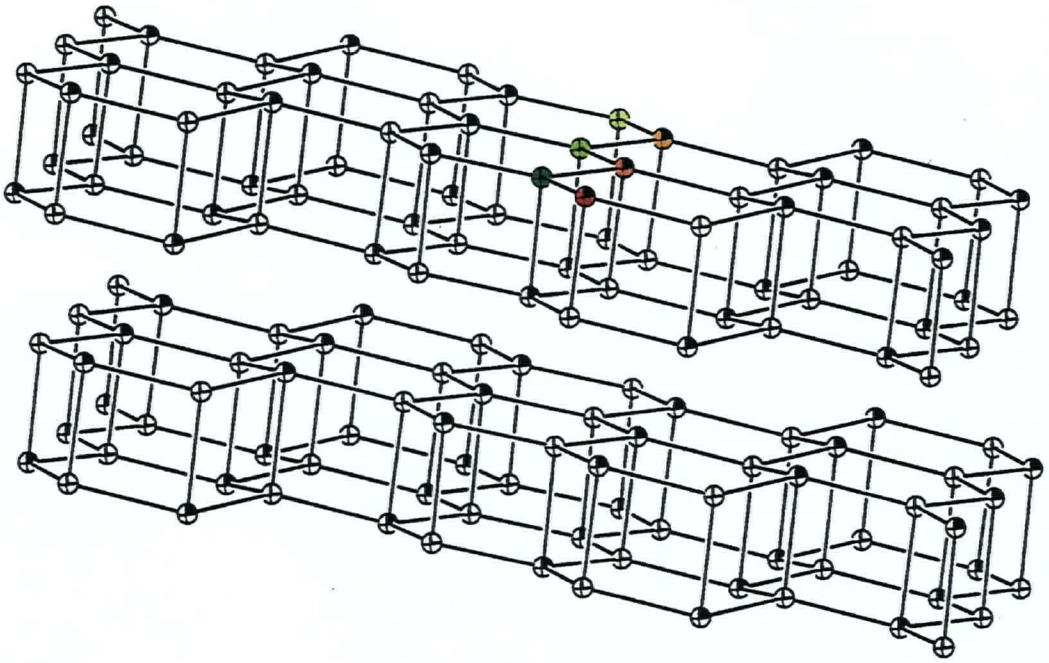

Figure 5.6 Iron ion connectivity diagram of a section of two double-layer sheets for the γ-phase of $[Fe_2(imid)_4(bipy)]_x$. Octahedral iron (red or semi-filled), tetrahedral iron (green or non-filled). View looking approximately down the *c* axis.

Interestingly, the β-phase has a unit cell volume six times larger than the α-phase, and two times larger than that of the γ-phase discussed above. This is attributed to the existence of six unique octahedral iron(II) chromophores and six unique tetrahedral iron(II) chromophores in the β-phase, as shown in Figure 5.7. Changes in bond distances and angles occurring in the β phase, in comparison to the other structural phases, are similar to those discussed for the α and γ-phases above. Crystallographic data and selected bond lengths and angles for the β-phase, are listed in Appendix I,

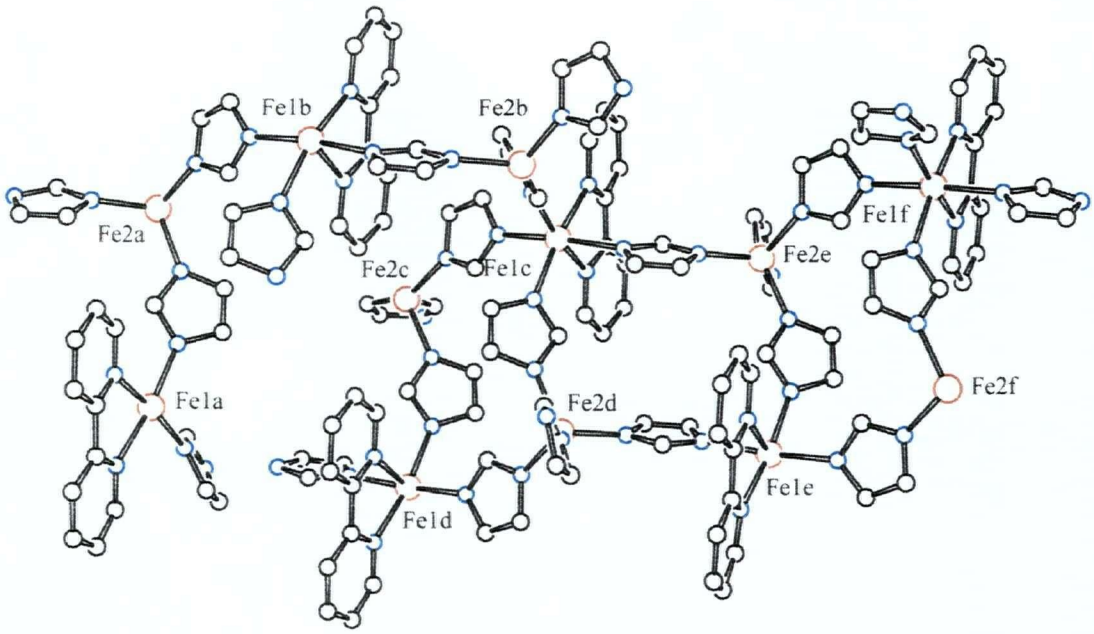

Figure 5.7 View of the asymmetric unit of $[Fe_2(imid)_4(bipy)]_x$ (β-phase, 143 K) and atom numbering scheme.

Tables I-8 and I-9, respectively. In the connectivity diagram for the γ-phase (Figure 5.6) going from left to right along a "row" (along the *a* axis) the octahedral centers are identical as are the tetrahedral centers. In contrast, in the β-phase there are two different and unique octahedral chromophores which alternate along the *a* axis. The same applies to the tetrahedral chromophores. The situation regarding the *c* axis is the same as for the γ-phase. As a result, the unit cell volume of the β-phase increases approximately two times compared to that of the γ-phase (*vide supra*).

The change in the asymmetric units determined for the α and γ phases (Figures 5. 2 and 5.5, respectively) is revealed on attempting to overlap the two structures around an octahedral iron centre. Thus, by matching the bipy ligands and one of the imidazolate bridging ligands from the α- and γ-phases, as shown in Figure 5.8, another imidazolate ligand (vertical position in Figure 5.8) in the γ-phase is oriented differently from the corresponding one in the α-phase.

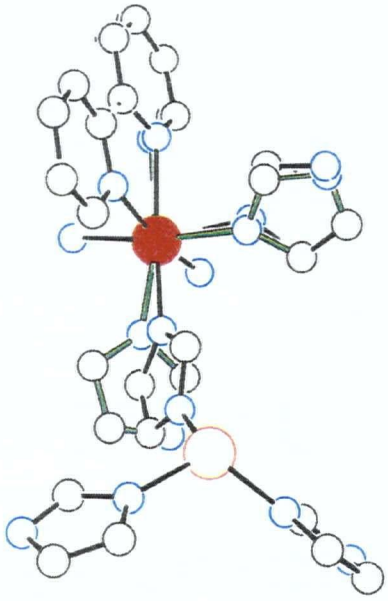

Figure 5.8 Comparison of coordination sphere geometries by overlapping octahedral irons (red circle) in the α- (black bonds) and γ- (green bonds) phases of $[Fe_2(imid)_4bipy]_x$.

In general, accordingly to X-ray diffraction, rotation of imidazolate moieties about the bridge axis seems to be the major structural difference between the three phases in $[Fe_2(imid)_4(bipy)]_x$.

5.2.2.3 MAGNETIC PROPERTIES

Variable temperature DC magnetic susceptibilities of a powdered sample of $[Fe_2(imid)_4(bipy)]_x$ were measured at fields of 500 and 10 000 G from 2 to 300 K. The μ_{eff} versus T plot (10 000 G, 2 to 300 K, Figure 5.9) shows a clear discontinuity near 135 K. Another irregularity in the same plot is barely apparent at slightly above 150 K. These two anomalies are attributed to structural phase transitions, as confirmed by low temperature X-ray diffraction studies (*vide supra*). The structural phase transitions have been studied in detail by AC and DC susceptibility measurements. These are presented following the discussion of the magnetic phase transition found in the γ-phase of this compound.

Figure 5.10 presents the χ versus T and μ_{eff} versus T data obtained for γ-$[Fe_2(imid)_4(bipy)]_x$ below 100 K at 500 G. The value of μ_{eff} decreases smoothly with temperature from 5.3 μ_B at 300 K to a low of 3.96 μ_B just above 11 K. Below this temperature, μ_{eff} increases abruptly to a maximum value of 12.6 μ_B at 3 K before decreasing again with temperature to 11.2 μ_B at 2 K. The onset of the magnetic transition at around 11 K is also observed in the χ versus T plot (Figure 5.10). The magnetic susceptibility, which increases smoothly with decreasing temperature below

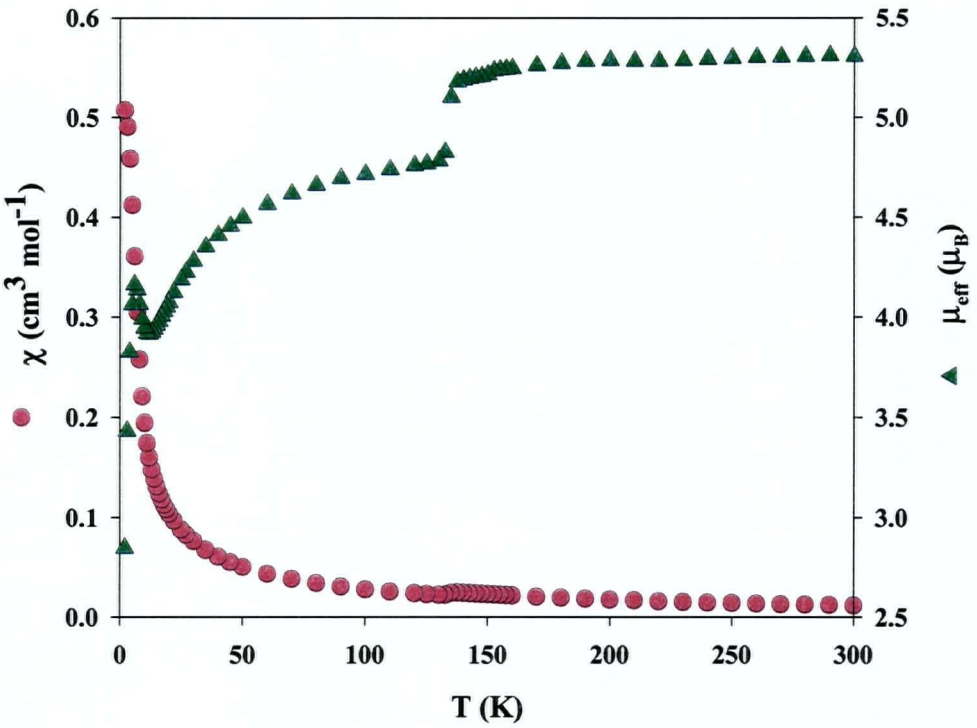

Figure 5.9 χ and μ_{eff} versus T plots at 10 000 G for $[Fe_2(imid)_2(bipy)]_x$.

300 K, rises abruptly as the temperature decreases below 11 K. The magnetization versus field plots at three temperatures shown in Figure 5.11, reflect this unusual magnetic behaviour. The plots are linear at 30 and 20 K and extrapolate to zero magnetization at zero applied field while distinct curvature is seen at 10 and 4.8 K. At 4.8 K the plot extrapolates to give a net magnetization at zero applied field. Cycling the applied field between +55 000 and –55 000 G at 4.8 K generates a hysteresis loop, the

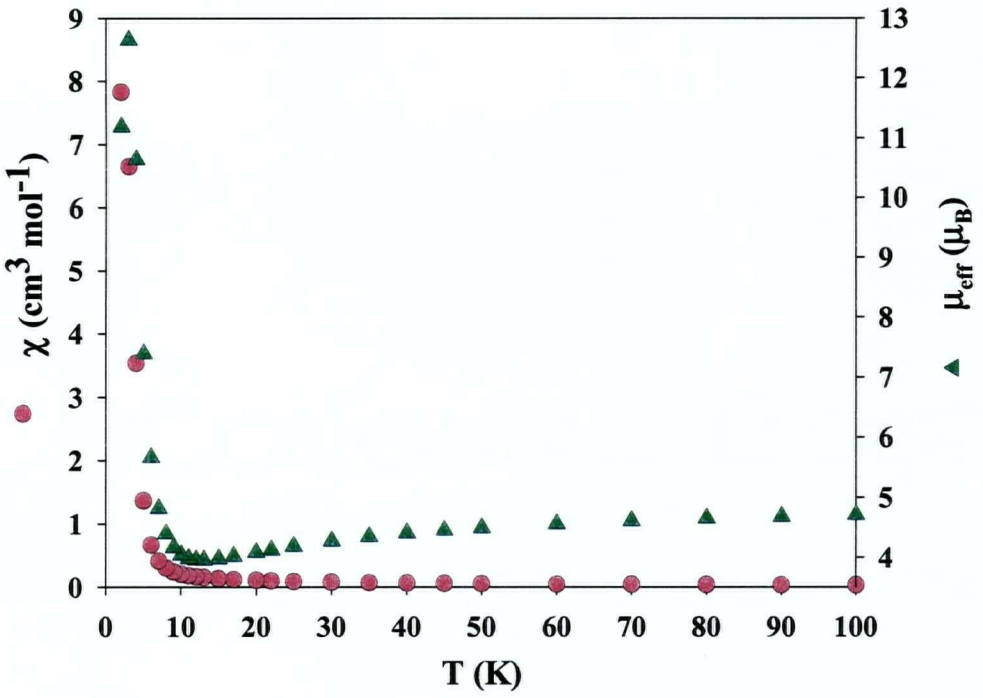

Figure 5.10 χ and μ_{eff} versus T plots at 500 G for γ- $[Fe_2(imid)_2(bipy)]_x$.

central portion of which is shown in Figure 5.12. From this is obtained a remnant magnetization of 200 cm^3Gmol^{-1} and a coercive field of 15 G.

Further evidence for structural phase transitions in $[Fe_2(imid)_4(bipy)]_x$ can be seen in the traditional Curie-Weiss analysis of the magnetic data. This analysis can provide evidence for the primary exchange process present in the system. A plot of χ^{-1}

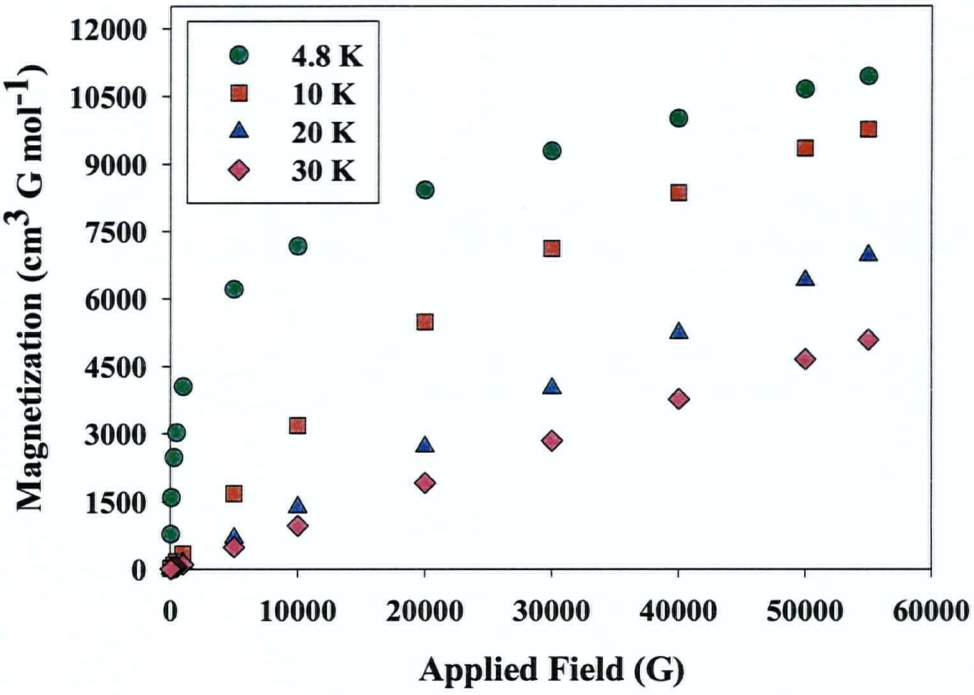

Figure 5.11 Magnetization versus applied field plots at different temperatures for γ-$[Fe_2(imid)_2(bipy)]_x$.

versus T (10 000 G; 2 – 300 K) for $[Fe_2(imid)_4(bipy)]_x$ (Figure 5.13) reveals two linear regions, corresponding to two of the three structural phases present. Detection of the β-phase in this plot is not possible, consistent with the fact that its magnetic properties are barely distinguishable from those of the α-phase. Fitting the data in Figure 5.13 to the Curie-Weiss equation yields: (i) employing data in the temperature range 300 – 170 K, C (Curie constant) = 3.60 cm^3Gmol^{-1}, θ (Weiss constant) = -6.7 K and (ii) for the range

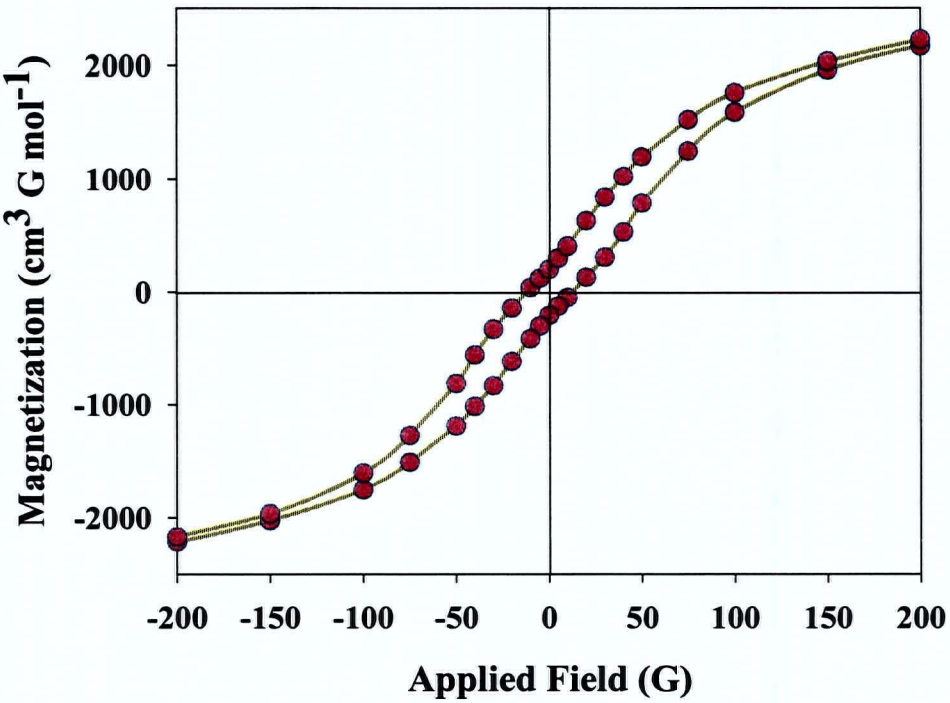

Figure 5.12 Magnetic hysteresis plot at 4.8 K for γ- $[Fe_2(imid)_4(bipy)]_x$.

120 – 30 K, C = 3.04 cm^3Gmol^{-1}, θ = -9.9 K. The observed negative Weiss constants are consistent with antiferromagnetic coupling as the primary exchange process operating here. However, the interpretation of these parameters is complicated by the fact that the three phases of $[Fe_2(imid)_4(bipy)]_x$ contain octahedral centres, which for high spin d^6 means first order orbital contribution and spin-orbit coupling. As a result these centres would show decreasing moments with temperature and negative Weiss

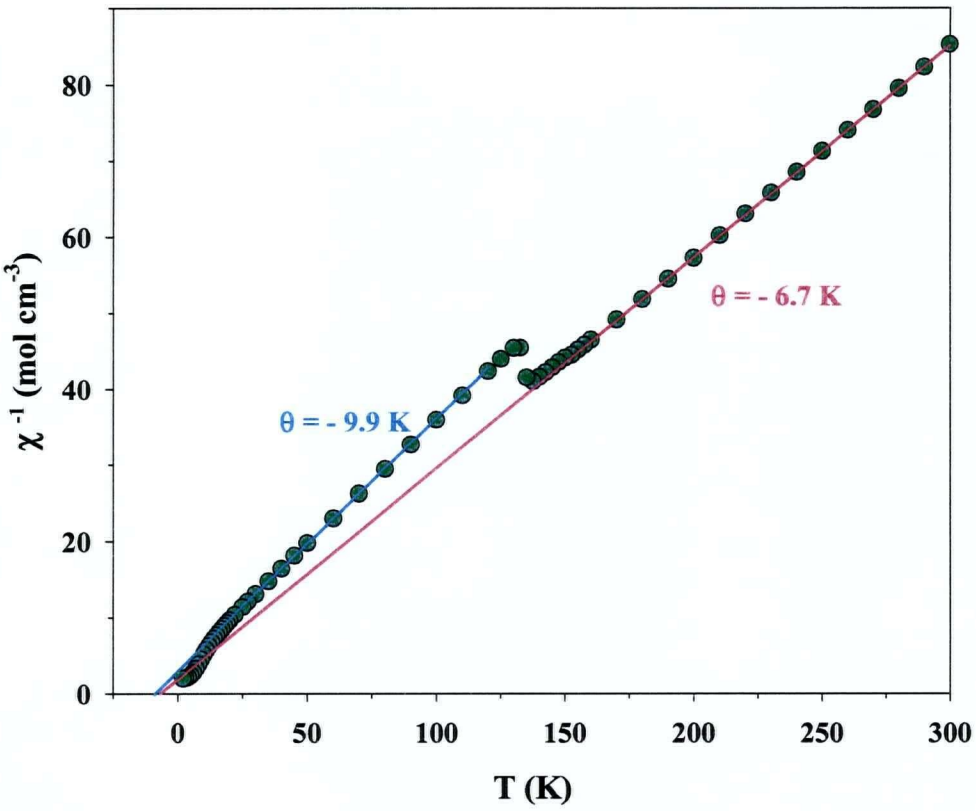

Figure 5.13 Plot of χ^{-1} versus temperature at 10 000 G for $[Fe_2(imid)_4(bipy)]_x$.

constants even in the absence of antiferromagnetic exchange. It seems reasonable to assume that the θ values here are a composite of single ion effects and exchange interactions but to determine the relative contributions would be difficult. Overall the results are consistent with $[Fe_2(imid)_4(bipy)]_x$ exhibiting antiferromagnetic exchange

interactions at high temperatures and, coupled with the observed net moment ground state, this classifies it as a weak ferromagnet. The magnetic behavior exhibited by γ-$[Fe_2(imid)_4(bipy)]_x$ is similar to that reported for $[Fe_3(imid)_6(imidH)_2]_x$ [1], $[Fe(2\text{-}meimid)_2 \cdot 0.13Cp_2Fe]_x$ [2], and $[Fe(4\text{-}abimid)_2]_x$ (Chapter 3) and it is possible that γ-$[Fe_2(imid)_4(bipy)]_x$ like the other systems listed, also exhibits canted-spin antiferromagnetism. This conclusion is supported by the fact that the highest magnetization reached, 10 940 cm^3Gmol^{-1} (at 4.8 K and 55 000 G), is significantly smaller than the theoretical saturation value of 22 300 cm^3Gmol^{-1} [5].

As described in Chapter 3, the spin canting angle, γ, can be estimated by extrapolating the plot of M versus H to $H = 0$ at a temperature below T_c. Doing this for γ-$[Fe_2(imid)_4(bipy)]_x$ gives a saturation moment ($M_s(0)$) of 6980 cm^3Gmol^{-1}, and from this, an estimation of the spin canting angle, γ, of ~ 17°.

It should be noted that unlike $[Fe(2\text{-}meimid)_2 \cdot 0.13Cp_2Fe]_x$ [2] and $[Fe(4\text{-}abimid)_2]_x$ (Chapter 3), γ-$[Fe_2(imid)_4(bipy)]_x$ has a structure in which the nearest neighbor interactions are between iron ions that differ significantly in their ligand chromophores. Because of the difference in g values, the size of the interacting magnetic dipoles will differ and, hence, even perfect antiparallel alignment of spins between neighbours would lead to a residual moment on the sheets. This form of ferrimagnetism, which was suggested to possibly occur in the 1-D polymer, polybis(1-methyl-2-thioimidazolate)iron(II) [7] (See Chapter 7), could be the cause of the

anomalous magnetic behaviour observed for γ-$[Fe_2(imid)_4(bipy)]_x$ or, at least, contribute significantly to it.

In an effort to determine the onset of the magnetic transition in γ-$[Fe_2(imid)_4(bipy)]_x$ the temperature dependence of the field-cooled magnetization (FCM), zero-field-cooled magnetization (ZFCM) and remnant magnetization (REM) were examined (Figure 5.14). The FCM curve, measured by cooling the sample under a DC field of 50 G, shows a clear increase in *M* in the 6 – 8 K region. On further cooling, this curve exhibits a maximum in the 2 – 3 K region. The derivative curve, d(FCM)/dT, has an extremum at 3.5 K, which can be considered as the critical temperature, T_c [8]. The ZFCM curve, measured by cooling the sample in zero field, then warming in a DC field of 50 G, exhibits a maximum at ~ 3 K and is significantly lower than the FCM curve at this temperature and at lower temperatures. The derivative curve, d(ZFCM)/dT, shows an extremum at 4.0 K. Thus, Tc for this system, as measured by the FCM-ZFCM experiment, can be considered as T_c = 3.75 K, which is the average temperature of those obtained from the FCM and ZFCM plots. Finally, REM, obtained by cooling the sample in a 50 G DC field, then collecting the data while warming it in zero field vanishes at a slightly higher temperature (at 5 K, as confirmed by looking at the data obtained) than T_c, which agrees better with the T_c determined by AC susceptibility measurements of γ-$[Fe_2(imid)_4(bipy)]_x$, shown below.

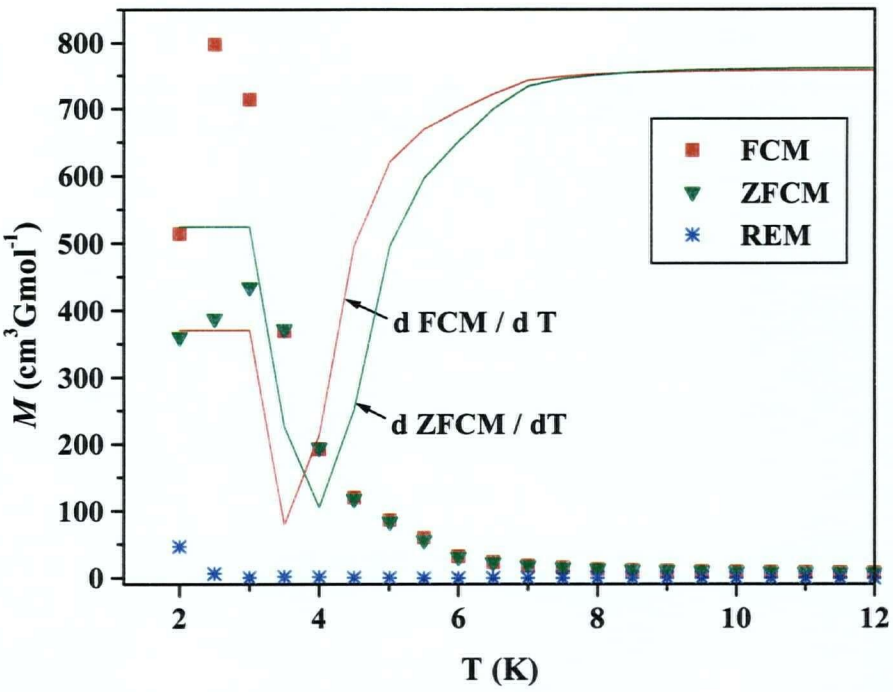

Figure 5.14 Plots of ZFCM, FCM and REM for γ-$[Fe_2(imid)_4(bipy)]_x$ at a DC field of 50 G.

Further information on the magnetic phase transition of γ-$[Fe_2(imid)_4(bipy)]_x$ can be deduced from AC magnetic susceptibility measurements. The in-phase, χ', and out-of-phase, χ", AC molar magnetic susceptibilities, with a zero static field and a 125 Hz oscillating field of 1 G, for γ-$[Fe_2(imid)_4(bipy)]_x$ are displayed in Figure 5.15. χ" is non-zero below 6.1 K, which is in agreement with the onset of a magnetic transition at that temperature. χ' and χ" peak at 5.8 and 5.7 K, respectively, proving the material γ-$[Fe_2(imid)_4(bipy)]_x$ is a genuine magnet at these temperatures.

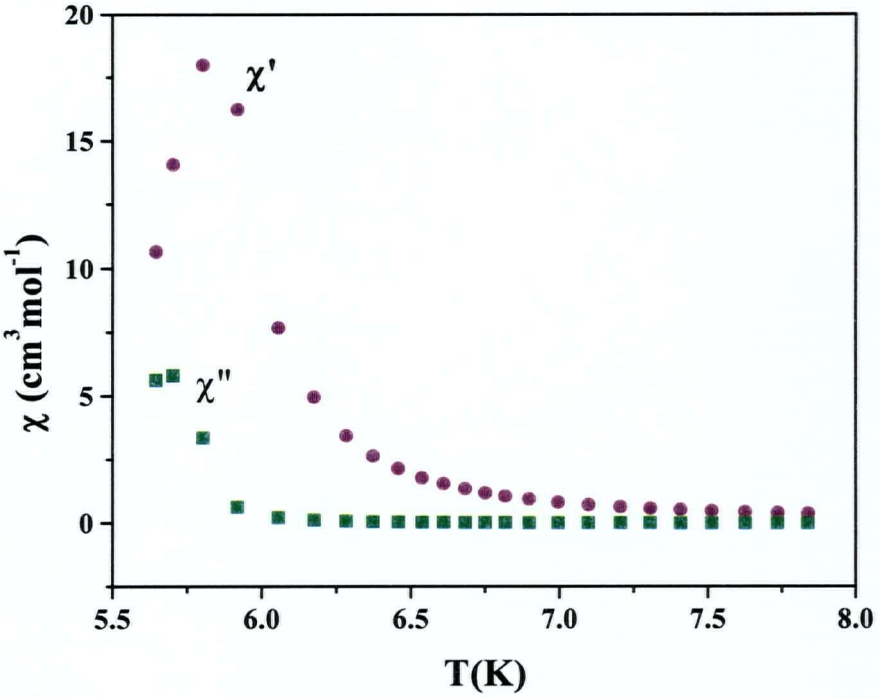

Figure 5.15 Temperature dependences of the in-phase, χ', and out-of-phase, χ'', AC magnetic susceptibilities for γ-$[Fe_2(imid)_4(bipy)]_x$ at f =125 Hz and H = 1 G.

In an effort to better characterize the structural phase transitions that occur in $[Fe_2(imid)_4(bipy)]_x$ detailed AC and DC magnetic susceptibilities measurements were made over the appropriate temperature ranges. It is the first time such studies have been made on a molecule-based magnet. The χT (DC) versus T plot, shown in Figure 5.16, reveals two inflections in the 130 – 160 K region following a cooling mode, the higher

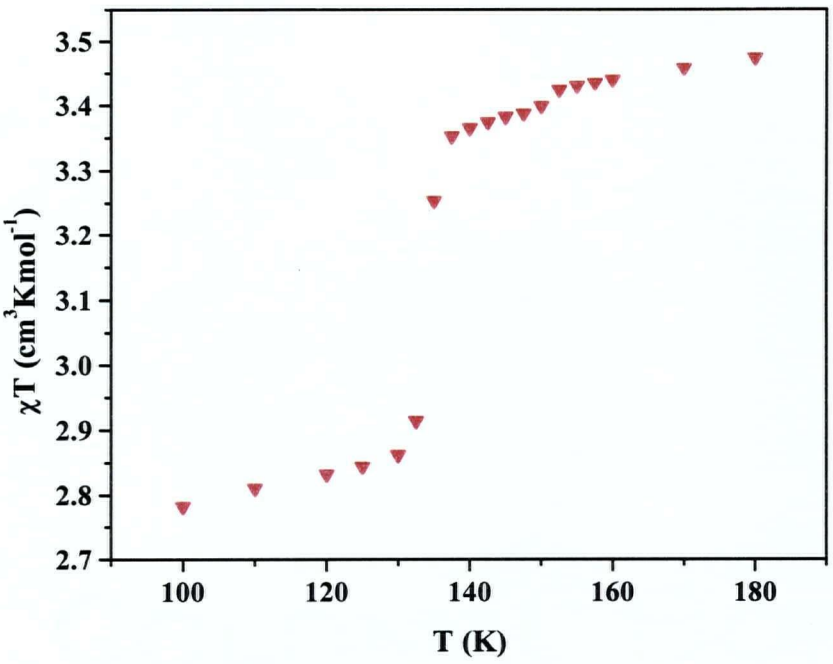

Figure 5.16 χT versus T for $[Fe_2(imid)_4(bipy)]_x$. H_{DC} = 10 000 G. Cooling mode.

temperature anomaly being less evident than the lower one. In order to determine the transition temperatures accurately, the temperature dependence of the derivative $d(\chi T)/dT$, in the cooling mode, was calculated and plotted as shown in Figure 5.17. This gave transition temperatures of 150 K for the $\alpha \rightarrow \beta$ transition and 135 K for the $\beta \rightarrow \gamma$ transition.

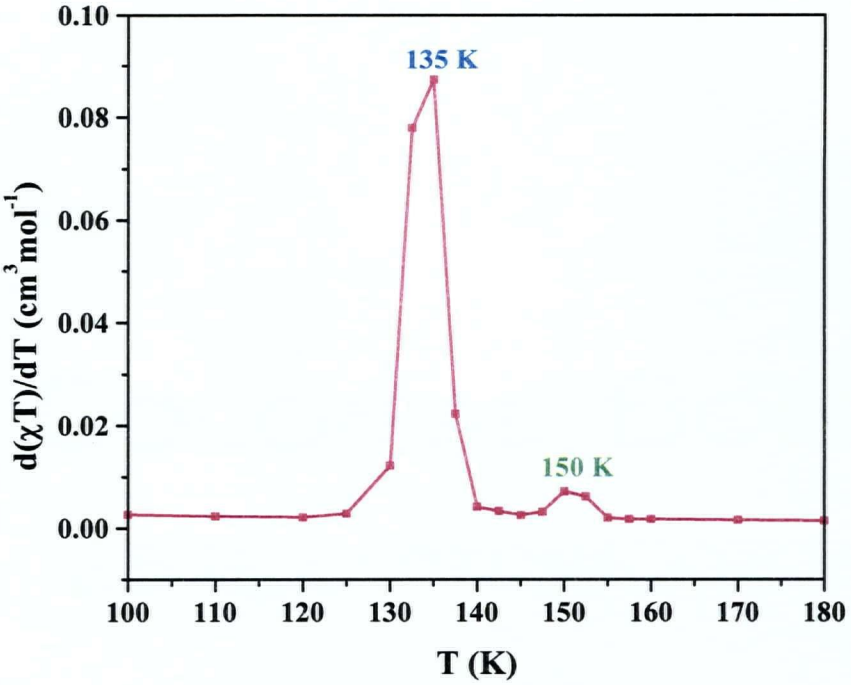

Figure 5.17 Temperature dependence of the derivatives d(χT)/dT (DC) in the cooling mode and determination of the transition temperatures for $[Fe_2(imid)_4(bipy)]_x$. H_{DC} = 10 000 G.

Further details on the two phase transitions occurring in $[Fe_2(imid)_4(bipy)]_x$, were obtained from DC magnetic susceptibility measurements in both, cooling and warming modes. Also, for higher accuracy, a higher-density data acquisition was carried out close to the phase transition temperature ranges. A DC field of 1 000 G was utilized in these studies with the hope of obtaining a better resolution of the high temperature phase transition. In Figure 5.18 the temperature-dependence of χT (100 – 190 K) is shown. As the temperature is lowered (cooling mode), χT is decreases

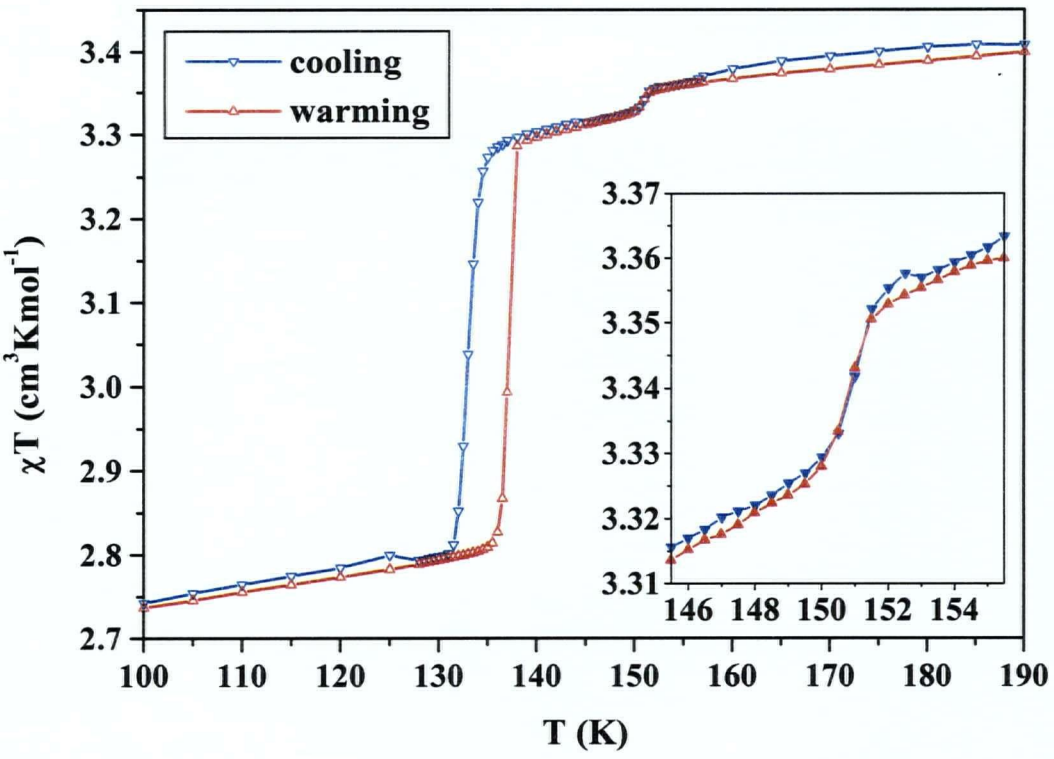

Figure 5.18 Cooling and warming modes χT versus temperature plots for $[Fe_2(imid)_4(bipy)]_x$. H_{DC}= 1 000 G. Insert plot shows an augmentation of the $\alpha \leftrightarrow \beta$ transition region.

slightly until it reaches a temperature of ~ 152 K, it then decreases abruptly until ~ 150 K ($\alpha \rightarrow \beta$) attaining a "plateau" between ~ 150 – ~ 138 K. Finally, χT diminishes abruptly between the temperatures of ~ 138 K and ~ 132 K ($\beta \rightarrow \gamma$) before "levelling off" again. As the temperature is increased (warming mode), the temperature where the χT rises sharply is shifted by ~ 5 K to ~ 137 K, giving rise to the hysteretic behaviour

shown in Figure 5.18. Hence, thermal hysteresis is evident for the low-temperature transition ($\gamma \leftrightarrow \beta$). This low temperature phase transition, occurring with thermal hysteresis, may be considered as being a first order transition [9]. Above 137 K, and following a warming mode, χT increases gradually, following the cooling curve in this region reasonably closely. The χT then increases abruptly over the 150 to 152 K region, again following the cooling mode closely, the abrupt change corresponding to the $\beta \rightarrow \alpha$ transition. In contrast to the $\beta \leftrightarrow \gamma$, there appears to be no significant hysteresis associated with the $\beta \leftrightarrow \alpha$ transition.

We note that above and below each of these transitions the data obtained in the warming mode are slightly below those obtained in the cooling mode. This could be because the $\alpha \rightarrow \beta$ and $\beta \rightarrow \gamma$ transitions involve cooperative interaction between chromophores which cause the final stages of the conversion to occur very slowly. Hence at each temperature studied on cooling a small amount of the higher temperature phase remains. On warming, at each temperature there is less of the high temperature phase "impurity" present and hence the χT value is slightly lower. This could of course be tested by allowing long periods (longer than 15 minutes allowed in the standard run) between collecting data points on cooling. In view of the relative minor effect observed, and the cost of doing the extended time runs, these experiments were not performed.

In order to determine the transition temperatures more accurately, the temperature dependence of the derivative $d(\chi T)/dT$, in the cooling and warming modes

[10], was calculated and plotted as shown in Figure 5.19. This gave transition temperatures of 151 K for the $\alpha \leftrightarrow \beta$ transition, and 135 K for the $\beta \leftrightarrow \gamma$ transition, the latter with a thermal hysteresis width of 4 K (133 – 137 K).

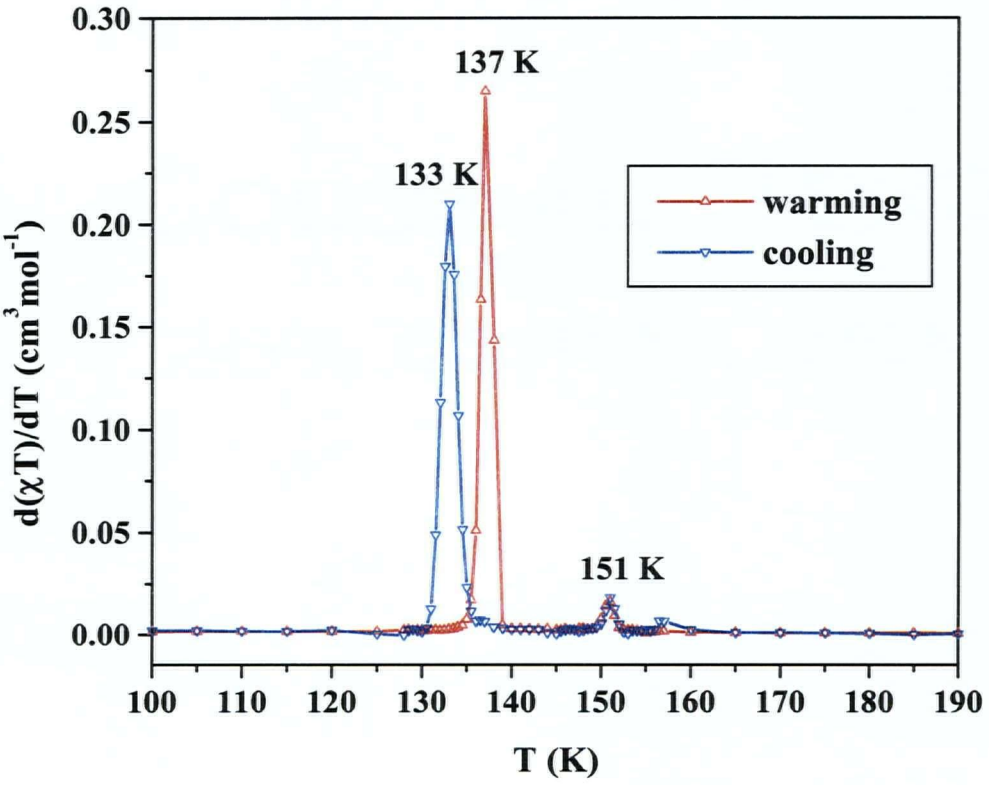

Figure 5.19 Temperature dependence of the derivatives d(χT)/dT (DC) in the cooling and warming modes and determination of the transition temperatures for $[Fe_2(imid)_4(bipy)]_x$. H_{DC} = 1 000 G.

A high-density AC magnetic susceptibility measurement study was also performed for the $\beta \leftrightarrow \gamma$ structural phase transition. χ versus temperature data, in the cooling mode, are shown in Figure 5.20. As in the DC magnetic susceptibility

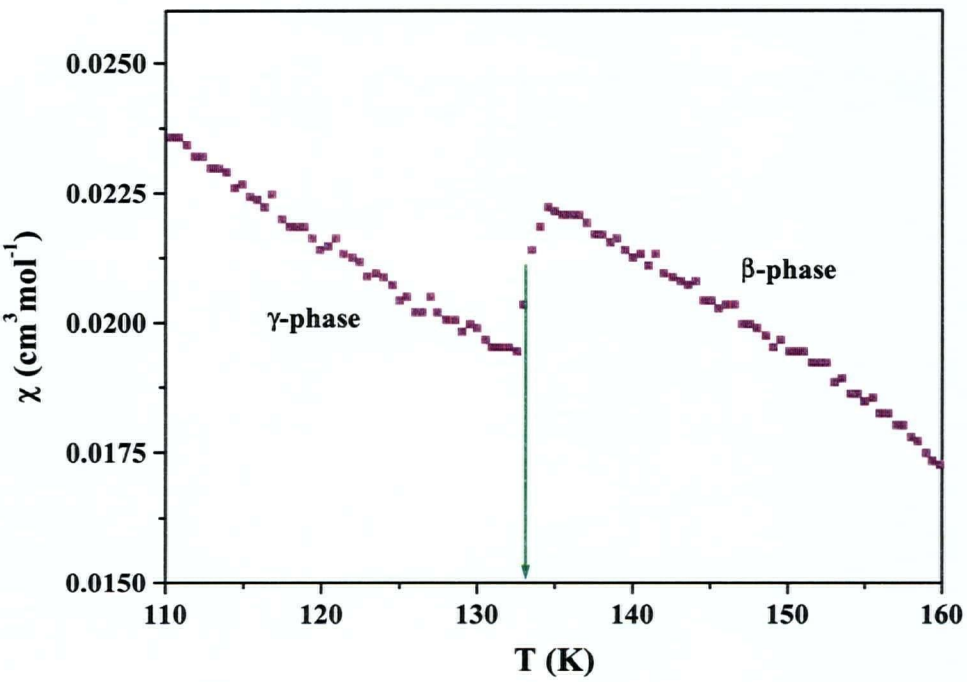

Figure 5.20 AC χ versus T plot for $[Fe_2(imid)_4(bipy)]_x$. Cooling mode. f = 500 Hz, H_{AC} = 2.5 G.

measurements, a break in the plot appears between 135 K and 132 K. Meanwhile, in the warming mode plot (Figure 5.21) the anomaly is shifted to higher temperatures, appearing between 135 K and 139 K. The thermal hysteresis of the low-temperature phase transition of $[Fe_2(imid)_4(bipy)]_x$ is also confirmed by the plot of χT (AC) versus T as shown in Figure 5.22. As before, transition temperatures may be determined more

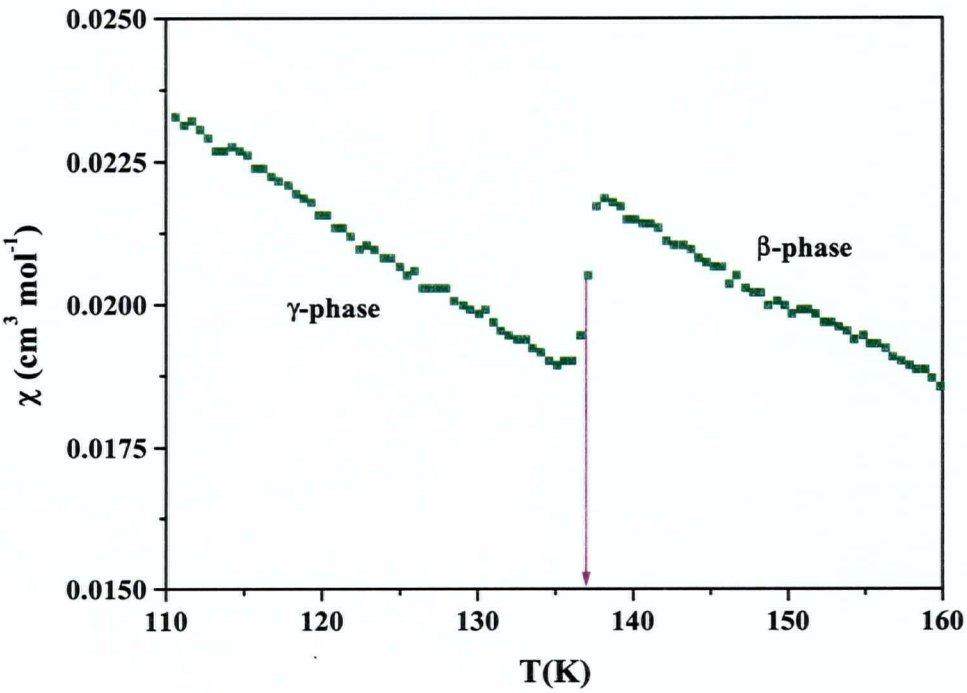

Figure 5.21 AC χ versus T plot for $[Fe_2(imid)_4(bipy)]_x$. Warming mode. f = 500 Hz, H_{AC} = 2.5 G.

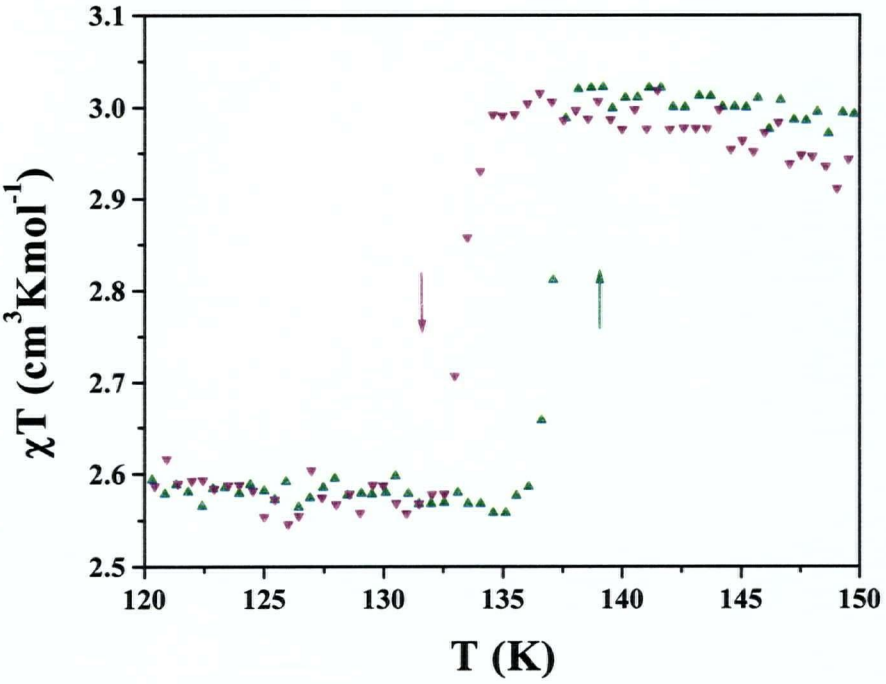

Figure 5.22 Temperature dependence of AC χT in the cooling and warming modes for $[Fe_2(imid)_4(bipy)]_x$. f = 500 Hz, H_{AC} = 2.5 G. Arrow down refers to cooling mode, arrow up refers to warming mode.

accurately from the extremes of the temperature dependences of the derivatives $d(\chi T)/dT$ in both the cooling and the warming mode [10]. This is shown in Figure 5.23. These transition temperatures are found to be 133 K in the cooling mode and 137 K in the warming mode in total agreement with the temperatures determined by the DC susceptibility measurements (*vide supra*). Hence, the width of the thermal hysteresis in the $\beta \leftrightarrow \gamma$ transition is 4 K.

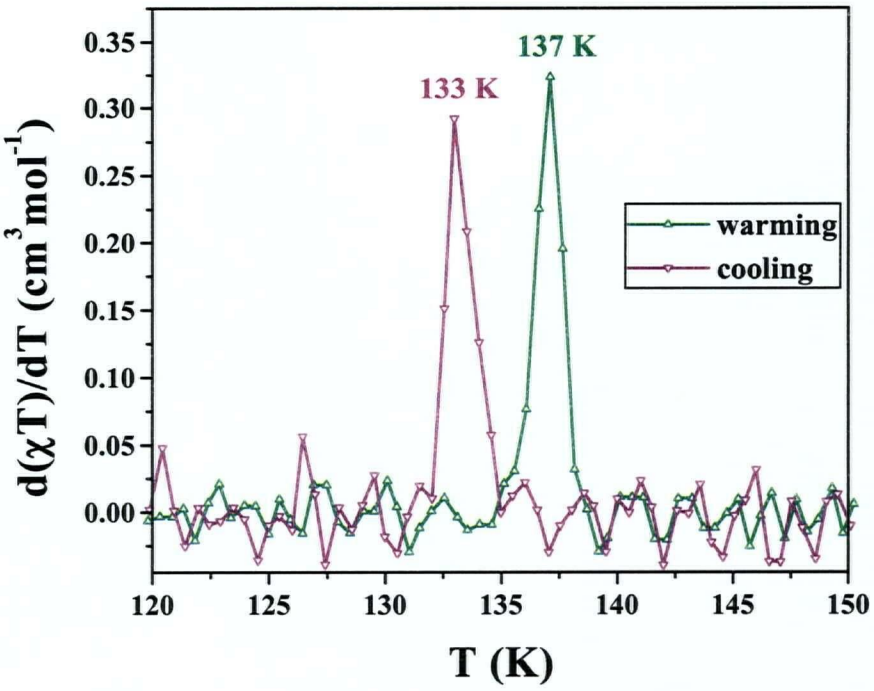

Figure 5.23 Temperature dependence of the derivatives d(χT)/dT (AC) in the cooling and warming modes and determination of the transition temperatures for the γ-phase of $[Fe_2(imid)_4(bipy)]_x$. f = 500 Hz, H_{AC} = 2.5 G.

In an attempt to study the $\alpha \leftrightarrow \beta$ transition in more detail, AC magnetic susceptibility measurements were carried out in the temperature range from 131 K to 171 K in both cooling and warming modes. Unfortunately, as seen in Figure 5.24, only the $\beta \leftrightarrow \gamma$ transition (showing hysteresis) was detected but no other anomaly was found in the cooling or warming mode corresponding to the $\alpha \leftrightarrow \beta$ transition. Apparently the difference in the magnetic properties between the α and β forms is too small to be observed in the AC measurements.

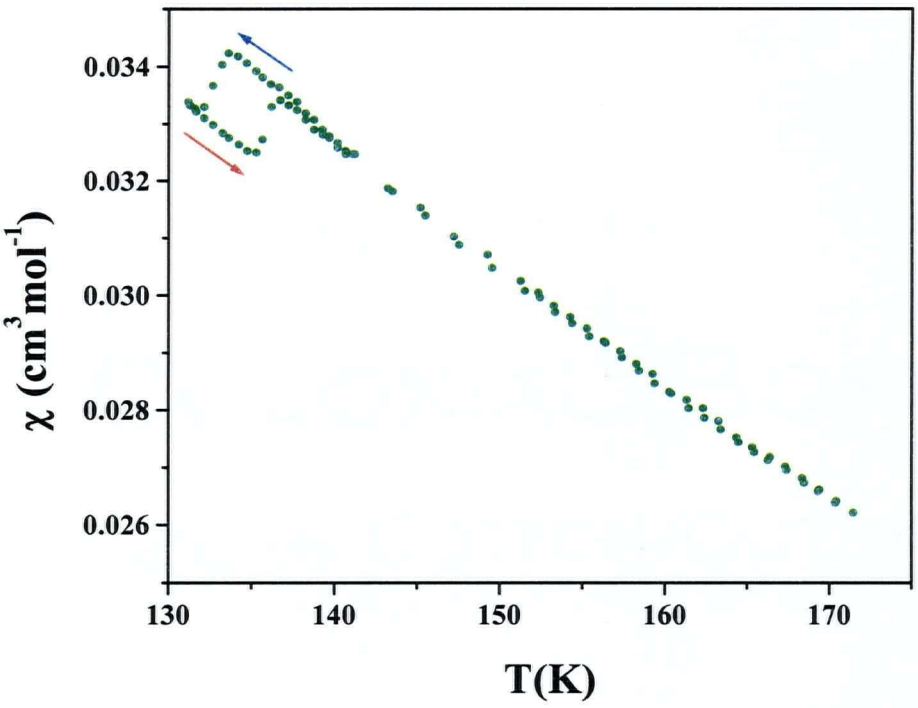

Figure 5.24 Cooling and warming mode AC χ versus temperature plots for $[Fe_2(imid)_4(bipy)]_x$. f = 500 Hz, H_{AC} = 2.5 G.

5.2.1.4 MÖSSBAUER SPECTROSCOPY

The room temperature Mössbauer spectrum of $[Fe_2(imid)_4(bipy)]_x$ (Figure 5.25) corresponds to two overlapping quadrupole doublets consistent with the X-ray

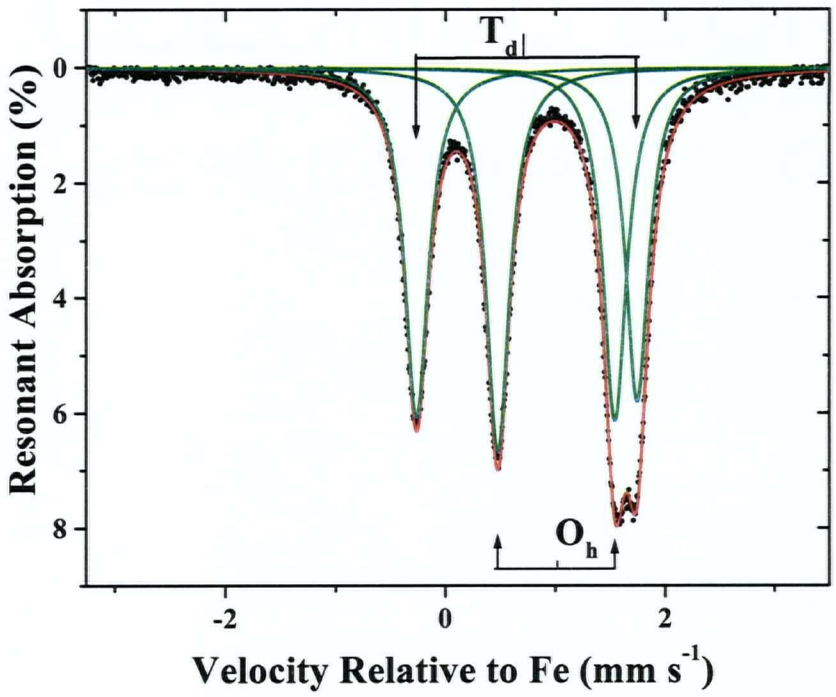

Figure 5.25 Mössbauer spectrum of $[Fe_2(imid)_4(bipy)]_x$ at 293 K.

crystallography results at that temperature, that indicate equal population of distorted six-and four-coordinate sites. The Mössbauer parameters obtained herein for the nominal T_d and O_h sites at 293K are: isomer shifts (δ) of 0.74 mm s^{-1} and 1.01 mm s^{-1}, and quadrupole splittings (ΔE) of 2.01 mm s^{-1} and 1.06 mm s^{-1}, respectively, values fairly characteristic of high-spin iron(II) with "all" nitrogen ligation [11]. ΔE values are not reliably diagnostic of coordination number for high-spin ferrous complexes. The

splitting value ranges can often overlap for four, five and six coordination environments (even with similar ligands) depending on the degree of distortion of the local coordination environment. On the other hand, isomer shifts have been found to be quite sensitive to coordination number for fixed spin state and similar ligation. Specifically, for spin quintet iron(II) with nitrogen or mixed nitrogen - halogen ligation, δ values for six coordination generally range from ~ +1.0 to 1.2 mm s^{-1} [11-13]; five-coordination from ~+0.85 to 0.95 mm s^{-1} [13-15] and four-coordination from ~ +0.70 to 0.85 mm s^{-1} [16] at room temperature. Hence, the present δ values in combination with the available literature results appear to unequivocally confirm the six- and four-coordinate nature of the iron of $[Fe_2(imid)_4(bipy)]_x$.

The structural phase transitions occurring in $[Fe_2(imid)_4(bipy)]_x$ were also examined meticulously with Mössbauer spectroscopy. In fact, the high-temperature transition ($\alpha \leftrightarrow \beta$) of $[Fe_2(imid)_4(bipy)]_x$ was first found using this spectroscopic technique, and later confirmed with the X-ray diffraction and DC susceptibility studies as already described. A set of Mössbauer spectra for $[Fe_2(imid)_4(bipy)]_x$, determined in the warming mode from 145.5 K to 175.1 K, is shown in Figure 5.26. According to this study the low-temperature ($\beta \leftrightarrow \gamma$) phase transition occurs between about 146.9 and 148.3 K, while the high-temperature phase transition occurs between about 160.2 and 167.7 K (Figure 5.26).

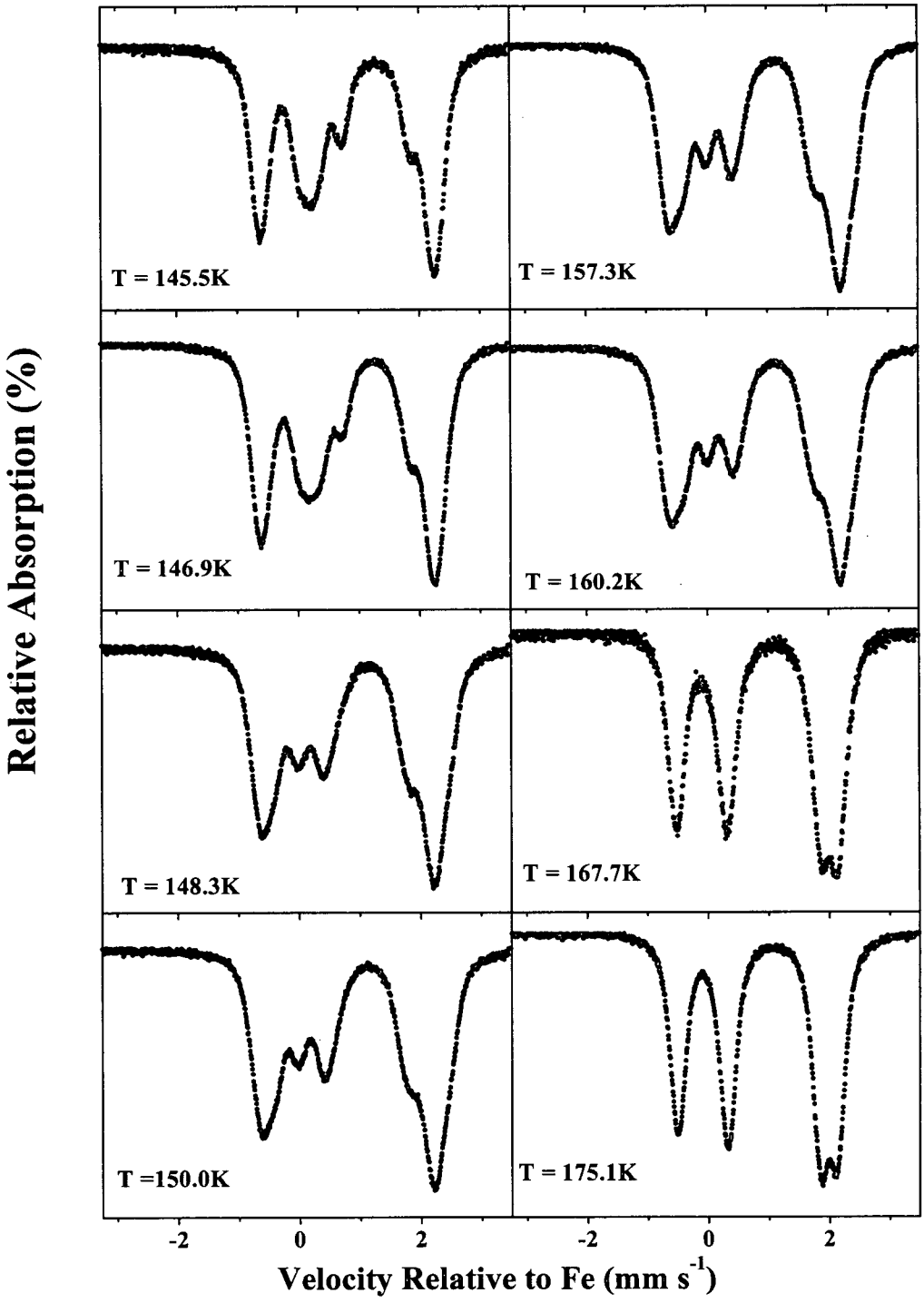

Figure 5.26 Mössbauer spectra in the warming mode for $[Fe_2(imid)_4(bipy)]$.

After heating a sample of $[Fe_2(imid)_4(bipy)]_x$ to 169.7 K, Mössbauer spectra were measured from 165.1 to 129.9 K (cooling mode). As shown in Figure 5.27, the data indicate that the high-temperature phase transition occurs between 165.1 and 162.7 K, while, the low-temperature phase transition occurs between 144.9 and 139.9 K. In the Mössbauer study, the low-temperature transition exhibits hysteresis of around 3 to 5 K and the high-temperature transition exhibits no significant hysteresis, in qualitative agreement with the AC and DC magnetic susceptibility studies. However, both structural phase transitions appear to occur at ~ 10 K higher than indicated by the DC and AC susceptibility studies. There is not a straightforward explanation for this, although, a possible explanation may involve the different time-scale of Mössbauer spectroscopy. It seems the microscopic Mössbauer effect detects the two phase transitions "earlier" than the bulk AC and DC magnetic susceptibility measurements in the cooling mode. However, in the warming mode, AC and DC susceptibility measurements detect the transitions "earlier" (*vide supra*). This situation may also be an experimental effect regarding these techniques. Mössbauer measurements were done on mulls while the AC and DC susceptibility measurements were performed on crystalline solids, which could be the source of the different phase transition detection temperatures.

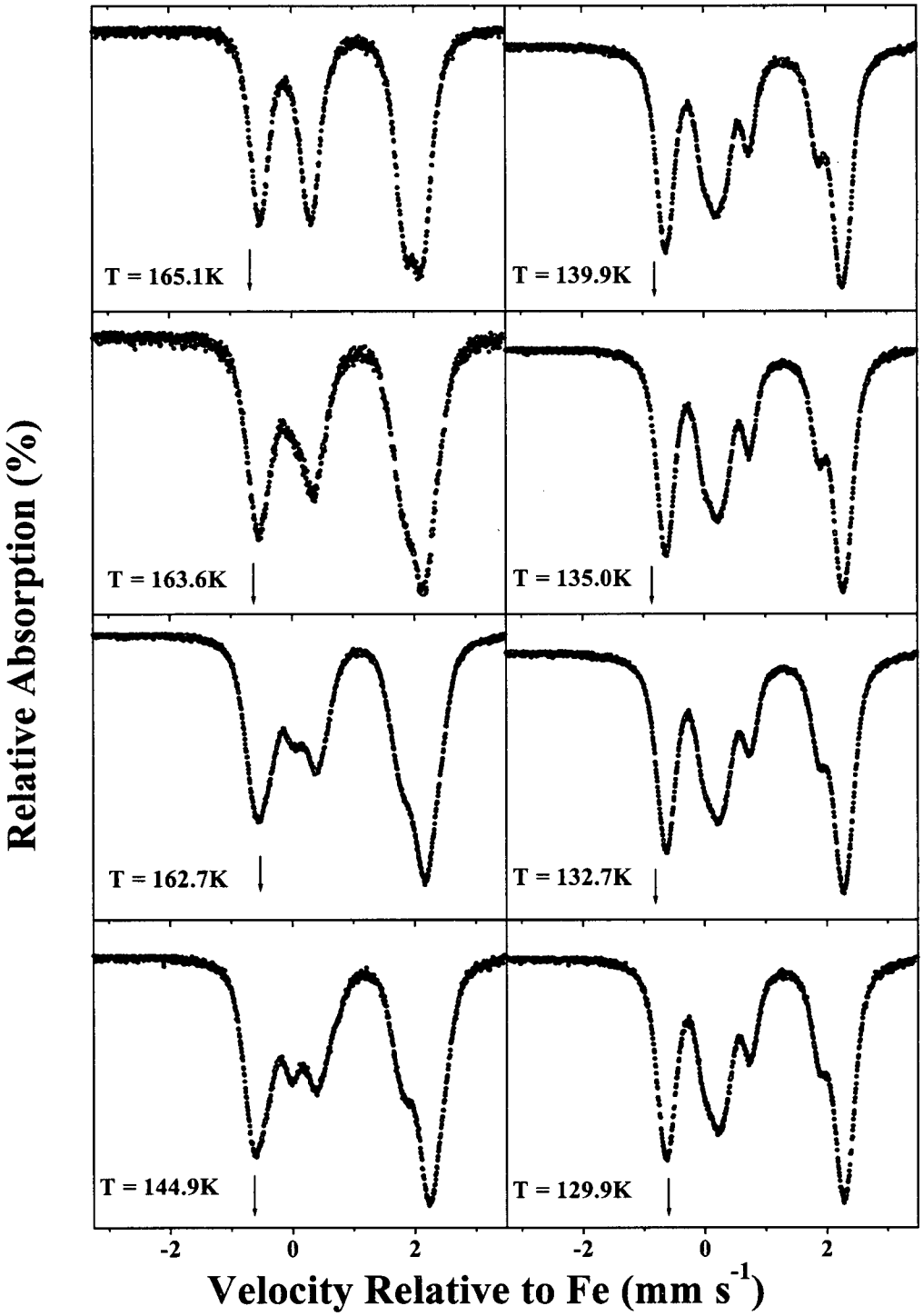

Figure 5.27 Mössbauer spectra in the cooling mode for $[Fe_2(imid)_4(bipy)]_x$.

5.3 POLY-2,2'-BIPYRIDINETETRAKIS(IMIDAZOLATO)DICOBALT(II)

5.3.1 RESULTS AND DISCUSSION

5.3.1.1 SYNTHESIS, THERMAL AND STRUCTURAL CHARACTERIZATION

The reaction of cobaltocene with imidazole and excess molten 2,2'-bipyridine generated, $[Co_2(imid)_4(bipy)]_x$, as a microcrystalline powder. Details of this reaction are given in Chapter 9, section 9.2.2.7.

Although this material could not be obtained in a form suitable for single crystal X-ray diffraction studies, it was possible to show by powder diffraction studies that it is isomorphous and probably isostructural with the room temperature form of $[Fe_2(imid)_4(bipy)]_x$. The X-ray powder diffractogram of $[Co_2(imid)_4(bipy)]_x$ coincides well with that calculated from the single-crystal data of $[Fe_2(imid)_4(bipy)]_x$ obtained at room temperature, employing the program PowderCell [17] (Figure 5.28). Indexing the X-ray powder diffractogram of $[Co_2(imid)_4(bipy)]_x$ using the program Celref [18], generated the lattice parameters: a = 10.521, b = 13.729 and c = 9.181 Å. These are very similar to the room temperature lattice parameters obtained for α-$[Fe_2(imid)_4(bipy)]_x$ (a = 10.507, b = 13.730 and c = 9.188 Å). The room temperature infrared spectra of α-$[Fe_2(imid)_4(bipy)]_x$ and $[Co_2(imid)_4(bipy)]_x$ were also found to exhibit the same vibrational bands at almost the same frequencies.

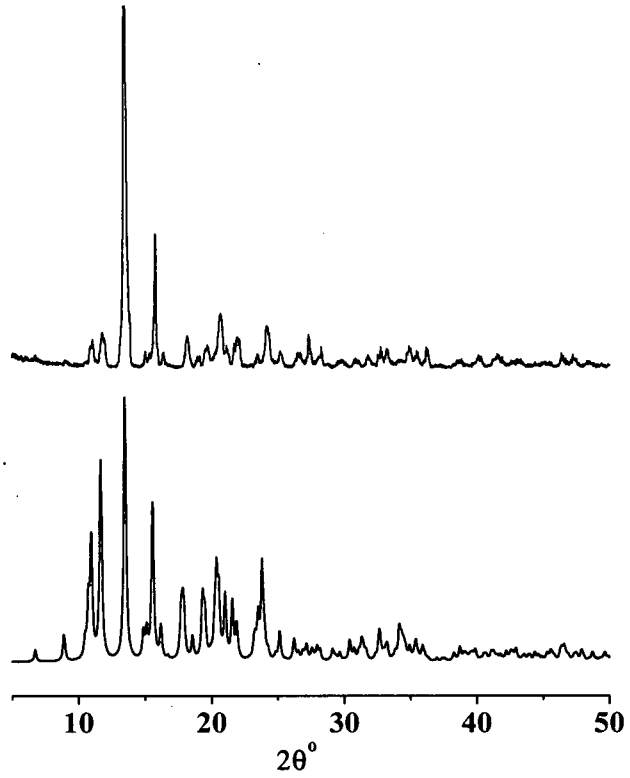

Figure 5.28 X-Ray powder diffractograms of $[Co_2(imid)_4(bipy)]_x$ (top, experimental) and $[Fe_2(imid)_4(bipy)]_x$ (bottom, calculated).

In contrast to the iron(II) analogue, $[Co_2(imid)_4(bipy)]_x$ is air-stable, but both compounds have properties consistent with polymeric structures, for example $[Co_2(imid)_4(bipy)]_x$ does not dissolve in common organic solvents and it is non-volatile. A thermal gravimetric study performed on the Co(II) material gave no evidence for decomposition until ~ 250 °C (Figure 5.29). The TGA plot follows a two step weight

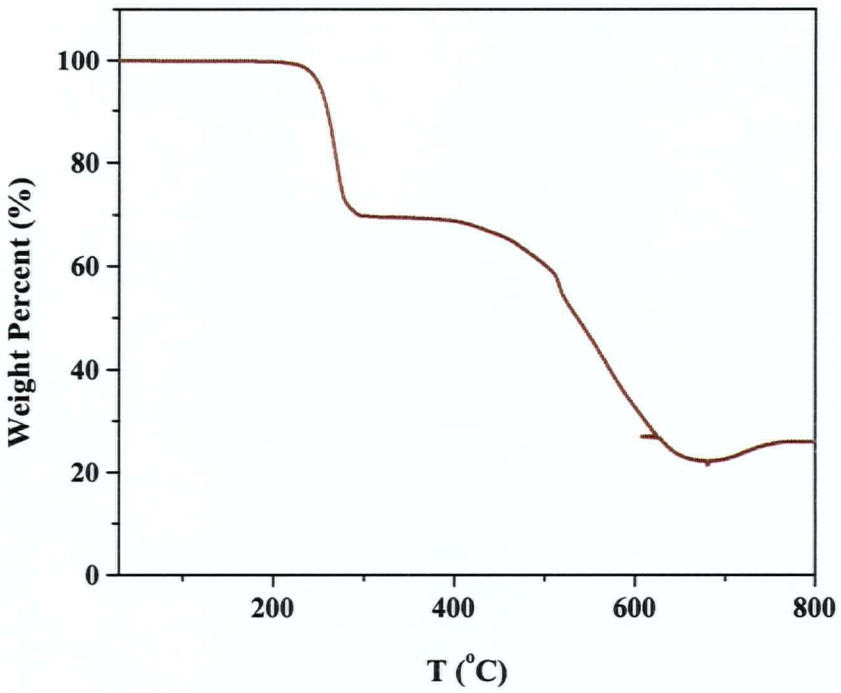

Figure 5.29 TGA plot for $[Co_2(imid)_4(bipy)]_x$.

loss profile and resembles that of $[Fe_2(imid)_4(bipy)]_x$. The first major weight loss (~ 30 %) occurs between 225 °C and 300 °C, and the second one, with a weight loss of ~ 47 % of the initial weight, happens between 390 °C and 660 °C. A weight percentage of ~ 25 % remains at the highest temperature studied, 800 °C. In contrast to the TGA plot of $[Fe_2(imid)_4(bipy)]_x$, there is a plateau between 300 °C and 390 °C in the plot for $[Co_2(imid)_4(bipy)]_x$. This plateau seems to correspond to the formation of $[Co(imid)_2]_x$ by loss of the bipyridine ligand (~ 29 %) in the first step of the thermal decomposition. A similar situation occurred when the thermal gravimetric study of

$[Co_3(imid)_6(imidH)_2]_x$ was carried out and $[Co(imid)_2]_x$ was obtained by the loss of the neutral imidazole molecules (Chapter 4, section 4.2).

5.3.1.2 MAGNETIC PROPERTIES

A noticeable difference in the magneto-structural behaviour of $[Co_2(imid)_4(bipy)]_x$ versus $[Fe_2(imid)_4(bipy)]_x$ is that whereas the latter shows a discontinuity in the μ_{eff} versus temperature plot at 135 K (Figure 5.9), no equivalent discontinuity is observed for $[Co_2(imid)_4(bipy)]_x$ (Figure 5.30). The cobalt derivative does not appear to undergo the structural phase transitions exhibited by $[Fe_2(imid)_4(bipy)]_x$. Otherwise the magnetic properties of $[Co_2(imid)_4(bipy)]_x$ parallel those of $[Fe_2(imid)_4(bipy)]_x$.

For $[Co_2(imid)_4(bipy)]_x$, the value of μ_{eff}, measured at an applied field of 500 G, decreases with decreasing temperature from 4.35 μ_B at 300 K to 2.89 μ_B at 13 K. Below 13 K it increases abruptly, signaling the onset of long-range ferromagnetic ordering (Figure 5.31). This magnetic behaviour is also seen in the χ versus T plot for the compound which shows an incipient maximum in χ just above 13 K and an abrupt rise in χ below this temperature. As the temperature is lowered further to 2 K, χ tends to saturation (Figure 5.31). Studies at an applied field of 10 000 G (Figure 5.30) show a less prominent increase in χ and μ_{eff} below T_c than observed in the 500 G data. This

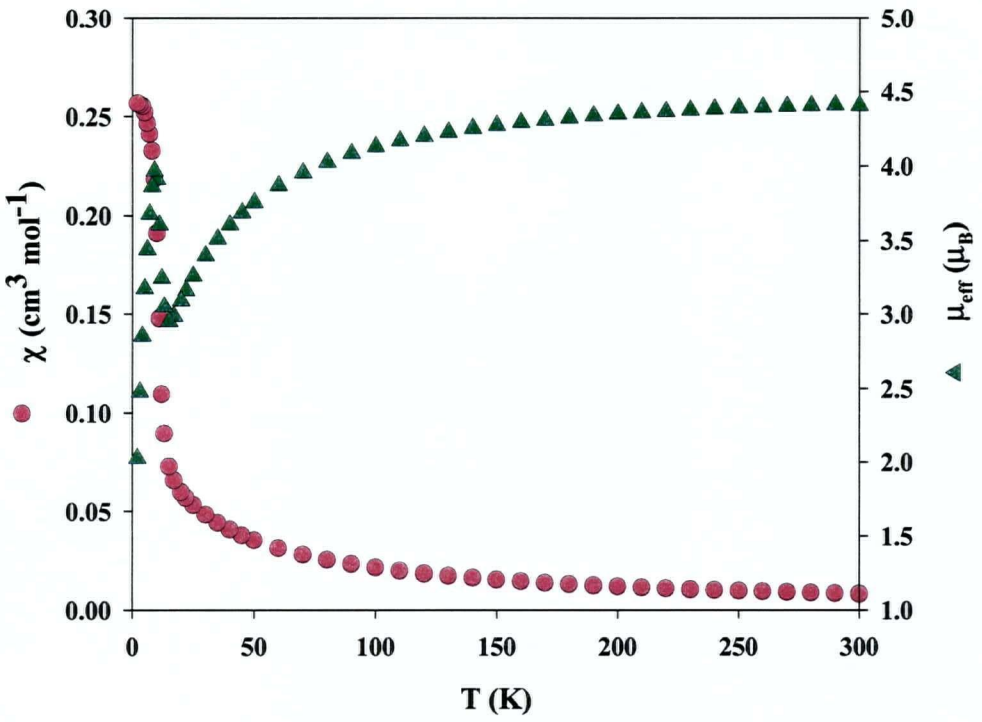

Figure 5.30 χ and μ_{eff} versus T plots at 10 000 G for $[Co_2(imid)_4(bipy)]_x$.

resembles the behaviour observed for $[Fe_2(imid)_4(bipy)]_x$. Nonetheless, for both $[Fe_2(imid)_4(bipy)]_x$ and $[Co_2(imid)_4(bipy)]_x$ the magnetic transition is clearly observed at this higher field (Figures 5.9 and 5.30, respectively).

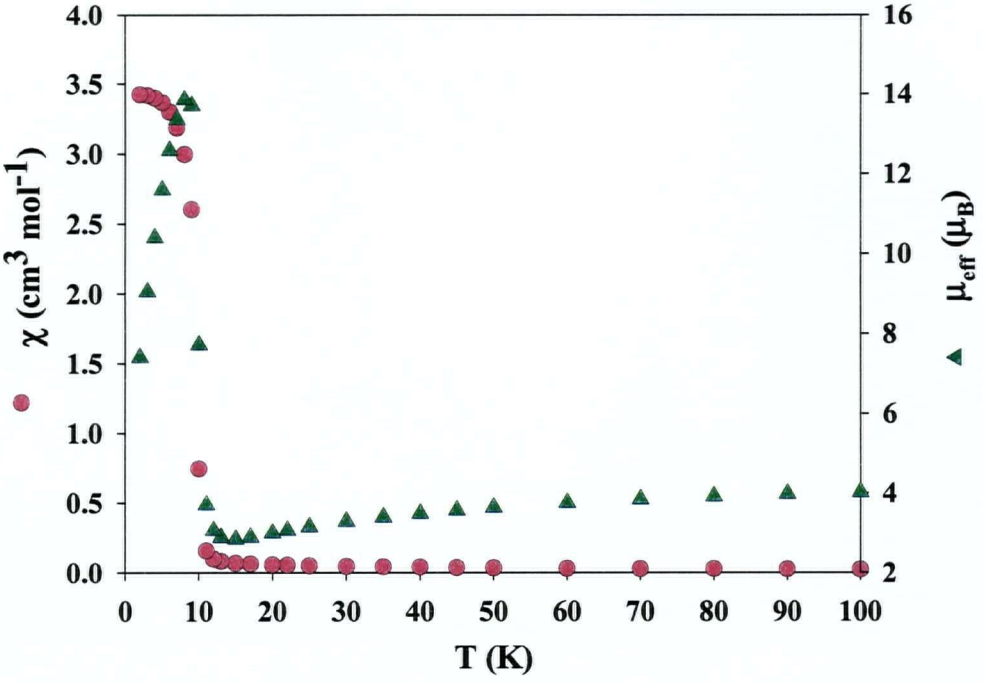

Figure 5.31 χ and μ_{eff} versus T plots at 500 G for $[Co_2(imid)_4(bipy)]_x$.

The effect of the low temperature magnetic transition in $[Co_2(imid)_4(bipy)]_x$ is seen in the magnetization versus applied field plots at different temperatures (Figure 5.32). At 4.8 K the plot is non-linear and, in contrast to the higher temperature plots, it does not extrapolate to zero at zero applied field. Cycling the applied field between +55 000 and –55 000 G at 4.8 K generates a hysteresis loop (Figure 5.33) from which a

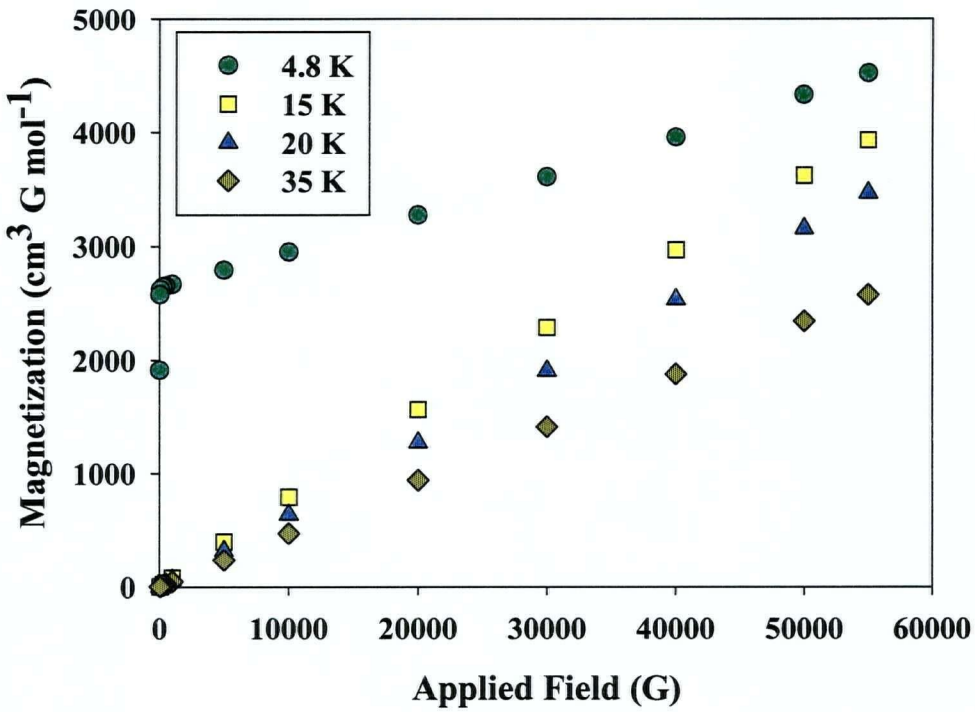

Figure 5.32 Magnetization versus applied field plots at different temperatures for $[Co_2(imid)_4(bipy)]_x$.

coercive field of 125 G and a remnant magnetization of 1900 cm^3Gmol^{-1} are obtained. A plot of χ^{-1} versus T (10 000 G data) is linear over the temperature range 300 – 25 K and a Curie-Weiss analysis of this data yields C = 2.64 cm^3Gmol^{-1} and θ = -25 K (Figure 5.34). As discussed above for $[Fe_2(imid)_4(bipy)]_x$, overall these magnetic

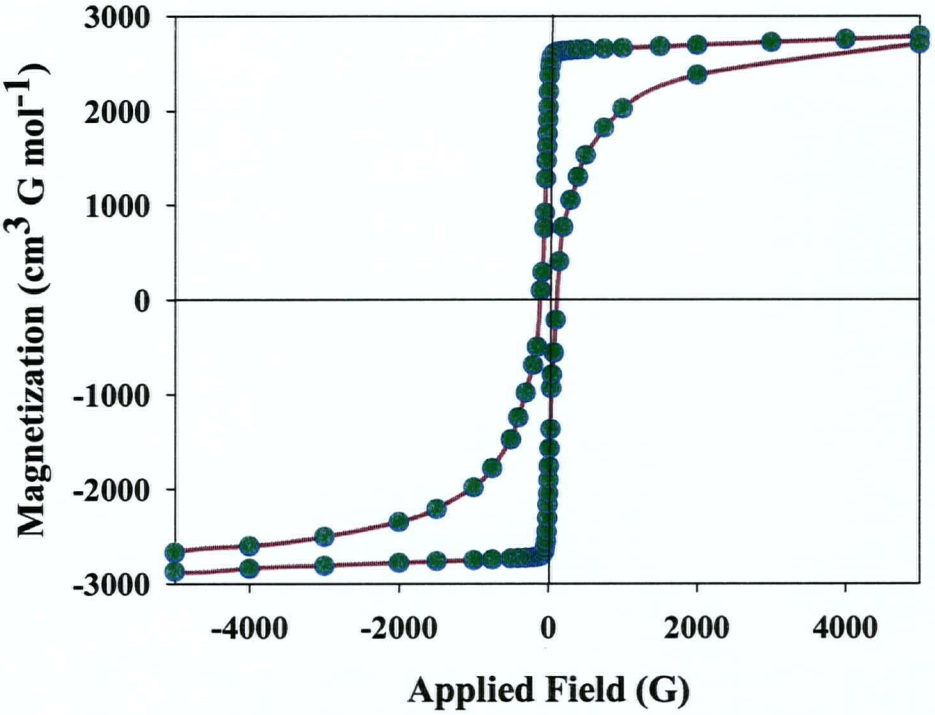

Figure 5.33 Magnetic hysteresis plots at 4.8 K for $[Co_2(imid)_4(bipy)]_x$.

properties classify $[Co_2(imid)_4(bipy)]_x$ as a weak ferromagnet. However, it should be noted that, since $[Co_2(imid)_4(bipy)]_x$ contains high spin octahedral d^7 metal centers and since such centres have first order orbital effects contributing to their magnetism, the comments made above concerning the interpretation of θ values for $[Fe_2(imid)_4(bipy)]_x$ apply here also.

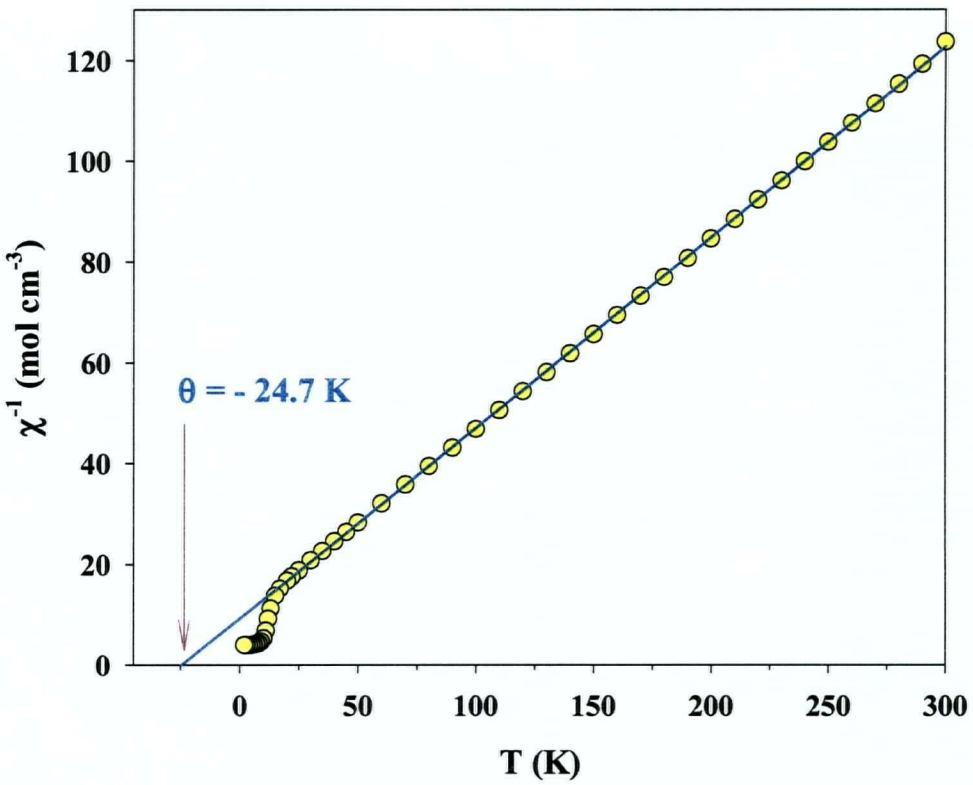

Figure 5.34 Plot of χ^{-1} versus temperature at 10 000 G for $[Co_2(imid)_4(bipy)]_x$.

The highest magnetization measured for $[Co_2(imid)_4(bipy)]_x$ (4 515 cm^3Gmol^{-1} at 4.8 K and 55 000 G) is significantly lower than the theoretical saturation value (16 766 cm^3Gmol^{-1} for a S = 3/2 system [5]). As discussed above for $[Fe_2(imid)_4(bipy)]_x$, this result is not inconsistent with spin canting or ferrimagnetic exchange providing the source of the residual spin at low temperatures.

Extrapolation of the M versus H plot to $H = 0$ on the magnetization curve obtained at 4.8 K (Figure 5.32), yields the spontaneous magnetization, $M_s(O) = 2640$ cm^3Gmol^{-1}. From this, the canting angle is calculated as described previously for $[Fe_2(imid)_4(bipy)]_x$, to be $\gamma \sim 9°$.

That this polymer behaves as a magnet below T_c is confirmed by the shape of the ZFCM, FCM and REM plots in Figure 5.35. The zero-field-cooled magnetization (ZFCM) under an applied field of 50 G showed a maximum at 9.0 K. The field-cooled magnetization (FCM) under an applied field of 50 G increased rapidly below 10 K to a maximum value of ~ 1370 cm^3Gmol^{-1} at 2 K (Figure 5.35). When the applied field was switched off at 2 K a remnant magnetization of ~ 1190 cm^3Gmol^{-1} remained that decreased upon warming and vanished at ~ 10 K. No ambiguities are found in these plots, in contrast to the ones for $[Fe_2(imid)_4(bipy)]_x$ where the derivative of the plots had to be calculated in order to estimate T_c. Thus, the temperatures for the highest slope of the FCM plot, the peak on the ZFCM plot, and the temperature at which REM vanishes, are all within the range between 9.0 and 10 K. Hence, the critical temperature of $[Co_2(imid)_4(bipy)]_x$ is determined as $T_c = 9.5$ K [8]. This temperature is in reasonably agreement with the onset temperature (~ 13 K) of the long-range magnetic ordering determined by DC susceptibility.

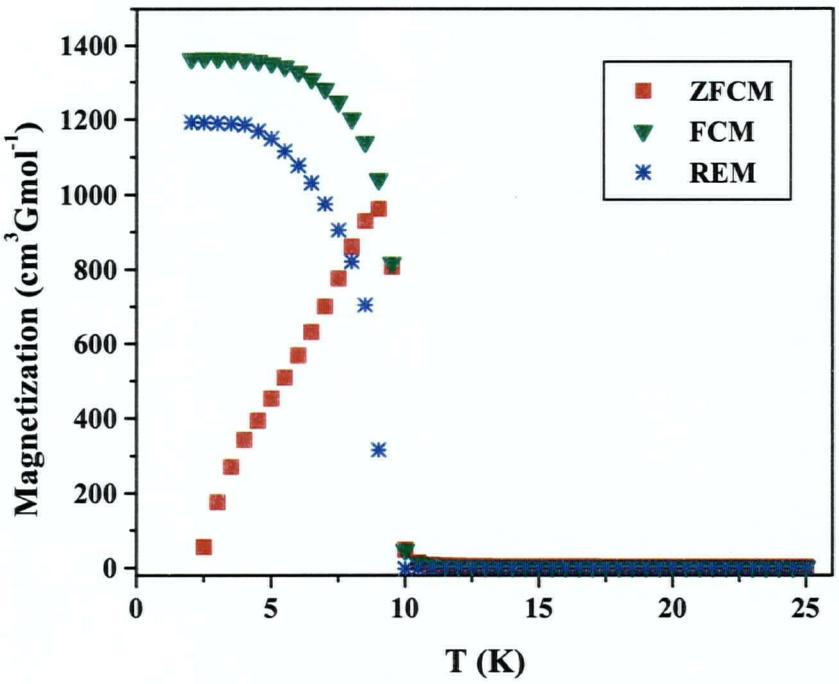

Figure 5.35 Plots of ZFCM, FCM and REM for $[Co_2(imid)_4(bipy)]_x$ using a DC field of 50 G.

5.4 SUMMARY AND CONCLUSIONS

$[Fe_2(imid)_4(bipy)]_x$, and the isomorphous cobalt compound, $[Co_2(imid)_4(bipy)]_x$, have 2-D extended structures in which double layered sheets of alternating tetrahedrally and octahedrally coordinated metal ions are linked by single bridging imidazolates. The octahedral metal centers are additionally coordinated by 2,2'-bipyridine ligands which occupy positions between the sheets, isolating the sheets from each other. The presence

of the two different iron centers in $[Fe_2(imid)_4(bipy)]_x$ is confirmed by ambient temperature Mössbauer studies.

The magnetic properties of these materials reveal a transition to long-range ferromagnetic order below 6 K for $[Fe_2(imid)_4(bipy)]_x$ and below 9.5 K for $[Co_2(imid)_4(bipy)]_x$. Both materials reveal magnetic hysteresis at 4.8 K. Analysis of the data yield, for $[Fe_2(imid)_4(bipy)]_x$ and $[Co_2(imid)_4(bipy)]_x$ respectively, coercive fields of 15 and 125 G and remnant magnetizations of 200 and 1900 cm^3Gmol^{-1}. Magnetic parameters for three pairs of analogous iron(II) and cobalt(II) imidazolate compounds, including γ-$[Fe_2(imid)_4(bipy)]_x$ and $[Co_2(imid)_4(bipy)]_x$, which exhibit weak ferromagnetism are shown in Table 5.1. For each pair, H_{coer} is always greater for the cobalt system suggesting cobalt magnets are generally harder than analogous iron ones. In contrast to what might have been expected it seems that the magnet strength, as measured by M_{rem}, is not a simple function of the number of unpaired electrons or canting angle. While the cobalt material has the highest M_{rem} in one pair it has the lower M_{rem} in the other two. Moreover, while the low M_{rem} for $[Co(4\text{-abimid})_2]_x$ seems consistent with a low canting angle (Chapter 3), the canting angle for $[Co_2(imid)_4(bipy)]_x$ is lower than that of its iron analogue yet the M_{rem} is greater for the cobalt system.

$[Fe_2(imid)_4(bipy)]_x$ is unique in presenting two structural phase transitions, at ~ 151 K and ~ 135 K, as determined by DC and AC magnetic susceptibility

Table 5.1 Magnetic parameters for three pairs of analogous iron(II) and cobalt(II) weak ferromagnets.

Compound	H_{coer} (G)	M_{rem} (cm^3Gmol^{-1})	Ref.
γ-$Fe_2(imid)_4(bipy)$	15	200	This Chapter
$Co_2(imid)_4(bipy)$	125	1900	This Chapter
$Fe(4\text{-abimid})_2$	80	2100	Chapter 3
$Co(4\text{-abimid})_2$	400	22	Chapter 3
$Fe_3(imid)_6(imidH)_2$	200	2000	[1]
$Co_3(imid)_6(imidH)_2$	4 140	175	Chapter 4

Abbreviations: imid = imidazolate, 4-abimid = 4-azabenzimidazolate, bipy = 2,2'-bipyridine.

measurements. These structural phase transitions have also been studied in detail by Mössbauer spectroscopy. These studies yielded transition temperatures of ~ 10 K higher than those determined by magnetic studies. Thermal hysteresis behavior is evident for

the low-temperature phase transition ($\beta \leftrightarrow \gamma$) as determined by DC and AC susceptibility as well as Mössbauer spectroscopy. Single crystal X-ray diffraction studies at 113 K and 143 K revealed that while the crystal integrity was retained, as well as the basic double layer structural motif found in the room temperature α-phase, there were significant changes in cell and bond parameters for the β- and γ-phases of $[Fe_2(imid)_4(bipy)]_x$.

To the author's knowledge this is the first time that two phase transitions have been detected in a molecule-based magnetic material ($[Fe_2(imid)_4(bipy)]_x$) and studied in detail by a combination of X-ray crystallography, AC and DC magnetic susceptibility measurements and Mössbauer spectroscopy.

References

1. S. J. Rettig, A. Storr, D. A. Summers, R. C. Thompson, and J. Trotter, *J Amer. Chem. Soc.* **119**, 8675 (1997).

2. S. J. Rettig, A. Storr, D. A. Summers, R. C. Thompson, and J. Trotter, *Can J. Chem.* **77**, 425 (1999).

3. S. J. Rettig, V. Sánchez, A. Storr, R. C. Thompson, and J. Trotter, *J. Chem. Soc., Dalton Trans.* 3931 (2000).

4. O. Kahn. *Molecular Magnetism.* VCH. New York. 1993. p. 321.

5. R. L. Carlin. *Magnetochemistry.* Springer-Verlag. Berlin. 1986. pp. 7-9.

6. F. Palacio, M. Andres, R. Horne, and A. J. van Duyeneveldt. J. Magn. Magn. Mater. **54-57**, 1487 (1986).

7. S. J. Rettig, V. Sánchez, A. Storr, R. C. Thompson, and J. Trotter. Inorg. Chem. **38**, 5920 (1999).

8. O. Kahn. *Acc. Chem. Res. 33* (10) 647 (2000).

9. C. N. R. Rao, and K. J. Rao. *Phase Transitions in Solids. An Approach to the Study of the Chemistry and Physics of Solids.* McGraw-Hill. London. 1978. pp. 17 – 24.

10. Y. Garcia, O. Kahn, L. Rabardel, B. Chansou, L. Salmon, and J. P. Tuchagues. *Inorg. Chem.* **38**, 4663 (1999).

11. N. N. Greenwood, and T. C. Gibb. *Mössbauer Spectroscopy.* Chapman and Hall Ltd. London. 1971.

12. B. W. Dockum, and W. M. Reiff. *Inorg. Chim.* Acta. **35**, 285 (1979).

13. F. F. Charron, and W. M. Reiff. *Inorg. Chem.* **25**, 2786 (1986).

14. W. M. Reiff, N. E. Erickson, and W. A. Baker. *Inorg. Chem.* **8**, 2119 (1969).

15. D. Sedney, M. Kahjehnassiri, and W. M. Reiff. *Inorg. Chem.***20**, (1981) 3476.

16. B. W. Dockum, and W. M. Reiff. *Inorg. Chim. Acta.* **120**, 61 (1986).

17. PowderCell, version 2.3, W. Krauss and G. Nolze, Federal Institute for Materials Research and Testing (BAM), Berlin, 1997.

18. LMGP-Suite of Programs for Interpretation of X-Ray Experiments, by Jean Laugiert and Bernard Bochu, ENSP/Laboratoire des Matériaux et du Génie Physique. BP 46. 38042 Saint Martin d'Hères, France. http://www.inpg.fr/LMGP and htpp://www.ccp14.ac.uk/tutorial/lmgp/.

Chapter 6 *POLY-2,2':6',2"-TERPYRIDINEOCTAKIS(IMIDAZOLATO)-TETRAIRON(II). A VERY SOFT 2-D MOLECULE-BASED MAGNET*

6.1 INTRODUCTION

The remarkable influence of 2,2'-bipyridine on the structures of the iron(II) and cobalt(II) imidazolate polymers was described in the previous chapter. The effect of their structural dimensionality on the physical and magnetic properties of these 2-D polymers, encouraged the investigation of similar systems utilizing a different neutral multi-dentate ligand, namely 2,2':6',2"-terpyridine (terpy). It was expected that, by virtue of the tridentate meridional coordination mode of terpy, the considerable geometric demands of this ligand might influence the structure of transition metal imidazolate polymers, in a similar way to the bipy ligand, yielding further examples of interesting two-dimensional extended systems.

The title compound, $[Fe_4(imid)_8(terpy)]_x$, was synthesized by the reaction of ferrocene with imidazole in the presence of terpyridine in a sealed tube at elevated temperatures. This polymer has a novel 2-D extended structure, as determined by an X-ray crystallography study, in which wrinkled sheets of four-coordinate (two unique centers of this type), five-coordinate and six-coordinate iron(II) ions are linked by

single bridging imidazolates. The presence of the four unique iron sites is confirmed by Mössbauer spectroscopy.

DC magnetic susceptibility measurements reveal antiferromagnetic interactions between metal centers above about 12 K, and the onset of a transition to a ferromagnetic state below this temperature. Long-range ferromagnetic ordering below T_c = 6.5 K is confirmed by AC magnetic susceptibility, zero-field-cooled magnetization and Mössbauer studies. A very unique hysteresis loop, determined by field-dependant magnetization studies, show the material to be a very soft molecule-based magnet.

6.2 RESULTS AND DISCUSSION

6.2.1 SYNTHESIS AND PHYSICAL PROPERTIES

Details of the synthesis of $[Fe_4(imid)_8(terpy)]_x$ are described in Chapter 9, section 9.2.1.4. Ferrocene, imidazole and terpyridine were sealed under vacuum in a Carius tube and the mixture was heated. The desired compound was isolated as green crystals suitable for X-ray crystallography.

$[Fe_4(imid)_8(terpy)]_x$ appeared to be moisture sensitive but could be handled briefly under normal atmospheric conditions. Powdered samples of this compound would turn red upon exposure to air for around a week. The compound is insoluble in

common organic solvents. The TGA plot obtained for $[Fe_4(imid)_8(terpy)]_x$ (Figure 6.1) shows the thermal robustness of this compound. There is no apparent decomposition of

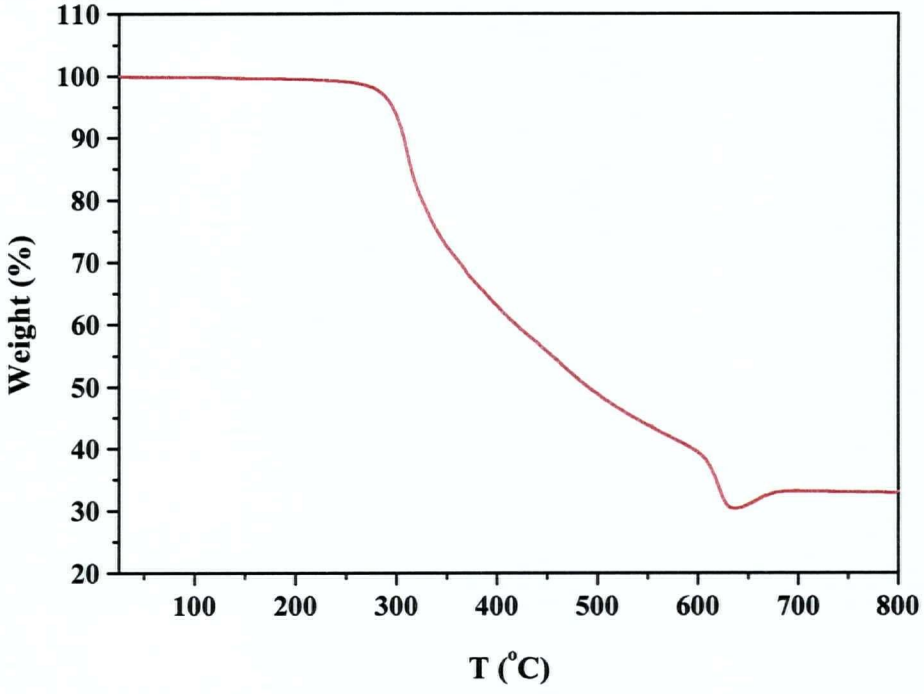

Figure 6.1 TGA plot of $[Fe_4(imid)_8(terpy)]_x$.

this polymer until a temperature of 270 °C is reached. A decrease in weight is observed between 270 °C and 630 °C, with ~ 69 % of the initial weight lost at the highest temperature. The thermal decomposition behavior shown by $[Fe_4(imid)_8(terpy)]_x$ is very similar to that exhibited by $[Fe_2(imid)_6(bipy)]_x$ (Chapter 5, section 5.2.1.1.)

6.2.2 X-RAY DIFFRACTION STUDIES

Single crystal X-ray diffraction studies reveal $[Fe_4(imid)_8(terpy)]_x$ to be comprised of distorted tetrahedral (two unique chromophores of this type), distorted trigonal bipyramidal and distorted octahedral iron(II) ions linked by single bridging imidazolates (Figure 6.2), forming a novel 2-D extended structure resembling wrinkled sheets (Figures 6.3, 6.4 and 6.5). Crystallographic data, atom coordinates, selected bond lengths and angles appear in Appendix I, Tables I-10 and I-11.

The six-coordinated metal centers are coordinated by bridging imidazolate ligands and terpy ligands (Figure 6.2) that occupy positions between the sheets, isolating the sheets from each other, as can be seen in Figure 6.3. This capping of iron centres by terpy controls the dimensionality, resulting in a 2-D polymer (Figure 6.3), in a manner similar to that observed in $[Fe_2(imid)_6(bipy)]_x$. An iron ion connectivity picture of a section of the structure of $[Fe_4(imid)_8(terpy)]_x$ is given in Figure 6.5.

The use of terpy to influence the structural dimensionality has been reported recently for hybrid metal oxides extended systems [1]. However, no reports on the presence of three different iron(II) chromophore geometries in the same coordination compound, were found in the literature.

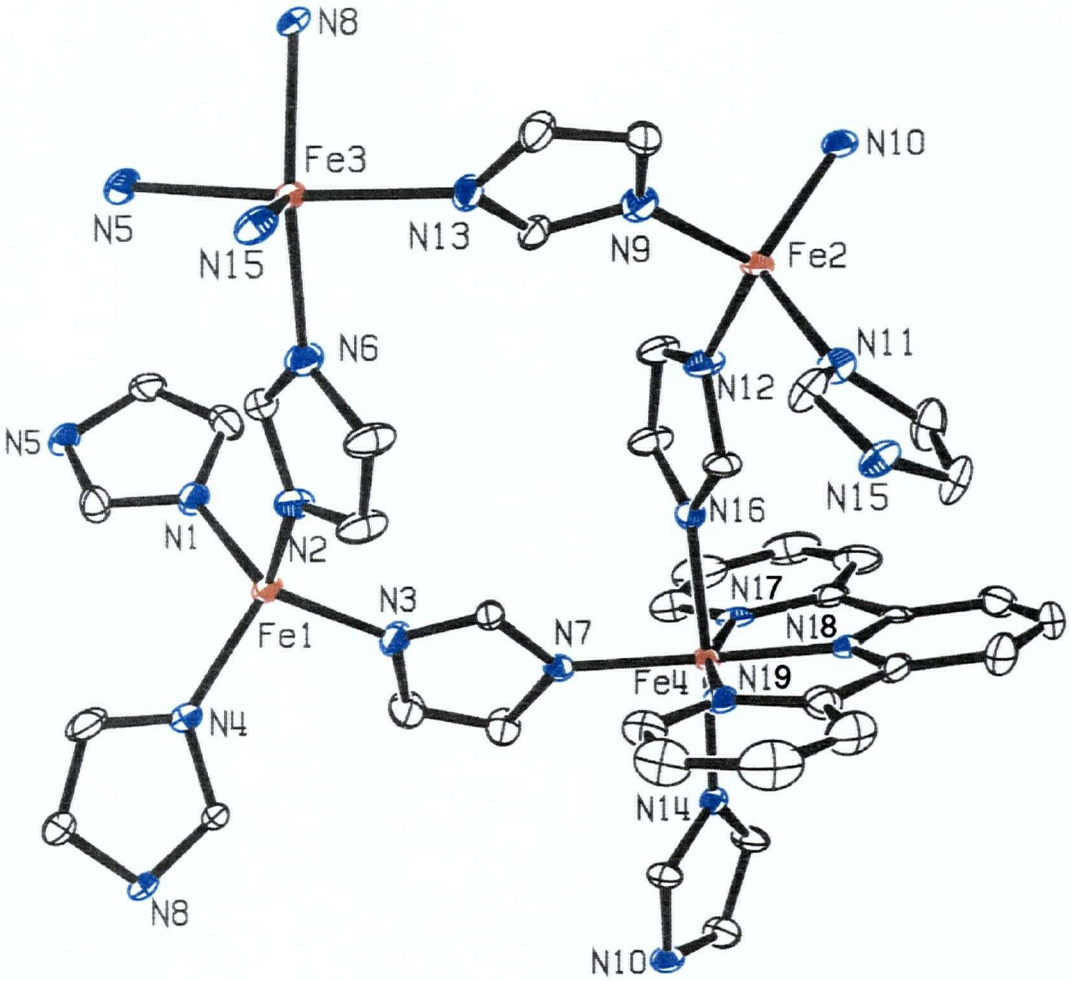

Figure 6.2 Repeat unit of $[Fe_4(imid)_8(terpy)]_x$ showing the atom numbering scheme; 33 % probability thermal ellipsoids are shown.

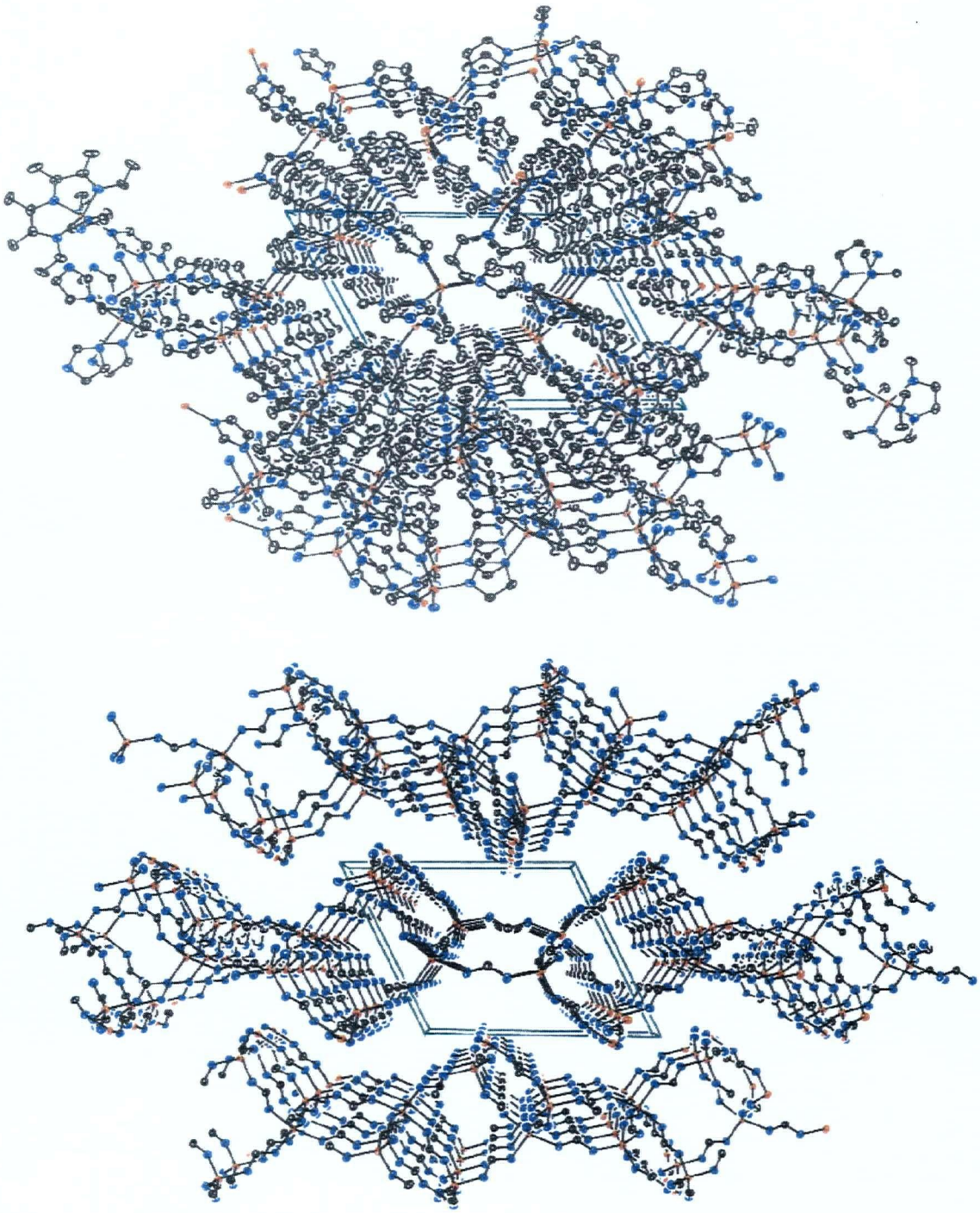

Figure 6.3 View of a section of $[Fe_4(imid)_8(terpy)]_x$ looking down the *a* axis. Terpy ligands and C-4 and C-5 of imidazolate ligands have been omitted in the bottom view for clarity. Hydrogen atoms are not shown.

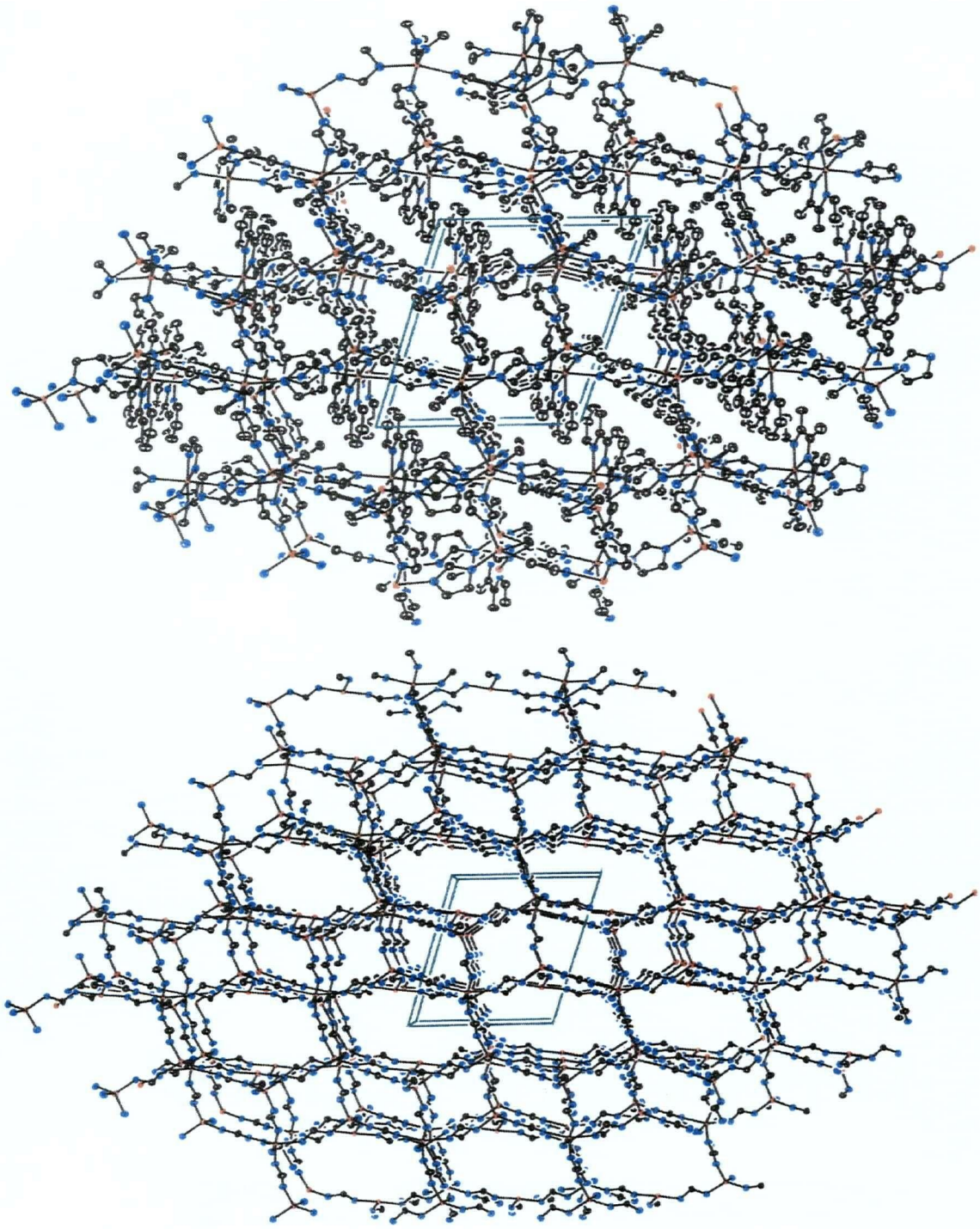

Figure 6.4 View of a section of $[Fe_4(imid)_8(terpy)]_x$ looking down the *b* axis. For clarity, terpy ligands and C-4 and C-5 of imidazolate ligands have been omitted in the bottom view. Hydrogen atoms are not shown.

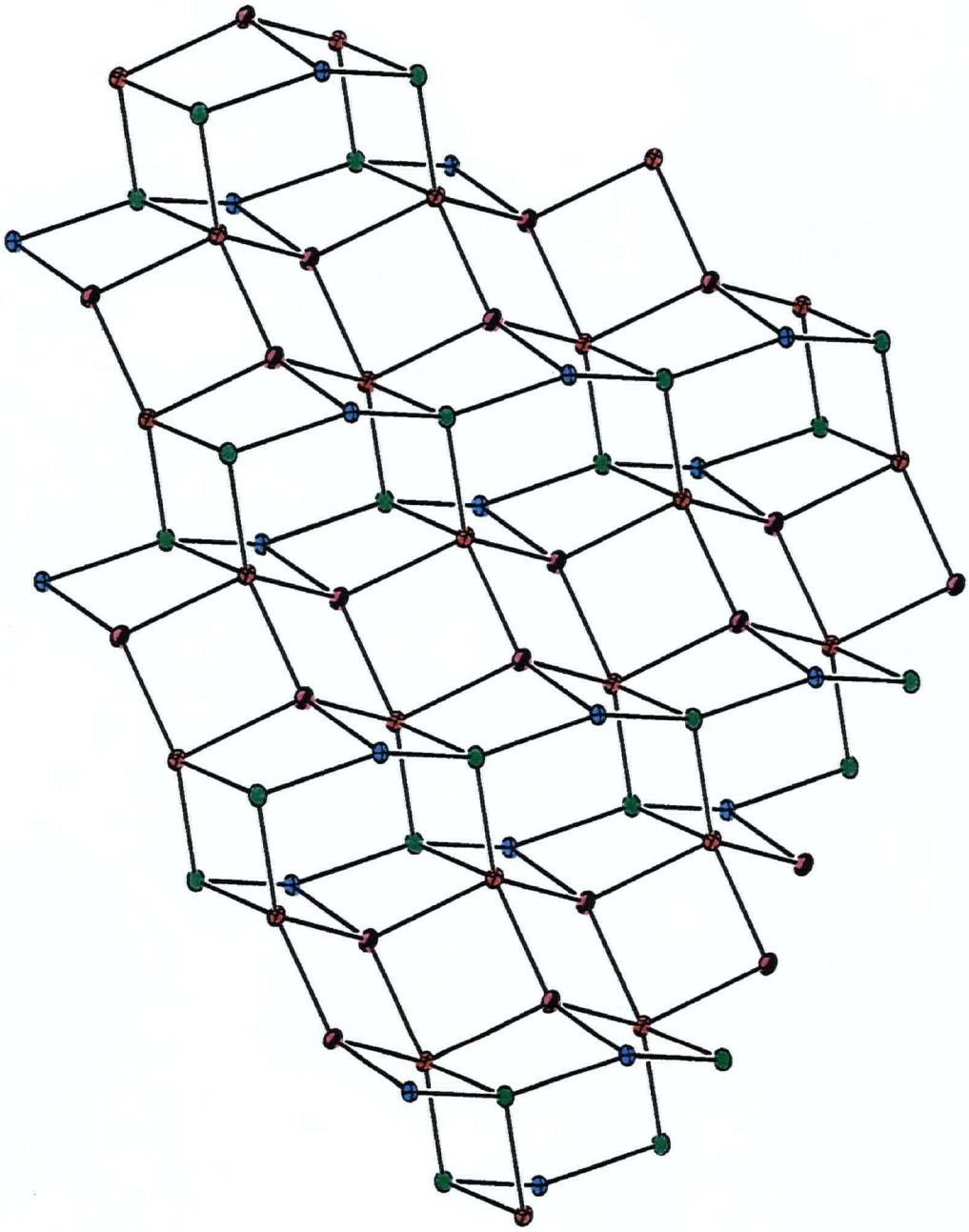

Figure 6.5 Iron ion connectivity diagram for a section of $[Fe_4(imid)_8(terpy)]_x$. Four-coordinate ions (green and pink/black ellipsoids), six-coordinate ions (blue ellipsoids) and five-coordinate ions (red ellipsoids).

6.2.3 MÖSSBAUER SPECTROSCOPY

The room temperature (293 K) Mössbauer spectrum of $[Fe_4(imid)_8(terpy)]_x$ shows the expected number of lines (eight) corresponding to the overlap of four quadrupole doublets [2] (Figure 6.6). This is consistent with the X-ray single crystal diffraction studies that show there are two unique tetrahedral, one unique trigonal pyramidal and one unique octahedral iron site, all of them distorted, in the framework of this compound (Figure 6.2).

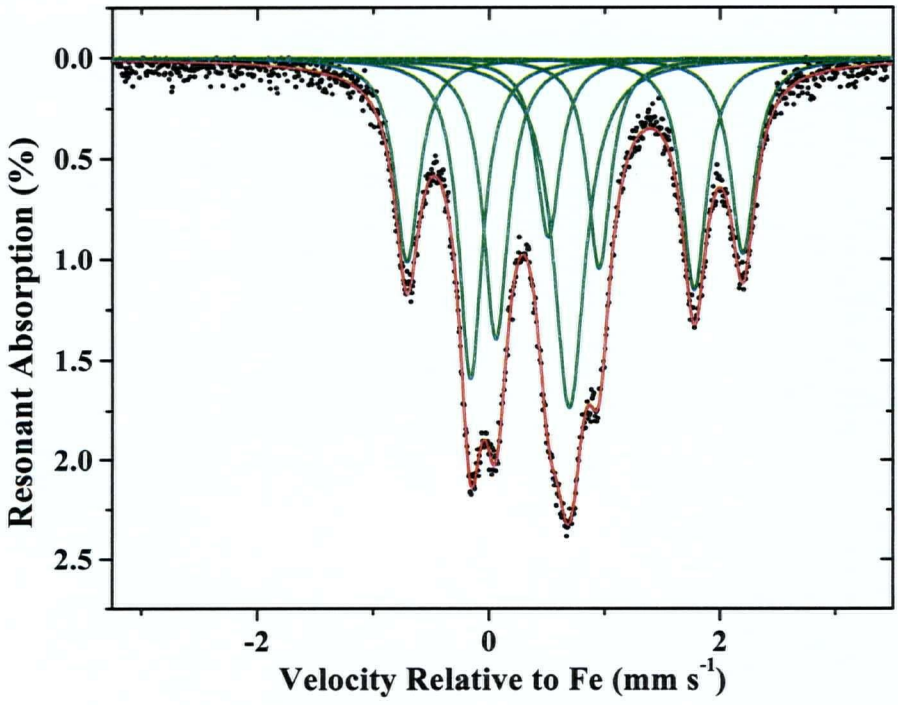

Figure 6.6 Mössbauer spectrum of $[Fe_4(imid)_8(terpy)]_x$ at 293 K.

6.2.4 MAGNETIC PROPERTIES

DC magnetic susceptibility and μ_{eff} versus temperature (2 – 300 K) data on powdered samples of $[Fe_4(imid)_8(terpy)]_x$ in an applied magnetic field of 10 000 G are shown in Figure 6.7. As the temperature is lowered, the μ_{eff} value decreases from 4.96 μ_B at 300 K to 4.27 μ_B at ~ 17 K. At about 16 K, μ_{eff} increases abruptly, reaching a maximum at about 7 K before decreasing with decreasing temperature in the lowest temperature region. The behavior exhibited by χ and μ_{eff} (Figure 6.7) suggests antiferromagnetic exchange between the metal centers in $[Fe_4(imid)_8(terpy)]_x$ above a temperature of ~ 16 K, and a ferromagnetic transition below this temperature.

DC susceptibility studies were also performed at 500 G for $[Fe_4(imid)_8(terpy)]_x$. The trend of the χ and μ_{eff} data versus temperature (2 – 50 K) are shown in Figure 6.8. The results show field dependence at low temperatures, particularly below ~ 12 K. The magnetic transition which is clearly seen in the 500 G data is comparable to that obtained from the 10 000 G data (Figure 6.7). A noticeable difference is that the onset temperature for the magnetic transition (temperature at which χ and μ_{eff} values start to increase) appears to be lower, ~ 12 K, at the lower field studied. This situation arises, perhaps, from the fact that the magnetic transition observed in $[Fe_4(imid)_8(terpy)]_x$ is not an abrupt one, but rather a gradual one. Therefore, it is not easily determined by DC susceptibility studies.

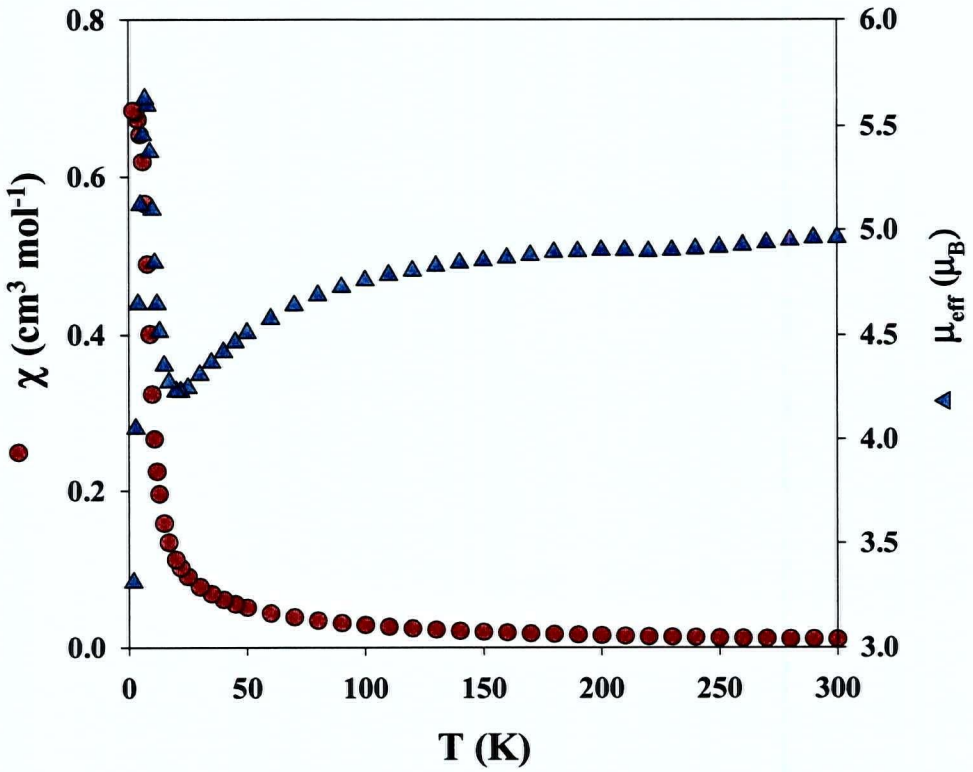

Figure 6.7 DC χ and μ_{eff} versus T at 10 000 G for $[Fe_4(imid)_8(terpy)]_x$.

The actual critical temperature of $[Fe_4(imid)_8(terpy)]_x$ was later confirmed by AC susceptibility measurements, Mössbauer spectroscopy and zero-field-cooled magnetization studies (*vide infra*).

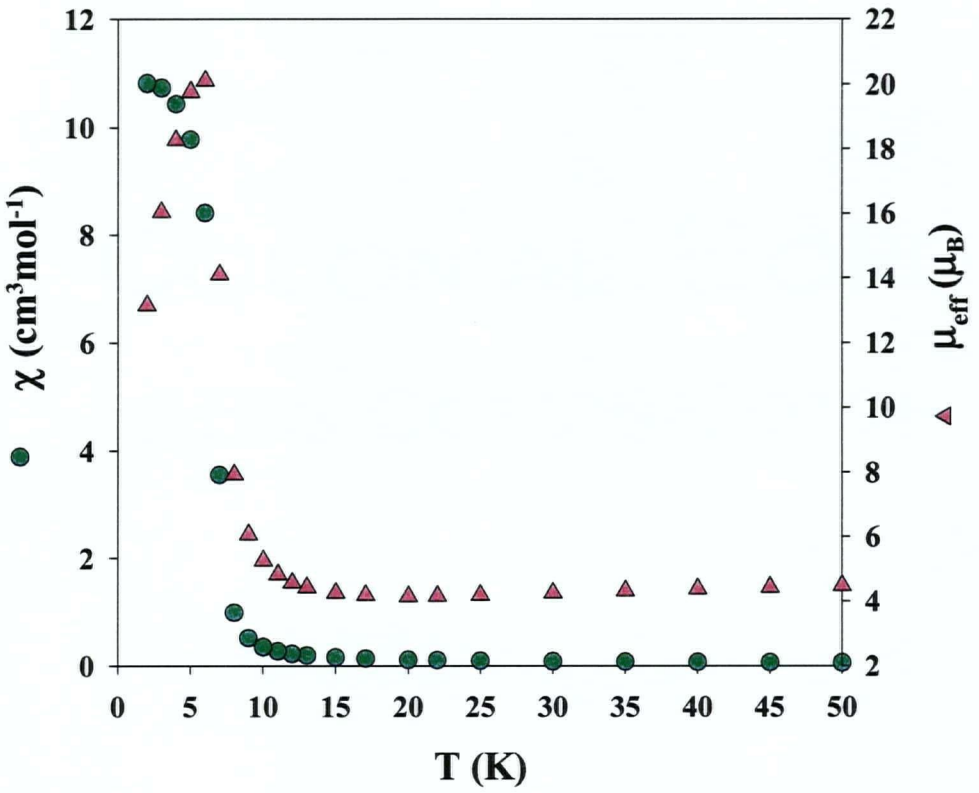

Figure 6.8 DC χ and μ_{eff} versus T at 500 G for $[Fe_4(imid)_8(terpy)]_x$.

AC magnetic susceptibility measurements on $[Fe_4(imid)_8(terpy)]_x$ revealed a ferromagnetic ordering at T_c = 6.35 K, which is determined as the χ' maximum (Figure 6.9). The fact that χ'' (out of phase component) is different from zero at T_c confirms definitively that there is a non-zero net moment ground state, as was also determined from the medium and high field (static) DC susceptibility studies mentioned above.

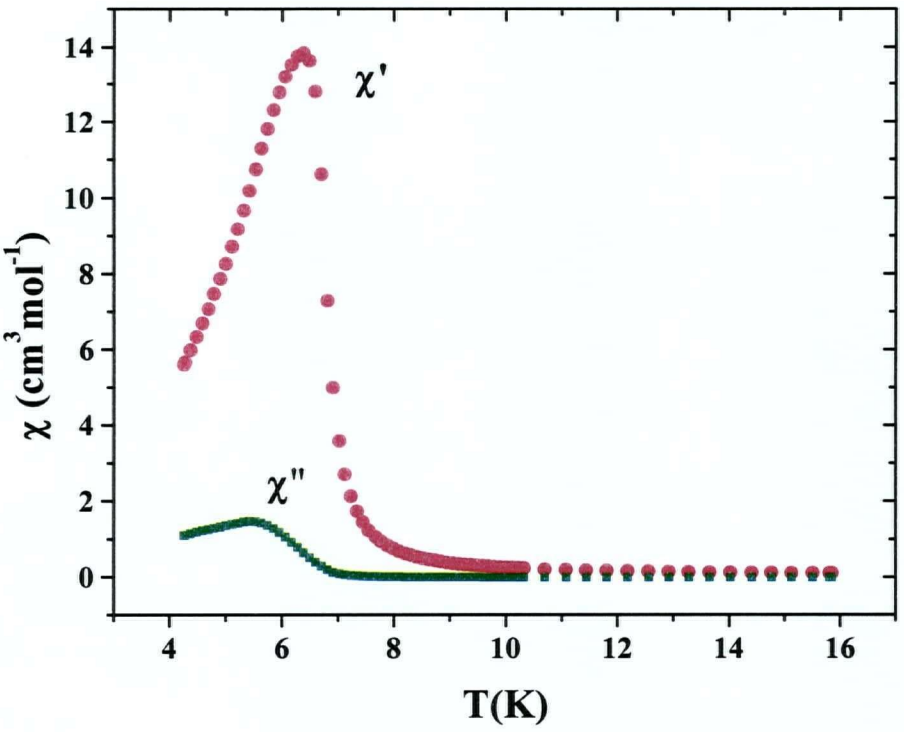

Figure 6.9 AC magnetic susceptibility for $[Fe_4(imid)_8(terpy)]_x$, H_{AC} = 1 G, f = 125 Hz.

The temperature of the onset of the magnetic transition in $[Fe_4(imid)_8(terpy)]_x$ was confirmed by the temperature dependence of the field-cooled magnetization (FCM), zero-field-cooled magnetization (ZFCM) and remnant magnetization (REM) studies (Figure 6.10). The FCM, measured by cooling the sample under a DC field of 50 G, shows an inflection around 7.5 K. According to the d(FCM)/dT plot the temperature of ~ 7 K can be considered as T_c (Figure 6.10). As is typically observed, the ZFCM,

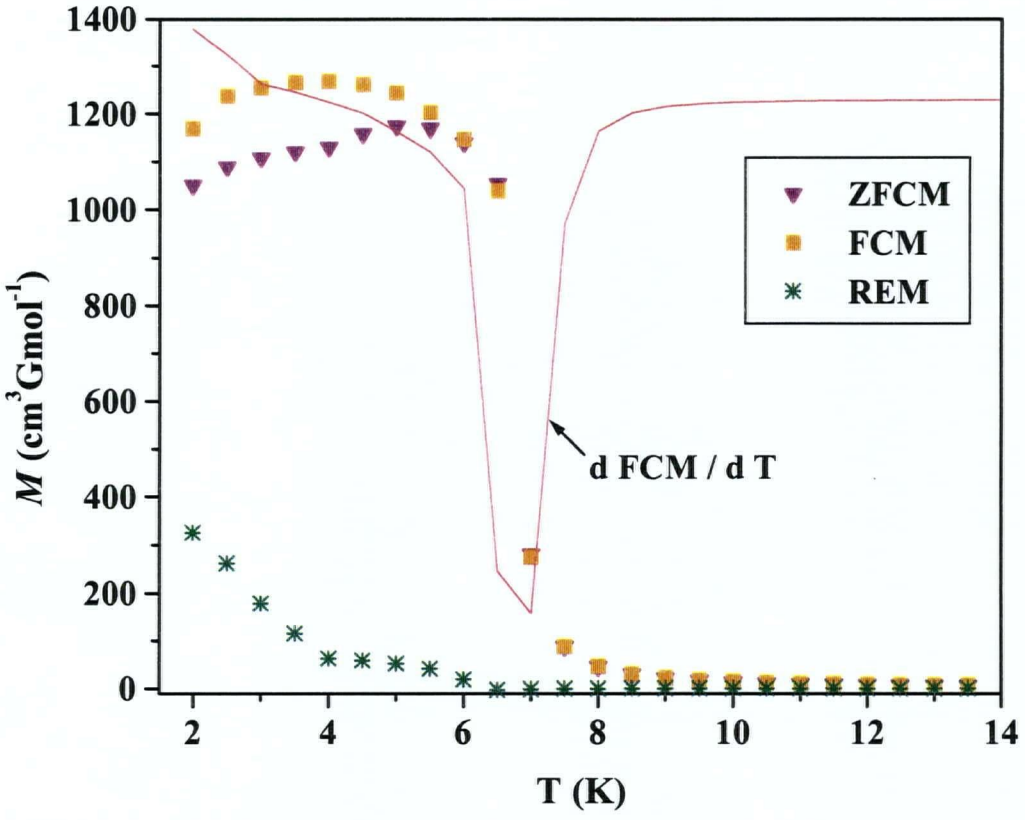

Figure 6.10 Plots of ZFCM, FCM and REM for $[Fe_4(imid)_8(terpy)]_x$. H_{DC} = 50 G.

measured by cooling the sample in zero field, then warming up under a DC field of 50 G , is lower than the FCM at all temperatures below T_c [3]. The REM, obtained by cooling the sample in a 50 G field, then warming up in zero field, vanishes at ~ T_c again as is expected These results confirm that $[Fe_4(imid)_8(terpy)]_x$ behaves as a weak ferromagnet below T_c = 7 K. This T_c value is in close agreement with that determined (T_c = 6.35 K) employing AC susceptibility measurements (vide supra).

Additional evidence for a ferromagnetic transition in $[Fe_4(imid)_8(terpy)]_x$ comes from magnetization versus DC applied field plots performed at different temperatures (Figure 6.11). At 20 K (above T_c), the plot is linear from 20 000 G to zero field and extrapolates to zero magnetization at zero applied field. The plot shows much more curvature at a temperature near T_c (10 K) and at temperatures below T_c (2 K and 4.8 K), the plots are not linear and extrapolate to a negative magnetization (not shown in Figure 6.11) at zero applied field (see following discussion).

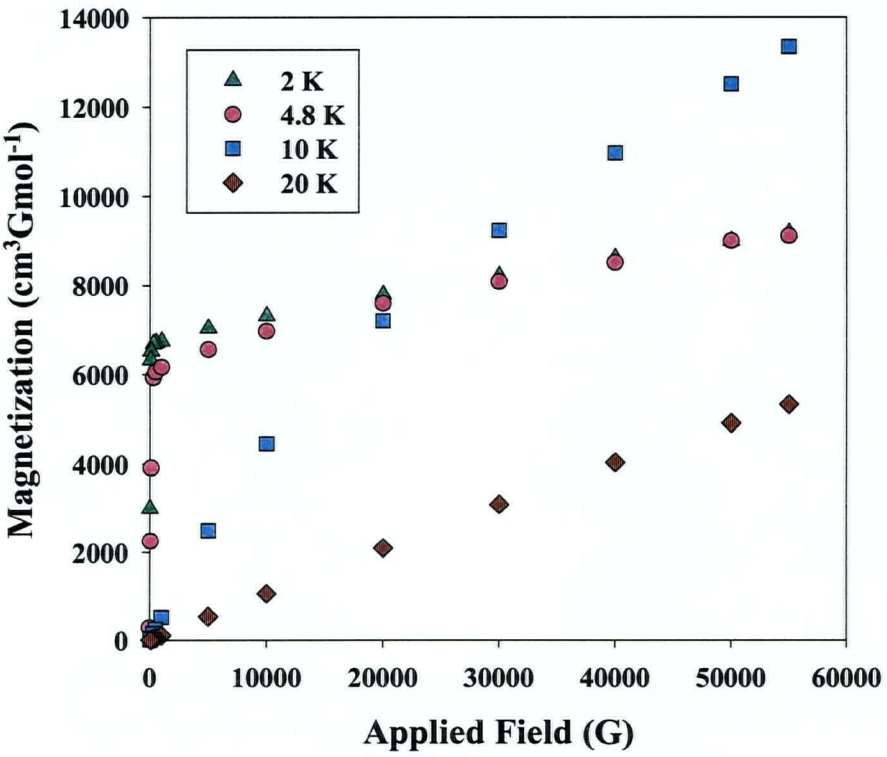

Figure 6.11 Plot of magnetization versus applied field at different temperatures for $[Fe_4(imid)_8(terpy)]_x$.

A hysteresis loop is produced by cycling the applied field between +55 000 and –55 000 G at 4.8 K (Figure 6.12), as expected for a material exhibiting long-range ferromagnetic ordering. From this hysteresis loop, a coercive field of ~ 5 G and a

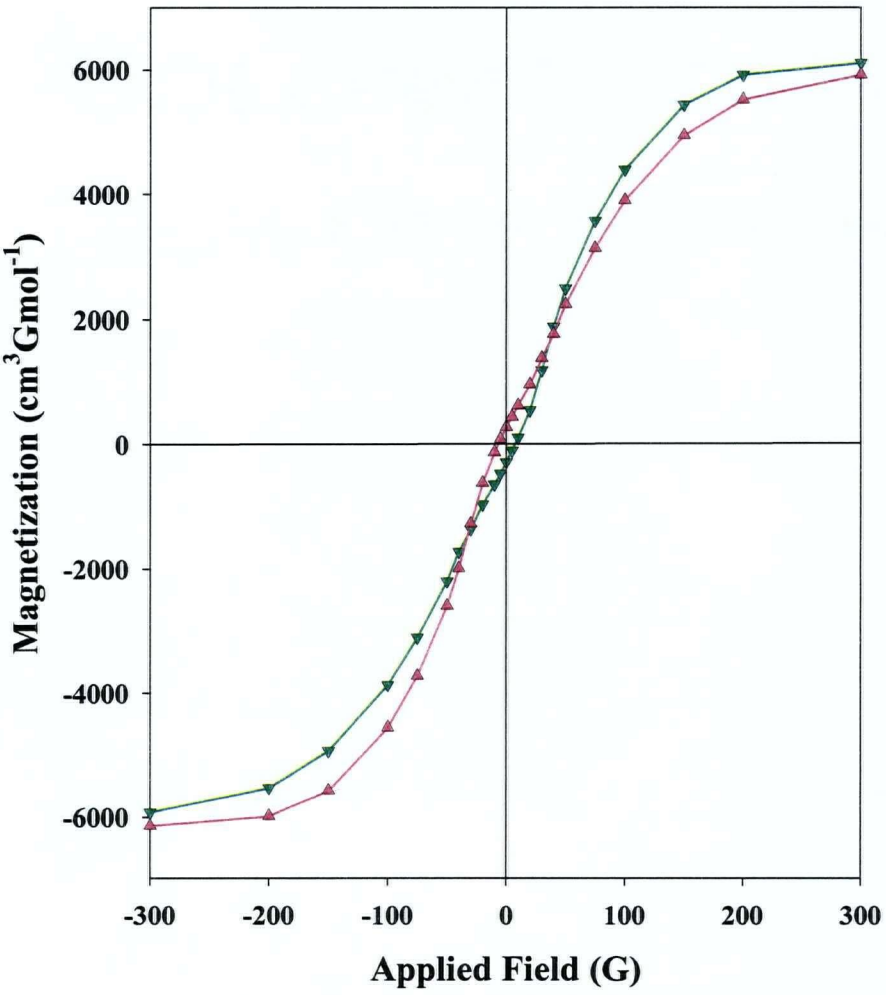

Figure 6.12 Field dependence of magnetization at 4.8 K for $[Fe_4(imid)_8(terpy)]_x$. Central portion of hysteresis loop shown. The data obtained on decreasing the applied field are shown as ▼ while the data obtained on increasing the applied filed are shown as ▲.

remnant magnetization of 40 cm^3Gmol^{-1}, are obtained. A magnet is said to be soft or hard according to whether the coercive field is small or large [3]. The very low value of the coercive field classifies $[Fe_4(imid)_8(terpy)]_x$ as a very soft molecule-based magnet. In a normal hysteresis loop (i.e., see Chapter 5, section 5.2.2.3) the down-field magnetization data approaching zero applied field are positive, while the up-field magnetization values are negative close to zero applied field. For $[Fe_4(imid)_8(terpy)]_x$, however, quite different behavior is observed. The down-field magnetization data actually cross the zero field line at negative magnetization values while the up-field data cross the zero field line at positive magnetization values. This results in a "crossing" of the down-field and up-field magnetization lines, generating a rare magnetization loop in the central part of the plot (Figure 6.12). Confirmation of this distinctive behavior was obtained in a separate experiment in which the applied field was cycled (-55 000 to +55 000) three times at 4.8 K. The results of this study, shown in Figure 6.13, confirmed that this unique magnetization loop is real and reproducible, since it appears in the same region in every one of the cycles carried out, and cannot be "removed' by repeatedly oscillating the applied field.

A possible explanation for the distinctive magnetization loop of $[Fe_4(imid)_8(terpy)]_x$ is the following. There are four unique iron chromophores in this compound, which can be identified accordingly to their coordination number as 4, 4', 5

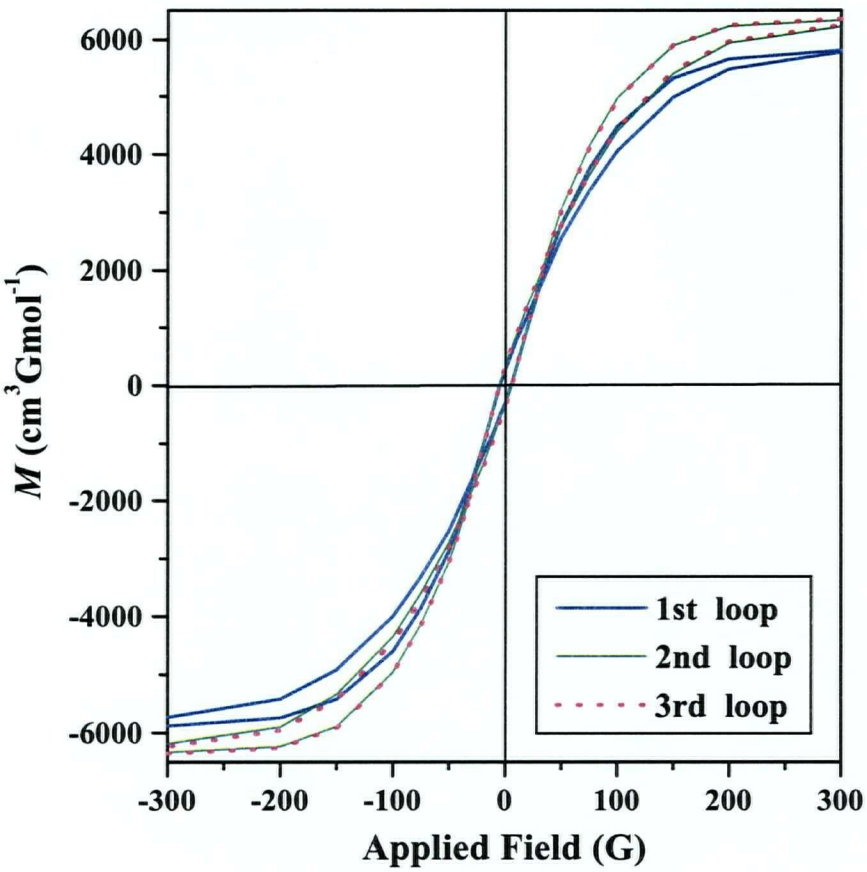

Figure 6.13 Field dependence of magnetization at 4.8 K for $[Fe_4(imid)_8(terpy)]_x$. Central portion of hysteresis loop shown.

and 6. The size of the magnetic dipole on each site will be different. For the sake of discussion we assume the dipole on site 5 is significantly smaller than those on the other three sites which, in turn are approximately the same. Assuming antiferromagnetic coupling, the connectivities require the spins in 4 and 4' to be parallel to each other, with the 5 and 6 site spins antiparallel to these as follows:

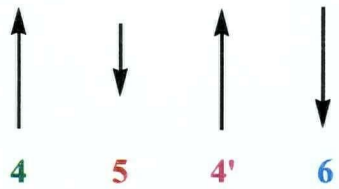

This arrangement would give a net spin ↑. We now speculate that as the positive H (↑) is reduced to zero all of the spins randomize (as expected in a material which is not a "magnet") except for the spin on 5, which retains a ↓ preference (caused by slow relaxation). This would give a negative M at $H = 0$. As H is increased in the negative direction H (↓) the spins on all sites orient with the reverse direction to that shown above, giving a net spin ↓. Then, reducing the negative H (↓) to zero all spins randomize except for the spin on 5, which retains the ↑ preference (slow relaxing). This situation gives a positive M at $H = 0$.

Support for the speculation above comes from Mössbauer studies. Preliminary results suggest that one of the sites undergoes magnetic hyperfine splitting owing to slow paramagnetic relaxation (not ordering) in the decreasing temperature range 77 to 7 K. Below the latter temperature all four sites are hyperfine split.

The magnetic properties of $[Fe_4(imid)_8(terpy)]_x$ are quite different from those of the other molecule-based magnets described in this thesis. While the primary

mechanism of exchange is antiferromagnetic, as in the other systems, in this case the anomalous magnetic behavior leading to a phase transition below 7 K appears to arise from the coupling of dipoles of different strengths, a form of ferrimagnetism. Moreover, rather than long-range ordering of all spins sites below T_c, three of the sites undergo rapid relaxation with the fourth retaining orientation in the field thus generating the net magnetization at zero applied field. It is hoped that more detailed study and analysis of the Mössbauer spectra of this material (currently ongoing) will permit us to identify the slow relaxing site and thereby remove some of the speculation surrounding the unique magnetic behavior of this material.

6.3 SUMMARY AND CONCLUSIONS

The reaction of ferrocene with molten imidazole and terpyridine yields green crystals of composition $[Fe_4(imid)_8(terpy)]_x$. The structure of this material has been determined by single crystal X-ray diffraction studies and is shown to consist of novel 2-D wrinkled sheets formed by four-coordinate (two unique ions of this type), five-coordinate and six-coordinate iron(II) ions linked by single bridging imidazolates. The six-coordinate metal ions are additionally coordinated by terpyridine ligands that occupy positions between the sheets, isolating the sheets from each other. The presence of four unique iron sites in $[Fe_4(imid)_8(terpy)]_x$ was confirmed by Mössbauer spectroscopy.

In the formation of this unique 2-D iron(II) imidazolate polymer, some degree of structural control has been introduced by the tridentate ligand, terpy, which occupies coordination sites on the metal ions and provides steric constrains, thus preventing spatial extension of the polymeric structure to three-dimensions.

DC magnetic susceptibility measurements reveal antiferromagnetic interactions between metal centers above a temperature of ~ 12 K and the onset of long range ferromagnetic ordering below this temperature. A transition to a ferromagnetic state below these temperatures was seen in both DC and AC susceptibilities and zero-field-cooled magnetization studies. The critical temperature, T_c ~ 6.5 K, for the magnetic transition was determined from these latter studies.

$[Fe_4(imid)_8(terpy)]_x$ represents another rare example of a 2-D coordination polymer exhibiting weak ferromagnetism at low temperatures. The compound shows a unique negative hysteresis loop and speculation to account for this points to the possibility of a form of ferromagnetic coupling combined with slow paramagnetic relaxation at low temperatures of one of the four unique metal centers. Additional insights into this matter are expected from ongoing Mössbauer studies. Regardless of the mechanism, this material does exhibit net magnetization at zero applied field (M_{rem} = 40 cm^3Gmol^{-1}) classifying it as a weak molecule-based magnet. Its coercive field of ~ 5 G classifies it as a very soft magnet.

References

1. P. J. Hagrman and J. Zubieta. *Inorg. Chem.* **39**, 5218 (2000).

2. N. Greenwood, T. C. Gibb. Mössbauer Spectroscopy, Chapman and Hall Ltd. London, 1971.

3 O. Kahn. *Acc. Chem. Res.* **33** (10) 647 (2000).

Chapter 7 POLYBIS(1-METHYL-2-THIOIMIDAZOLATO)IRON(II). A ONE-DIMENSIONAL MATERIAL EXHIBITING LONG-RANGE MAGNETIC ORDERING

7.1 INTRODUCTION

As described before, metal polymers formed with bridging imidazolate ligands are usually of high dimensionality (2-D or 3-D) as a result of the 1,3-positioning of the N-donor atoms of the imidazolate moiety, which allows the formation of single bridges between metal centers. However, with the N-1 position blocked with a methyl substituent, as it is in the case for the ligand precursor 1-methyl-2-thiolimidazole (1-Me-2-SH-imid), deprotonation of the thiol functionality would generate a bridging ligand, 1-Me-2-S-imid, capable of forming double bridges between Fe(II) centers in a rod like polymer [1]. Previous studies had revealed this type of bonding mode for this ligand in the dimeric molecules $[Me_2Ga(1\text{-}Me\text{-}2\text{-}S\text{-}imid)]_2$ and $[Mo(\eta^3\text{-}C_3H_5)(CO)_2(1\text{-}Me\text{-}2\text{-}S\text{-}imid)]_2$ [2].

The rod-like 1-D structural motif was observed in the material characterized here, $[Fe(1\text{-}Me\text{-}2\text{-}S\text{-}imid)_2{\cdot}0.5Cp_2Fe]_x$. Interestingly, the phenomenon of long-range

ferromagnetic ordering below a critical temperature, previously seen only in 1,3-diazolate complexes with 2-D and 3-D extended lattices (Chapters 3, 4, 5 and 6), is observed in this unique Fe(II) coordination polymer.

An article containing most of the results discussed in this chapter has been published [1].

7.2 RESULTS AND DISCUSSION

7.2.1 SYNTHESIS, PHYSICAL AND THERMAL PROPERTIES

Details of the synthesis of $[Fe(1\text{-}Me\text{-}2\text{-}S\text{-}imid)_2 \cdot 0.5Cp_2Fe]_x$ are described in Chapter 9, section 9.2.1.5. Following the success of the previously reported reactions of ferrocene with imidazole and 2-methyl imidazole, which generate crystalline polymers [3, 4], the synthetic method involving ferrocene and the molten ligand precursor was utilized here. The desired compound was isolated as golden needle-like crystals.

$[Fe(1\text{-}Me\text{-}2\text{-}S\text{-}imid)_2 \cdot 0.5Cp_2Fe]_x$ appeared to be fairly air-stable and could be handled briefly under normal atmospheric conditions. The compound is insoluble in common organic solvents and water. The complex is non-volatile. Thermal gravimetric analysis (35 °C to 800 °C) measurements were made and the TGA plot is shown in Figure 7.1. These results show the complex to be thermally stable to 197 °C. Decomposition with continuous weight loss occurs from 197 to 800 °C with a total

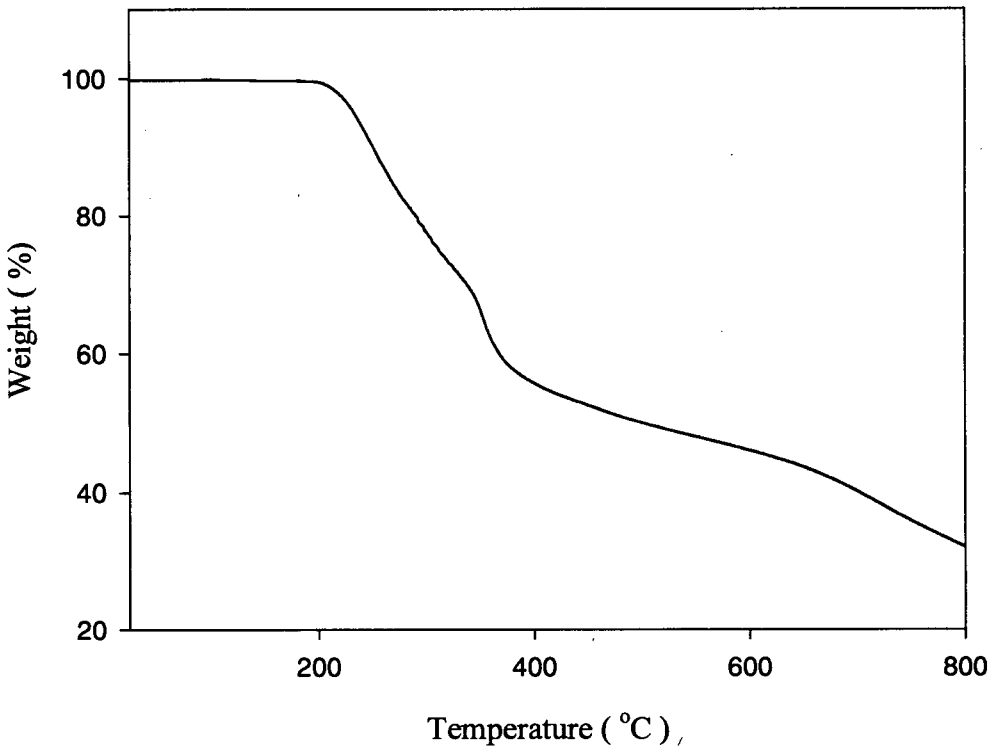

Figure 7.1 TGA plot for $[Fe(1\text{-}Me\text{-}2\text{-}S\text{-}imid)_2 \cdot 0.5Cp_2Fe]_x$.

weight loss of 69% of the initial mass. This compares favorably to a 65% loss that would occur if only FeS remains at 800 °C.

7.2.2 X-RAY CRYSTALLOGRAPHY

The structure of a section of the polymer chain is shown in Figure 7.2, and a view of the lattice, almost parallel to the polymer chain, is depicted in Figure 7.3. Crystallographic data, atom coordinates, selected bond lengths and angles appear in Appendix I, Tables I-12 and I-13. The structure consists of chains of distorted tetrahedral iron(II) ions double-bridged by the 1-methyl-2-thioimidazolate ligands, giving rise to eight-membered rings linked by the Fe ions in a pseudospiro conformation (Figure 7.2). The ligands bind through the unsubstituted nitrogen (N2 in Figure 7.2) and the sulfur atoms and orient along the chain in a manner that leads to distinctive FeN_4 and FeS_4 chromophores which alternate throughout the polymer chains.

These structural characteristics produce a rod-like shape to the polymeric chain (Figure 7.3). The Fe(2)–N bond distances are significantly shorter at 2.054 Å than the Fe(1)–S bonds at 2.368 Å. The S–Fe(1)–S bond angles are close to tetrahedral, ranging from 108.32° to 110.05°, while the N–Fe(2)–N angles are further from tetrahedral ranging from 104.91° to 119.05°. Molecules of ferrocene, one for every two repeating units in the chain, are trapped between the polymer chains (Figure 7.3). These molecules cannot be removed by thermolysis without decomposition of the polymer (See Figure 7.1).

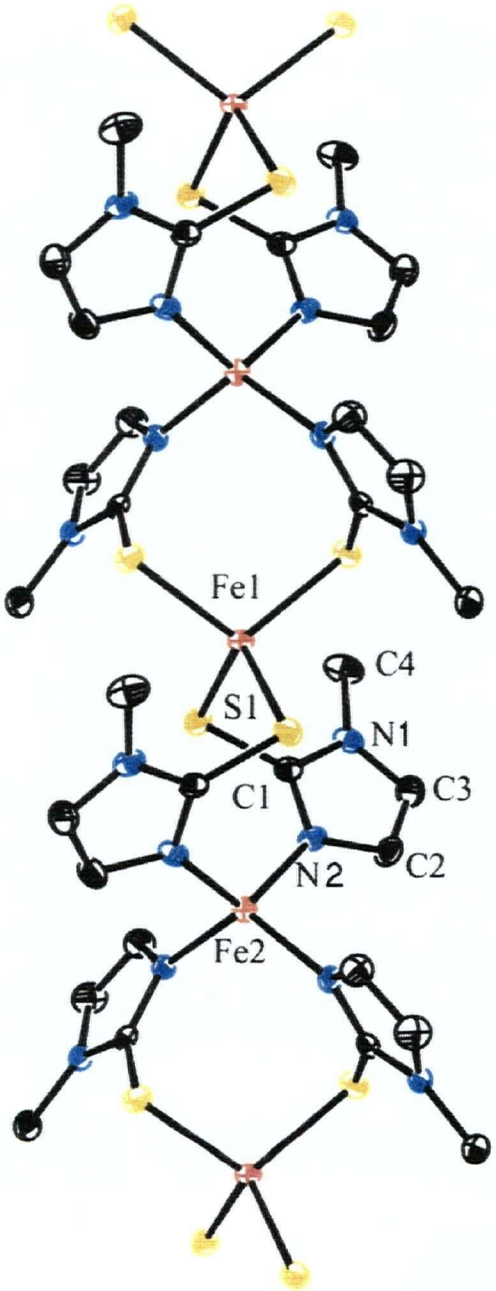

Figure 7.2 Molecular structure of the polymer chain of $[Fe(1\text{-Me-2-S-imid})_2 \cdot 0.5Cp_2Fe]_x$ showing the atom numbering scheme; 33 % probability thermal ellipsoids are shown. (Hydrogen atoms are omitted).

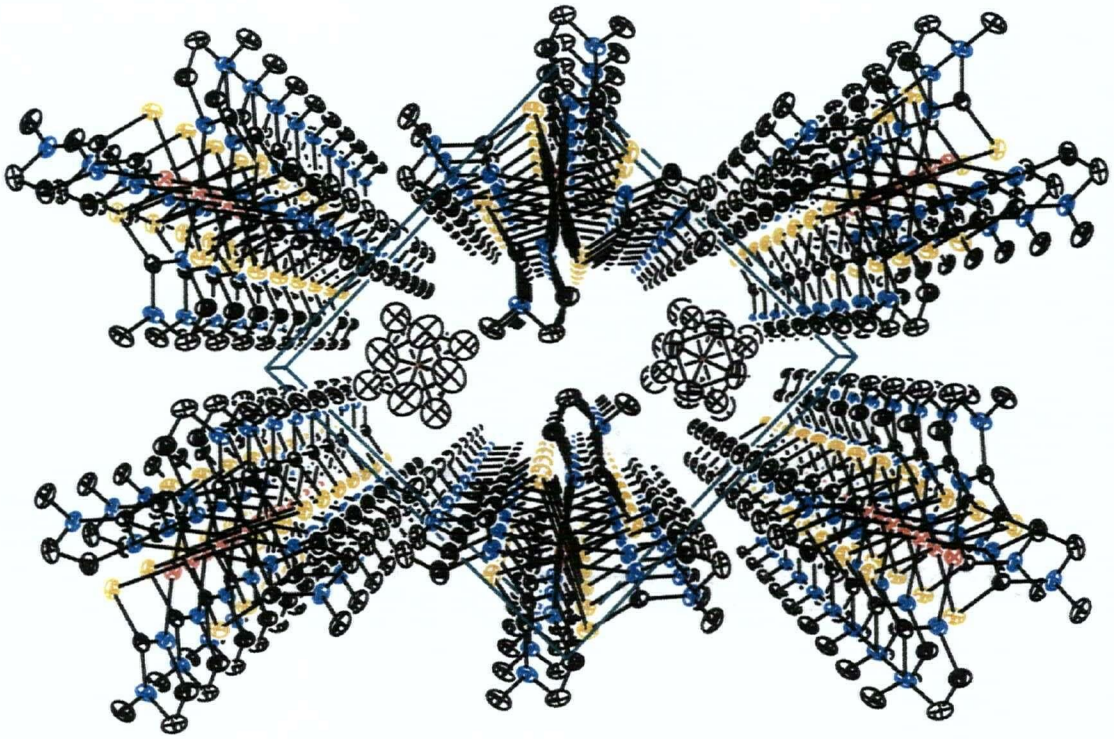

Figure 7.3. View of the crystal structure of $[Fe(1\text{-Me-2-S-imid})_2 \cdot 0.5Cp_2Fe]_x$ down the *c* axis. 50 % thermal ellipsoids are shown.

7.2.3 MAGNETIC PROPERTIES

The DC magnetic susceptibilities, χ, and χT versus temperature, on powdered samples of $[Fe(1\text{-}Me\text{-}2\text{-}S\text{-}imid)_2 \cdot 0.5Cp_2Fe]_x$ in an applied magnetic field of 500 G, are shown in Figure 7.4. As the temperature is lowered from 300 K, the χT value decreases. At about 8 K, χT increases abruptly, reaching a maximum at about 5 K before decreasing with decreasing temperature in the lowest temperature region. The behavior suggests antiferromagnetic exchange between the metal centers above the critical temperature, T_c, of 5 K (this temperature confirmed by AC susceptibility and Mössbauer measurements (*vide infra*)), and a ferromagnetic transition below this temperature.

AC susceptibility measurements indicate the ferromagnetic ordering at T_c = 5 K, which is determined as the average temperature between the χ' plot maximum at 5.20 K and the χ'' plot maximum at 4.85 K [3] (Figure 7.5). The fact that χ'' (out of phase or imaginary component) is different from zero at T_c confirms unequivocally that there is a non-zero net moment ground state. Therefore, the near zero field results reveal the presence of a long-range ferromagnetic order below T_c in concordance with the DC susceptibility studies discussed above.

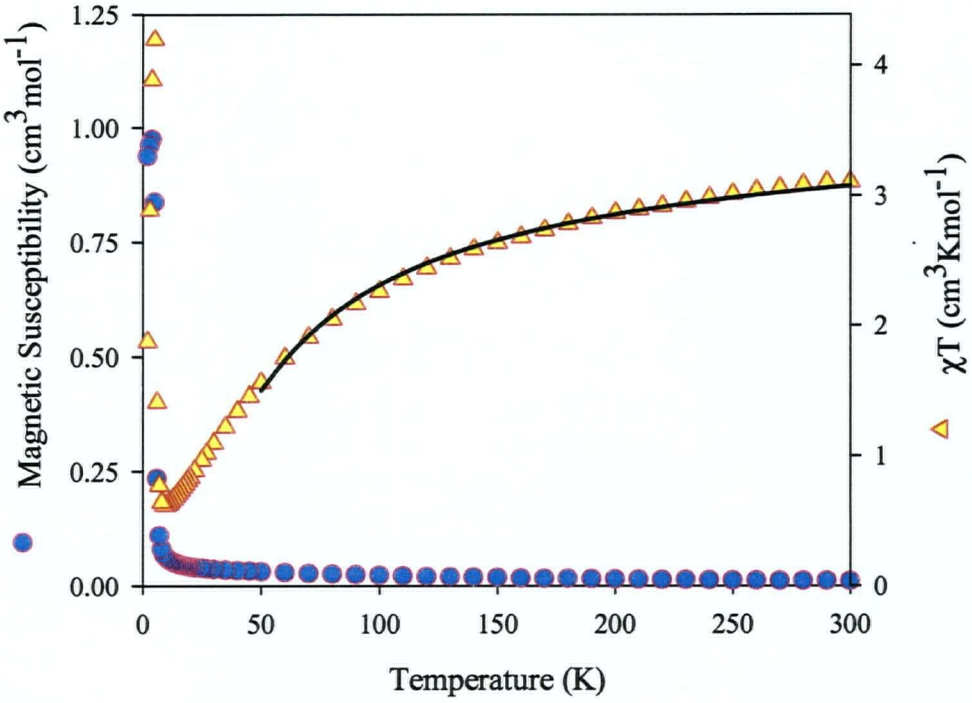

Figure 7.4 DC χ and χT versus temperature plots at 500 G for $[Fe(1\text{-Me-2-S-imid})_2 \cdot 0.5Cp_2Fe]_x$ The line is from theory as described in the text.

Support for a ferromagnetic transition comes from magnetization versus applied field plots at different temperatures (Figure 7.6). At 15 K (above T_c), the plot is linear to over 20 000 G and extrapolates to zero magnetization at zero applied field. At temperatures below T_c, the plots are not linear and extrapolate to yield net magnetization at zero applied field.

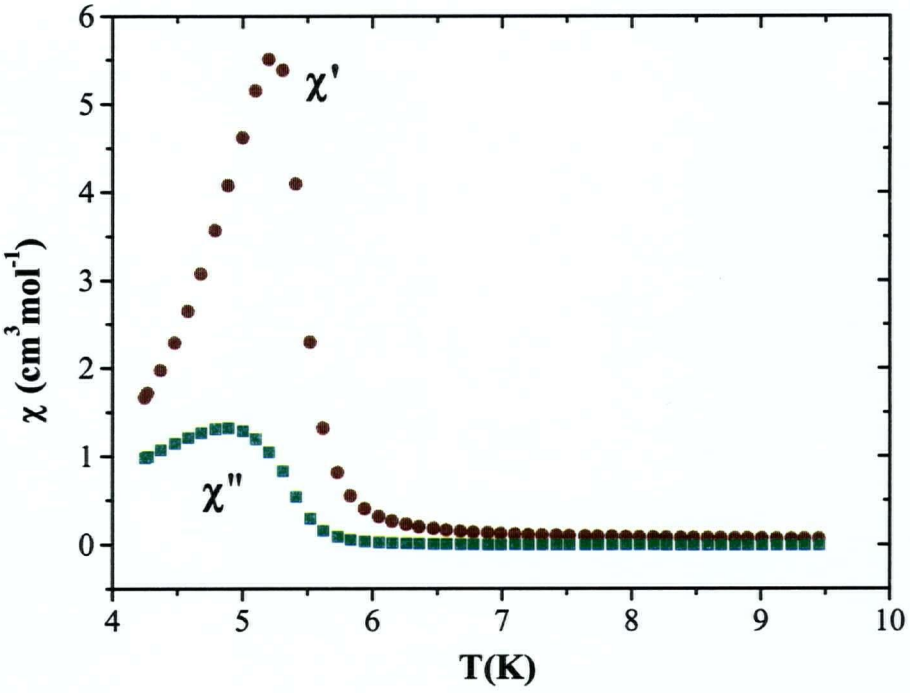

Figure 7.5 AC magnetic susceptibility for $[Fe(1\text{-Me-2-S-imid})_2 \cdot 0.5Cp_2Fe]_x$, H_{AC} = 1 G, f = 125 Hz.

Cycling the applied field between +55 000 and –55 000 G at 4.8 K generates a hysteresis loop (Figure 7.7), as expected for a material exhibiting long-range ferromagnetic ordering. From this hysteresis loop, a coercive field of 40 G and a remnant magnetization of 190 cm^3 G mol^{-1}, are obtained.

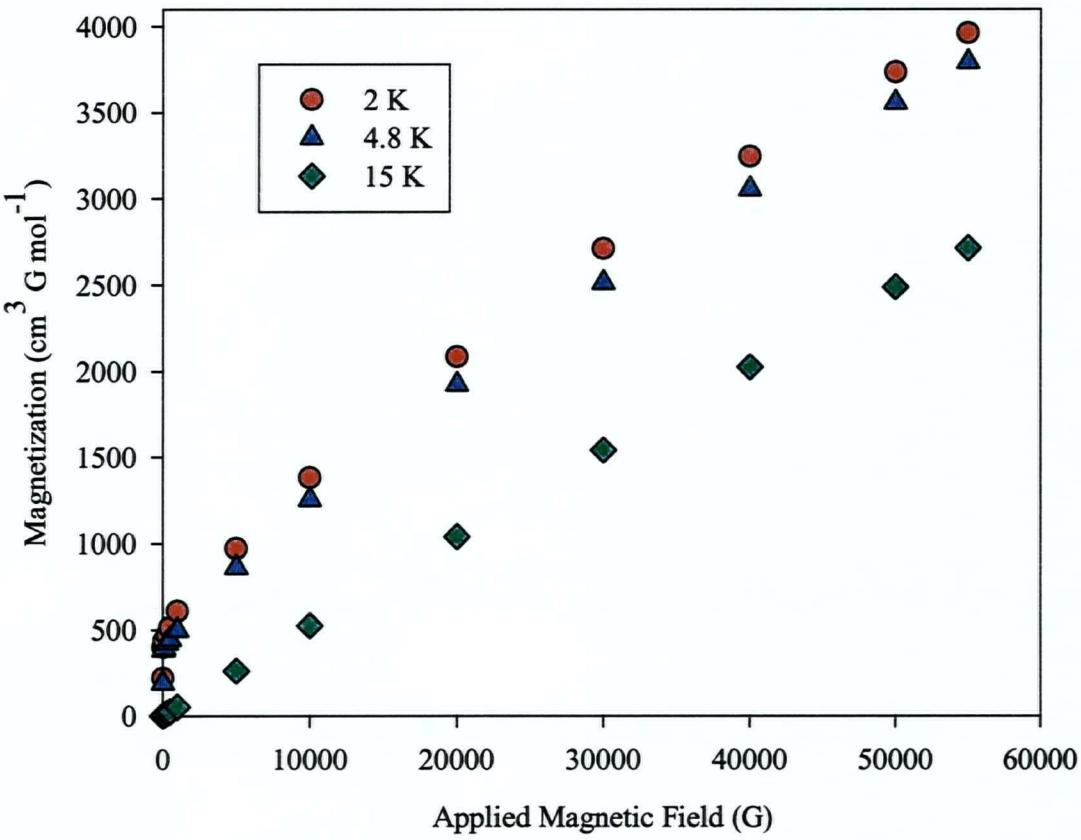

Figure 7.6 Plot of magnetization versus applied field at three temperatures for $[Fe(1\text{-Me-2-S-imid})_2 \cdot 0.5Cp_2Fe]_x$.

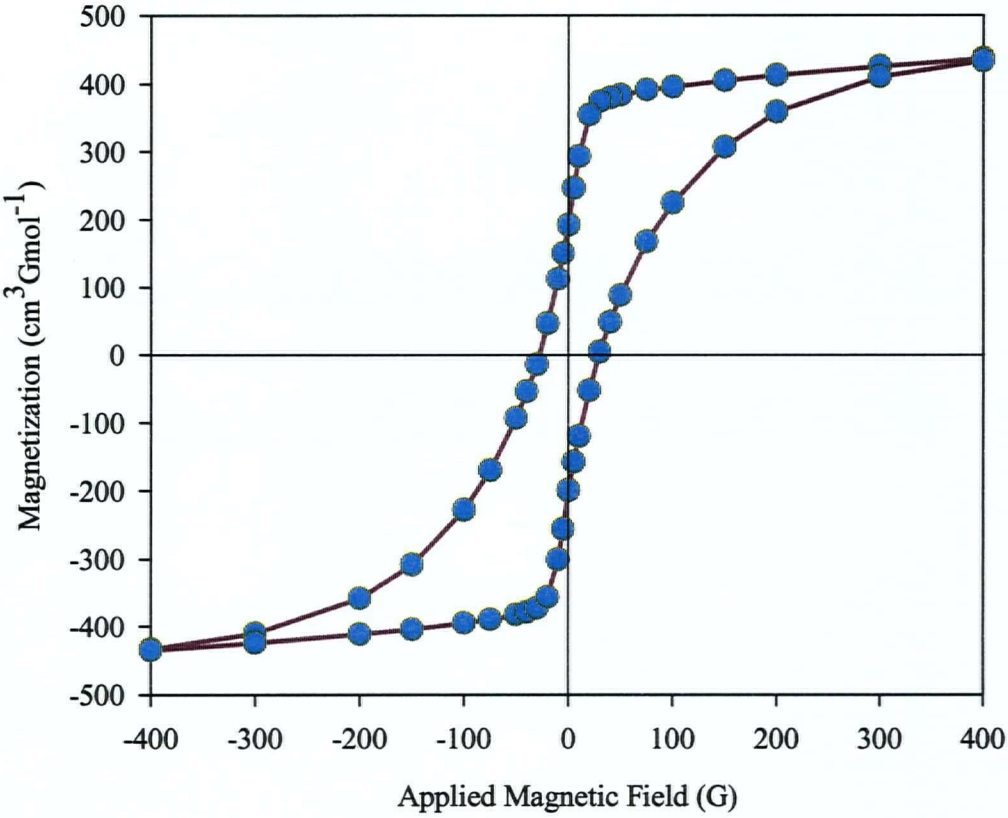

Figure 7.7 Field dependence of magnetization at 4.8 K for $[Fe(1\text{-Me-2-S-imid})_2 \cdot 0.5Cp_2Fe]_x$. Central portion of hysteresis loop shown.

Magnetic susceptibilities were measured as a function of temperature at 10 000 and 50 000 G as well as at 500 G (Figure 7.8). The results show field dependence at low temperatures, particularly below T_c. The magnetic transition which is clearly seen in the

500 G data is much less pronounced in the 10 000 G data and is absent at 50 000 G. The ferromagnetic ordering is clearly repressed by large applied fields.

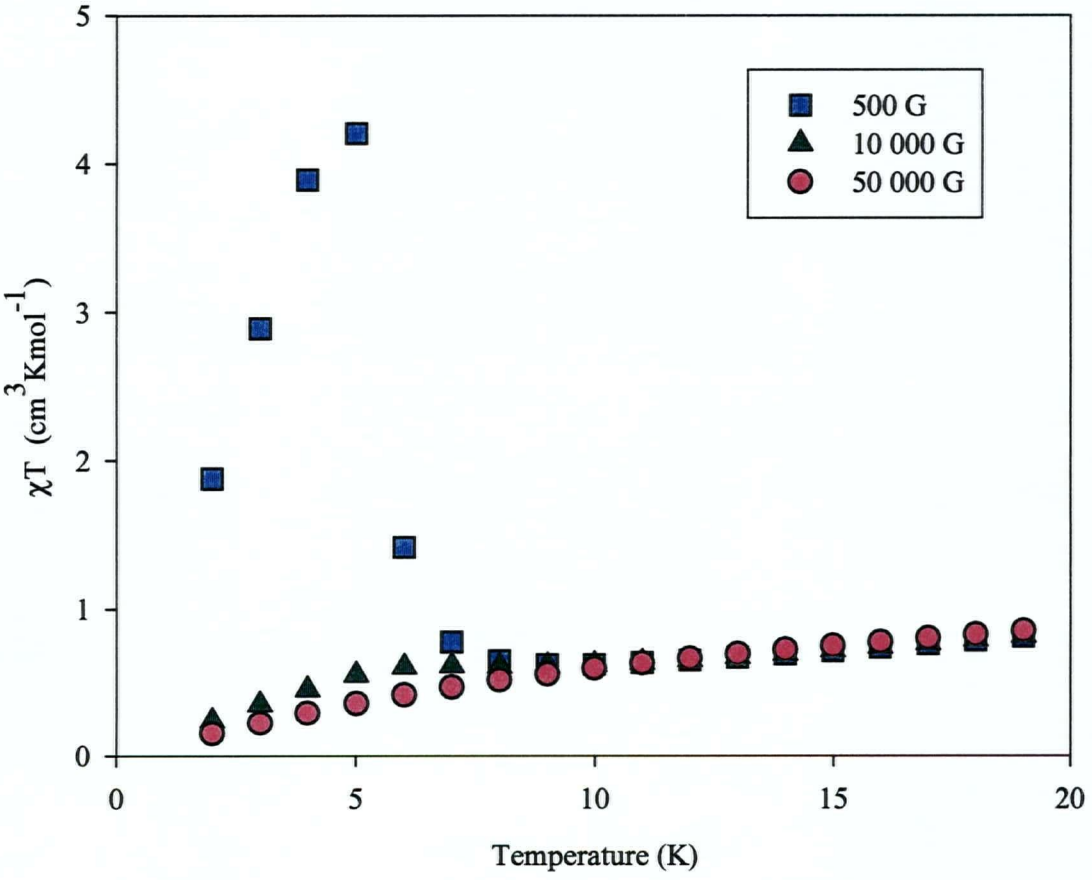

Figure 7.8 Plot of χT versus temperature at three values of applied field for $[Fe(1\text{-Me-2-S-imid})_2 \cdot 0.5Cp_2Fe]_x$.

The magnetic properties of $[Fe(1\text{-Me-2-S-imid})_2 \cdot 0.5Cp_2Fe]_x$ parallel closely those of $[Fe_3(imid)_6(imidH)_2]_x$ [4], $[Fe(4\text{-imidazol-acetate})_2]_x$ [5], and $[Fe(2\text{-Me-imid})_2 \cdot 0.13Cp_2Fe]_x$ [6], compounds for which the primary exchange process is considered to involve antiferromagnetic coupling between iron centers with a canting of spins. A spin-canted structure for the compound studied here is also supported by the fact that the highest magnetization reached (3960 cm^3 G mol^{-1} at 2 K and 55 000 G) is significantly smaller than the theoretical saturation value (22 300 cm^3 g mol^{-1}) [7]. Additional support for the canted spin structure comes from structural data. These show a feature characteristic of such systems, that of a systematic alternation of the relative orientation of neighboring metal chromophores [4]. As a measure of this, the dihedral angle between the S(1)–Fe(1)–S(1)^c and N(1)^d–Fe(2)–N(1)^e planes is 27.6°. Therefore, antiferromagnetic coupling between neighboring metal centers along the chain can occur with imperfect antiparallel alignment of spins, leading to residual spins on the chains. Ferromagnetic ordering of the residual spins generates long-range three-dimensional magnetic ordering and spontaneous magnetization at low temperatures. It should be noted that the chains in $[Fe(1\text{-Me-2-S-imid})_2 \cdot 0.5Cp_2Fe]_x$ are isolated (Figure 7.3), and therefore, any interchain interaction cannot be mediated by bonding interactions. This contrasts with the situation for $[Fe_3(imid)_6(imidH)_2]_x$ [4] and $[Fe(2\text{-Me-imid})_2 \cdot 0.13Cp_2Fe]_x$ [6] where covalent bonding interactions connect the paramagnetic centers in three dimensions and for $[Fe(4\text{-imidazol-acetate})_2]_x$ [5], where hydrogen-bonding interactions connect sheets of covalently linked metal centers. Such considerations may play an important role in determining the magnitude of the coercive

field in these systems, as $[Fe(1\text{-Me-2-S-imid})_2 \cdot 0.5Cp_2Fe]_x$ exhibits the smallest coercive field of the four compounds considered here.

Further evidence in support of the primary antiferromagnetic intrachain coupling in $[Fe(1\text{-Me-2-S-imid})_2 \cdot 0.5Cp_2Fe]_x$ can be gathered by examining fits of the magnetic susceptibility in the high temperature region to the expression derived employing an isotropic Hamiltonian of the form $H = -2JS_1 \cdot S_2$ for a linear chain of antiferromagnetically coupled $S = 2$ centers [8], as was previously done for $[Fe(pz)_2]_x$ (Chapter 2). That equation is

$$\chi = \left(Ng^2\beta^2 / kT\right)\left[\frac{2 + 71.938x^2}{1 + 10.482x + 955.56x^3}\right]$$

where $x = |J| / kT$, J is the exchange coupling constant and g is the Landé factor. By employing susceptibility data obtained at the three different fields (500, 10 000 and 50 000 G), no satisfactory fits were obtained when data below 50 K were included. Good fits were, however, obtained for data in the range 50–300 K as is illustrated for the 500 G χT data in Figure 7.4. The lack of agreement between theory and experiment at low temperatures is not surprising since the model does not accommodate the effects of residual spin due to spin canting or interchain interactions, both of which are more pronounced at low temperatures. The theory line shown in Figure 7.5 was calculated with

$-J = 3.92(6)$ cm^{-1} and $g = 2.21(1)$ ($F = 0.00033$). The model used is limited by the fact it employs a single g value, while the structure of the compound requires different g values for the FeN_4 and FeS_4 chromophores. The best-fit g value of 2.21 presumably approximates the average g for the system. The strength of the antiferromagnetic coupling in this compound, as judged by the magnitude of $-J$, seems to be slightly greater than that seen in $[Fe_3(imid)_6(imidH)_2]_x$ [4] and $[Fe(2\text{-meimid})_2 \cdot 0.13Cp_2Fe]_x$ [6] for which $-J$ values of 2.3 and 2.75 cm^{-1}, respectively, have been reported.

The alternation in chromophore type and, therefore, g value along the chain should generate important magnetic consequences for this antiferromagnetically coupled system. The size of the individual magnetic dipoles will alternate along the chain, and even perfect antiparallel alignment between neighbors will lead to a residual moment on the chain, which can be considered as an example of ferrimagnetism. This same phenomenon was described in earlier chapters as a possible cause of the residual spin on the lattices of $[Fe_2(imid)_4(bipy)]_x$ (Chapter 5) and $[Fe_4(imid)_8(terpy)]_x$ (Chapter 6). While this probably contributes to the observed magnetic properties of the system, a simple calculation indicates it cannot be the sole source of the residual chain magnetization. The saturation magnetization, M_S, for a $S = 2$ center is [7]

$$M_S = Ng\beta S$$

The net saturation magnetization, M_{net}, for a chain of perfect antiparallel coupled $S = 2$ metal centers with regularly alternation of g values is, per mole of metal center,

$$M_{net} = \frac{1}{2}\Delta M_S = N\beta\Delta g$$

Inserting 3960 cm^3 G mol^{-1} (the magnetization measured at 2 K and 55 000 G) for M_{net} in the above equation yields a Δg value of 0.71. Hence, an unrealistically large difference in g values for the FeN_4 and FeS_4 chromophores would be required to invoke ferrimagnetism to account for the largest magnetization (not even saturation magnetization) observed. Therefore, spin canting is likely the primary source of the residual magnetization on the chains, although ferrimagnetism cannot be ruled out as a contributing factor. This latter phenomenon is further discussed in the following section.

7.2.4 MÖSSBAUER SPECTROSCOPY

The room temperature Mössbauer spectrum of $[Fe(1\text{-Me-2-S-imid})_2 \cdot 0.5Cp_2Fe]_x$ corresponds to three overlapping quadrupole doublets (Figure 7.9), which are consistent with the X-ray single crystal diffraction studies that indicate equal population of distorted four coordinated (tetrahedral) FeN_4 and FeS_4 sites and half as many ferrocene molecules

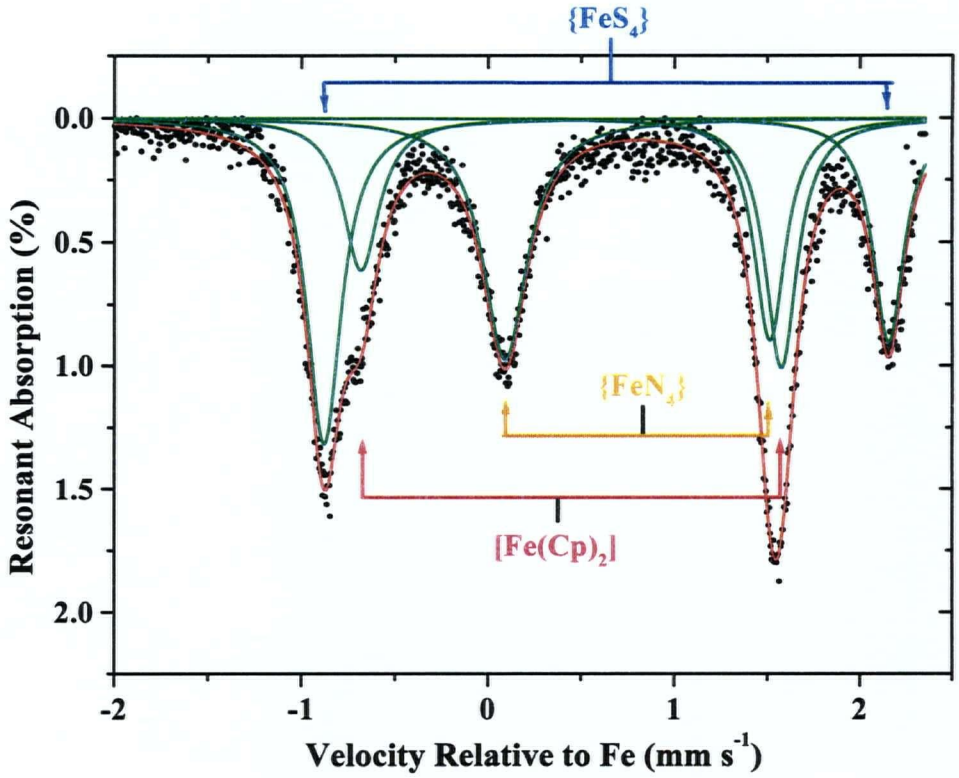

Figure 7.9 Mössbauer spectrum of $[Fe(1\text{-Me-2-S-imid})_2 \cdot 0.5Cp_2Fe]_x$ at 293 K.

between the polymeric chains (Figures 7.2 and 7.3). The corresponding Mössbauer parameters (isomer shift (δ), quadrupole splitting (ΔE)) for FeN_4, FeS_4 and $Fe(Cp)_2$ sites at 293 K are (0.8 mms^{-1}, 1.42 mms^{-1}), (0.64 mms^{-1}, 3.03 mms^{-1}) and (0.45 mms^{-1}, 2.26 mms^{-1}) respectively. These are fairly typical values for iron(II) FeN_4 and FeS_4 and for the S = 0 ferrocene [9]. The results at 77 K are (0.94 mms^{-1}, 2.52 mms^{-1}), (0.76 mms^{-1}, 3.30 mms^{-1}) and (0.52 mms^{-1}, 2.41 mms^{-1}) respectively (Figure 7.10).

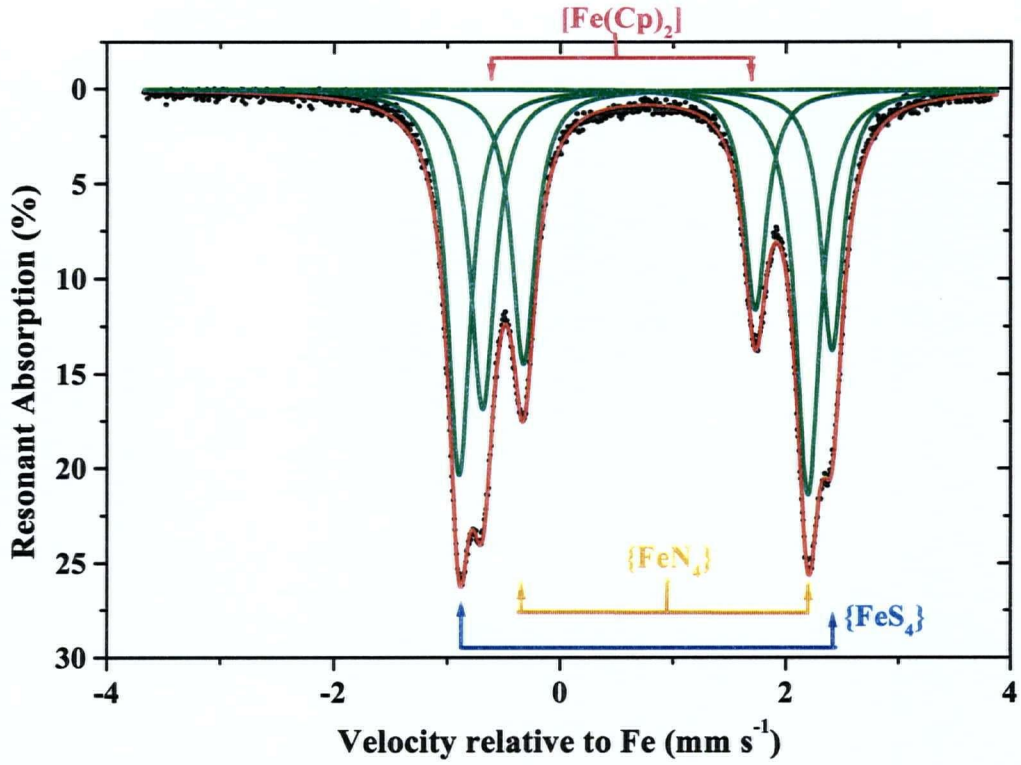

Figure 7.10 Mössbauer spectrum of $[Fe(1\text{-Me-2-S-imid})_2 \cdot 0.5Cp_2Fe]_x$ at 77 K.

As mentioned in Chapter 3, section 3.2.3, the splitting value ranges can often overlap for four, five and six coordination environments (even with similar ligands) depending on the degree of distortion of the local coordination environment [9-11]. On the other hand, isomer shifts have been found to be quite sensitive to coordination number for fixed spin states and similar ligation [9-14]. For tetrahedral FeS_4 chromophores, there is even further reduction of the isomer shift relative to FeN_4 to

values ranging from ~ +0.60 mms^{-1} to 0.75 mms^{-1} owing to the increased covalence of the sulfur ligation environment [15, 16]. Thus, the present δ values in conjuction with the available literature results appear to unequivocally further confirm the four coordinate, tetrahedral FeN_4 and FeS_4, nature of the high spin iron(II) of $[Fe(1\text{-}Me\text{-}2\text{-}S\text{-}imid)_2 \cdot 0.5Cp_2Fe]_x$ and the presence of ferrocene.

As expected, the Mössbauer spectrum of the magnetically ordered phase of $[Fe(1\text{-}Me\text{-}2\text{-}S\text{-}imid)_2 \cdot 0.5Cp_2Fe]_x$ (Figure 7.11) corresponds to the overlap of two Zeeman patterns and the well known (δ = 0.55 mm s^{-1}, ΔE = 2.47 mm s^{-1}) quadrupole doublet of ferrocene. The extreme transition pairs of the FeN_4 and FeS_4 hyperfine patterns, and the doublet of ferrocene, are designated with arrows in Figure 7.11.

The FeS_4 site exhibits a smaller temperature dependence than FeN_4 (< +0.3 mm s^{-1} vs +1.1 mm s^{-1}) over the decreasing temperature range 293 K to 77 K, and has an absolute value of quadrupole splitting larger than that for FeN_4 chromophore by ~ 0.8 mm s^{-1} at 77 K. These observations indicate a significantly larger low symmetry ligand field component splitting (Δ) of the ground ^5E term of the regular tetrahedron to the nondegenerate ^5B and ^5A states of distorted FeS_4 and, in addition, a concomitant greater quenching of the orbital contributions to the moment for FeS_4 than FeN_4 via the

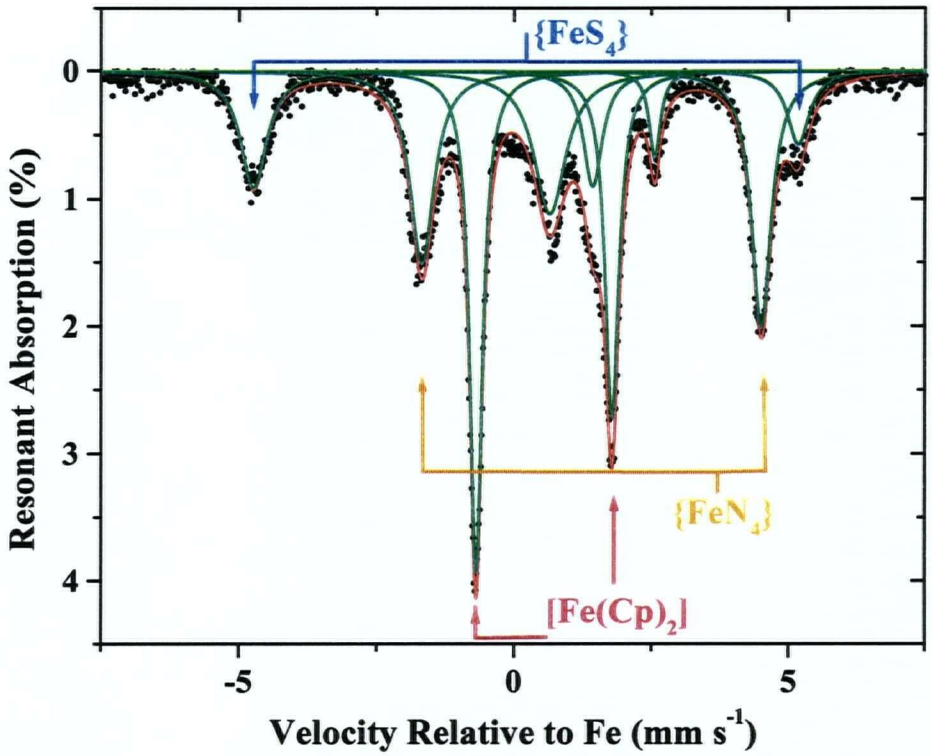

Figure 7.11 Mössbauer spectrum of $[Fe(1\text{-Me-2-S-imid})_2 \cdot 0.5Cp_2Fe]_x$ at 4.2 K.

usual first order and spin-orbit coupling effects [9, 17]. These effects can lead to significant differences in the effective g values for the FeN_4 and FeS_4 chromophores with g likely closer to 2 for the latter. These arguments support the possibility of the existence of a subtler intrinsic "intra-chain ferrimagnetism", which arises from g factor modulation (alternation) along the polymeric chain contributing, thus, to the weak ferromagnetism exhibited by $[Fe(1\text{-Me-2-S-imid})_2 \cdot 0.5Cp_2Fe]_x$.

7.3 SUMMARY AND CONCLUSIONS

$[Fe(1\text{-}Me\text{-}2\text{-}S\text{-}imid)_2 \cdot 0.5Cp_2Fe]_x$ has a rod-like polymer structure in which iron ions are double bridged by 1-methyl-2-thioimidazolate ligands. The metal chromophores alternate along the chain between FeS_4 and FeN_4. DC magnetization studies on powdered samples reveal a net magnetization at zero field and temperatures below 8 K. AC magnetization studies confirm the long-range ferromagnetic order in this system and permit an accurate evaluation of the critical temperature, T_c = 5 K. Magnetization versus applied field studies at 4.8 K generate a hysteresis loop with a remnant magnetization of 190 cm^3Gmol^{-1} and a coercive field of 40 G. Antiferromagnetic intrachain coupling with spin canting generating residual spin on the chains that undergo long-range ferromagnetic ordering is believed to be a probable cause of the magnetic behaviour observed for this material. An alternative explanation for the weak ferromagnetism exhibited by $[Fe(1\text{-}Me\text{-}2\text{-}S\text{-}imid)_2 \cdot 0.5Cp_2Fe]_x$, which is the alternation of the *g* values along the polymer chain, has been considered following the Mössbauer spectroscopy results, in particular the temperature dependence and limiting values of the quadrupole splittings of the paramagnetic ferrous sites of this system. It is concluded that both mechanisms are probably operative here.

$[Fe(1\text{-}Me\text{-}2\text{-}S\text{-}imid)_2 \cdot 0.5Cp_2Fe]_x$ possesses very unique and complex magnetic properties which may require further study to make a definitive assessment of the dominant phenomenon, spin canting versus g factor differences, that generates the

magnetic ground state of this system. Determination of the magnetic structure by neutron diffraction studies could provide new insights to this matter; however, sufficiently large, deuterated, single crystal samples of $[Fe(1\text{-Me-2-S-imid})_2 \cdot 0.5Cp_2Fe]_x$ would be required for this work.

References

1. S. J. Rettig, V. Sánchez, A. Storr, R. C. Thompson, and J. Trotter, *Inorg. Chem.* **38**, 5920 (1999).

2. D. A. Cooper, S. J. Rettig; A. Storr, and J. Trotter. *Can. J. Chem.* **64**, 1643 (1986).

3. O. Kahn. *Acc. Chem. Res.* **33** (10) 647 (2000).

4. S. J. Rettig, A. Storr, D. A. Summers, R. C. Thompson, and J. Trotter. *J. Am. Chem. Soc.* **119**, 8675 (1997).

5. S. J. Rettig, A. Storr, D. A. Summers, R. C. Thompson, and J. Trotter. *Can. J. Chem.* **77**, 425 (1999).

6. M. A. Martinez-Lorente, V. Petrouleas, R. Poinsot, J. P. Tuchagues,, J. M. Savariault, and M. Drillon, *Inorg. Chem.* **30**, 3587 (1991).

7. R. L. Carlin. *Magnetochemistry*. Springer-Verlag. Berlin. 1986.

8. W. Hiller, J. Strahle, A. Datz, M. Hanack, W. F. Hatfield, and P. Gutlich, *J. Am. Chem. Soc.* **106**, 329 (1984).

9. N.N. Greenwood and T. C. Gibb. *Mössbauer Spectroscopy*. Chapman and Hall Ltd. London. 1971.

10. B. W. Dockum , and W. M. Reiff. *Inorganica Chimica Acta.* **35**, 285 (1979).

11. F. F. Charron, and W. M. Reiff. *Inorg. Chem.* **25**, 2786 (1986).

12. W. M. Reiff, N. E. Erickson, and W. A. Baker. *Inorg. Chem.* **8**, 2119 (1969).

13. D. Sedney, M. Kahjehnassiri, and W. M. Reiff. *Inorg. Chem.* **20**, 3476 (1981).

14. B. W. Dockum, and W. M. Reiff. *Inorganica Chimica Acta.* **120**, 61 (1986).

15. W. M. Reiff, I.E. Grey, A. Fan, Z. Eliezer, and H. Steinfink. *J. Solid State Chem.*, **13**, 32 (1975).

16. K. K. Rao, M. C. W. Evans, R. Cammack, D. O. Hall, C. L. Thompson, P. J. Jackson, and C. E. Johnson. *Biochem, J.* **129**, 1063 (1972).

17. R. M. Golding, K. F. Mok, and J. F. Duncan. *Inorg. Chem.* **5**, 774 (1966).

Chapter 8 GENERAL SUMMARY AND SUGGESTIONS FOR FUTURE WORK

8.1 GENERAL SUMMARY

This dissertation describes an investigation of the synthesis, structural and physical characterization, and in particular the magnetic properties, of one-, two- and three-dimensional transition metal polymers involving pyrazolate and, mainly, imidazolate and imidazolate derived ligands as bridging species.

1,2-Diazolates (pyrazolates) in combination with divalent paramagnetic transition metals typically form 1-D chain structures with double-bridging azolate ligands, materials which show short-range antiferromagnetic interactions between metal centers. A new compound in this series, $[Fe(pz)_2]_x$, has been synthesized and structurally and magnetically characterized. As expected, the structure of this 1-D polymer resembles a chain, due to the double-bridging characteristic of the pyrazolate ligands. Also as expected, this compound exhibited short-range antiferromagnetic exchange, with $-J$ = 0.591(5) cm^{-1}, a value that represents the weak antiferromagnetism occurring between the tetrahedral metal centers in this compound.

In contrast, when 1,3-diazolates ligands (imidazolates) were utilized, extended 2-D and 3-D lattices with singly bridging azolates between the metal centers were obtained.

Many of these materials were shown to exhibit, at low temperatures, net magnetization in zero applied field, a property which classifies them as molecule-based magnets.

The reaction of ferrocene with molten 4-azabenzimidazole resulted in the isolation of a 3-D iron(II) coordination polymer. This compound was obtained as a crystalline material and its structure determined by single crystal X-ray diffraction. The structure involves a unique single (non-interpenetrating), totally covalent, diamondoid array of Fe(II) centers, which are single bridged by the 1,3-diazolate ligands into a 3-D array of fused rings each containing six distorted tetrahedral Fe(II) centers. Replacing ferrocene by cobaltocene produced the cobalt analogue as a microcrystalline compound. X-ray powder diffraction studies revealed the two compounds are isomorphous. Variable temperature DC magnetic susceptibility studies on these compounds reveal antiferromagnetic coupling between neighboring metal ions above about 20 K for the iron compound and 11 K for the cobalt analogue. Below these temperatures both materials show long-range ferromagnetic ordering. This behaviour suggests canted-spin structures are present in these compounds. By cycling the DC applied field at 4.8 K, hysteresis loops with M_{rem} of 2100 and 22 cm^3Gmol^{-1} and H_{coer} of 80 and 100 G were obtained for $[Fe(4\text{-abimid})_2]_x$ and the cobalt analogue, respectively. AC magnetic susceptibility studies confirmed the magnetic transition occurring in $[Fe(4\text{-abimid})_2]_x$. Mössbauer spectroscopy studies in this compound revealed a ferromagnetic transition at 18 K and the possibility of a structural phase transition at low temperature.

The cobalt(II) compounds, $[Co(imid)_2]_x$, $[Co(benzimid)_2]_x$ and $[Co_3(imid)_6(imidH)_2]_x$, all exhibited a sudden increase in their magnetic moments below temperatures of ~ 16, 13 and 15 K, respectively, and magnetic hysteresis behavior at temperatures lower than these. X-ray powder diffraction studies showed $[Co_3(imid)_6(imidH)_2]_x$ to be isomorphous with the iron analogue which was reported previously [1], and which has a 3-D structure with single-bridging imidazolate ligands. The structures of the other two cobalt compounds are not known with certainty but are thought to be 3-D as well. Thus, according to their magnetic properties, these three cobalt compounds are considered to belong to the class of materials known as molecule-based magnets. In addition, two other cobalt imidazolate compounds, $[Co(2\text{-meimid})_2]_x$ and $[Co(4\text{-meimid})_2]_x$, where studied. However, these two compounds, which likely have 3-D structures also, show only weak antiferromagnetic coupling with no strong evidence of a transition to a ferromagnetic state at low temperatures. The lack of definitive structural information for these cobalt polymers precluded further explanation of their magnetic behaviours.

Other transition metal imidazolate compounds synthesized included nickel(II) benzimidazolate, the characterization of which showed it to be the first reported molecule-based magnet containing nickel(II) ions. This compound exhibits net magnetization at zero applied field, and ZFCM and FCM curve shapes that reveal long-range ferromagnetic ordering below a T_c of ~ 6.5 K. In addition, three copper(II) imidazolate compounds, $[Cu(2\text{-meimid})_2]_x$, $[Cu(benzimid)_2]_x$ and

$[Cu(4,5\text{-dichloroimid})_2]_x$, were found to be molecule-based magnets. This was revealed by DC magnetic susceptibility studies, that show an increase in both χ and μ_{eff} at temperatures of ~ 25, 15 and 14 K, respectively. Also, the presence of a hysteresis loop in field-dependent magnetization studies at low temperature as well as ZFCM-FCM experiments confirmed the existence of a magnetic transition to a long-range ferromagnetic state for these three copper compounds. Two additional copper(II) imidazolates, $[Cu(imid)_2]_x$ and $[Cu(4\text{-meimid})_2]_x$, were prepared. These showed only weak antiferromagnetic behaviour and gave no evidence for long-range magnetic order.

Efforts to modify the molecular dimensionality, and hence the magnetic properties, of transition metal imidazolates by incorporating neutral chelating ligands into the lattice resulted in the formation of $[Fe_2(imid)_4(bipy)]_x$ and its cobalt analogue. Single crystal X-ray diffraction studies on $[Fe_2(imid)_4(bipy)]_x$ show a structure involving double layer sheets of iron ions single-bridged by imidazolate ligands. Four- and six-coordinated ions alternate in the lattice, the latter ions being coordinated by the bipy ligands in addition to the bridging imidazolates. This capping of iron centres by bipy controls the dimensionality, resulting in the 2-D polymer. $[Fe_2(imid)_4(bipy)]_x$ is unique in showing two structural phase transitions at ~ 151 K and ~ 135 K, which have been characterized by a combination of single crystal X-ray-diffraction, DC and AC magnetic susceptibility and Mössbauer spectroscopy studies. In addition, $[Fe_2(imid)_4(bipy)]_x$ shows a sharp increase in the DC magnetic susceptibility below 11 K, and a non-zero AC out-of-phase magnetic susceptibility below that temperature, indicative of a transition to a

ferromagnetically ordered state at low temperatures. Variable temperature DC magnetic susceptibility studies on $[Fe_2(imid)_4(bipy)]_x$ and the cobalt analogue revealed antiferromagnetic coupling between neighbouring metal ions above T_c (11 and 13 K respectively). Below T_c both materials exhibit long-range ferromagnetic ordering. The presence of canted-spin structures in both compounds is suggested by this behaviour; however, a novel type of ferrimagnetism, due to the systematic alternation of four- and six-coordinate chromophores has also been invoked as a possible mechanism for the observed magnetic behaviour.

$[Fe_4(imid)_8(terpy)]_x$ has a novel 2-D extended structure in which "wrinkled" sheets of four-coordinate (two unique centers of this type), five-coordinate and six-coordinate iron ions are linked by single-bridging imidazolate ligands. The six – coordinate metal centers are additionally coordinated by terpy ligands that occupy positions between the sheets, isolating the sheets from each other. The presence of four unique iron sites was confirmed by Mössbauer spectroscopy. DC magnetic susceptibility measurements revealed antiferromagnetic interactions between metal centers above T_c and a transition to a ferromagnetic state below this temperature. A T_c of 6.5 K, was confirmed by AC magnetic susceptibility and ZFCM-FCM-REM studies. Magnetic hysteresis studies revealed the magnetic properties of this system to be unique among the imidazolate systems studied here. Negative magnetizations at zero field were explained by invoking a mechanism in which three of the four unique sites act as fast relaxing

paramagnets with the fourth acting as a slow relaxing paramagnet and generating the observed magnetization in zero field.

$[Fe(1\text{-}Me\text{-}2\text{-}S\text{-}imid)_2 \cdot 0.5\ Cp_2Fe]_x$ has a unique rod-like polymer structure in which iron ions are double bridged by 1-methyl-2-thioimidazolate ligands. FeS_4 and FeN_4 metal chromophores alternate along the chains. Magnetic studies showed a net magnetization at zero field and temperatures below 8 K. Magnetization versus applied field studies at 4.8 K generate a hysteresis loop with a remnant magnetization of 190 cm^3Gmol^{-1} and a coercive field of 40 G. Antiferromagnetic intrachain coupling with spin canting was proposed to generate residual spin on the chains that undergo long-range ferromagnetic order below ~ 8 K. Due to the alternation on the FeS_4 and FeN_4 chromophores throughout the chains, a possible novel type of ferrimagnetism has also been proposed to contribute to the magnetic ordering exhibited by this compound. Mössbauer spectroscopy provided unambiguous evidence for the presence of the two iron chromophores and ferrocene as well as the magnetic transition in this compound. This material provides a relatively rare example of a molecule-based magnet in which the covalent connectivities in the lattice are 1-D.

In summary, a relatively new family of molecule-based magnets incorporating imidazolate-based ligands as mediators of magnetic exchange between the metal ions has been established in this work. It has been demonstrated that heterocyclic azolate ligands with two donor nitrogens separated by a single carbon in the ring (as in the imidazolate

ion) will form single ligand bridges and extended structures. Moreover these ligands will create a bridge geometry that leads to a systematic alternation in the relative orientation of neighboring chromophores in the lattice, a situation that can produce significant spin canting and, as a consequence, long-range ferromagnetic ordering at low temperatures.

Examples now exist of iron(II) complexes incorporating imidazolate-based ligands which, as confirmed by single crystal X-ray diffraction, have 1-D $\{[Fe(1\text{-}Me\text{-}2\text{-}S\text{-}imid)_2 \cdot 0.5Cp_2Fe]_x\}$, 2-D $\{[Fe_2(imid)_6bipy)]_x$ and $[Fe_4(imid)_8(terpy)]_x\}$, and 3-D $\{[Fe(4\text{-}abimid)_2]_x\}$ extended covalent lattices. All of these compounds exhibit magnetic properties that classify them as molecule-based magnets.

8.2 SUGGESTIONS FOR FUTURE WORK

In order to learn more about the possible low-temperature structural phase transition occurring in $[Fe(4\text{-}abimid)_2]_x$ a single crystal X-ray diffraction study at He temperatures is required. This may allow a better understanding of the magnetic properties of this diamondoid compound. In addition, neutron diffraction studies would contribute to the complete understanding of the magnetic properties.

In regard to the cobalt(II), nickel(II) an copper(II) imidazolate polymers, further synthetic attempts to produce single crystals suitable for X-ray diffraction studies would be worthwhile.

Incorporation of other chelating ligands (such as 5,5'-dimethyl-2,2'-bipy) into metal imidazolate structures to obtain compounds similar to $[Fe_2(imid)_4(bipy)]_x$ and $[Fe_4(imid)_8(terpy)]_x$ is encouraged to try to generate extended 2-D systems with subtle structural modifications. This would allow the investigation of the effect of such structural changes on magnetic properties. Moreover, especially for materials similar to $[Fe_2(imid)_4(bipy)]_x$, the study of potential structural phase transitions in these systems would be of significant interest.

Due to the complex magnetic properties found in $[Fe(1\text{-}Me\text{-}2\text{-}S\text{-}imid)_2 \cdot 0.5\ Cp_2Fe]_x$, and in order to get more insight about the predominant phenomenon (spin-canting versus *g* factor differences) responsible for the long-range ferromagnetic ordering exhibited by this material, neutron diffraction studies could be attempted. This would require the synthesis of large, deuterated, single crystals of the compound.

Finally, the pyrazole complexes $[Cu(pzH)_4(NO_3)_2]$, $[Co(pzH)_4(NO_3)_2]$, and $[Ni(pzH)_4(NO_3)_2]$ as well as $[Co(2\text{-}(2\text{-}py)benzimidH)_3(ClO_4)_2]$ (py = pyridine) were synthesized in the course of this work. These materials have the potential to be used as building blocks for the formation of hetero-bimetallic ferrimagnetic 1-D, 2-D or 3-D networks [2].

References

1. S. J. Rettig, A. Storr, D. A. Summers, R. C. Thompson and J. Trotter, *J Amer. Chem. Soc.* **119**, 8675 (1997).

2. F. Lambert, J-P. Renault, C. Policar, I. Morgenstern-Badarau, and M. Cesario. *Chem. Commun.* 35 (2000).

Chapter 9 *EXPERIMENTAL*

9.1 INTRODUCTION

The experimental details of this work including synthetic aspects and materials employed are described here. The instruments and methods employed in the physical characterization of the compounds studied are also described.

9.2 SYNTHESES

The chemicals used in this thesis were of reagent grade and were used without further purification. The commercial sources for most of chemical reagents utilized in the syntheses carried out in the present work are given in Table 9.1. The majority of compounds prepared here are air stable, hence they were synthesized without special precautions. Those compounds that exhibited sensitivity to oxygen or moisture were prepared using Schlenk techniques and handled in a Vacuum Atmospheres Corporation Model HE 43-2 Dri-Lab glovebox under a dinitrogen atmosphere. All solvents used with these air-sensitive compounds were free of water and deoxygenated. The solvents were dried using the following methods: acetonitrile was refluxed with phosphorous pentoxide and distilled under dinitrogen; benzene was refluxed with potassium metal

and distilled under dinitrogen; xylenes were refluxed with sodium and benzophenone and distilled under dinitrogen.

Table 9.1 Commercial source of most chemical reagents employed in this thesis (continued overleaf).

Compound	Commercial source
Acetonitrile	Aldrich
4-Azabenzimidazole	Aldrich
Benzene	Aldrich
Benzimidazole	Eastman
4,5-dichloroimidazole	Aldrich
Cobaltocene	Strem
Cobalt chloride hexahydrate	Fisher
Cobalt nitrate hexahydrate	Mallinckrodt
Copper sulphate pentahydrate	J. T. Baker
Ferrocene	Strem
imidazole	Aldrich
2-mercapto-1-methylimidazole	Lancaster
2-methylimidazole	Lancaster

4-methylimidazole	Aldrich
3,5-dimethylpyrazole	Aldrich
Nickel nitrate hexahydrate	Mallinckrodt
Phosphorous pentoxide	BDH
Potassium hydroxide	AnalaR
Pyrazole	Aldrich
2-(2-pyridyl)benzimidazole	Aldrich
2,2'-bipyridine	Matheson, Coleman & Bell
2,2':6',2"-terpyridine	Matheson, Coleman & Bell
Sodium hydroxide	AnalaR
Xylenes	Aldrich

9.2.1 IRON(II) AZOLATE POLYMERS

9.2.1.1 Polybis(pyrazolato)iron(II), $[Fe(pz)_2]_x$

Ferrocene (0.3 g, 1.6 mmol), and pyrazole (0.2 g, 2.9 mmol) were mixed in a Carius tube, and then sealed under vacuum. The mixture was heated to 145 °C for 5 days. During that time, product in the form of needles crystallized from the orange solution. After cooling to room temperature, the Carius tube was opened under a dinitrogen atmosphere. The product was extracted by washing the solid obtained

thoroughly with acetonitrile. It was isolated as red-brown air-sensitive crystals suitable for X-ray crystallographic analysis. Yield 0.11 g (37 %). Analysis calculated for $C_6H_6FeN_4$: C 37.9; H 3.2; N 29.5; found: C 37.7; H 3.4; N 29.4.

9.2.1.2 Poly-2,2'-bipyridinetetrakis(imidazolato)diiron(II), $[Fe_2(imid)_4(bipy)]_x$.

Ferrocene (0.3 g, 1.6 mmol), imidazole (0.2 g, 2.9 mmol) and excess 2,2-bipyridine (0.5 g, 3.2 mmol) were placed in a Carius tube which was sealed under vacuum. The tube was heated to 130 °C for 2 days. Under those conditions, the original orange solution of ferrocene in molten ligand became a mixture of dark crystals and brown solution. Upon cooling to room temperature, the product appeared to be a crystalline dark brown-green solid embedded in non-reacted ligand, ligand precursors and ferrocene. The Carius tube was opened under a dinitrogen atmosphere. The excess of ligand and ligand precursors was extracted with acetonitrile and benzene solvents. The product was isolated as dark green moisture sensitive crystals suitable for X-ray crystallographic analysis. Yield 0.52 g (60 %). Analysis calculated for $C_{22}H_{20}Fe_2N_{10}$: C 49.3; H 3.8; N 26.1; found: C 49.6; H 3.7; N 26.4.

9.2.1.3 Polybis(4-azabenzimidazolato)iron(II), $[Fe(4\text{-abimid})_2]_x$.

Ferrocene (0.2 g, 1.07 mmol) and 4-azabenzimidazole (0.512g, 4.3 mmol) were placed in a Carius tube which was sealed under vacuum. The tube was heated at 145 °C

for 6 days. Under these conditions, the original orange solution of ferrocene in molten 4-azabenzimidazole became a mixture of brown-red solid and an orange solution. Upon cooling to room temperature, the product appeared as a crystalline brown solid embedded in the excess, non-reacted imidazole. The Carius tube was opened under a dinitrogen atmosphere. The excess of 4-azabenzimidazole was extracted with dry and oxygen-free acetonitrile and xylenes. The product, which did not decompose in air for periods up to two months (longer periods of time were not examined), was isolated as amber-green crystals suitable for single crystal X-ray analysis. Yield 0.052 g (16 %). Analysis calculated for $C_{12}H_8FeN_6$: C 49.3; H, 2.8; N 28.7; found: C 49.4; H 2.7; N 28.4.

9.2.1.4 Poly-2,2':6', 2"-terpyridine octakis(imidazolato)tetrairon(II), $[Fe_4(imid)_8(terpy)]_x$.

Ferrocene (0.30 g, 1.63 mmol), imidazole (0.22 g, 3.26 mmol) and 2,2':6',2"-terpyridine (0.38 g, 1.63 mmol) were placed in a Carius tube which was sealed under vacuum. The tube was heated to 135 °C for 3 days. Under those conditions, the original orange solution of ferrocene in molten ligand became a mixture of dark crystals and brown solution. Upon cooling to room temperature, the product appeared to be a crystalline dark green solid embedded in non-reacted ligand, ligand precursors, and ferrocene. The Carius tube was opened under a dinitrogen atmosphere. The excess of ligand and ligand precursors was extracted with acetonitrile and toluene solvents. The

product was isolated as dark green moisture sensitive crystals suitable for X-ray crystallographic analysis. Yield 0.43 g (26 %). Analysis calculated for $C_{39}H_{35}Fe_4N_{19}$: C 47.2; H 3.5; N 26.8; found: C 47.5; H 3.6; N 26.9.

9.2.1.5 Polybis(1-methyl-2-thioimidazolato)iron(II)hemidicyclopentadienyliron (II), $[Fe(1\text{-}Me\text{-}2\text{-}S\text{-}imid)_2 \cdot 0.5\ Cp_2Fe]_x$.

Ferrocene (0.5 g, 2.68 mmol) and an excess of 2-mercapto-1-methylimidazole (1.5 g, 13.14 mmol) were combined in a Carius tube which was sealed under vacuum. This mixture was heated at 145 °C for 6 days. During this period, a dark red solution of ferrocene in molten ligand is obtained and light yellow crystals deposited from the solution. The reaction mixture was then allowed to cool down to room temperature, and the Carius tube was opened under a dinitrogen atmosphere. The excess of ligand precursor was extracted with dry and oxygen-free acetonitrile, and residual ferrocene was removed with dry toluene. The compound was isolated as golden needle crystals, which were stable for at least a month of exposure to air (longer periods of time were not investigated). Yield 0.094 g (9 %). Analysis calculated for $C_{13}H_{15}Fe_{1.5}N_4S_2$: C 41.6; H 4.0; N 14.9; found: C 41.5; H 4.0; N 14.7.

9.2.2 COBALT(II) IMIDAZOLATE POLYMERS

9.2.2.1 Polybis(imidazolato)cobalt(II), $[Co(imid)_2]_x$.

Cobalt(II) nitrate hexahydrate (7.5 g, 33 mmol) was dissolved in 10 ml of hot water and added dropwise to a solution of imidazole (3.4 g, 50 mmol) in 40 ml of hot water. The mixture was brought to boil and then immediately filtered. The solid obtained was washed with hot water first, then with acetone. The product was isolated as a microcrystalline purple powder and was dried *in vacuo* at 100 °C. Yield 0.25 g (5%). Analysis calculated for $C_6H_6N_4Co$: C 37.3, H 3.1, N 29.0; found: C 37.6, H 3.0, N 28.7. This compound was also obtained by removal (thermolysis) of two molecules of neutral imidazole from compound $[Co_3(imid)_6(imidH)_2]_x$ (see section 9.2.2.5 below). This thermal treatment of $[Co_3(imid)_6(imidH)_2]_x$ was carried out under a flux of dinitrogen utilizing a TA Instruments TGA 51 unit. A thirty minute isotherm at 325 °C was programmed in the instrument in order to remove the neutral imidazole completely. Analysis found: C 37.1, H 3.0, N 28.8.

9.2.2.2 Polybis(2-methylimidazolato)cobalt(II), $[Co(2\text{-}meimid)_2]_x$.

Cobalt(II) nitrate hexahydrate (1.0 g, 3.7 mmol) was dissolved in 10 ml of ethanol and added dropwise to a solution of 2-methylimidazole (3.0 g, 37 mmol) in 40 ml of ethanol. The purple precipitate which formed immediately was filtered off,

washed with ethanol, and dried for 1 hour at 115 °C. Yield 0.15 g (18 %). Analysis calculated for $C_8H_{10}CoN_4$: C 43.4, H 4.6, N 25.3; found: C 43.0, H 4.3, N 24.9.

9.2.2.3 Polybis(4-methylimidazolato)cobalt(II), $[Co(4\text{-meimid})_2]_x$.

Cobalt(II) chloride hexahydrate (1.0 g, 4.2 mmol) was dissolved in 15 ml of water and added dropwise to a solution of 4-methylimidazole (3.0 g, 37 mmol) in 30 ml of water. Sodium hydroxide (1.48 g, 37 mmol) was dissolved in 5 ml of water and added dropwise to the mixture to complete the precipitation of a fine purple powder. The precipitate was filtered off, washed with water and then ethanol, and air-dried at room temperature. Yield 0.36 g (39 %). Analysis calculated for $C_8H_{10}CoN_4$: C 43.5, H 4.6, N 25.3; found: C 43.6, H 4.5, N 25.0.

9.2.2.4 Polybis(benzimidazolato)cobalt(II), $[Co(benzimid)_2]_x$.

Benzimidazole (11.8 g, 100 mmol) was dissolved in 20 ml of hot water and added to a solution of cobalt(II) nitrate hexahydrate (15.0 g, 51.5 mmol) dissolved in 80 ml of hot water. A purple precipitate formed immediately. The mixture was brought to boil. After the solution was cooled, the precipitate was filtered off, washed with ethanol, water and acetone, and dried under vacuum. Yield 5.1 g (34 %). Analysis calculated. for $C_{14}H_{10}CoN_4$: C 57.3, H 3.4, N 19.1; found: C 57.5, H 3.3, N 19.2.

9.2.2.5 Polybis(imidazole)hexa(imidazolato)tricobalt(II), $[Co_3(imid)_6(imidH)_2]_x$.

This compound was obtained as a purple powder by heating, to 150 °C for 5 days, a mixture of an excess of imidazole (2.0 g, 26 mmol) with cobaltocene (0.2 g, 1.06 mmol) in a sealed and evacuated Carius tube. Dry xylenes and acetonitrile were used to isolate the product from residual ligand precursor. Yield 0.34 g (45 %). Analysis calculated for $C_{24}H_{26}Co_3N_{16}$: C 40.3, H 3.6, N 31.3; found: C 40.8, H 3.6, N 31.2.

9.2.2.6 Polybis(4-azabenzimidazolate)cobalt(II), $[Co(4\text{-abimid})_2]_x$.

Cobaltocene(0.2 g, 1.06 mmol) and 4-azabenzimidazole (0.512g, 4.3 mmol) were placed in a Carius tube which was sealed under vacuum. The tube was heated at 145 °C for 4 days. Upon cooling to room temperature, the Carius tube was opened under a dinitrogen atmosphere. The excess of 4-azabenzimidazole was extracted with dry and oxygen-free acetonitrile and xylenes. The polymer was isolated as a dark purple microcrystalline solid. Yield 0.09 g (29 %). Analysis calculated for $C_{12}H_8CoN_6$: C 48.8; H 2.7; N 28.5; found: C 50.1; H 2.8; N 28.4. Repeated analysis on two different samples of $[Co(4\text{-abimid})_2]_x$ consistently gave good H and N results and high C. There is no explanation for the high C except to suggest there may be small amounts of solvent trapped in the sample.

9.2.2.7 Poly-2,2'-bipyridinetetrakis(imidazolato)dicobalt(II), $[Co_2(imid)_4(bipy)]_x$.

Cobaltocene (0.3 g, 1.6 mmol), imidazole (0.2 g, 2.9 mmol) and excess 2,2'-bipyridine (0.5 g, 3.2 mmol) were placed in a Carius tube which was sealed under vacuum. The tube was heated to 130 °C for 2 days. The Carius tube was opened under a dinitrogen atmosphere. The excess of ligand and ligand precursors was extracted with acetonitrile and benzene solvents. The product was obtained as a purple microcrystalline solid. Yield 0.47 g (54 %). Analysis calculated for $C_{22}H_{20}Co_2N_{10}$: C 48.7; H 3.7; N 25.8. Found: C 49.0; H 3.7; N 25.6.

9.2.3 NICKEL(II) IMIDAZOLATE POLYMER

9.2.3.1 Polybis(benzimidazolato)nickel(II), $[Ni(benzimid)_2]_x$.

Benzimidazole (11.8 g, 100 mmol) was dissolved in 20 ml of hot water and added to a solution of nickel(II) nitrate hexahydrate (15.0 g, 51.5 mmol) dissolved in 80 ml of hot water. A light violet precipitate was formed immediately. The mixture was brought to the boil. After the solution was cooled, the precipitate was filtered off, washed with ethanol, water and acetone, and dried under vacuum. Yield 0.82 g (5 %). Analysis calculated for $C_{14}H_{10}NiN_4$: C 57.5, H 3.4, N 19.2; found: C 57.2, H 3.4, N 19.2.

9.2.4 COPPER IMIDAZOLATE POLYMERS

In the following syntheses, wherever copper is used as a reactant it refers to copper metal beads (3-5 mm diameter) which had been cleaned by washing them with 12 M HCl, water, and acetone prior to use.

9.2.4.1 Polybis(imidazolato)copper(II), $[Cu(imid)_2]_x$.

Copper (8.13g, 128 mmol) and imidazole (10 g, 147 mmol) were placed in a 100 ml round-bottomed flask fitted with a condenser. The reaction mixture was heated to 110 °C and air was bubbled into the mixture via a Pyrex tube for 48 h. A dark blue solid began to form. Sublimed imidazole was periodically scraped back into the reaction flask during the reaction. Upon cooling, the solidified mixture was extracted with ethanol, suction filtered, and further washed with acetone, and air-dried at room temperature. The dark blue powdery compound was isolated by physical separation from the copper shot. A 84 % yield was obtained based on amount of copper reacted. Analysis calculated for $C_6H_6CuN_4$: C 36.4, H 3.1, N 28.3; found: C 36.5, H 3.0, N 27.9.

9.2.4.2 Polybis(2-methylimidazolato)copper(II), $[Cu(2\text{-}meimid)_2]_x$.

Copper (1.9 g, 30 mmol) and an ethanolic solution (~ 75 ml) of 2-methylimidazole (3.0 g, 37 mmol) were placed in a round-bottomed flask. The reaction

mixture was stirred at room temperature for 3 days. A dark brown precipitate, which formed, was suction filtered and washed thoroughly with ethanol and acetone. Air drying at room temperature yielded a light brown powder. A 77 % yield was obtained (based on amount of copper reacted). Analysis calculated for $C_8H_{10}CuN_4$: C 42.6, H 4.5, N 24.8; found: C 42.4, H 4.3, N 24.5.

9.2.4.3 Polybis(4-methylimidazolato)copper(II), $[Cu(4\text{-meimid})_2]_x$.

Copper(II) sulphate hexahydrate (1.0 g, 3.7 mmol) was dissolved in 15 ml of water and added dropwise to a solution of 4-methylimidazole (3.0 g, 37 mmol) in 50 ml of water. 35 ml of a 1 M aqueous solution of NH_3 was added dropwise to the mixture to complete the precipitation of a fine brown powder. The precipitate was filtered off, washed with water and then ethanol, and air-dried at room temperature. A brown powdery solid was obtained. Yield 0.57 g (68 %). Analysis calculated for $C_8H_{10}CuN_4$: C 42.6, H 4.5, N 24.8; found: C 42.6, H 4.5, N 24.5.

9.2.4.4 Polybis(benzimidazolato)copper(II), $[Cu(benzimid)_2]_x$.

Clean copper beads (1.0 g, 16 mmol) and an ethanolic solution of benzimidazole (3.6 g, 30 mmol) were placed in a round bottom flask. After 5 days of vigorous stirring of the solution at room temperature, a red precipitate was formed. The solid was suction filtered and washed with ethanol. After air drying at room temperature the compound

was obtained as a red powder. 79 % yield was obtained based on amount of copper reacted. Analysis calculated for $C_{14}H_{10}CuN_4$: C 56.5, H 3.4, N 18.8; found: C 56.2, H 3.4, N 18.6.

9.2.4.5 Polybis(4,5-dichloroimidazolato)copper(II), $[Cu(4,5\text{-dichloroimid})_2]_x$.

Copper(II) sulphate pentahydrate (1.0 g, 4.0 mmol) was dissolved in 15 ml of water and added dropwise to a solution of 4,5-dichloroimidazole (3.0 g, 22 mmol) in 60 ml of hot water. 20 ml of a 1 M aqueous solution of NH_3 was added dropwise to the mixture to complete the precipitation of a fine gray-pink precipitate. The precipitate was filtered off, washed with water and then ethanol, and air dried at room temperature. A violet powdery product was obtained. Yield 0.37 g (28 %). Analysis calculated for $C_6H_2Cl_4CuN_4$: C 21.5, H 0.6, N 16.7; found: C 21.6, H 0.8, N 17.0.

9.3 PHYSICAL METHODS

9.3.1 MAGNETIC SUSCEPTIBILITY MEASUREMENTS

DC magnetic susceptibility measurements were performed using a Quantum Design (MPMS) SQUID magnetometer. These measurements were made at temperatures over the range 2-300 K and, unless otherwise stated, at applied fields of 500 and 10 000 G. Magnetization studies as a function of field strength (0-55 000 G)

were made at several temperatures and hysteresis magnetization data were obtained by oscillating the applied magnetic field between +55 000 G and –55 000 G usually at 4.8 K. The sample holder is made of PVC plastic and is designed to go undetected by the magnetometer. The PVC sample holder and details regarding the use of the equipment have been described before [1]. Magnetic susceptibilities were corrected for background and for the diamagnetism of all atoms using Pascal's constants [2]. All magnetic measurements were done on fine powdered samples and the data reported here are on a per mole of metal ion basis. Temperature calibrations on the SQUID magnetometer are performed using an external platinum resistance thermometer and a temperature accuracy within 0.1% is attained. Magnetic susceptibility signals were calibrated using ultra-pure nickel standard and accuracy within 1% is obtained.

When a material is suspected to behave as a molecule-based magnet below a T_c, such as the majority of the transition metal imidazolate compounds described in this thesis, certain precautions must be taken in the determination of its magnetic properties, to avoid misleading results. Problems are encountered if the remnant magnetization present after the collection of one set of magnetic data is not removed before another set of magnetic data is collected. If not removed, the remnant magnetization may influence or dominate any new magnetic signal detected by the magnetometer. A convenient way to remove this magnetization is to heat the sample above its T_c, then, set the applied field to zero by oscillating the field between positive and negative values (decreasing the magnitude of the field in each oscillation), and finally cooling the sample to the

desired temperature in zero applied field. This procedure was applied to every molecule-based magnet investigated in this dissertation.

AC magnetic susceptibility measurements were made by W. M. Reiff at Northeastern University using a Lake Shore Cryotronics Co. Model 7000 AC susceptometer, generally over the temperature range 4.2 K to 30 K in an AC field of 1.0 G or 2.5 G at frequencies of 125 Hz or 500 Hz.

9.3.2 SINGLE CRYSTAL X-RAY DIFFRACTION

Measurements were made by S. J. Rettig and B. O. Patrick of this Department using either a Rigaku/ADSC CCD diffractometer or a Rigaku AFC6S diffractometer, both with graphite monochromated Mo-Kα radiation. The low-temperature single crystal X-ray diffraction study of $[Fe_2(imid)_4(bipy)]_x$ was performed by B. O. Patrick.

9.3.3 POWDER X-RAY DIFFRACTION

Powder diffractograms were recorded at room temperature on a Rigaku Rotaflex RU-200BH rotating anode powder X-ray diffractometer (graphite monochromated Cu *K*α radiation). Samples were prepared by applying a hexanes slurry of the compound onto a glass plate and allowing the solvent to evaporate.

9.3.4 ELEMENTAL ANALYSIS

Microanalysis were performed by P. Borda of this Department. A Carlo Erba Model 1106 or a Fisons (Erba) Instruments EA 1108 CHN-O Elemental Analyzer were utilized for determination of carbon, hydrogen and nitrogen percentages. Elemental analyses are considered to have an absolute accuracy within ±0.3%.

9.3.5 MÖSSBAUER SPECTROSCOPY

The Mössbauer spectra were obtained by W. M. Reiff at Northeastern University using a conventional constant acceleration spectrometer operated in multichannel scaling mode. The gamma ray source (Du Pont- Merck Co.) consisted of 51.5 mCi of Co^{57} in a rhodium metal matrix that was maintained at ambient temperature. The spectrometer was calibrated using a 6-micron thick natural abundance iron foil. Isomer shifts are reported relative to the center of the magnetic hyperfine pattern of the latter foil taken as zero velocity. Apiezon-N grease mull samples (where the compounds studied were in a macro-crystalline form), were used in all measurements carried out. Sample temperature variation was achieved using a standard exchange gas liquid helium cryostat (Cryo Industries of America, Inc.) with temperature measurement and control based on silicon diode thermometry in conjunction with a 10 microampere excitation source (Lakeshore Cryotronics, Inc). Spectra were fit to unconstrained Lorentzians using the program ORIGIN (Microcal Software, Inc.).

9.3.6 ELECTRONIC SPECTROSCOPY

Electronic spectra (200-3000 nm) were obtained at room temperature using a Varian Cary 5 UV-Vis-NIR spectrophotometer. Samples were prepared as Nujol mulls pressed between quartz plates.

9.3.7 TGA

Thermal gravimetric analysis (35 °C to 800 °C) was done using a TA Instruments TA 2000 system with a TGA 51 unit. Powdered samples (7 –12 mg) were heated in a dinitrogen atmosphere at a rate of 10 °C per minute to a maximum temperature of 800 °C.

9.3.8 INFRARED SPECTROSCOPY

Infrared spectra (4000-400 cm^{-1}) were recorded at room temperature on a Bomem FTIR spectrophotometer using KBr disk samples or Nujol mulls pressed between KBr disks. Band frequencies are accurate to within ±4 cm^{-1}.

9.3.9 NMR SPECTROSCOPY

Nuclear magnetic resonance spectra were recorded in a Bruker AC-200 FT-NMR Spectrometer. NMR solvents were used as internal standards for calibration of the observed chemical shifts.

References

1. M. K. Ehlert. Ph. D. Thesis. University of British Columbia, 1992.

2. E. Konig. *Landolt-Börstein Numerical Data and Functional Relationships in Science and Technology*. New Series, Vol. II/2. K. H. Hellwege and A. M Hellwege Eds. Springer-Verlag, Berlin, 1966.

APPENDIX I SINGLE CRYSTAL X-RAY DIFFRACTION DATA

Table I-1 Crystallographic data for $[Fe(pz)_2]_x$

Molecular formula	$C_6H_6FeN_4$
fw	94.99
Crystal system	orthorhombic
Space group	Ibam (No. 72)
a/Å	7.515(2)
b/Å	14.604(4)
c/Å	7.359(1)
V/Å^3	807.7(2)
Z	8
D_c/g cm^{-3}	1.562
μ (MoKα)/cm^{-1}	18.02
Crystal size/mm	0.50 x 0.10 x 0.10
R(*F*)[a]	0.024
Rw (F^2)[a]	0.032

[a] $R(F) = \Sigma||F_0|-|F_C||/\Sigma|F_0|$, $Rw\ (F^2) = (\Sigma w||F_0^2|-|F_C^2||/\Sigma w|F_0^2|^2)^{1/2}$

Table I-2 Selected bond lengths (Å) and angles (°) for $[Fe(pz)_2]_x$ with estimated standard deviations in parentheses.

Fe(1)—N(1)	2.027(1)	N(1)—C(3)	1.337(2)
N(1)—Fe(1)—N(1a)	110.27(6)	N(1)—Fe(1)—N(1b)	108.93(6)
N(1)—Fe(1)—N(1c)	109.22(6)	N(1a)—Fe(1)—N(1b)	109.22(9)
N(1a)—Fe(1)—N(1c)	108.93(9)	N(1b)—Fe(1)—N(1c)	110.27(9)

Table I-3 Crystallographic data[a] for $[Fe(4\text{-abimid})_2]_x$.

Molecular formula	$C_{12}H_6FeN_6$
fw	292.08
Crystal system	orthorhombic
Space group	$P2_12_12_1$ (No. 19)
a/Å	9.655(2)
b/Å	10.3403(6)
c/Å	12.4671(7)
U/Å^3	1244.6(2)
Z	4

D_c/g cm^{-3}	1.559
F(000)	592.00
μ (MoKα)/cm^{-1}	12.04
Crystal size/mm	0.15 x 0.20 x 0.20
$2\theta_{max}$/°	60.1
Total reflections	11118
Unique reflections	3233
No. with $I \geq 3\sigma(I)$	1685
No. of variables	172
R; Rw (F, $I \geq 3\sigma(I)$)	0.034; 0.024
R; Rw (F^2, all data)	0.084; 0.055
gof	1.22

---

[a] Temperature 180 K, Rigaku/ADSC CCD diffractometer, Mo $K\alpha$ (λ = 0.71069), graphite monochromator, takeoff angle 6.0°, aperture 94.0 x 94.0 mm at a distance of 39.22(7) mm from the crystal, $\sigma^2(F_2) = (C + B)$/Lp2 (C = scan count, B = background count), function minimized $\Sigma w(|F_0^2|-|F_C^2|)^2$ where $w = 1/\sigma^2(F^2)$, $R(F) = \Sigma||F_0|-|F_C||/\Sigma|F_0|$, $Rw\ (F^2) = (\Sigma w||F_0^2|-|F_C^2||/\Sigma w|F_0^2|^2)^{1/2}$, and gof = $[\Sigma w(|F_0^2|-|F_C^2|)^2/(m-n)]^{1/2}$.

Table I-4 Selected bond lengths (Å) and angles (°) for $[Fe(4\text{-abimid})_2]_x$ with estimated standard deviations in parentheses*.

Fe(1)—N(1)	2.030(3)	Fe(1)—N(2)[a]	2.046(3)
Fe(1)—N(4)	2.044(3)	Fe(1)—N(5)[b]	2.034(3)
N(1)—Fe(1)—N(2)[a]	110.39(11)	N(1)—Fe(1)—N(4)	102.10(11)
N(1)—Fe(1)—N(5)[b]	111.76(11)	N(2)[a]—Fe(1)—N(4)	104.31(11)
N(2)[a]—Fe(1)—N(5)[b]	109.55(11)	N(4)—Fe(1)—N(5)[b]	118.24(11)
Fe(1)—N(1)—C(1)	128.8(3)	Fe(1)—N(1)—C(6)	127.8(2)
Fe(1)[c]—N(2)—C(2)	132.6(2)	Fe(1)[c]—N(2)—C(1)	123.5(2)
Fe(1)—N(4)—C(12)	131.1(2)	Fe(1)—N(4)—C(7)	124.1(3)
Fe(1)[d]—N(5)—C(7)	127.6(2)	Fe(1)[d]—N(5)—C(8)	129.1(2)

* Superscripts refer to symmetry operations: (a) –1/2+x, 3/2-y, 1-z (b) 1-x, -1/2+y, 3/2-z (c) 1/2+x, 3/2-y, 1-z (d) 1-x, 1/2+y, 3/2-z

Table I-5 Crystallographic data for α- and γ-$[Fe_2(imid)_4(bipy)]_x$.

	α-phase	γ-phase
Molecular formula	$C_{22}H_{20}Fe_2N_{10}$	$C_{22}H_{20}Fe_2N_{10}$
fw	536.16	536.16
Crystal system	triclinic	triclinic
Space group	$P\bar{1}$ (No. 2)	$P\bar{1}$ (No. 2)
a, Å	10.507(4)	10.4138(5)
b, Å	13.730(4)	13.5075(5)
c, Å	9.188(3)	26.060(1)
α, deg	106.51(3)	104.530(2)
β, deg	108.32(3)	93.892(2)
γ, deg	80.84(3)	100.512(2)
V, $Å^3$	1202.9(2)	3646.0(2)
Z	2	2
ρ_{calc}, g/cm^3	1.480	1.542
μ (MoKα), cm^{-1}	12.36	12.88
Crystal size, mm	0.35 x 0.15 x 0.15	0.45 x 0.35 x 0.20
T, K	293	113

$R(F)^a$	0.034	0.035
$R_w(F^2)^a$	0.030	0.049

[a] $R(F) = \Sigma||F_0|-|F_C||/\Sigma|F_0|$, $Rw(F^2) = (\Sigma w||F_0^2|-|F_C^2||/\Sigma w|F_0^2|^2)^{1/2}$

Table I-6 Selected bond lengths (Å) for α- and γ-$[Fe_2(imid)_4(bipy)]_x$, with estimated standard deviations in parentheses.

α-phase		γ-phase	
Fe(1)—N(1)	2.262(2)	Fe(1)—N(10)	2.314(2)
Fe(1)—N(2)	2.299(2)	Fe(1)—N(9)	2.217(2)
Fe(1)—N(3)	2.196(2)	Fe(1)—N(7)	2.207(2)
Fe(1)—N(5)	2.153(2)	Fe(1)—N(3)	2.162(3)
Fe(1)—N(8)	2.192(2)	Fe(1)—N(1)	2.195(2)
Fe(1)—N(10)	2.153(2)	Fe(1)—N(5)	2.136(2)
Fe(2)—N(4)	2.024(2)	Fe(2)—N(6)	2.019(2)
Fe(2)—N(6)	2.036(2)	Fe(2)—N(4)	2.032(2)
Fe(2)—N(7)	2.027(2)	Fe(2)—N(2)	2.030(2)
Fe(2)—N(9)	2.028(2)	Fe(2)—N(11)	2.024(2)

Fe(3)—N(12)	2.186(2)
Fe(3)—N(13)	2.152(3)
Fe(3)—N(15)	2.155(2)
Fe(3)—N(17)	2.263(2)
Fe(3)—N(18)	2.302(2)
Fe(3)—N(22)	2.187(2)
Fe(4)—N(16)	2.035(2)
Fe(4)—N(19)	2.024(2)
Fe(4)—N(21)	2.039(2)
Fe(4)—N(23)	2.037(2)
Fe(5)—N(20)	2.011(2)
Fe(5)—N(24)	2.019(2)
Fe(5)—N(25)	2.016(2)
Fe(5)—N(27)	2.003(2)
Fe(5)—N(29)	1.957(2)
Fe(5)—N(30)	1.970(2)
Fe(6)—N(8)	2.059(2)
Fe(6)—N(14)	2.056(3)
Fe(6)—N(26)	2.034(2)
Fe(6)—N(28)	2.038(2)

Table I-7 Selected bond angles (°) for α- and γ-$[Fe_2(imid)_4(bipy)]_x$, with estimated standard deviations in parentheses.

α-phase		γ-phase	
N(1)—Fe(1)—N(2)	71.78(9)	N(10)—Fe(1)—N(9)	72.54(9)
N(1)—Fe(1)—N(3)	89.68(9)	N(10)—Fe(1)—N(7)	90.02(9)
N(1)—Fe(1)—N(5)	168.22(9)	N(10)—Fe(1)—N(3)	169.59(9)
N(1)—Fe(1)—N(8)	88.91(8)	N(10)—Fe(1)—N(1)	81.33(9)
N(1)—Fe(1)—N(10)	97.12(9)	N(10)—Fe(1)—N(5)	96.67(9)
N(2)—Fe(1)—N(3)	88.99(9)	N(9)—Fe(1)—N(7)	90.02(9)
N(2)—Fe(1)—N(5)	96.51(9)	N(9)—Fe(1)—N(3)	98.33(9)
N(2)—Fe(1)—N(8)	83.61(9)	N(9)—Fe(1)—N(1)	89.42(9)
N(2)—Fe(1)—N(10)	168.33(9)	N(9)—Fe(1)—N(5)	169.21(9)
N(3)—Fe(1)—N(5)	88.75(9)	N(7)—Fe(1)—N(3)	87.98(9)
N(3)—Fe(1)—N(8)	172.53(9)	N(7)—Fe(1)—N(1)	172.19(9)
N(3)—Fe(1)—N(10)	94.65(9)	N(7)—Fe(1)—N(5)	93.82(9)
N(5)—Fe(1)—N(8)	91.14(9)	N(3)—Fe(1)—N(1)	91.13(9)
N(5)—Fe(1)—N(10)	94.65(9)	N(3)—Fe(1)—N(5)	92.3(1)
N(8)—Fe(1)—N(10)	92.80(9)	N(1)—Fe(1)—N(5)	93.97(9)
N(4)—Fe(2)—N(6)	111.3(1)	N(6)—Fe(2)—N(4)	108.7(1)

N(4)—Fe(2)—N(7)	110.15(9)	N(6)—Fe(2)—N(2)	109.1(1)
N(4)—Fe(2)—N(9)	106.96(9)	N(6)—Fe(2)—N(11)	117.8(1)
N(6)—Fe(2)—N(7)	105.33(9)	N(4)—Fe(2)—N(11)	102.9(1)
N(6)—Fe(2)—N(9)	105.47(9)	N(2)—Fe(2)—N(11)	107.4(1)
N(7)—Fe(2)—N(9)	117.6(1)	N(2)—Fe(2)—N(11)	107.4(1)
		N(12)—Fe(3)—N(13)	86.85(9)
		N(12)—Fe(3)—N(15)	93.51(9)
		N(12)—Fe(3)—N(17)	87.41(9)
		N(12)—Fe(3)—N(18)	89.78(9)
		N(12)—Fe(3)—N(22)	174.26(9)
		N(13)—Fe(3)—N(15)	97.3(1)
		N(13)—Fe(3)—N(17)	163.39(9)
		N(13)—Fe(3)—N(18)	92.67(9)
		N(13)—Fe(3)—N(22)	92.21(9)
		N(15)—Fe(3)—N(17)	98.56(9)
		N(15)—Fe(3)—N(18)	169.6(1)
		N(15)—Fe(3)—N(22)	92..22(9)
		N(17)—Fe(3)—N(18)	71.73(9)
		N(17)—Fe(3)—N(22)	91.95(9)
		N(18)—Fe(3)—N(22)	84.61(8)
		N(16)—Fe(4)—N(19)	109.1(1)

N(16)—Fe(4)—N(21)	114.8(1)
N(16)—Fe(4)—N(23)	104.2(1)
N(19)—Fe(4)—N(21)	112.7(1)
N(19)—Fe(4)—N(23)	109.9(1)
N(21)—Fe(4)—N(23)	105.7(1)
N(20)—Fe(5)—N(24)	88.41(1)
N(20)—Fe(5)—N(25)	92.31(9)
N(20)—Fe(5)—N(27)	177.71(9)
N(20)—Fe(5)—N(29)	90.9(1)
N(20)—Fe(5)—N(30)	90.98(9)
N(24)—Fe(5)—N(25)	89.2(1)
N(24)—Fe(5)—N(27)	91.7(1)
N(24)—Fe(5)—N(29)	176.8(1)
N(24)—Fe(5)—N(30)	95.1(1)
N(25)—Fe(5)—N(27)	89.98(9)
N(25)—Fe(5)—N(29)	94.0(1)
N(25)—Fe(5)—N(30)	174.7(1)
N(27)—Fe(5)—N(29)	88.9(1)
N(27)—Fe(5)—N(30)	86.73(1)
N(29)—Fe(5)—N(30)	81.8(1)
N(8)—Fe(6)—N(14)	114.8(1)

N(8)—Fe(6)—N(26)	105.95(9)
N(8)—Fe(6)—N(28)	104.74(9)
N(14)—Fe(6)—N(26)	102.7(1)
N(14)—Fe(6)—N(28)	100.8(9)
N(26)—Fe(6)—N(28)	128.3(1)

Table I-8 Crystallographic data for β-$[Fe_2(imid)_4(bipy)]_x$.

Molecular formula	$C_{22}H_{20}Fe_2N_{10}$
fw	536.16
Crystal system	triclinic
Space group	$P\bar{1}$ (No. 2)
a, Å	17.1338(4)
b, Å	18.5426(4)
c, Å	23.6199(3)
α, deg	80.424(3)
β, deg	75.364(3)
γ, deg	80.826(3)
V, $Å^3$	7105.1(2)

Z	2
ρ_{calc}, g/cm^3	1.440
μ (MoKα), cm^{-1}	12.36
Crystal size, mm	0.25 x 0.20 x 0.20
T, K	143
$R(F^a, I \geq 2\sigma(I))$	0.145
$R_w(F^2)^a$	0.339

[a] $R(F) = \Sigma||F_0|-|F_C||/\Sigma|F_0|$, $Rw(F^2) = (\Sigma w||F_0^2|-|F_C^2||/\Sigma w|F_0^2|^2)^{1/2}$

Table I-9 Selected bond angles (°) for β-$[Fe_2(imid)_4(bipy)]_x$, with estimated standard deviations in parentheses.

Fe(1a)—N(5a)	2.139(2)	Fe(1a)—N(3)	2.144(2)
Fe(1a)—N(8a)	2.193(2)	Fe(1a)—N(20)	2.197(2)
Fe(1a)—N(2a)	2.263(2)	Fe(1a)—N(1a)	2.299(2)
Fe(1b)—N(13)	2.155(2)	Fe(1b)—N(38)	2.170(2)
Fe(1b)—N(10a)	2.181(2)	Fe(1b)—N(15)	2.188(2)
Fe(1b)—N(2b)	2.215(2)	Fe(1b)—N(1b)	2.280(2)
Fe(1c)—N(18)	2.145(2)	Fe(1c)—N(23)	2.174(2)

Fe(1c)—N(25)	2.201(2)	Fe(1c)—N(48)	2.218(2)
Fe(1c)—N(2c)	2.246(2)	Fe(1c)—N(1c)	2.273(2)
Fe(1d)—N(28)	2.130(3)	Fe(1d)—N(30)	2.159(2)
Fe(1d)—N(33)	2.167(2)	Fe(1d)—N(35)	2.185(2)
Fe(1d)—N(1d)	2.232(2)	Fe(1d)—N(2d)	2.276(2)
Fe(1e)—N(45)	2.155(2)	Fe(1e)—N(50)	2.168(2)
Fe(1e)—N(40)	2.170(2)	Fe(1e)—N(43)	2.189(2)
Fe(1e)—N(2e)	2.220(2)	Fe(1e)—N(1e)	2.310(2)
Fe(1f)—N(59)	2.132(2)	Fe(1f)—N(58)	2.140(2)
Fe(1f)—N(55)	2.187(2)	Fe(1f)—N(1f)	2.196(2)
Fe(1f)—N(52)	2.199(2)	Fe(1f)—N(2f)	2.254(2)
Fe(2a)—N(9a)	2.031(2)	Fe(2a)—N(7a)	2.039(2)
Fe(2a)—N(57)	2.046(2)	Fe(2a)—N(6a)	2.046(2)
Fe(2b)—N(19)	2.018(2)	Fe(2b)—N(17)	2.023(2)
Fe(2b)—N(16)	2.039(2)	Fe(2b)—N(14)	2.047(2)
Fe(2c)—N(27)	2.017(2)	Fe(2c)—N(56)	2.038(3)
Fe(2c)—N(26)	2.040(2)	Fe(2c)—N(29)	2.041(2)
Fe(2d)—N(36)	2.015(2)	Fe(2d)—N(39)	2.024(2)
Fe(2d)—N(37)	2.036(2)	Fe(2d)—N(24)	2.044(2)
Fe(2e)—N(49)	2.004(2)	Fe(2e)—N(46)	2.013(2)
Fe(2e)—N(47)	2.017(3)	Fe(2e)—N(51)	2.027(2)

Fe(2f)—N(44)	2.027(2)	Fe(2f)—N(34)	2.028(2)
Fe(2f)—N(4)	2.034(2)	Fe(2f)—N(60)	2.044(2)

N(5a)—Fe(1a)—N(3)	94.02(9)	N(5a)—Fe(1a)—N(8a)	90.32(9)
N(5a)—Fe(1a)—N(20)	91.28(9)	N(5a)—Fe(1a)—N(2a)	168.13(9)
N(5a)—Fe(1a)—N(1a)	96.43(9)	N(3)—Fe(1a)—N(8a)	95.07(9)
N(3)—Fe(1a)—N(20)	92.93(9)	N(3)—Fe(1a)—N(2a)	97.83(9)
N(3)—Fe(1a)—N(1a)	168.34(9)	N(8a)—Fe(1a)—N(20)	171.71(9)
N(8a)—Fe(1a)—N(2a)	89.37(9)	N(8a)—Fe(1a)—N(1a)	90.03(9)
N(20)—Fe(1a)—N(2a)	87.40(9)	N(20)—Fe(1a)—N(1a)	81.71(9)
N(2a)—Fe(1a)—N(1a)	71.70(9)	N(13)—Fe(1b)—N(38)	96.83(9)
N(13)—Fe(1b)—N(10a)	89.03(9)	N(13)—Fe(1b)—N(15)	86.65(9)
N(13)—Fe(1b)—N(2b)	167.04(9)	N(13)—Fe(1b)—N(1b)	94.46(9)
N(38)—Fe(1b)—N(10a)	92.06(9)	N(38)—Fe(1b)—N(15)	93.52(9)
N(38)—Fe(1b)—N(2b)	95.95(9)	N(38)—Fe(1b)—N(1b)	168.23(1)
N(10a)—Fe(1b)—N(15)	173.31(1)	N(10a)—Fe(1b)—N(2b)	92.68(9)
N(10a)—Fe(1b)—N(1b)	84.80(9)	N(15)—Fe(1b)—N(2b)	90.41(9)
N(15)—Fe(1b)—N(1b)	90.44(9)	N(2b)—Fe(1b)—N(1b)	72.92(9)
N(18)—Fe(1c)—N(23)	95.44(9)	N(18)—Fe(1c)—N(25)	93.39(9)
N(18)—Fe(1c)—N(48)	94.65(9)	N(18)—Fe(1c)—N(2c)	167.72(9)
N(18)—Fe(1c)—N(1c)	95.59(9)	N(23)—Fe(1c)—N(25)	92.08(9)

N(23)—Fe(1c)—N(48)	87.94(9)	N(23)—Fe(1c)—N(2c)	96.52(9)
N(23)—Fe(1c)—N(1c)	168.92(9)	N(25)—Fe(1c)—N(48)	171.92(9)
N(25)—Fe(1c)—N(2c)	83.45(9)	N(25)—Fe(1c)—N(1c)	88.27(9)
N(48)—Fe(1c)—N(2c)	88.52(9)	N(48)—Fe(1c)—N(1c)	90.17(9)
N(2c)—Fe(1c)—N(1c)	72.51(9)	N(28)—Fe(1d)—N(30)	96.83(9)
N(28)—Fe(1d)—N(33)	87.64(9)	N(28)—Fe(1d)—N(35)	91.86(9)
N(28)—Fe(1d)—N(1d)	167.05(9)	N(28)—Fe(1d)—N(2d)	94.71(9)
N(30)—Fe(1d)—N(33)	94.57(9)	N(30)—Fe(1d)—N(35)	91.38(9)
N(30)—Fe(1d)—N(1d)	96.06(9)	N(30)—Fe(1d)—N(2d)	167.74(9)
N(33)—Fe(1d)—N(35)	174.05(9)	N(33)—Fe(1d)—N(1d)	90.04(9)
N(33)—Fe(1d)—N(2d)	90.04(8)	N(35)—Fe(1d)—N(1d)	89.13(9)
N(35)—Fe(1d)—N(2d)	84.09(9)	N(1d)—Fe(1d)—N(2d)	72.54(9)
N(45)—Fe(1e)—N(50)	94.20(9)	N(45)—Fe(1e)—N(40)	88.28(9)
N(45)—Fe(1e)—N(43)	89.94(9)	N(45)—Fe(1e)—N(2e)	167.49(9)
N(45)—Fe(1e)—N(1e)	95.37(9)	N(50)—Fe(1e)—N(40)	95.81(9)
N(50)—Fe(1e)—N(43)	91.25(9)	N(50)—Fe(1e)—N(2e)	98.27(8)
N(50)—Fe(1e)—N(1e)	169.10(1)	N(40)—Fe(1e)—N(43)	172.83(1)
N(40)—Fe(1e)—N(2e)	89.47(9)	N(40)—Fe(1e)—N(1e)	89.70(9)
N(43)—Fe(1e)—N(2e)	90.79(9)	N(43)—Fe(1e)—N(1e)	83.56(9)
N(2e)—Fe(1e)—N(1e)	72.31(9)	N(59)—Fe(1f)—N(58)	95.54(9)
N(59)—Fe(1f)—N(55)	88.76(9)	N(59)—Fe(1f)—N(1f)	168.91(9)

N(59)—Fe(1f)—N(52)	90.51(9)	N(59)—Fe(1f)—N(2f)	95.51(9)
N(58)—Fe(1f)—N(55)	93.11(9)	N(58)—Fe(1f)—N(1f)	95.54(9)
N(58)—Fe(1f)—N(52)	91.41(9)	N(58)—Fe(1f)—N(2f)	167.83(9)
N(55)—Fe(1f)—N(1f)	90.83(9)	N(55)—Fe(1f)—N(52)	175.47(9)
N(55)—Fe(1f)—N(2f)	92.19(9)	N(1f)—Fe(1f)—N(52)	89.03(9)
N(1f)—Fe(1f)—N(2f)	73.43(9)	N(52)—Fe(1f)—N(2f)	83.43(9)
N(9a)—Fe(2a)—N(7a)	107.79(9)	N(9a)—Fe(2a)—N(57)	121.74(9)
N(9a)—Fe(2a)—N(6a)	104.89(9)	N(7a)—Fe(2a)—N(57)	107.55(9)
N(7a)—Fe(2a)—N(6a)	110.75(1)	N(57)—Fe(2a)—N(6a)	103.87(1)
N(19)—Fe(2b)—N(17)	121.11(1)	N(19)—Fe(2b)—N(16)	110.79(1)
N(19)—Fe(2b)—N(14)	103.99(9)	N(17)—Fe(2b)—N(16)	103.86(9)
N(17)—Fe(2b)—N(14)	105.39(9)	N(16)—Fe(2b)—N(14)	111.63(9)
N(27)—Fe(2c)—N(56)	114.60(9)	N(27)—Fe(2c)—N(26)	101.65(9)
N(27)—Fe(2c)—N(29)	105.06(9)	N(56)—Fe(2c)—N(26)	110.12(9)
N(56)—Fe(2c)—N(29)	105.71(9)	N(26)—Fe(2c)—N(29)	119.96(9)
N(36)—Fe(2d)—N(39)	110.82(9)	N(36)—Fe(2d)—N(37)	117.48(9)
N(36)—Fe(2d)—N(24)	104.15(9)	N(39)—Fe(2d)—N(37)	108.69(9)
N(39)—Fe(2d)—N(24)	109.56(9)	N(37)—Fe(2d)—N(24)	105.76(9)
N(49)—Fe(2e)—N(46)	102.63(9)	N(49)—Fe(2e)—N(47)	109.23(9)
N(49)—Fe(2e)—N(51)	116.70(9)	N(46)—Fe(2e)—N(47)	112.01(9)
N(46)—Fe(2e)—N(51)	106.94(9)	N(47)—Fe(2e)—N(51)	109.21(9)

N(44)—Fe(2f)—N(34)	109.88(9)	N(44)—Fe(2f)—N(4)	118.24(9)
N(44)—Fe(2f)—N(60)	105.60(1)	N(34)—Fe(2f)—N(4)	107.07(1)
N(34)—Fe(2f)—N(60)	112.57(1)	N(4)—Fe(2f)—N(60)	103.44(9)

Table I-10 Crystallographic data for $[Fe_4(imid)_8(terpy)]_x$.

Molecular formula	$C_{39}H_{35}Fe_4N_{19}$
fw	993.22
Crystal system	triclinic
Space group	$P\bar{1}$ (No. 2)
a/Å	11.351(2)
b/Å	13.628(1)
c/Å	15.748(4)
α, deg	113.550(3)
β, deg	103.696(3)
γ, deg	91.826(3)
V, Å^3	2147.6(6)
Z	2
D_c/g cm^{-3}	1.536
F(000)	1012.0

μ (MoKα)/cm^{-1}	13.77
Crystal size/mm	0.6 x 0.10 x 0.03
$2\theta_{max}$/°	56.0
Total reflections	18208
Unique reflections	8100
No. with $I \geq 3\sigma(I)$	4793
No. of variables	559
R; Rw (F, $I \geq 3\sigma(I)$)	0.039; 0.049
R; Rw (F^2, all data)	0.079; 0.114
gof	1.07

[a] Temperature 173 K, Rigaku/ADSC CCD diffractometer, Mo $K\alpha$ (λ = 0.71069), graphite monochromator, takeoff angle 6.0°, aperture 94.0 x 94.0 mm at a distance of 40.48 mm from the crystal, $\sigma^2(F_2) = (C + B)/\text{Lp2}$ (C = scan count, B = background count), function minimized $\Sigma w(|F_0^2|-|F_C^2|)^2$ where $w = 1/\sigma^2(F^2)$, $R(F) = \Sigma||F_0|-|F_C||/\Sigma|F_0|$, $Rw\ (F^2) = (\Sigma w||F_0^2|-|F_C^2||/\Sigma w|F_0^2|^2)^{1/2}$, and gof = $[\Sigma w(|F_0^2|-|F_C^2|)^2/(m-n)]^{1/2}$.

Table I-11 Selected bond lengths (Å) and angles (°) for $[Fe_4(imid)_8(terpy)]_x$.

Fe(1)—N(1)	2.023(4)	Fe(1)—N(2)	2.037(4)

Fe(1)—N(3)	2.025(4)	Fe(1)—N(4)	2.040(4)
Fe(2)—N(12)	2.017(4)	Fe(2)—N(10)	2.024(4)
Fe(2)—N(11)	2.030(4)	Fe(2)—N(9)	2.041(4)
Fe(3)—N(15)	2.072(4)	Fe(3)—N(8)	2.141(3)
Fe(3)—N(5)	2.148(4)	Fe(3)—N(13)	2.151(4)
Fe(3)—N(6)	2.156(3)	Fe(4)—N(18)	1.858(4)
Fe(4)—N(19)	1.961(4)	Fe(4)—N(17)	1.976(4)
Fe(4)—N(14)	1.992(3)	Fe(4)—N(16)	1.994(3)
Fe(4)—N(7)	2.002(4)		

N(1)—Fe(1)—N(3)	108.64(2)	N(1)—Fe(1)—N(2)	106.85(1)
N(1)—Fe(1)—N(4)	115.61(2)	N(3)—Fe(1)—N(2)	113.50(2)
N(3)—Fe(1)—N(4)	106.08(2)	N(2)—Fe(1)—N(4)	106.35(2)
N(12)—Fe(2)—N(10)	113.58(2)	N(12)—Fe(2)—N(11)	101.56(2)
N(12)—Fe(2)—N(9)	114.32(2)	N(10)—Fe(2)—N(11)	117.24(2)
N(10)—Fe(2)—N(9)	108.15(1)	N(11)—Fe(2)—N(9)	101.52(2)
N(15)—Fe(3)—N(8)	104.10(1)	N(15)—Fe(3)—N(5)	99.03(2)
N(15)—Fe(3)—N(13)	98.28(2)	N(15)—Fe(3)—N(6)	101.55(1)
N(8)—Fe(3)—N(5)	86.73(1)	N(8)—Fe(3)—N(13)	87.50(1)
N(8)—Fe(3)—N(6)	154.30(2)	N(5)—Fe(3)—N(13)	162.61(2)
N(5)—Fe(3)—N(6)	90.75(1)	N(13)—Fe(3)—N(6)	87.36(1)

N(18)—Fe(4)—N(19)	81.95(2)	N(18)—Fe(4)—N(17)	81.48(2)
N(18)—Fe(4)—N(14)	93.25(1)	N(18)—Fe(4)—N(16)	90.73(1)
N(18)—Fe(4)—N(7)	178.60(1)	N(19)—Fe(4)—N(17)	163.43(2)
N(19)—Fe(4)—N(14)	90.97(1)	N(19)—Fe(4)—N(16)	87.77(1)
N(19)—Fe(4)—N(7)	98.37(2)	N(17)—Fe(4)—N(14)	90.07(1)
N(17)—Fe(4)—N(16)	92.35(1)	N(17)—Fe(4)—N(7)	98.19(2)
N(14)—Fe(4)—N(16)	175.62(1)	N(14)—Fe(4)—N(7)	88.11(1)
N(16)—Fe(4)—N(7)	87.93(1)		

Table I-12 Crystallographic data for $[Fe(1\text{-Me-2-S-imid})_2 \cdot 0.5Cp_2Fe]_x$.[a]

Molecular formula	$C_{13}H_{15}Fe_{1.5}N_4S_2$
fw	375.18
Space group	P4/n (No. 85)
a, Å	13.2862(7)
c, Å	8.7665(4)
V, Å^3	1547.49(11)
Z	4
ρ_{calc}, g/cm^3	1.610
F(000)	768

radiation	Mo
μ, cm^{-1}	16.88
λ, Å	0.71069
R	0.077
R_w	0.063
T, °C	-93

---

[a] $R = \Sigma||Fo^2|-|Fc^2||/\Sigma|Fo^2|$, $R_W = (\Sigma w(|Fo^2|-|Fc^2|)^2/\Sigma w\, Fo^4)^{1/2}$

Table I-13 Selected bond lengths (Å) and angles (°) for [Fe(1-Me-2-S-imid)$_2$·0.5Cp$_2$Fe]$_x$.*

Fe(1)—S(1)	2.3677(8)	Fe(2)—N(1)	2.054(2)
S(1)—C(1)	1.732(3)	N(1)—C(1)	1.342(3)
N(1)—C(2)	1.383(4)	N(2)—C(1)	1.364(3)
N(2)—C(3)	1.375(4)	N(2)—C(4)	1.455(4)
C(2)—C(3)	1.358(4)		

S(1)—Fe(1)—S(1)[a]	110.05(2)	S(1)—Fe(1)—S(1)[b]	110.05(2)
S(1)—Fe(1)—S(1)[c]	108.32(4)	N(1)—Fe(2)—N(1)[d]	104.91(6)

N(1)—Fe(2)—N(1)^{e}	104.91(6)	N(1)—Fe(2)—N(1)^{c}	119.05(13)
Fe(1)—S(1)—C(1)	95.67(10)	Fe(2)—N(1)—C(1)	125.9(2)
Fe(2)—N(1)—C(2)	128.0(2)	C(1)—N(1)—C(2)	106.0(2)
C(1)—N(2)—C(3)	108.0(3)	C(1)—N(2)—C(4)	126.5(3)
C(3)—N(2)—C(4)	125.5(3)	S(1)—C(1)—N(1)	125.4(2)
S(1)—C(1)—N(2)	124.7(2)	N(1)—C(1)—N(2)	109.9(3)
N(1)—C(2)—C(3)	109.9(3)	N(2)—C(3)—C(2)	106.2(3)

*Superscript numbers refer to symmetry operation

(a) ½+y, 1-x, -z *(b)* 1-y, -1/2+x, -z *(c)* 3/2-x,1/2-y, z *(d)* ½+y,1-x,1-z
(e) 1-y, -1/2+x, 1-z